Assemblage des alliages de magnésium laminés à chaud par soudage friction malaxage et soudage laser : approche expérimentale vers une compréhension des propriétés mécaniques

Loreleï Commin

▶ **To cite this version:**

Loreleï Commin. Assemblage des alliages de magnésium laminés à chaud par soudage friction malaxage et soudage laser : approche expérimentale vers une compréhension des propriétés mécaniques. Sciences de l'ingénieur [physics]. Arts et Métiers ParisTech, 2008. Français. NNT : 2008ENAM0025 . pastel-00004253

HAL Id: pastel-00004253
https://pastel.hal.science/pastel-00004253

Submitted on 5 Dec 2008

HAL is a multi-disciplinary open access archive for the deposit and dissemination of scientific research documents, whether they are published or not. The documents may come from teaching and research institutions in France or abroad, or from public or private research centers.

L'archive ouverte pluridisciplinaire **HAL**, est destinée au dépôt et à la diffusion de documents scientifiques de niveau recherche, publiés ou non, émanant des établissements d'enseignement et de recherche français ou étrangers, des laboratoires publics ou privés.

N°: 2008 ENAM 0025

Ecole doctorale n° 432 : Sciences des Métiers de l'Ingénieur

T H È S E

pour obtenir le grade de

Docteur
de
l'École Nationale Supérieure d'Arts et Métiers

Spécialité "Matériaux, Mécanique"

présentée et soutenue publiquement
par

Loreleï COMMIN

le 9 octobre 2008

ASSEMBLAGE DES ALLIAGES DE MAGNESIUM LAMINES A CHAUD PAR SOUDAGE FRICTION MALAXAGE ET SOUDAGE LASER - APPROCHE EXPERIMENTALE VERS UNE COMPREHENSION DES PROPRIETES MECANIQUES -

Directeur de thèse : ***Laurent BARRALLIER***

Co-encadrement de la thèse : ***Jean-Éric MASSE***

Jury :

M. Fabrice PIERRON, Professeur, LMPF, ENSAM, Châlons en Champagne ..... Président
M. Philip WITHERS, Professeur, Manchester University ..... Rapporteur
M. Alexis DESCHAMPS, Professeur, SIMAP, INPG ..... Rapporteur
M. Laurent BARRALLIER, Professeur, MécaSurf, ENSAM, Aix en Provence ..... Examinateur
M. Jean-Éric MASSE, Maître de Conférences, MécaSurf, ENSAM, Aix en Provence ..... Examinateur
Mme. Myriam DUMONT, Maître de Conférences, IM2NP, Université Cézanne, Marseille .... Examinateur
M. Claudio DALLE DONNE, Docteur, Chef de département, EADS-IW ..... Examinateur

Laboratoire MécaSurf
ENSAM, CER d'Aix en Provence

L'ENSAM est un Grand Etablissement dépendant du Ministère de l'Education Nationale, composé de huit centres :
AIX-EN-PROVENCE ANGERS BORDEAUX CHÂLONS-EN-CHAMPAGNE CLUNY LILLE METZ PARIS

à ma famille, à Mme Charrier qui a cru en moi au tout début

Acknowledgements

I would like to thank Arts et Métiers ParisTech and especially MécaSurf laboratory for having given to me the opportunity to do such an interesting PhD thesis.

I would like to thank the panel for his participation, his enthousiastic and interesting discussion during my viva.

In particular, I wish to express my gratitude to my supervisor, Pr. Laurent Barrallier, MécaSurf laboratory, Arts et Métiers ParisTech, Aix en Provence, for having relied on me and for his valuable suggestions during this work.

Many thanks to Dr. Jean-Éric Masse, MécaSurf laboratory, Arts et Métiers ParisTech, Aix en Provence, for his supervision, advices and encouragement.

I would like to thank Pr. Fabrice Pierron, LMPF, Arts et Métiers ParisTech, Châlons en Champagne, for having taken the head of the panel and for his collabration to my work that made me join his team this year.

Special thanks to Dr. Myriam Dumont, IM2NP, Paul Cezanne University, Marseille, for her invaluable help and support throughout these three years.

I wish to express my appreciation to Pr. Philip Withers, Manchester Universtity for having accepted to review my PhD thesis, for his scientific interest in my work and his valuable suggestions and discussion.

I wish to express my gratitude to Pr. Alexis Deschamps, INPG, Grenoble, for having accepted to review my work and for his scientific views and relevant suggestions.

I would like to thank Dr. Claudio Dalle Donne, EADS-Innovation Works, for his participation to the panel and his valuable suggestions during the viva.

I would like to thank for their help :

- Dr. René Rotinat of LMPF, Arts et Métiers ParisTech, Châlons en Champagne, for his contribution through speckle interferometry analysis ;
- Dr. Wahib Saikaly and Dr.Thomas Neisius of CP2M laboratory, Paul Cezanne University, Marseille for their help with TEM investigation ;
- The neutron diffraction experiment local contacts : Darren Hughes and Olivier Isnard from ILL, Grenoble, Robert Wimpory from HMI, Berlin and Vincent Klosek from LLB, Saclay.

Many thanks also to the members of AEROMAG Project, Paul Lyon and Bruce Davis from Magnesium Elektron, Sébastien Wolff and Peter Juchmann from Salzgitter Magnesium Technologie, Gaël Khelifati from EADS-IWF and especially Tommy Brunzel, and Elke Hombergsmeier from EADS-IWG, Ottobrunn for their help with Friction Stir Welding.

Additionnal thanks go to for Jean-François Mathieu, Jean-Philippe Martin and the MécaSurf Team for their time and assistance.

Finally, I thank (soon-Dr.) Asma Belhadj for her friendship et my friends and family for their support.

Remerciements

Je remercie Arts et Métiers ParisTech et le laboratoire MécaSurf pour m'avoir apporté un sujet de thèse si intéressant.

Je remercie chaleureusement les membres du jury pour leur enthousiasme, leur discussion intéressante et l'intêret qu'ils ont porté à mon travail.

Je tiens à remercier Monsieur Laurent Barrallier, Professeur des Universités, MécaSurf, Arts et Métiers ParisTech, Aix en Provence, pour m'avoir accueilli dans son équipe et avoir dirigé mes travaux de recherche. Je le remercie pour son implication, ses compétences et pour m'avoir accordé sa confiance pour mener à bien le projet AEROMAG.

Je remercie aussi Monsieur Jean-Éric Masse, Maître de Conférences, MécaSurf, Arts et Métiers ParisTech, Aix en Provence, pour son co-encadrement de thèse et sa bonne humeur.

Je remercie Monsieur Fabrice Pierron, Professeur des Universités, LMPF, Arts et Métiers ParisTech, Châlons en Champagne, pour avoir accepté de présider mon jury de thèse et pour m'accueillir dans son équipe afin de prolonger notre collaboration.

Je remercie chaleureusement Madame Myriam Dumont, Maître de Conférences, IM2NP, Université Paul Cezanne, Marseille, pour avoir participé à mon jury de thèse, pour ses conseils et pour son aide précieuse tout au long de ces trois années.

Je remercie Monsieur Philip Withers, Professeur à l'Université de Manchester pour m'avoir fait l'honneur d'être rapporteur de ma thèse, pour l'intérêt qu'il a porté à mon travail, son apport à la discussion et ses suggestions intéressantes.

Je remercie Monsieur Alexis Deschamps, Professeur des Universités, INPG, Grenoble, d'avoir accepté d'être rapporteur de ce travail, pour son regard averti et ses remarques très pertinentes sur mon travail.

Je remercie Monsieur Claudio Dalle Donne, Chef du département "Metallic Technologies and Surface Engineering", EADS Innovation Works, pour m'avoir fait l'honneur d'être examinateur de ma thèse et pour ses suggestions judicieuses pendant ma soutenance.

Je remercie pour leur aide et leur participation à mes travaux :

- René Rotinat du LMPF, Arts et Métiers ParisTech, Châlons en Champagne pour l'analyse d'interférométrie speckle ;
- Wahib Saikaly et Thomas Neisius du CP2M, Université Paul Cezanne, Marseille pour leur aide pendant les essais MET.
- les "local contacts" sur les différents instruments de diffraction des neutrons que j'ai utilisés : Darren Hughes et Olivier Isnard de l'ILL, Grenoble, Robert Wimpory du HMI, Berlin et Vincent Klosek du LLB, Saclay.

Merci aux membres du projet AEROMAG, Paul Lyon et Bruce Davis de Magnesium Elektron, Sébastien Wolff et Peter Juchmann de Salzgitter Magnesium Technologie, Gaël Khelifati d'EADS-IWF et plus spécialement à Tommy Brunzel, et Elke Hombergsmeier d'EADS-IWG,

Ottobrunn pour leur aide pendant les essais Friction Stir Welding.

Merci à Jean-François Mathieu, Jean-Philippe Martin et l'équipe MécaSurf pour leur aide et leur accueil chaleureux.

Pour finir, je tiens à remercier la très prochainement-Dr. Asma Belhadj pour son amitié, mes amis et ma famille pour leur soutien.

Résumé étendu

Introduction

Cette thèse s'inscrit dans le cadre du projet européen AEROMAG qui réunit universités européennes (Arts et Métiers Paristech, INPG, Université de Vienne, Université de Patras, Université de Thessalie, Université de Naples), industries du secteur aéronautique (EADS, Airbus, Eurocopter) et industries du secteur du magnésium (MEL, Alonim, Palbam, Technion, Otto Fuchs, Salzgitter Magnesium Technologies) pour développer l'utilisation des alliages de magnésium corroyés dans l'industrie aéronautique. Les alliages d'aluminium majoritairement utilisés en aéronautique ont été largement étudiés en vue d'optimiser leurs propriétés structurelles, de sorte qu'il ne reste que très peu d'améliorations potentielles pour réduire le poids des structures en aluminium [1]. Les alliages de magnésium sont potentiellement intéressants pour ces applications en raison de leur faible densité, qui est de 35% inférieure à celle de l'aluminium. Leur utilisation a pour objectif de diminuer la masse de certaines structures et composants et ainsi de diminuer la consommation de carburant et, de ce fait, obtenir une réduction des coûts opérationnels et des émissions de polluants. L'objectif de ce projet est de démontrer la pertinence de l'utilisation d'alliages de magnésium à la place des alliages d'aluminium pour certains composants (alliages 5xxx pour les composants non structuraux et alliages 2xxx pour des applications structurelles secondaires) et donc de développer des alliages de magnésium ayant un rapport, propriétés mécaniques sur densité, plus important que celui des alliages d'aluminium.
Par ailleurs, les technologies d'assemblage de ces alliages méritent une étude plus précise, notamment l'application de différentes techniques de soudage aux alliages de magnésium. Deux techniques de soudage ont été sélectionnées en vue de leur application dans l'industrie aéronautique : le soudage laser et le soudage par Friction Malaxage (FSW). En effet l'assemblage de pièces de magnésium par soudage laser et FSW présente des soudures de meilleure qualité que celles obtenues par les procédés conventionnels (à arc) mais demande encore une évaluation précise des différents paramètres mis en jeu [2]. Les alliages de magnésium qui ont servi de matériau d'étude à cette thèse ont été produit par laminage à chaud par un des partenaires du projet : Salzgitter Magnesium Technologie. Le laminage à chaud de ces alliages a donné lieu à une étude propre au sein du projet AEROMAG, car c'est une opération très délicate en raison de la mauvaise formabilité du magnésium. Les alliages de magnésium étudiés sont l'AZ31 pour sa relativement bonne formabilité, l'AZ61 pour l'amélioration des propriétés mécaniques qu'il procure comparativement à l'AZ31 et le WE43 pour sa meilleure résistance à la corrosion. L'apport de cette thèse au projet européen AEROMAG consiste en deux axes principaux.
Tout d'abord, l'objectif sera de déterminer et d'optimiser les paramètres des différents procédés de soudages cités précédemment. Les procédés de soudage seront instrumentés de manière à déterminer l'influence de l'apport de chaleur et des déformations (pour le FSW) générées lors du

soudage. Ensuite, l'étude se focalisera sur la caractérisation de la microstructure et des propriétés mécaniques des joints soudés par rapport à celle des alliages de base.

Matériaux étudiés et techniques expérimentales employées

Cette étude porte sur des alliages de magnésium laminés à chaud (AZ31, AZ61 et WE43). En raison de la structure cristalline hexagonale compacte du magnésium, les alliages de magnésium ont une faible formabilité, ce qui rend les procédés de mise en forme par déformation, comme le laminage, très difficile à mettre en oeuvre. Quelques études portent qur l'AZ31 laminé [3, 4, 5] mais les alliages AZ61 et WE43 ont été laminés avec succès pour la première fois dans le cadre de ce projet par Salzgitter Magnesium Technologie. L'assemblage de ces alliages a été fait par soudage Friction Malaxage au Centre Commun de Recherche d'EADS en France (EADS-IWF) et en Allemagne (EADS-IWG), par soudage laser $C0_2$ au laboratoire MécaSurf d'Arts et Métiers Paristech et par laser Nd :YAG à EADS-IWF. Dans un premiers temps des joints pleine matière ont été effectués afin de déterminer le Domaine de Soudabilité Opérationnel (DSO) puis des joints bord à bord ont été produits pour l'étude microstructurale et mécanique des soudures. Les essais de soudage ont été instrumentés à l'aide de thermocouples (pour le soudage FSW et laser CO_2) et de jauges de déformation (pour le soudage FSW) afin de relier les paramètres de soudage aux températures et aux déformations générées par les procédés. L'évolution de la microstructure (nature des phases, taille de grains, précipitation, textures) lors du soudage a été étudiée grâce aux techniques suivantes :

- diffraction des rayons X (DRX) ;
- diffraction des neutrons (DRN) ;
- microscopie optique ;
- microscopie électronique à balayage (MEB) couplée à de la Spectroscopie à Dispersion d'Energie (EDS) et à de la diffraction des électrons rétro-diffusés (EBSD) ;
- microscope électronique à balayage à effet de champ (SFEG) ;
- microscope électronique à transmission (MET).

L'évolution de la microdureté a été déterminée par des essais Vickers et celle du comportement mécanique par des essais de traction, dont certains couplés à de l'interférométrie speckle pour étudier la localisation des déformations. Les contraintes résiduelles ont été analysées par diffraction des rayons X et des neutrons.

Soudage des alliages de magnésium

La détermination du domaine de soudabilité opérationnel pour le soudage FSW et laser CO_2 a été effectuée par soudage pleine matière. Les paramètres critiques suivants on été identifiés pour chaque procédé de soudage :

Pour le FSW :

- Vitesse de rotation de l'outil ;
- Vitesse de soudage ;
- Géométrie de l'outil ;
- Force appliquée.

Pour le Laser CO_2 :

- Puissance du faisceau ;

– Vitesse de soudage ;
– Distance focale ;
– Protection gazeuse.

Une large gamme de paramètres de soudages a été balayée de manière à étudier leur influence respective. A partir de l'étude des défauts observés dans les soudures, les domaines de soudabilité opérationnels ont été établis pour chacun des procédés (Figure 1 et Figure 2).

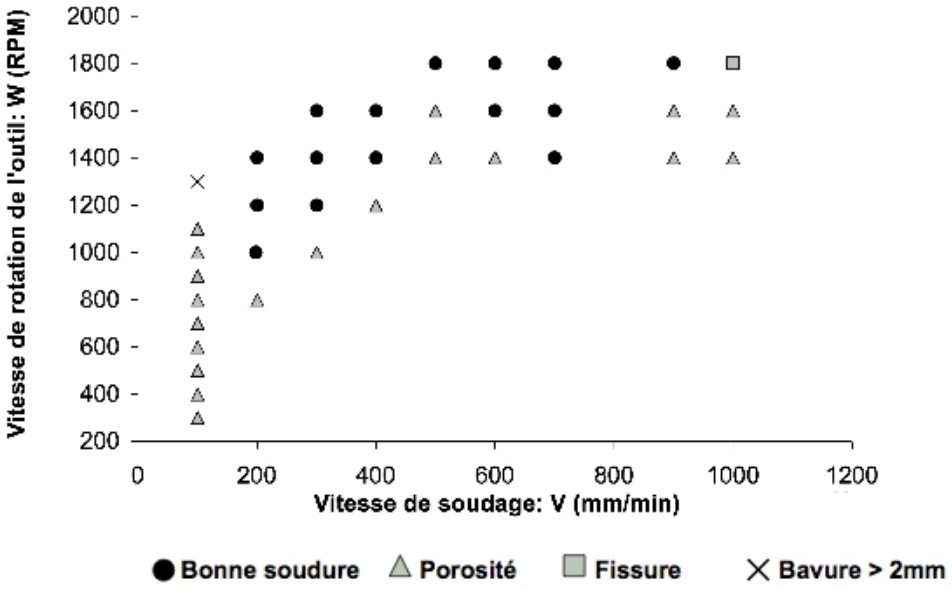

Fig. 1 – Domaine de soudabilité opérationnel du soudage FSW (diamètre du pion 4 mm, diamètre de l'épaulement 10 mm) pour l'AZ31.

Les essais de soudage bord à bord ont été intrumentés à l'aide de thermocouples (Figure 3).

L'étude du trou en fin de soudure FSW a permis de caractériser les flux de matière et la formation du joint soudé. La microstructure de la bavure conséquente au FSW montre des zones recristallisées et des zones maclées, décrivant ainsi l'influence des déformations subies.

Caratérisation des soudures d'AZ31 optimisées

Suite à la détermination des domaines de soudabilité opérationnels, des joints soudés bord à bord ont été produits par FSW et par laser avec des paramètres optimisés (1000 tr/min, 200 mm/min pour le FSW et 2,4 kW, 7000 mm/min pour le soudage laser). L'étude s'est focalisée sur l'alliage AZ31. La microstructure des joints soudés FSW se décompose en quatre zones : noyau (nugget), zone affectée thermomécaniquement (ZATM), zone affectée thermiquement (ZAT) et matériau de base (Figure 4) ; tandis que les joints soudés laser comprennent trois zones : zone fondue, zone affectée thermiquement (ZAT) et matériau de base (Figure 5).

La taille de grains et l'évolution de la précipitation dans chacune des zones microstructurales citées précedemment a été étudiée. Le matériau de base (AZ31 laminé à chaud) est constitué de

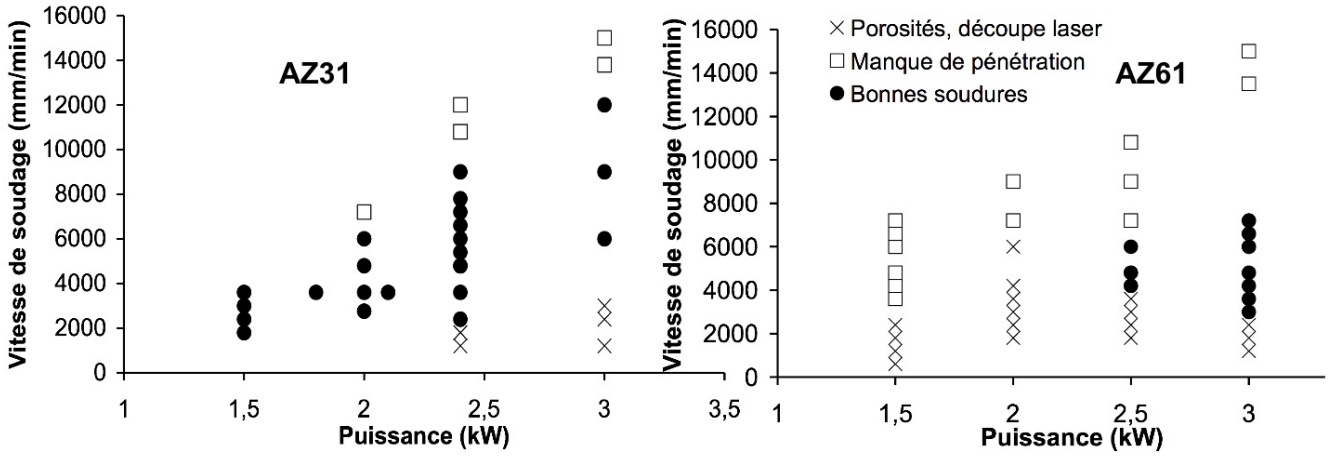

FIG. 2 – Domaine de soudabilité opérationnel du soudage laser CO_2 (f=0mm, débit gazeux d'hélium = 40 l/min) pour l'AZ31 et l'AZ61.

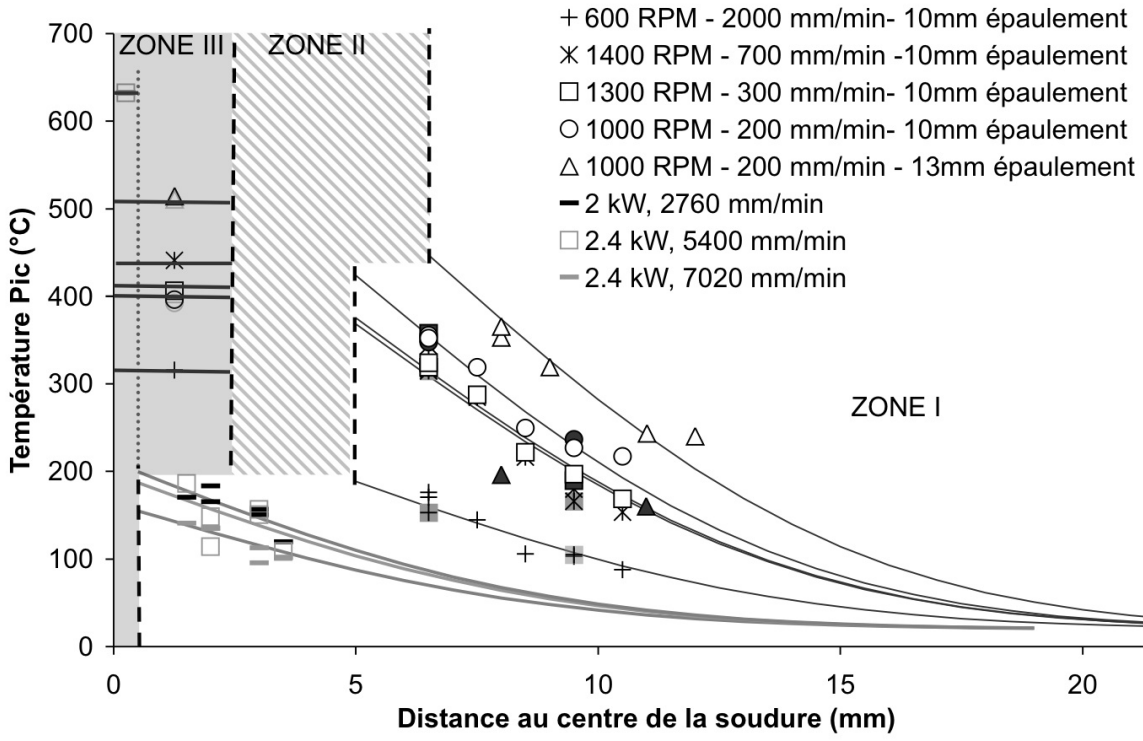

FIG. 3 – Évolution de la température lors du soudage FSW et laser. Les points de donnée grisés correspondent au côté avançant du FSW.

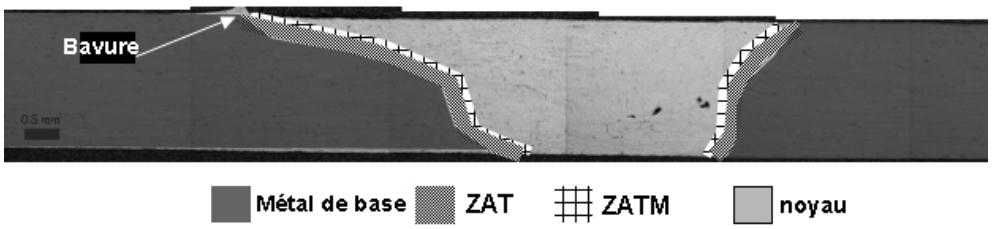

FIG. 4 – Microstructure des joints soudés FSW.

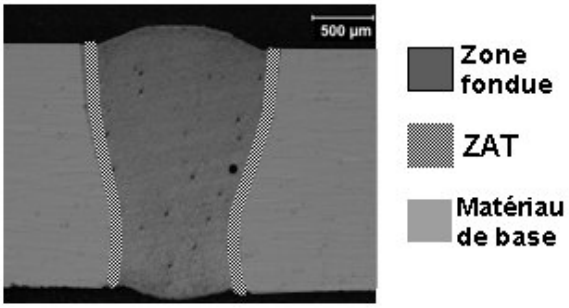

FIG. 5 – Microstructure des joints soudés laser.

petits grains équiaxes de 10 μm de diamètre. Ce n'est pas un alliage à précipitation mais on note la présence de précipités Al_8Mn_5 intergranulaires de l'ordre de quelques microns et des précipités Al_8Mn_5 intragranulaires nanométriques. Le laminage a produit une très forte texture selon le plan basal du magnésium. Le soudage FSW de l'AZ31 laminé entraîne une évolution de la taille de grains (affinement dans le noyau, grains déformés dans la ZATM) mais pas de modification de la précipitation, tandis que le soudage laser donne lieu à l'apparition de $Mg_{17}(Al,Zn)_{12}$ dans la zone fondue et à la conservation de la taille de grains. L'apparition de bandes de cisaillement suite au soudage dans la ZAT a été identifiée. En ce qui concerne l'évolution de l'orientation des grains, le FSW entraîne un alignement de la normale au plan basal avec la direction de soudage (Figure 6) et le soudage laser crée une texture quelconque dans la zone fondue (Figure 7).

La faible anisotropie élastique de l'AZ31 a été vérifiée et ainsi les analyses de contraintes ont été menées en négligeant l'influence des textures. Les procédés de soudage génèrent des contraintes résiduelles liées aux fortes déformations du FSW, à la resolidification lors du soudage laser et au bridage des tôles durant le soudage. Des pics de contraintes en traction sont observés dans la ZATM dans le sens longitudinal et en compression dans le noyau dans le sens transverse. Des contraintes de traction sont générées dans la zone fondue lors du soudage laser. Ensuite, l'étude s'est portée sur l'évolution des propriétés mécaniques. Les profils de microdureté à travers les joints soudés laser et FSW n'ont pas révélé de variation importante. Les essais de traction du matériau de base AZ31 laminé ont montré une anisotropie des propriétés mécaniques. Une chute importante des propriétés mécaniques est observée après soudage FSW (Figure 8). Le couplage des essais de traction avec de l'interférométrie speckle a montré une localisation des déformations

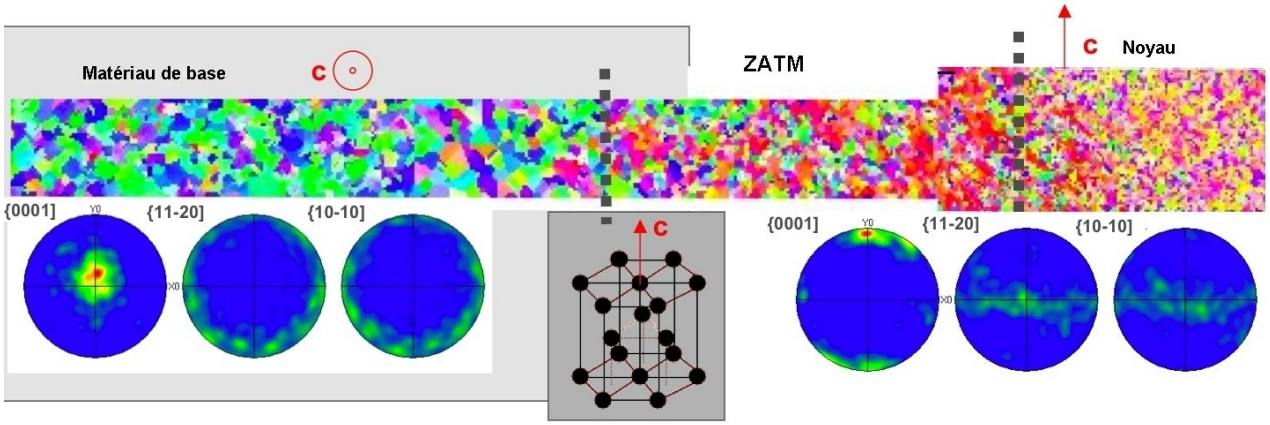

FIG. 6 – Cartes EBSD d'une soudure FSW et les figures de pôle correspondantes. L'analyse a été faite 100 μm sous la surface supérieure du joint soudé.

dans la ZATM. C'est dans cette zone que s'est produite la rupture des échantillons. L'analyse des faciès de rupture a révélé des zones de rupture à la fois ductile et fragile. La rupture des joints soudés laser s'est produite dans le matériau de base, mais même si la résistance maximale de l'AZ31 est conservée, il y a eu une diminution de la limite d'élasticité et de l'allongement à la rupture (Figure 8).

Des traitements thermiques (mise en solution, revenu) de relaxation des contraintes ont été pratiqués sur les soudures et les échantillons traités ont été testés en traction. En ce qui concerne les soudures FSW les propriétés initiales de l'AZ31 n'ont pu être recouvrées. Les traitements de détente ont permis de restaurer la ductilité dans le cas des soudures laser.

Discussion générale

Les résultats obtenus dans cette étude permettent une meilleure compréhension des relations entre les procédés de soudage, la qualité des soudures obtenues, la microstructure et les propriétés mécaniques de joints soudés. Grâce aux mesures de températures pendant le soudage, une relation a pu être établie entre les paramètres de soudage et les températures générées :

$$\frac{T_{\text{noyau}}}{Tm} = K.\left(\frac{W^2}{V.10^4}\right)^{\alpha} \tag{1}$$

avec Tm = 610 °C la température de fusion de l'AZ31, et les constantes α = 0.0442 et K = 0.8052 pour le soudage FSW.

Pour le soudage laser, un paramètre clé permettant de rationnaliser les propriétés du matériau après soudage est l'apport de chaleur (H). Cet apport de chaleur peut être relié aux paramètres de soudage :

$$\mathrm{H} = \eta.\left(\frac{P}{V}\right) \tag{2}$$

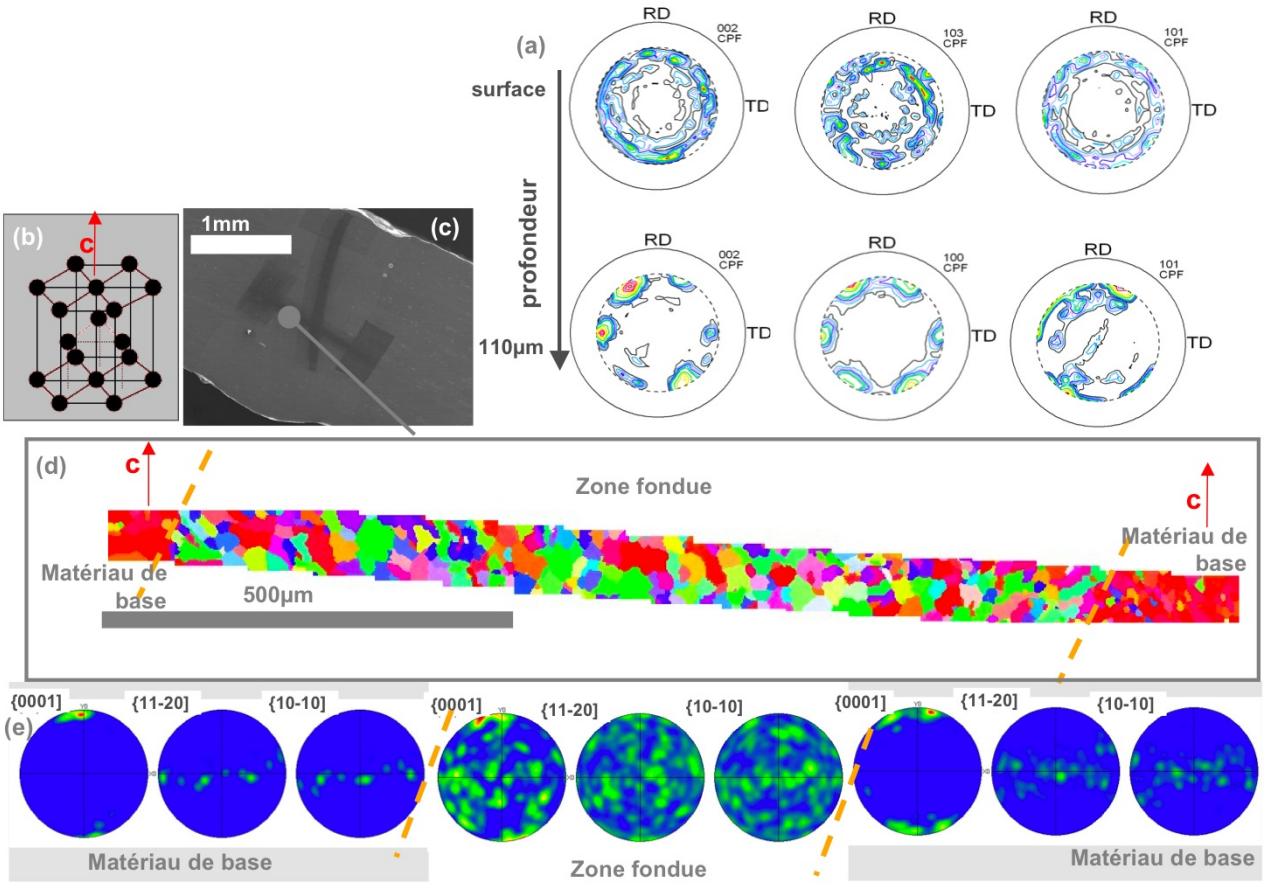

FIG. 7 – (a) Figures de pôle de la zone fondue déterminées par DRX , (b) schéma de la structure hexagonale compacte (c) localisation de l'analyse EBSD,l'analyse a été faite à mi-épaisseur dans la section de la soudure, (d) cartes EBSD de la section du joint soudé laser et (e) figures de pôle correspondantes.

avec P la puissance du laser, V la vitesse de soudage et η l'efficacité du soudage, (ici on considère η=1). Les conditions pour obtenir des soudures satisfaisantes ont pu être établies :

- une température de soudage FSW minimale d'environ 410˚C (c.a.d. $W^2/V > 4000$ tr^{2}min^{-1}.mm^{-1}) ;
- un apport de chaleur entre 20 et 45 J/mm pour le soudage laser CO_2.

Une importante diminution des propriétés mécaniques a été observée suite au soudage FSW comparée au soudage laser. Le comportement est différent en raison des facteurs suivants :

- La microstructure : l'hétérogénéité de la taille de grains dans les joints soudés FSW n'influe pas sur le comportement mécanique des joints soudés. En ce qui concerne les joints soudés laser, la présence de la phase $Mg_{17}(Al,Zn)_{12}$ entraîne une diminution de la ductilité dans les joints soudés ;
- Les bandes de cisaillement : la présence de bandes de cisaillement entraîne une localisation des déformations dans ces zones et ainsi influence les propriétés mécaniques des joints

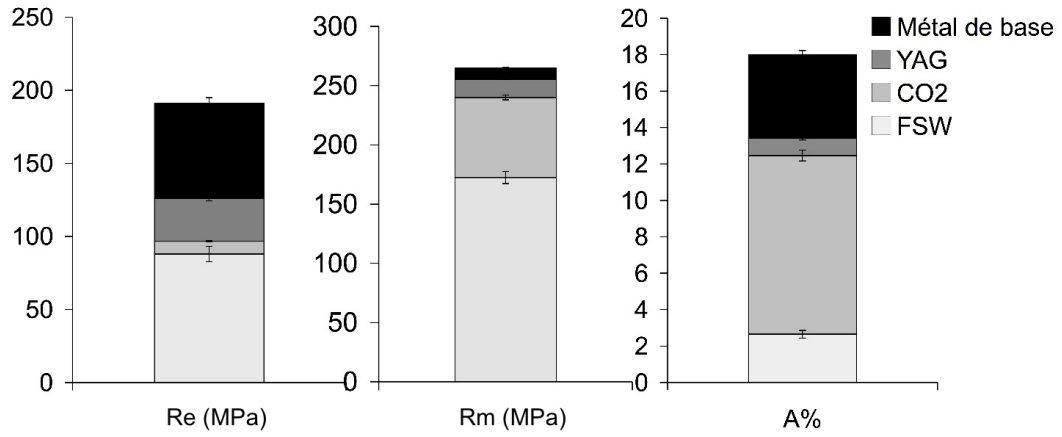

FIG. 8 – Propriétés mécaniques des joints soudés bord-à-bord comparées à celles du matériau de base AZ31.

soudés FSW et laser ;
- Les textures : l'évolution des textures lors du FSW et du soudage laser entraîne une modification des mécanismes de déformation ;
- Les contraintes résiduelles : l'important niveau des contraintes résiduelles dans la ZATM entraîne la rupture des joints soudés FSW (Figure 9). L'influence des contraintes résiduelles sur les joints soudés laser est beaucoup moins importante.

Les traitements thermiques après soudage n'ont pas permis de recouvrer les propriétés mécaniques du matériau de base. Cela s'explique par la perte de l'effet du laminage après soudage. Le même phénomène a été observé dans les alliages à durcissement structural AZ61 et WE43 laminés. Lorsqu'on compare les propriétés spécifiques des alliages de magnésium étudiés et des joints soudés aux alliages d'aluminium AA5083 et AA2024, on observe que les alliages de magnésium constituent une alternative envisageable (Figure 10).

Conclusions

Des alliages laminés de magnésium ont été utilisés dans cette étude. Ils présentent donc des spécificités par rapport aux alliages de fonderie généralement utilisés : une forte texture de fibre selon le plan basal et une fort écrouissage. L'état initial du matériau de base influence les propriétés mécaniques des soudures. En ce qui concerne le FSW, l'évolution des textures, l'apparition de bandes de cisaillement et le niveau élevé de contraintes résiduelles entraînent une importante diminution des propriétés mécaniques. Les traitements thermiques après soudage n'ont pas permis de restaurer les propriétés du matériau de base. Par contre, le soudage laser des tôles laminées s'est montré beaucoup plus approprié. Il entraîne moins de porosités que dans le cas de matériaux de fonderie. La perte de ductilité suite au soudage a pu être compensée grâce à des traitements thermiques. Ainsi, le soudage laser est plus adapté pour souder des alliages corroyés et a montré des résultats prometteurs dans le cadre de ce projet pour l'assemblage de tôles laminées d'AZ31. Lors de la comparaison avec le soudage laser d'alliages laminés de

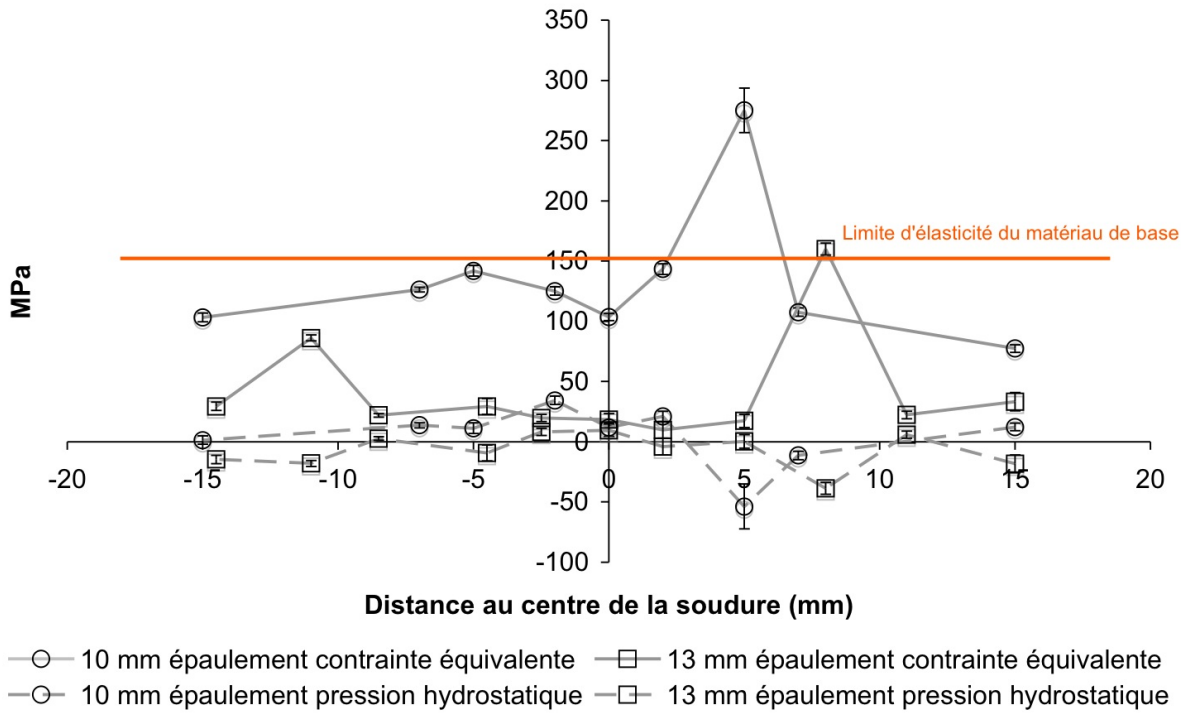

FIG. 9 – Évolution de la contrainte équivalente et de la pression hydrostatique après chargement mécanique dans les joints soudés FSW (1000 tr/min, 200 mm/min, pion : 5 mm pin / épaulement : 10 mm) and (1000 tr/min, 200 mm/min, pion : 5 mm pin / épaulement : 13 mm).

magnésium à durcissement structural, l'utilisation de traitements thermiques n'a pas permis de recouvrer les propriétés mécaniques de l'alliage de base. Enfin, en comparant les propriétés spécifiques des alliages de magnésium à celles des alliages d'aluminium AA5083 et AA2024, on observe que les alliages de magnésium constituent une alternative intéressante aux alliages d'aluminium.

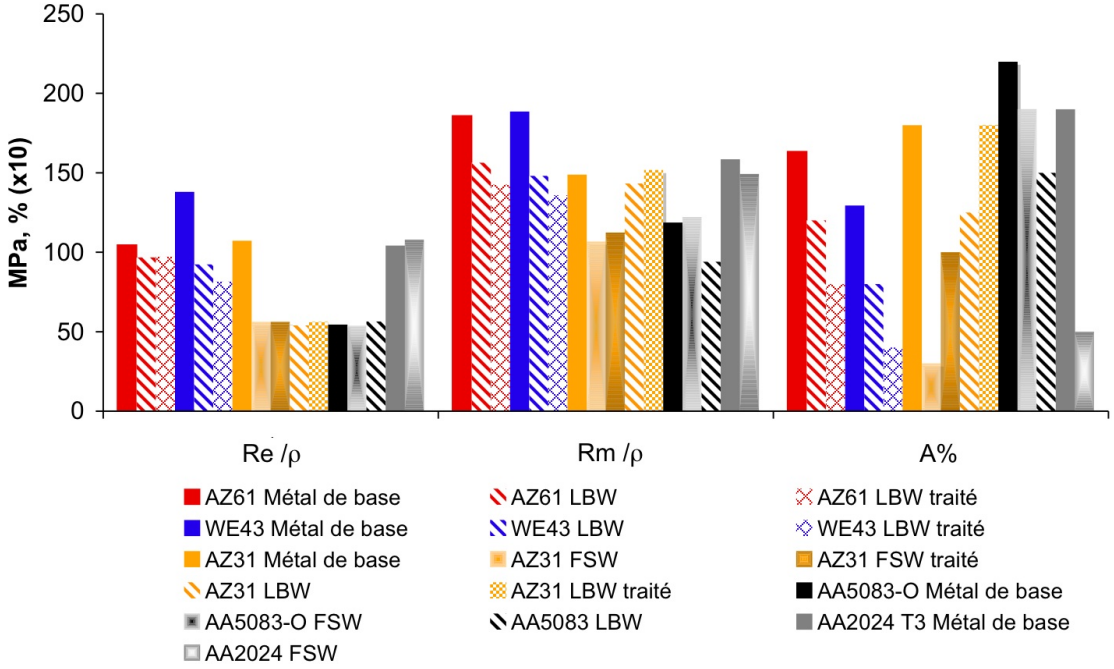

FIG. 10 – Propriétés spécifiques des alliages de magnésium et d'aluminium [6, 7, 8, 9].

List of Symbols

W	RPM|tr.min^{-1}	FSW Tool Rotation rate	Vitesse de rotation de l'outil FSW
V	mm.min^{-1}	Welding speed	Vitesse de soudage
F	kW	Laser Power	Puissance du laser
f	mm	Distance between the laser focal point position and the workpiece top surface	Distance entre le point focal du laser et la surface supérieure de la pièce
H	J.mm^{-1}	Heat input	Apport de chaleur
YS, R_e	MPa	Yield Strenght	Limite d'élasticité en traction uniaxiale
UTS, R_m	MPa	Ultimate tensile strength	Contrainte maximale en traction uniaxiale
$\underline{S}$		Stiffness tensor	Tenseur de Rigidité
$\underline{C}$		Compliance tensor	Tenseur de Souplesse
T	°C	Temperature	Température
t	s	Time	Temps
ρ	g.cm^{-3}	Density	Masse volumique
λ	nm	Wavelength	Longueur d'onde
E	GPa	Young Modulus	Module d'Young
ν		Poisson ratio	Coefficient de Poisson
σ_{eq}	MPa	Equivalent stress	Contrainte équivalente suivant von Mises
pH	MPa	Hydrostatic stress	Pression hydrostatique
d_{hkl}	nm	Interplanar distance	Distance interréticulaire des plans {hkl}
θ	°	Bragg angle	Angle de Bragg
$at.\%$		Atomic percent	Pourcentage atomique
$wt.\%$		Weight percent	Pourcentage massique
R	8,314 J.K^{-1}.mol^{-1}	Gas constant	Constante des gaz parfaits
HAZ|ZAT		Heat affected zone	Zone affectée thermiquement
TMAZ|ZATM		Thermomechanically affected zone	Zone affectée thermo-mécaniquement

Table des matières

1 Introduction **19**
1.1 Introduction générale 19
1.2 Soudage des alliages de magnésium 19
1.3 Objectifs du projet 20

2 Bibliographie **21**
2.1 Connaissances générales sur les alliages de magnésium 21
2.2 Procédés de soudage 24
2.3 Procédé Friction Malaxage 25
2.4 Procédé de soudage laser 32
2.5 Flux de matériau et histoire thermique due au soudage friction malaxage et au soudage laser 38
2.6 Evolution microstructurale lors du soudage friction malaxage 42
2.7 Evolution microstructurale lors du soudage laser 44
2.8 Evolution des propriétés mécaniques lors du soudage friction malaxage 45
2.9 Evolution des propriétés mécaniques lors du soudage laser 47
2.10 Conclusions 48

3 Matériaux, procédés et techniques expérimentales employées **51**
3.1 Matériaux analysés 51
3.2 Soudage 52
3.3 Techniques expérimentales 56

4 Procédés de soudage **67**
4.1 Introduction 67
4.2 Description des soudures FSW et laser 67
4.3 Qualité des soudures 67
4.4 Influence des paramètres de soudage sur la qualité des soudures 69
4.5 Détermination de l'histoire thermique 76
4.6 Flux de matériaux pendant le FSW 79

4.7 Conclusion 86

5 Caractérisation des soudures optimisées de l'alliage de magnésium de nuance AZ31 87
5.1 Introduction 87
5.2 Evolution de la microstructure 87
5.3 Evolution des textures 107
5.4 Evolution des contraintes résiduelles 114
5.5 Evolution des propriétés mécaniques 122
5.7 Conclusions 133

6 Discussion générale 135
6.1 Introduction 135
6.2 Relations entre les paramètres de soudage, la température de soudage, la microstructure et la qualité des soudures 135
6.3 Potentialité et comparaison des procédés FSW et laser pour assembler l'AZ31 140
6.4 Comparaison avec les alliages de magnésium à durcissement structural 144
6.5 Potentialité d'une application des alliages de magnésium dans l'industrie aéronautique 146

7 Conclusions 149

Contents

Acknowledgements **iii**

Remerciements **v**

Résumé étendu **vii**

List of Symbols **xvii**

1 Introduction **19**
1.1 General . . . 19
1.2 Welding magnesium alloys . . . 19
1.3 Project objectives and outline . . . 20

2 Literature survey **21**
2.1 Magnesium alloy basic knowledge . . . 21
2.1.1 Magnesium physical properties . . . 21
2.1.2 Alloying elements . . . 21
2.1.3 Magnesium alloy designation . . . 21
2.1.4 Magnesium-Aluminium binary system . . . 22
2.1.5 Magnesium slip system mechanisms . . . 22
2.1.6 Manufacturing magnesium alloys . . . 22
2.1.7 Magnesium alloy properties . . . 24
2.2 Welding process . . . 24
2.2.1 Introduction . . . 24
2.2.2 FSW and LBW of aluminium alloys . . . 25
2.3 Friction Stir Welding process . . . 25
2.3.1 Introduction . . . 25
2.3.2 Description of the process . . . 25
2.3.3 Process parameters . . . 25
2.3.3.1 Tool geometry . . . 25
2.3.3.2 Welding parameters . . . 28
2.3.3.3 Joint design . . . 31
2.3.3.4 Sample preparation . . . 32
2.3.3.5 Conclusion . . . 32
2.4 Laser Beam Welding process . . . 32
2.4.1 Introduction . . . 32

2.4.2 Principle of Laser Beam Welding . . . 33
2.4.3 CO_2 Laser Welding . . . 33
2.4.3.1 Laser power . . . 33
2.4.3.2 Welding speed . . . 34
2.4.3.3 Shielding gas . . . 35
2.4.3.4 Focal plane position . . . 36
2.4.3.5 Sample preparation . . . 36
2.4.3.6 Process tolerance . . . 36
2.4.4 Nd:YAG laser welding . . . 36
2.4.4.1 Laser power . . . 36
2.4.4.2 Welding speed . . . 37
2.4.4.3 Shielding gas . . . 37
2.4.4.4 Focal plane position . . . 37
2.4.4.5 Sample preparation . . . 38
2.4.5 Comparison between CO_2 and Nd :YAG lasers . . . 38
2.5 Material flow and thermal histories experienced during Friction Stir Welding and Laser Beam Welding . . . 38
2.5.1 Introduction . . . 38
2.5.2 Metal flow visualisation in FSW . . . 39
2.5.3 FSW Temperature distribution . . . 40
2.5.4 LBW Temperature distribution . . . 41
2.6 FSW Microstructural evolution . . . 42
2.6.1 Introduction . . . 42
2.6.2 FSW Nugget . . . 43
2.6.3 FSW Thermo-mechanically affected zone . . . 44
2.6.4 FSW Heat affected zone . . . 44
2.6.5 FSW texture evolution . . . 44
2.7 LBW Microstructural evolution . . . 44
2.8 FSW Weld properties . . . 45
2.8.1 Introduction . . . 45
2.8.2 Hardness . . . 45
2.8.3 Tensile properties . . . 46
2.8.4 Residual stress . . . 46
2.9 LBW weld properties . . . 47
2.9.1 Hardness . . . 47
2.9.2 Tensile properties . . . 48
2.9.3 Residual stress . . . 48
2.10 Conclusion . . . 48

3 Experimental **51**
3.1 Materials used . . . 51
3.1.1 Introduction . . . 51
3.1.2 AZ31 magnesium alloy . . . 51
3.1.3 AZ61 magnesium alloy . . . 51
3.1.4 WE43 magnesium alloy . . . 52
3.2 Welding Process . . . 52

3.2.1 Sample preparation prior to welding . . . 52
3.2.2 Friction Stir Welding . . . 52
3.2.3 Laser Beam Welding . . . 53
3.2.3.1 Nd:YAG LBW . . . 53
3.2.3.2 CO_2 LBW . . . 54
3.2.4 Measurements performed during welding processes . . . 54
3.2.4.1 Introduction . . . 54
3.2.4.2 FSW . . . 55
3.2.4.3 CO_2 LBW . . . 55
3.2.5 Weld quality control . . . 56
3.3 Experimental procedures . . . 56
3.3.1 Introduction . . . 56
3.3.2 Optical Microscopy . . . 57
3.3.2.1 Sample preparation . . . 57
3.3.2.2 Facilities . . . 57
3.3.3 Scanning Electron Microscopy and Energy Dispersive Spectroscopy . . . 58
3.3.3.1 Sample preparation . . . 58
3.3.3.2 Facilities . . . 58
3.3.4 Electron Back Scattered Diffraction . . . 58
3.3.4.1 Sample preparation . . . 58
3.3.4.2 Facilities . . . 59
3.3.5 Transmission Electron Microscope . . . 59
3.3.5.1 Sample preparation: Electropolishing . . . 59
3.3.5.2 Sample preparation: Focused Ion Beam . . . 59
3.3.5.3 TEM Facilities . . . 59
3.3.6 X-Ray Diffraction . . . 59
3.3.7 Neutron diffraction . . . 61
3.3.8 Microhardness tests . . . 64
3.3.9 Tensile tests . . . 64

4 Welding processes 67
4.1 Introduction . . . 67
4.2 Description of the Friction Stir Welds and of the Laser Beam Welds . . . 67
4.3 Weld quality . . . 67
4.4 Influence of processing parameters on weld quality . . . 69
4.4.1 FSW rotation rate, W (RPM) . . . 71
4.4.2 FSW welding speed, V (mm/min) . . . 71
4.4.3 FSW applied pressure, F (kN) . . . 71
4.4.4 LBW laser power, P (kW) . . . 73
4.4.5 LBW welding speed, V (mm/min) . . . 73
4.4.6 LBW focal distance, f (mm) . . . 74
4.4.7 LBW shielding gas flow, V (l/min) . . . 75
4.4.8 Influence of alloy conductivity on weld quality . . . 76
4.4.9 Process windows . . . 76
4.5 Thermal history determination . . . 76
4.5.1 Introduction . . . 76

4.5.2 Experimental data . . . 78
4.6 Material flow in FSW . . . 79
4.6.1 FSW hole . . . 79
4.6.2 FSW flash . . . 86
4.7 Conclusion . . . 86

5 Characterization of AZ31 optimized welds 87
5.1 Introduction . . . 87
5.2 Microstructure evolution . . . 87
5.2.1 AZ31-O base metal . . . 87
5.2.1.1 Grain structure . . . 87
5.2.1.2 Precipitation . . . 88
5.2.2 Microstructure observed after heat treatments . . . 91
5.2.3 Weld structure . . . 91
5.2.4 HAZ . . . 91
5.2.4.1 Shear bands . . . 92
5.2.5 Friction Stir Welding TMAZ . . . 99
5.2.6 Friction Stir Welding nugget . . . 100
5.2.7 Laser fusion zone . . . 102
5.2.8 Conclusion . . . 107
5.3 Texture evolution . . . 107
5.3.1 Introduction . . . 107
5.3.2 Base metal texture . . . 109
5.3.3 FSW texture evolution . . . 110
5.3.3.1 Neutron diffraction . . . 110
5.3.3.2 X-ray diffraction (XRD) . . . 111
5.3.3.3 Electron Back Scattered Diffraction (EBSD) . . . 112
5.3.4 LBW texture evolution . . . 112
5.3.5 Grain misorientations in FSW . . . 113
5.3.6 Conclusion . . . 114
5.4 Residual stress evolution . . . 114
5.4.1 Introduction . . . 114
5.4.2 Influence of the material anisotropy . . . 115
5.4.3 Residual stresses in AZ31 base metal . . . 116
5.4.4 Residual stresses induced by FSW . . . 117
5.4.4.1 Strain gages . . . 117
5.4.4.2 X-ray diffraction (XRD) . . . 118
5.4.4.3 Neutron Diffraction . . . 119
5.4.5 Comparison between the methods used . . . 121
5.4.6 Residual stresses induced by LBW . . . 121
5.4.7 Conclusion . . . 122
5.5 Evolution of mechanical properties . . . 122
5.5.1 Introduction . . . 122
5.5.2 FSW microhardness evolution . . . 122
5.5.3 LBW microhardness evolution . . . 123
5.5.4 Conventional tensile tests . . . 125

5.5.5 Speckle interferometry coupled tensile tests . . . 130
5.5.6 Conclusion . . . 130
5.6 Post-weld heat treatments . . . 130
5.6.1 Introduction . . . 130
5.6.2 Mechanical properties after post-weld heat treatments . . . 130
5.6.3 Conclusion . . . 133
5.7 Conclusions . . . 133

6 General discussion 135
6.1 Introduction . . . 135
6.2 Relationship between Processing parameters, Processing temperature, Microstructure and Weld Quality . . . 135
6.2.1 Determination of the FSW nugget temperature (i.e. FSW maximum temperature) from the grain microstructure . . . 136
6.2.2 Determination of the LBW maximum temperature from the microstructure 136
6.2.3 Relationship between processing parameters and heat generation. . . . 138
6.2.3.1 FSW . . . 138
6.2.3.2 Relationship with weld quality . . . 139
6.3 Efficiency of LBW and FSW for joining AZ31 magnesium alloys . . . 140
6.3.1 Influence of microstructure evolution . . . 140
6.3.2 Influence of texture evolution . . . 141
6.3.3 Influence of shear bands . . . 141
6.3.4 Influence of residual stresses . . . 142
6.4 Comparison with precipitation hardened Magnesium alloys . . . 144
6.5 Comparison with the aeronautic industry requirements . . . 146

7 Conclusions 149

List of Figures

1 Domaine de soudabilité opérationnel du soudage FSW (diamètre du pion 4 mm, diamètre de l'épaulement 10 mm) pour l'AZ31. ix
2 Domaine de soudabilité opérationnel du soudage laser CO_2 (f=0mm, débit gazeux d'hélium = 40 l/min) pour l'AZ31 et l'AZ61. x
3 Évolution de la température lors du soudage FSW et laser. Les points de donnée grisés correspondent au côté avançant du FSW. x
4 Microstructure des joints soudés FSW. xi
5 Microstructure des joints soudés laser. xi
6 Cartes EBSD d'une soudure FSW et les figures de pôle correspondantes. L'analyse a été faite 100 μm sous la surface supérieure du joint soudé. xii
7 (a) Figures de pôle de la zone fondue déterminées par DRX , (b) schéma de la structure hexagonale compacte (c) localisation de l'analyse EBSD,l'analyse a été faite à mi-épaisseur dans la section de la soudure, (d) cartes EBSD de la section du joint soudé laser et (e) figures de pôle correspondantes. xiii
8 Propriétés mécaniques des joints soudés bord-à-bord comparées à celles du matériau de base AZ31. xiv
9 Évolution de la contrainte équivalente et de la pression hydrostatique après chargement mécanique dans les joints soudés FSW (1000 tr/min, 200 mm/min, pion : 5 mm pin / épaulement : 10 mm) and (1000 tr/min, 200 mm/min, pion : 5 mm pin / épaulement : 13 mm). xv
10 Propriétés spécifiques des alliages de magnésium et d'aluminium [6, 7, 8, 9]. . . . xvi

2.1 Magnesium-aluminium phase diagram [10]. 23
2.2 Hexagonal close packed crystal planes and directions relevant to (a) slip of dislocations with the <a> type Burgers vector and (b) slip of dislocations with $< c + a >$ Burgers vector and one of the $10\bar{1}2$ habit planes of the most common twinning mode [11]. 23
2.3 FSW process description. 26
2.4 Picture of a conventional FSW tool. 27
2.5 Sketches of Whorl™ pins[12]. 27
2.6 Tool shoulder geometries[13]. 28
2.7 Influence of welding speed and tool rotation rate on weldability of AZ91D.[14]. . 29
2.8 Tensile strenght evolution with welding speed and tool rotation rate [15]. 30
2.9 Tensile properties versus "rotational/transverse speed" in the stir zone (SZ) and in the transition zone (TZ)[16]. 31

2.10 Joint configurations for friction stir welding: (a) square butt, (b) multiple lap joint (c) fillet joint, (d) T butt joint, (e) T lap joint, and (f) edge butt.[17]. . . . 32
2.11 Influence of laser power on the penetration depth (A) and on the weld width (B) for WE43 alloy [18, 19]. 34
2.12 Influence of welding speed on the penetration depth (A) and on the weld width (B) for WE43 alloy [18, 19]. 34
2.13 Influence of shielding gas on the weld width for AZ61 alloy [20]. 35
2.14 Influence of welding speed on the weld width and penetration depth [21]. 37
2.15 FSW flow visualisation using plasticine (W = 1500 RPM, V = 1 mm/s) [22]. . . 39
2.16 Influence of tool rotation rate on peak temperature for a 6061Al-T6 FSW (V = 120 mm/min)[23]. 40
2.17 Variation of peak temperature for a 6061Al-T6 FSW weld made with and without pin (W = 400 RPM, V = 120 mm/min)[23] 41
2.18 IR images captured (a) parallel and (b) perpendicular to the direction of welding seam during AZ31 hybrid laser-TIG welding process [24]. 42
2.19 Sketch of FSW cross-section showing the different microstructural zones [25]. . . 42
2.20 (a) basi-shaped and (b) elliptical nugget [17]. 43
2.21 Sketch of basal plane rearrangement in the base metal, TMAZ and nugget [4] . . 44
2.22 Hardness evolution in the stir zone function of the grain size[26]. 45
2.23 Longitudinal residual stress distribution in FSW 6013Al-T4 welds determined by different measurement methods (W = 2500 RPM, V = 1000 mm/min, tool shoulder diameter: 15 mm) [17]. 46
2.24 Comparison between the longitudinal residual stresses of AZ31 FSW determined using the contour method and neutron diffraction. The diffraction data include SPF (Single peak fitting method, pyramidal peak) and Rietveld results [5]. . . . 47
2.25 Residual stress profiles of the LBW AZ31B magnesium alloy: (a) top side and (b) bottom side of the weld, z is the distance from the surface at which the measurements were performed [3]. 49

3.1 FSW Experiment. 53
3.2 FSW Processing parameters studied, 4 mm diameter pin, 10 mm diameter shoulder. 54
3.3 CO_2 LBW experiment. 55
3.4 CCD measurements, the coloring corresponds to the strain level. 56
3.5 Radiography of a FSW weld 56
3.6 Interaction volume of 20 kV electron beam with Mg calculated using Montecarlo simulation [27]. 58
3.7 (a) Electropolished TEM sample and (b) Sample prepared using FIB. 60
3.8 Major direction considered in the welds studied. 61
3.9 (a) HMI-E3 experiment (b) ILL-D1B experiment. 62
3.10 Z shift versus the gage volume barycenter. 63
3.11 (a) Simulated intensities and (b) simulated 2 θ angles, versus the gage volume barycenter. 63
3.12 Correction of (a) measured intensities and (b) 2 θ angles. 64
3.13 Evolution of microhardness with load applied. 65
3.14 Waterjet cutting dumbell preparation. 65

3.15 Dumbell specimen dimensions. 66

4.1 Macrographs of AZ31 FSWeld structure (a) top surface and (b) bottom surface. . 68
4.2 Macrograph of AZ31 LBWeld. 68
4.3 Defects observed in AZ31 FSW: Optical micrograph of (a) porosity in FSW (W = 800 RPM, V = 100 mm/min), and (b) crack in FSW (W = 1800 RPM, V = 1000 mm/min), macrograph of (c) flash and surface corrosion in FSW (W = 400 RPM, V = 100 mm/min), (e) Radiography of FSW (W = 800-1100 RPM, V = 100 mm/min) exhibiting tunneling, flash and pin wear. 69
4.4 EDS-SEM analysis of AZ31 FSW (W = 1100 RPM, V = 100 mm/min), white zones are typical of a high element content. (a) SE image, (b) Fe EDS map showing higher Fe content in the particles and (c) Mg EDS map showing lower Mg content in the particles. 70
4.5 Defects observed in AZ31 LBW: Optical micrograph of (a) porosity in CO_2 LBW (P = 2 kW, V = 2.76 m/min, f = -2 mmm, gas flux = 40 l/min), (b) weld cracking in CO_2 LBW (P = 3 kW, V = 3.6 m/min, f = 0 mmm, gas flux = 40 l/min), (c) lack of penetration in CO_2 LBW (P = 2.4 kW, V = 12 m/min, f = 16 mmm, gas flux = 40 l/min), (d) sag of weld pool in CO_2 LBW (P = 3kW, V = 4.2 m/min, f = 0 mmm, gas flux = 40 l/min) (e) Macrograph of laser cutting in CO_2 LBW (P = 3 kW, V = 1.2 m/min, f = 0 mmm, gas flux = 40 l/min). 70
4.6 Digital images of the superficial aspect of several "bead on plate" AZ31 welds (a) W= 400 RPM V=100 mm/min, (b) W= 700 RPM V=100 mm/min, (c) W= 900 RPM V=100 mm/min, (d) W= 1600 RPM V=400 mm/min, (e) W= 1600 RPM V=600 mm/min, (f) W= 1600 RPM V=1000 mm/min. 71
4.7 Influence of processing parameters on AZ31 FSW quality. 72
4.8 Influence of the welding speed on the flash size for AZ31 FSW (W = 1000 RPM). 72
4.9 Digital image showing the influence of the applied pressure (from 5.2 to 6.5 kN) on the weld quality for AZ31 FSW (W = 1000 RPM, V = 200 mm/min). 73
4.10 Influence of the laser power on (a) the weld width for AZ31 LBW (V = 3600 mm/min) (b) the penetration depth for AZ61 LBW (V = 7200 mm/min). . . . 73
4.11 Influence of the welding speed on (a) the weld width for AZ31 LBW (P = 2.4 kW) (b) the penetration depth for AZ61 LBW (P = 1.5 kW). 74
4.12 Influence of the focal distance on the weld quality for WE43 LBW (P = 3 kW). 74
4.13 Influence of the focal distance on the weld width for AZ61 LBW (P = 3 kW, V = 7200 mm/min). 75
4.14 Influence of the shielding gas (a) 0 l/min, (b) 40 l/min, (c) 60 l/min, (d) >60 l/min for AZ61 LBW (P = 3 kW, V = 7200 mm/min). 75
4.15 Macrograph of sound welds produced using back shielding gas for (a) AZ61 LBW (P = 3 kW, V = 2200 mm/min) and (b) WE43 LBW (P = 3 kW, V = 2200 mm/min). 76
4.16 Influence of the alloy conductivity on the penetration depth and bead width. . . 77
4.17 LBW Process window (f=0 mm, He gas flow = 40 l/min) for (a) AZ31, (b) AZ61. 77
4.18 Location of the thermocouples during FSW processing. 78
4.19 Location of the thermocouples during LBW processing. 79
4.20 Temperature measurement during FSW (W = 600 RPM, V = 2000 mm/min). . 80
4.21 Temperature measurement during LBW (P = 2 kW, V = 4600 mm/min). 80

4.22 Peak temperature measured versus distance from weld centre during FSW and LBW. The filled features correspond to the advancing side data. 81
4.23 Sketch of the FSW hole location. 81
4.24 Optical micrograph of the FSW section showing material flow. 81
4.25 SE images of the FSW hole and the intergranular precipitation aligning with the material flow. 82
4.26 FSW hole micrographs: (a-b) SE images of the crack observed at the end of the weld line, (c) SE image of the Al_8Mn_5 precipitates observed along the crack, (d) Optical micrograph of crack on the bottom surface of the weld, (e-f) Microstructure at the shoulder edge, (g) Microstructure behind the pin. 84
4.27 Optical micrograph of the plate junction where originated the crack. 85
4.28 EBSD map of the end of the crack (a) Band contrast colouring, (b) All Euler colouring. 85
4.29 Optical micrographs of (a) FSW flash, (b) grain growth in the curved area, (c) microstructure gradients, (d) twinned microstructure in the folded area, (e) recrystallised microstructure, (f) microstructure gradient in a narrow flash area. . . 86

5.1 Optical micrograph of AZ31 observed along (a) the top surface, (b) the rolling direction and (c) the transverse direction. 88
5.2 (a) Optical micrograph of Aluminium Manganese particles aligned along the rolling direction in AZ31 base metal, (b) SE images of Aluminium Manganese particles, (c) corresponding Mg EDS map (d) Al EDS map and (e) Mn EDS map, white zones are typical of a high element content. 89
5.3 Nanoprecipitates in AZ31 base metal. 89
5.4 Nanoprecipitate size distribution. 90
5.5 EDX-TEM chemical analysis of (a) smaller and (b) larger nanoprecipitates in AZ31 base metal. Analysis was performed along the red line which can be seen on the Bright Field image. 90
5.6 Identification of substructure in SAED pattern corresponding to Al_8Mn_5 in $[11\bar{2}0]$ zone axis (white) with α-Mg [0001] zone axis matrix (orange). 91
5.7 (a) Grain structure and precipitation observed by (b) SEM and (c) TEM of 550 $^{\circ}$C heat treated sample. 92
5.8 Microstructure of FSWeld section. 92
5.9 Microstructure of LBWeld section. 93
5.10 Macrographs of shear band features in FSW butt welds (a) W = 1000 RPM, V = 2000 mm/min top surface (b) W = 1300 RPM, V = 300 mm/min bottom surface, (c) W = 1000 RPM, V = 200 mm/min (13 mm shoulder diameter) bottom surface, the white arrows help to visualize the shear bands. 93
5.11 Macrographs of shear band features in LBW butt welds (a) Nd:YAG 2.4 kW, 7 m/min, (b) CO_2 2 kW, 3 m/min, (c) CO_2 2.5 kW, 3.5 m/min, and optical micrograph of shear bands in Nd:YAG (2.4 kW, 7 m/min). 94
5.12 Optical microstructure showing adiabatic shear bands (ASB) in an impacted dual-phase steel [28]. 95
5.13 Optical micrograph of one shear band in FSW (13 mm shoulder diameter, W = 1000 RPM, V = 200 mm/min). 96
5.14 Optical micrograph of shear band in Nd:YAG (2.4 kW, 7 m/min). 97

5.15 Influence of the FSW processing parameters on shear band spacing and shear band length. 97
5.16 All-Euler EBSD map of a shear band and associated pole figures in FSW (13 mm shoulder, W = 1000 RPM, V = 200 mm/min). 98
5.17 Microhardness evolution across a shear band in FSW (13 mm shoulder, W = 1000 RPM, V = 200 mm/min), the shaded area corresponds to the shear band. 98
5.18 Grain size evolution in the TMAZ for FSW (tool 4mm pin / 10mm shoulder): (a) 600 RPM, 100 mm/min and (b) 1800 RPM, 1000 mm/min. 99
5.19 SEM analysis of precipitation in the TMAZ for 4 mm pin, 10 mm shoulder diameter FSW W = 1000 RPM, V = 200 mm/min. 99
5.20 TEM analysis of precipitation in the TMAZ for 5 mm pin, 10 mm shoulder diameter FSW W = 1000 RPM, V = 200 mm/min. 100
5.21 Nugget grain size evolution with W and V parameters for 4 mm pin, 10 mm shoulder diameter FSW (a) W = 600 RPM, V = 100 mm/min, (b) W = 1400 RPM, V = 200 mm/min, (c) W = 1400 RPM, V = 700 mm/min, (d) W = 1800 RPM, V = 600 mm/min, (e) W = 1800 RPM, V = 1000 mm/min and (f) grain size dispersion. 101
5.22 Grain size evolution with shoulder diameter for 1000 RPM, 200 mm/min butt FSW (a-c) 13mm shoulder diameter, (d-f) 10mm shoulder diameter. 101
5.23 SEM analysis of precipitation in the nugget for 4 mm pin, 10 mm shoulder diameter FSW W = 1000 RPM, V = 200 mm/min. 102
5.24 Intragranular precipitation evolution in the butt weld nugget (tool 5 mm pin / 10 mm shoulder): (a) (600 RPM, 2000 mm/min), (b) (1000 RPM, 200 mm/min) and (c) base metal. 102
5.25 Optical micrograph of Nd:YAG LBW section (2.4 kW, 7000 mm/min). 103
5.26 Intergranular Al_8Mn_5 precipitation and Al-rich second phase in Nd:YAG LBW fusion zone (2.4 kW, 7000 mm/min) (a) SEM observation, (b) and (c) SFEG observations. 103
5.27 EDS-SEM analysis of Nd:YAG LBW after SiO_2 polishing (2.4 kW, 7000 mm/min) (a) BSE image, EDS measurement location in the fusion zone and (c) EDS analysis results. 104
5.28 XRD Phase analysis of Nd:YAG LBW fusion zone (2.4 kW, 7000 mm/min). . . 104
5.29 TEM analysis of Nd:YAG LBW fusion zone precipitation (2.4 kW, 7000 mm/min) (b) Brigth field image, (c) Brigth field image of the profile analysis location across a large precipitate and a small one, (d) the corresponding EDS profile, (e) Brigth field image of the profile analysis location across a large precipitate and without any small one, (f) the corresponding EDS profile, (g) the EDS maps of a large particle with a small one inside, compared to (a) base metal. 105
5.30 TEM Bright field image of MgO in Nd:YAG LBW fusion zone (2.4 kW, 7000 mm/min) and corresponding SAED pattern of α-Mg [001] zone axis matrix with MgO rings substructure. 106
5.31 Optical micrograph of Nd:YAG LBW fusion zone (2.4 kW, 7000 mm/min). . . . 106
5.32 Grain size determination using EBSD of Nd:YAG LBW fusion zone (2.4 kW, 7000 mm/min): (a) All Euler EBSD map, (b) SE image and (c) BSE image of the analysed area. 107

5.33 Evolution of CO_2 LBW fusion zone grain size with heat input. 108
5.34 Optical Micrograph of CO_2 LBW fusion zone grain size processed at several heat input: (a) H=50 J/mm (P=1.5 kW,V=1800 mm/min), (b) H=150 J/mm (P=1.5 kW,V=600 mm/min). 108
5.35 XRD Pole figures of AZ31 base metal. 109
5.36 Neutron diffraction and XRD Pole figures of FSW. 110
5.37 Evolution of diffracted intensity across FSW, the shaded area corresponds to the weld zone. 111
5.38 EBSD maps of FSW top surface and corresponding calculated pole figures. . . . 112
5.39 (a) XRD Pole figures of LBW fusion zone, (b) sketch of the hcp crystal (c) EBSD analysis location in the mid-thickness weld section, through the weld width, (d) EBSD maps of LBW section (IPF colouring) and (e) corresponding pole figures. 113
5.40 Misorientation angle distribution in FSW. 114
5.41 Young's modulus of (a) Magnesium singlecrystal, (b) Magnesium isotropic polycristal and (c) hot rolled AZ31. 116
5.42 Base metal residual stress tensor components versus measurement depth, in grey the calculation without taking into account the ODF and in black the calculation taking into account the ODF. 117
5.43 Comparison between the stress evolutions during welding (strain gages) with the XRD results for FSW (1000 RPM, 200 mm/min, tool 5 mm pin / 13 mm shoulder).118
5.44 XRD Equivalent stress and Hydrostatic stress evolution across FSWeld (1000 RPM, 200 mm/min, tool 5 mm pin / 10 mm shoulder). 119
5.45 Stress map across FSWeld. 120
5.46 Longitudinal stress evolution and transverse stress evolution across FSWelds. . . 120
5.47 Residual stress evolution across FSWelds, the shaded area corresponds to the weld zone. 121
5.48 Residual stress evolution between base metal and LBW fusion zone. 122
5.49 Microhardness evolution across FSWelds. 123
5.50 Microhardness evolution with grain size in FSWelds. 124
5.51 Microhardness evolution across LBWelds. 124
5.52 Tensile properties of AZ31 base metal in rolling direction, Transverse Direction and 45 °Direction. 125
5.53 Tensile properties of AZ31 FSW and LBW butt welds. 126
5.54 Fracture location in AZ31 FSW butt welds: (a) 45°fracture, (b) crack on the bottom surface and (c) fracture in the advancing side TMAZ. 127
5.55 Tensile fractographies of FSW butt welds. 128
5.56 Fracture location in AZ31 LBW butt welds. 128
5.57 Tensile fractographies of AZ31 LBW butt welds: (a), (b) ductile pattern and (c), (d) partly brittle pattern. 129
5.58 Tensile fractographies of AZ31 base metal in (a) Rolling direction, (b) 45 °direction and (c) Transverse direction. 129
5.59 (a) Speckle interferometry analysis localtion, (b) Evolution of ϵ_{xx}, (c) Evolution of ϵ_{yy}, (d) Evolution of ϵ_{xy} and (e) Evolution of U_z. 131
5.60 Tensile curves of heat treated samples compared to AZ31 base metal and samples as welded. 132

5.61 Optical micrographs of grain structure in heat treated LBW. 133
5.62 Comparison of tensile properties of butt welds resulting from different welding process to base metal ones. 134

6.1 Temperature evolution in FSW and LBW. The filled features correspond to the FSW advancing side data. The data in Zone III correspond to the nugget temperatures calculated using Chang model for FSW and to fusion zone temperatures for LBW. 137
6.2 Nugget temperature versus W^2/V ratio. 138
6.3 Nugget temperature versus weld quality for FSW bead on plate (tool 4mm pin / 10mm shoulder). 139
6.4 Heat input versus weld quality for LBW bead on plate. 140
6.5 Evolution of UTS and Yield Stress with the nugget temperature during FSW butt welding. 141
6.6 Speckle analysis during tensile test showing the strain localisation in the FSW shear bands (ϵ_{xx} analysis with a better resolution (less pixels fitting) than in the Figure 5.59 (a)). 142
6.7 Equivalent stress and Hydrostatic stress evolution after tensile loading across FSWelds (1000 RPM, 200 mm/min, tool 5mm pin / 10mm shoulder) and (1000 RPM, 200 mm/min, tool 5 mm pin / 13 mm shoulder). 143
6.8 Equivalent stress and Hydrostatic stress evolution after tensile loading across LBWelds (2.4 kW, 7000 mm/min). 143
6.9 Optical micrographs of hot rolled (a) AZ61 and (b) WE43 base metals. 144
6.10 SE images of (a) AZ61 Fusion zone, (b) AZ61 HAZ, (c) AZ61 base metal, (d) WE43 Fusion zone, (e) WE43 HAZ and (f) WE43 base metal. 145
6.11 Microhardness profiles across AZ31, AZ61 and WE43 LBW processed at P = 3kW, V = 7 m/min. 145
6.12 Comparison between AZ31, AZ61 and WE43 mechanical properties after LBW. . 146
6.13 Specific properties of magnesium alloys compared to aluminium alloys [6, 7, 8, 9]. 147

List of Tables

2.1 Magnesium alloy ASTM designation. 22
2.2 Properties of pure magnesium, aluminium and iron. 24
2.3 Comparison between CO_2 and Nd:YAG Laser Beam Welding. 38

3.1 AZ31 chemical specification from MEL. 51
3.2 AZ61 chemical specification from MEL. 52
3.3 WE43 chemical specification from MEL. (*Rare Earth other than Nd) 52
3.4 Tool designation. 52
3.5 Overview of the Neutron diffraction experiments performed. 64

4.1 Magnesium alloy thermal conductivity. 76

5.1 Microstructure observed. 109

6.1 Thermal history of welds. 137
6.2 Aluminium and magnesium alloys density. 146

Chapter 1

Introduction

1.1 General

Nowadays, weight reduction is a very important issue in aircraft industy. The aluminium alloys that are generally used in the aerospace industry are already optimized for aeronautic requirements, so that little further improvements are expected. Therefore using new materials is an alternative solution to achieve weight reduction. One of them would be to use fibre-reinforced composite [1]. But their application is limited in terms of thermal stability, electric properties, damage tolerance and their high cost restricted their use to high requirement primary structure applications.

Another alternative solution would be to use lightweight metals. Magnesium alloys are driving increasing interest in replacing aluminium alloys, because of their high specific properties. Indeed, magnesium density is 35% lower than aluminium one. Using magnesium alloys could result in a component weight reduction and then fuel savings. This will then induce a reduction in operating costs and pollution emissions of 10% [1]. The strength requirements for these new materials will be to reach AA5058 aluminium alloy properties for non-structural applications and AA2024 aluminium alloy properties for secondary structure applications [1]. Magnesium alloys are already used in the automotive industry, but only as cast products; and the production and use of wrought magnesium alloys are very limited [1]. Developing wrought products would allow to get improved mechanical properties and manufacturing process, which match the aeronautic requirements.

1.2 Welding magnesium alloys

Increasing the use of magnesium alloys, the need of reliable joining process will arise. Conventional welding processes result in a wide range of defects and then in a loss of mechanical properties. Then, welding magnesium alloys is still an issue. New joining techniques, such as Laser Beam Welding (LBW) and Friction Stir Welding (FSW), could be an alternative. But their application to wrought magnesium alloys still need research investigations.

1.3 Project objectives and outline

This PhD thesis is part of the AEROMAG [1] "Aeronautical Application of Wrought Magnesium" (Project N° AST4-CT-2005-516152) which was supported by the European Union. It was aimed at developing the use of wrought magnesium alloys in the aeronautic industry. This study focused on hot rolled magnesium sheets produced by Salzgitter Magnesium Technologie, who is one of the AEROMAG partners. Several alloys were used:

- AZ31 for its good formability,
- AZ61 for its mechanical properties,
- WE43 for its mechanical properties and corrosion resistance.

This PhD thesis objectives are to assess the efficiency of joining hot rolled magnesium alloys with FSW and LBW. The first step will be to determine the process window for each process and each alloy. Afterwards, the study will focus on the analysis of optimized AZ31 welds in term of microstructure and mechanical properties. Finally, the process instrumentation will be useful to study the thermal and thermomechanical mechanisms associated with each process. The relationships between processing parameters, temperature distribution, weld quality and weld microstructure will be established. The hardening and strengthening mechanisms involved will be investigated. The comparison between the alloys studied and with the aeronautical requirements will lead to discuss the efficiency of using FSW and LBW to join hot rolled magnesium alloys.

[1] AEROMAG Partners: EADS, Airbus, Eurocopter, Arts et Métiers Paristech, INPG, Université de Vienne, Université de Patras, Université de Thessalie, Université de Naples, MEL, Alonim, Palbam, Technion, Otto Fuchs, Salzgitter Magnesium Technologies

Chapter 2

Literature survey

2.1 Magnesium alloy basic knowledge

2.1.1 Magnesium physical properties

Magnesium was first discovered in 1808 by Sir Humphry Davy. It represents 2.5 % of the earth's crust and 0.14 % of the earth's ocean water [29]. The density of magnesium at 20 °C is 1.738 g/cm^3 and therefore it is the lightest metal available so far. Magnesium has a hexagonal lattice structure and has an atomic diameter (0.160 nm) that allows for solid solubility with a wide range of elements.

2.1.2 Alloying elements

Alloying is used to improve magnesium properties. The most common alloying elements are aluminum, zinc, manganese, zirconium, silver, yttrium and rare earth elements. Copper, nickel and iron have to be controlled properly to insure the quality of magnesium alloys [29]. Aluminum additions increase the alloy hardness and strength, but reduce its ductility. Manganese is used as an iron removal agent to enhance corrosion resistance. Zinc has been found to improve room temperature strength, corrosion resistance, and precipitation hardenability [29]. Zirconium is a grain refiner in magnesium alloys but cannot be used in alloys containing Al or Mn, as it forms stable compounds [29]. Silver additions are used to improve the age hardening of magnesium alloys, but it has been limited due to the high costs induced. Yttrium is used to impart high temperature creep resistance to magnesium. Rare earth additions include cerium, lanthanum, neodymium, gadolinium, and praseodymium. They are used to increase high temperature strength, creep resistance, and to reduce casting porosity [29].

2.1.3 Magnesium alloy designation

The ASTM (American Society for Testing and Materials) magnesium alloy designation has been widely adopted. This method includes two letters followed by two numbers. The two letters are the letter abbreviations given to the two largest alloying elements, and the numbers are the weight percent of these alloying elements. Table 2.1 lists the one-letter abbreviations for the most commonly used alloying elements [29].

Letter	Alloying element
A	Aluminium
C	Copper
E	Rare earth metals
H	Thorium
J	Strontium
K	Zirconium
L	Lithium
M	Manganese
Q	Silver
S	Silicon
W	Yttrium
X	Calcium
Z	Zinc

Table 2.1: Magnesium alloy ASTM designation.

2.1.4 Magnesium-Aluminium binary system

Two of the alloys that will be studied (AZ31 and AZ61) are based on the Magnesium-Aluminium binary system. The maximum solubility of Al in Mg ranges from 2.1 wt% at 25 ˚C to 12.6 wt% at the eutectic temperature of 437 ˚C. Figure 2.1 shows the Mg-Al phase diagram [10]. Mg-Al alloy precipitation can be modified by heat treatments but $Mg_{17}Al_{12}$ precipitates form in an incoherent manner and then they have a limited strenghtening effect [30].

2.1.5 Magnesium slip system mechanisms

Magnesium slip systems are described in Figure 2.2. Magnesium main dislocation slip system is (0001) basal slip [11, 31, 32]. It exhibits the lowest critical resolved shear stress (CRSS = 0.45–0.81 MPa) [3]. The other slip mechanisms available in Magnesium single crystal include $(10\bar{1}0)$ prismatic and $(10\bar{1}1)$ pyramidal slips [11]. These non-basal slip mechanisms were only observed at elevated temperatures (>180 ˚C) [32], increasing the magnesium alloy formability at high temperature. In addition to dislocation slip, $\{10\bar{1}2\}<10\bar{1}1>$ mechanical twinning can easily occur in magnesium alloys [11]. The amount of strain that twinning can accommodate is directly proportional to the volume fraction of crystal which has twinned. Twinning can only accommodate a 6.5% maximum amount of tensile strain [11].

2.1.6 Manufacturing magnesium alloys

Although magnesium can be fabricated by all manufacturing techniques, this research focuses on wrought alloys. Wrought products are obtained by working the metal into a desired shape. The formability of magnesium alloys is very low and then they can not be cold worked. Magnesium alloys can be hot worked using extrusion, rolling, and forging processes. Most of the industrial applications deal with cast magnesium alloys, very few works were performed on wrought alloys and then, the magnesium alloys available as wrought products are very limited. Indeed, the forming properties of magnesium are very low because of its hexagonal structure. Rolling

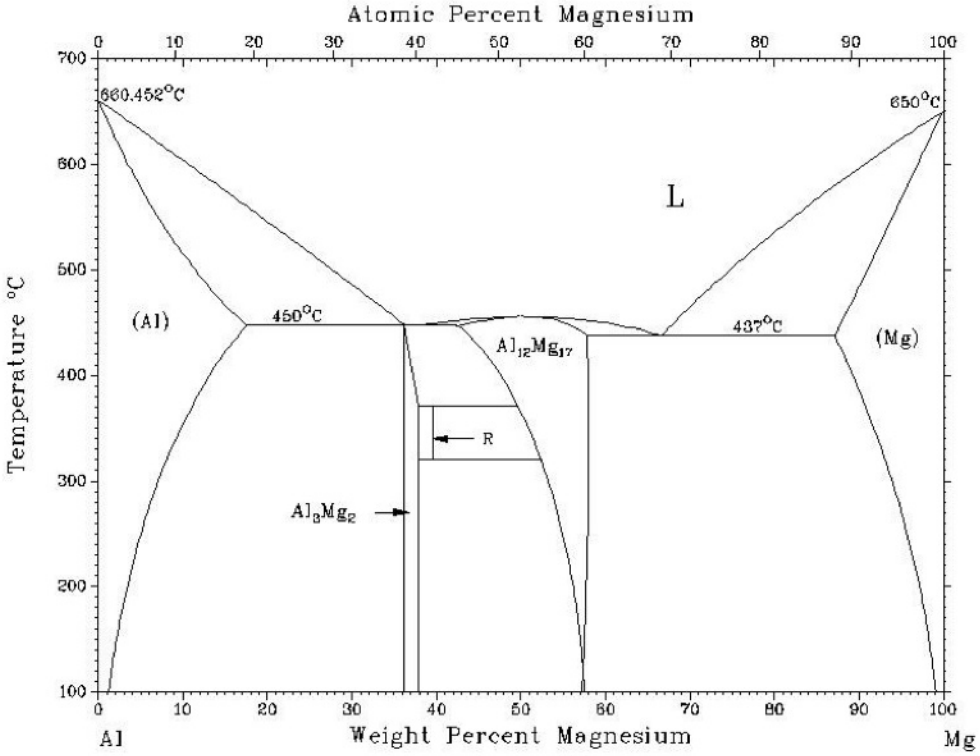

Figure 2.1: Magnesium-aluminium phase diagram [10].

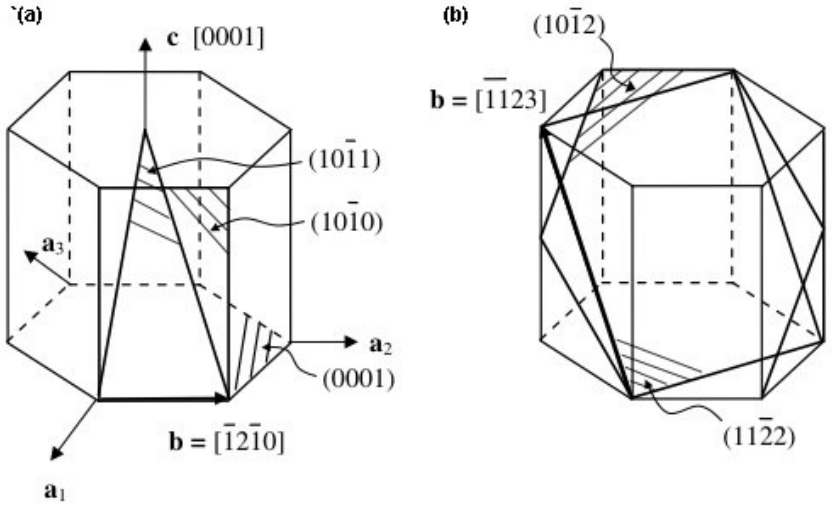

Figure 2.2: Hexagonal close packed crystal planes and directions relevant to (a) slip of dislocations with the <a> type Burgers vector and (b) slip of dislocations with $< c + a >$ Burgers vector and one of the $10\bar{1}2$ habit planes of the most common twinning mode [11].

magnesium alloys is itself an issue which led to many studies [33, 11, 34, 35]. Indeed, during plastic deformation, magnesium alloys develop a strong texture that influences the production process and the resulting mechanical properties. To date, this has induced major limitations in the commercial production of magnesium wrougth plates.

2.1.7 Magnesium alloy properties

The main interest in magnesium alloys is that they are the lightest metallic materials available so far (magnesium density is about 1.74 g/cm^3). So they have excellent specific properties and they are aiming at replacing steel and aluminium in many structural applications. However, magnesium alloys have limited strength, fatigue and creep resistance at elevated temperatures, low stiffness, limited ductility. The formability of magnesium alloys is inferior to those of other metallic materials such as steel and aluminium alloys because of the hexagonal close packed (HCP) structure, but it can be improved by grain refinement [36, 37]. In general, they have about the same corrosion resistance in common environments as mild steel, but are less corrosion resistant than aluminium alloys. They also have poor surface properties such as low hardness, wear and corrosion resistance, and they exhibit a large shrinkage during solidification. Magnesium alloys are then still under development to improve their properties. Table 2.2 shows magnesium properties compared to those of iron and aluminium.

Properties	Magnesium	Aluminium	Iron
Density(g/cm^3)	1.74	2.38	7.87
Melting point ($^\circ$C)	650	660	1535
Coefficient of thermal expansion ($^\circ$C^{-1})	$2.61.10^{-5}$	$2.4.10^{-6}$	$12.2.10^{-5}$
Elastic modulus (GPa)	44	68	200
UTS (MPa)	90	100	540
Specific elastic modulus (GPa.g^{-1}.cm^3)	25	28	25
Specific UTS (MPa.g^{-1}.cm^3)	52	42	69

Table 2.2: Properties of pure magnesium, aluminium and iron.

2.2 Welding process

2.2.1 Introduction

With magnesium alloys increasing applications, having reliable joining process is required, but welding magnesium alloys still faces many challenges. Indeed, welding magnesium alloys has been used till now only to repair structures because of the occurrence of many defects such as oxide films, cracks and cavities. Magnesium alloys can be joined using a wide variety of processes, but conventional processes have exhibited some disadvantages such as a large heat affected zone (HAZ), porosity, evaporative loss of the alloying elements and high residual stresses [2]. Laser Beam Welding and Friction Stir Welding are then alternative methods, which could overcome the above disadvantages. FSW is a solid state joining process and then it produces pore-free joints. The thermal gradients and the microstructural changes are smoother. LBW can be performed at high welding speed, reducing the HAZ and then is more suitable to manufacture

industrial parts than conventional arc processes [20]. However, the laser and FSW weldability of magnesium alloys is still an issue.

2.2.2 FSW and LBW of aluminium alloys

FSW and LBW are mature processes to join aluminium alloys and a wide variety of studies and industrial applications result from them, especially in automotive and aeronautics industries [38]. FSW was invented and experimentally proven by Thomas et al.[39] at The Welding Institute (TWI) of UK in 1991. It was initially applied to aluminium alloys. The FSW studies of aluminium alloys have led to an extensive review article [17]. FSW applications are found in shipbuilding, rail transport, automotive, small-component manufacturing, and aerospace [17]. Laser beam welding is widely used to join aluminium alloys [40, 41, 42] in automotive and aeronautic industries.

2.3 Friction Stir Welding process

2.3.1 Introduction

Friction stir welding is a solid-state joining technique [39, 43]. It was initially developed to join aluminium alloys (such as highly alloyed 2xxx and 7xxx series), which could not be welded using conventional processes because of their solidification microstructure and because the porosity occurring in the fusion zone induced a far too important loss in the joint mechanical properties. Indeed, FSW can achieve metallic bonding below the material melting point, and then it is avoiding many of the metallurgical problems associated with the solidification process such as porosity and cracking. Moreover, the other advantages of FSW over conventional techniques are that no sample preparation, shielding gas or consumable filler material is required.

2.3.2 Description of the process

The basic principle of the FSW process is illustrated on Figure 2.3. A non-consumable rotating tool composed by a pin and a shoulder is inserted into the abutting edges of the plates to be joined, which are clamped to prevent the joint faces from being forced apart. Due to the friction between the tool and the sample, the matter is heated up without reaching the material melting point. Then, the material around the pin is softening which allows the tool to traverse along the weld line. The combination of the tool rotation and its translation makes the plasticized material to be transferred from the front of the pin to the back of the pin and to be forged by the tool shoulder contact. Using this process can achieve from 0.8 to 65 mm thick welds for several materials including aluminium alloys, copper, magnesium, lead, and zinc.

2.3.3 Process parameters

2.3.3.1 Tool geometry

The tool is composed of a pin and a shoulder, which is described in Figure 2.4.

The tool is firstly used to produce the heat needed to soften the material and then its second function is to induce the flow of material. The pin is stirring the material and contributes to generate heat. The other heating contribution is due to the friction between the shoulder and

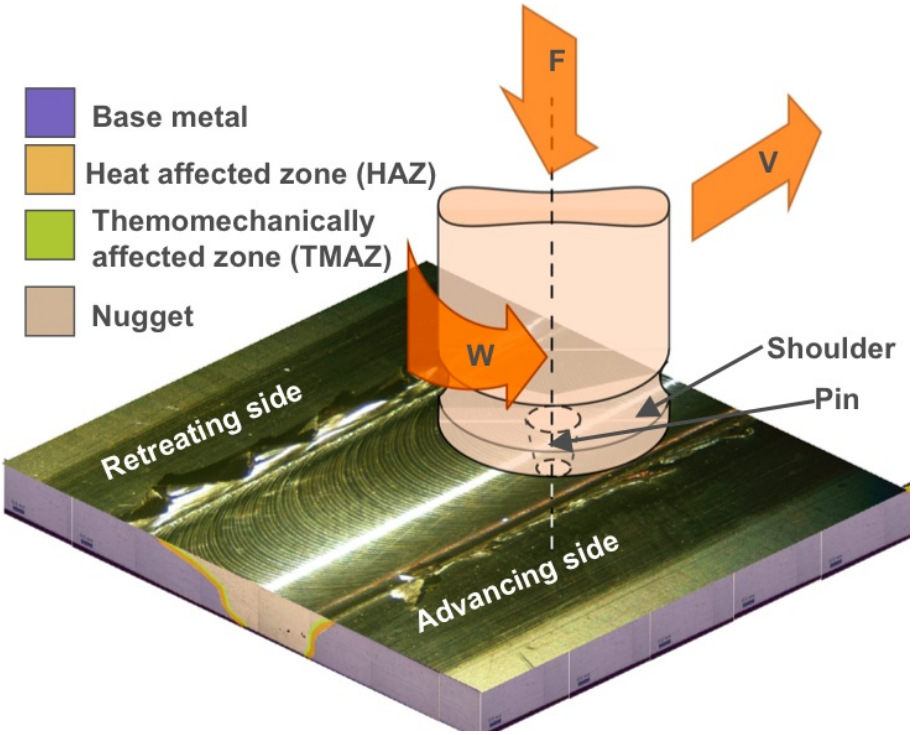

Figure 2.3: FSW process description.

the workpiece. The shoulder also prevents from the plasticized material to be pushed away. The geometry of the tool is an important parameter influencing the material flow and then, the quality of the weld. The pin diameter is generally equal to thickness of the parts to be welded and the pin length is slightly shorter than the part thickness [44].

Different studies have been previously done to assess the most suitable tool geometry. Boz et al. [45] observed that the welds made with square cross-section stirrer exhibited a large amount of cracks and porosities, resulting in a dramatic drop in the tensile strength of the material. Wang et al. [46] found that better welds were achieved, using cone or screw pin than when using a cylindrical pin.

New tool designs have been developed to further improve material flow. Figure 2.5 describes the Whorl ™ probes developed by TWI. The distance between each helicoïdal ridge must be greater than the thickness of the ridge itself to achieve a more effective flow of the plasticized material around the tool [47].

A variation on the Whorl™ probe is the MX-Triflute™ which is resulting in a narrower, more parallel sided weld region.

These two kinds of pin displace less material than a cylindrical tool of the same root diameter [13]. Indeed, theWhorl™ reduces the displaced volume by about 60%, while the MX Triflute ™ reduces the displaced volume by about 70%. The different complex features which can be seen on both tool, have been designed to:

- reduce welding force,
- improve material flow,

Figure 2.4: Picture of a conventional FSW tool.

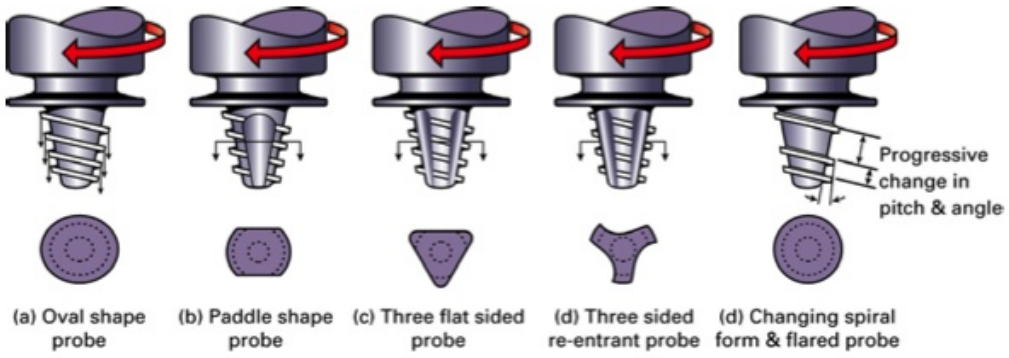

Figure 2.5: Sketches of Whorl™ pins[12].

- increase the pin / material interface and then heat generation.
The main reason for these pin geometries to be more efficient than conventional cylindrical pins is the ratio of the swept to pin volume [13]. For 25 mm thick plates, Thomas et al. [13] found this ratio to be 1.1:1 for conventional cylindrical pin, 1.8:1 for the Whorl™ and 2.6:1 for the MX-Triflute™ pin (for pins with similar root diameters and pin length). For threaded pins, the pitch of the ridges is also an important parameter. The ridges enable plasticized material to be deviated in the required direction and to move the oxides from the weld centre to the surface. Boz et al. [45] studied threaded pin stirrer with different pitch (0.85, 1.10, 1.40 and 2 mm). They observed that 1.4 and 2 mm threaded pins could not produce sound weld, because the material was compelled out and accumulated towards the shoulder. When using 0.85 and 1.10 mm threaded pins, the weld strength was higher than the base metal one, due to the heat generated, which is improving plasticity. McClure et al. [44] investigated 6 mm diameter pin with different thread pitch (0.55, 0.78, 1.26, 1.89 per mm). It resulted in welds without porosity apart from the 0.55 mm one. When using large pitch threaded pin, the deformation within the weld zone is not sufficient. Then, oxides are still large enough to interfere with metal flow and produce defect such as porosity or lack of fusion.
FSW can be also used to produce lap joints. In this case, the weld region is required to be wider to achieve sound welds. Specially designed tools such as Flared-Triflute™ and A-skew™ have been developed for this purpose.

The tool shoulder geometry can also be improved by adding special re-entrant features capable of entrapping plasticized material [47]. Figure 2.6 shows various shoulder geometries. Zettler at al. studied two different 13 mm diameter shoulder geometries: scroll shoulder (tilted between 0 and 1°) and concave shoulder (tilt = 1.5°) [48]. For the same W/V (W = tool rotation rate, V = welding speed) ratio, the scroll shoulder produced smoother weld surface and lower welding temperatures than concave shoulder.

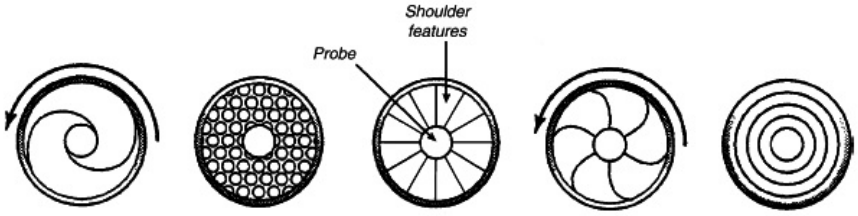

Figure 2.6: Tool shoulder geometries[13].

So, the tool geometries are of major importance in the FSW process and have to be adapted to each piece geometry and material to be welded.

2.3.3.2 Welding parameters

Tool rotation rate (W) and welding speed (V) Several studies have been done to investigate the effect of welding speed and tool rotation rate on the weldability of magnesium alloys (see Figure 2.7). These two parameters are critical to perform sound welds as they directly influence the heat input and then the flow of plastic material. The heat input per unit length

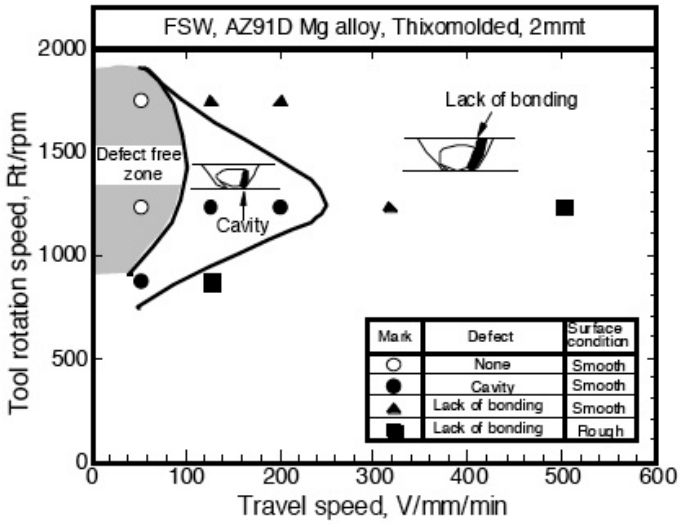

Figure 2.7: Influence of welding speed and tool rotation rate on weldability of AZ91D.[14].

can be expressed by:

$$\text{Heat Input} = \left(\frac{Q}{V}\right) \tag{2.1}$$

where Q = heat generated by friction and V = welding speed. The heat generated by friction increases with the tool rotation rate but not in a monotonic way as the coefficient of friction at the interface also varies with tool rotation rate [17]. Therefore, increasing tool rotation rate or decreasing welding speed induces a higher temperature, an easier flow and then, it enhances weldability. This is consistent with all the studies carried out previously [49, 26, 14, 50, 51, 52].

They reported that for a constant welding speed, a low tool rotation rate was leading to the formation of inner voids because the frictional heat was not sufficient to promote material flow [26, 14, 52]. These defects disappeared with increasing W, but with a further increase, inner voids, lack of bonding and surface crack due to excess expelling of the material are created [14, 49, 53].

Experiments performed at a constant tool rotation rate, showed that increasing welding speed was resulting in inside voids and lack of bonding caused by the insufficient material flow [26, 14, 50]. Yan et al. [52] observed that as it was decreasing the temperature in the weld, a low welding speed could provide a controlled dynamic recrystallisation leading to a fine grained structure. Gharacheh et al. [16] who used the W/V ratio as processing parameter, observed that increasing this ratio was leading to an increase in the heat input, an improved material flow and then, a wider and deeper weld nugget. The hardness increased with increasing welding speed [15]. Increasing welding speed over a critical value was seen to decrease the ultimate tensile strength while the yield strength was kept constant [49, 50, 52, 46].

Increasing the tool rotation rate resulted in an increase in the tensile strength [50, 15] (see Figure 2.8).Incresaing the welding speed produced an increase in the weld tensile strength until reaching the base metal tensile strength. With a further increase in welding speed, the weld

tensile strength droped, that was attributed to the grain refinement.

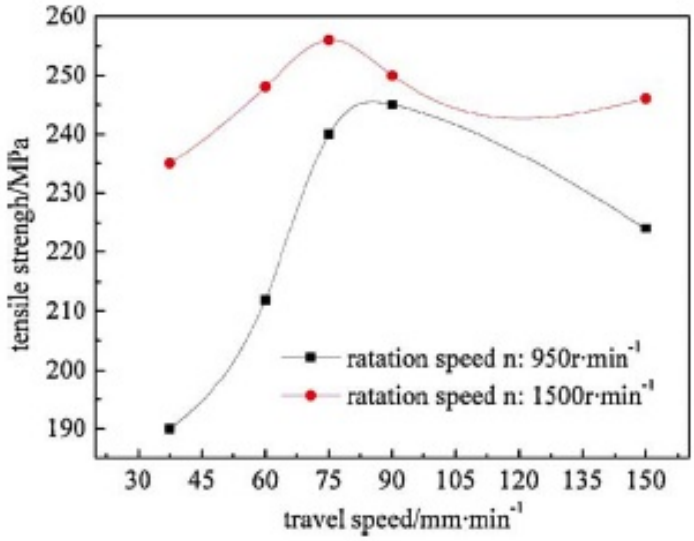

Figure 2.8: Tensile strenght evolution with welding speed and tool rotation rate [15].

Gharacheh et al. [16] used the W/V ratio to study the influence of processing parameters on the mechanical properties. They observed that increasing W/V ratio resulted in a decrease in yield strength (YS), ultimate tensile strength (UTS), and elongation (see Figure 2.9).

Welding pressure Zhang et al. [51] studied the influence of welding pressure at the same welding rate (i.e. V = 200 mm/min, W = 1000 RPM). The welding pressure is affecting the temperature produced by friction. Then, increasing welding pressure produced sound welds while at low pressure, pore formation was occurring.

Tilt angle A suitable tilt angle of the tool must be chosen to ensure the optimum efficiency of the tool. But this parameter is not widely discussed in the literature. It mainly depends on the shoulder geometry. It is usually set to 3°for plain shoulder [49, 14], and varied to 1.5°for concave shoulder and between 0 and 1°for scroll shoulder [48].

Insertion depth The insertion depth has to be controlled, mainly when using smooth tool shoulders. Indeed if it is too deep, a large amount of flash is produced, leading to local thinning of the welded plates, because the shoulder penetrates the material. When the insertion depth is too shallow, there is no contact between the shoulder and the workpiece surface, which prevents from a suitable stirring and induces surface groove formation.

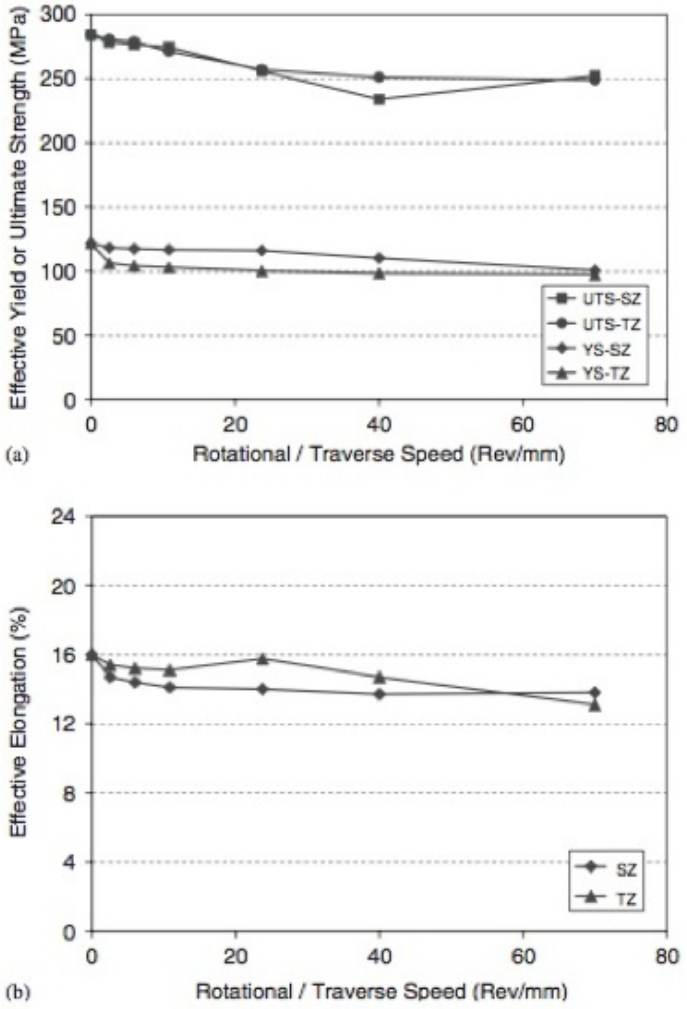

Figure 2.9: Tensile properties versus "rotational/transverse speed" in the stir zone (SZ) and in the transition zone (TZ)[16].

Preheating or cooling It can be necessary to preheat samples to process FSW on materials having high melting point such as steel and titanium or high conductivity such as copper, as the heat produced by the process may not be sufficient. Cooling can be useful to prevent from grain growth and precipitate dissolution, when welding materials with low melting point such as aluminium and magnesium.

2.3.3.3 Joint design

The joint configurations that can be achieved with FSW are mainly butt joints and lap joints (see Figure 2.10). But the configuration mainly studied in the literature is butt joint [26, 14, 50, 16].

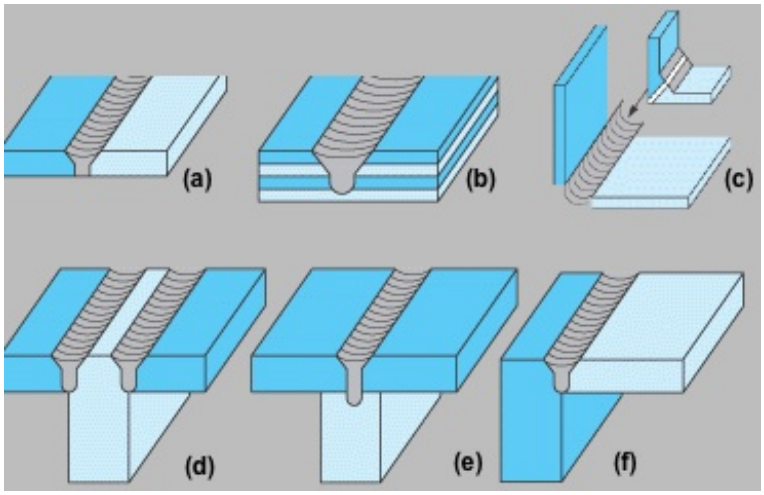

Figure 2.10: Joint configurations for friction stir welding: (a) square butt, (b) multiple lap joint (c) fillet joint, (d) T butt joint, (e) T lap joint, and (f) edge butt.[17].

2.3.3.4 Sample preparation

Normally, FSW process does not need any special sample preparation, but in the case of magnesium alloys, it has been reported that samples were lightly sanded and then cleaned with acetone [48, 50].

2.3.3.5 Conclusion

In conclusion, many parameters can be considered in FSW. In our case the following parameters were studied:

- the shoulder diameter,
- the tool rotation rate,
- the welding speed,
- the welding pressure.

2.4 Laser Beam Welding process

2.4.1 Introduction

Laser welding of magnesium alloys appears to be a challenge itself. Indeed, the ability to produce laser welds depends on the properties of the material to be welded. Then, magnesium being characterised by quite unfavourable properties [2] (i.e. low absorptivity of laser beams, strong tendency to oxidize, high thermal conductivity, high coefficient of thermal expansion, low melting temperature, wide solidification temperature range, high solidification shrinkage, a tendency to form low melting-point constituents, low viscosity, low surface tensions, high

solubility for hydrogen in the liquid state, and absence of color change at the melting point temperature), processing is expected to be an issue [2]. So, many troubles are expected when welding by laser these alloys such as unstable weld pool, substantial spatter [54, 55, 56, 57], a strong tendency to drop-through for large weld pools [56], sag of the weld pool , undercut [58], porous oxide inclusions, loss of alloying elements [54, 55], excessive pore formation [59, 60], liquation and solidification cracking [61]. However, Weisheit et al reported that laser welding of wrought alloys was far more achievable than welding die cast alloys whose gas content increases pore formation [62].
The two main types of laser used are CO_2 and Nd:YAG. Previous works were aimed to identify the processing parameters, which are influencing the process stability and repeatability. A condensed review of those will be exposed in this section. No filler material will be used in our study and 2 mm thick plates will be used, the review will then focused on LBW of thin plates without filler material.

2.4.2 Principle of Laser Beam Welding

LBW consists in the laser beam focalisation on the workpiece surface. The high power density then created, induces metal ionisation and then plasma is formed. The vaporisation of the surface progressively forms a depression in the workpiece and then a keyhole, which allows the laser energy in-depth absorption. The melted metal will progressively fill the keyhole during the laser displacement, to form the weld. The two laser sources available are CO_2 and Nd:YAG. CO_2 consists in a mixture of CO_2, N_2 and noble gases. The nitrogen discharge in CO_2 molecules activate the laser emission. The Nd:YAG (neodymium-doped yttrium aluminium garnet) consists in Nd^{3+} ions inserted in YAG crystal, the excitation is supplied by laser diodes. Nd:YAG laser light (λ=1.06 μm) has a much higher absorption degree than CO_2 laser light (λ=10.6 μm).

2.4.3 CO_2 Laser Welding

It is generally accepted that the heat input parameter, defined as the ratio of beam power to beam travel speed, is well suited for describing LBW process. However, Marya et al. [63] demonstrated that this parameter was not convenient, and that, the effect of the laser power and the welding speed parameters have to be differentiated.

2.4.3.1 Laser power

The laser power is a critical parameter to obtain a full penetration depth and to control the weld bead profile. Wang et al [20] showed that the weld width becomes larger with increasing laser power. Dhahri et al. [18, 19] studied the effect of laser power on the penetration depth and weld width for WE43 alloy welded at a speed of 33 mm/s and a focused diameter of 0.25 mm. Figure 2.11 shows that increasing beam power led to deeper and wider beads and the threshold power to achieve full penetration is 1 kW (i.e. a power density of 2 MW/cm^2).

Marya et al. [63] observed, at low beam powers, some chevronlike pattern, which is also called “ripples”. The mechanism of ripples formation is related to the effects of surface tension on the weld pool during solidification[64]. They also observed that the thickness in the weld area was slightly higher, a phenomenon which is called “crowning” or “humping”. Leong et al. [54, 55] assumed that at low irradiance, the spatter and the evaporative losses would be minimized. They showed that for 1.8 mm AZ31 plates sound welds were produced at 2.5 kW

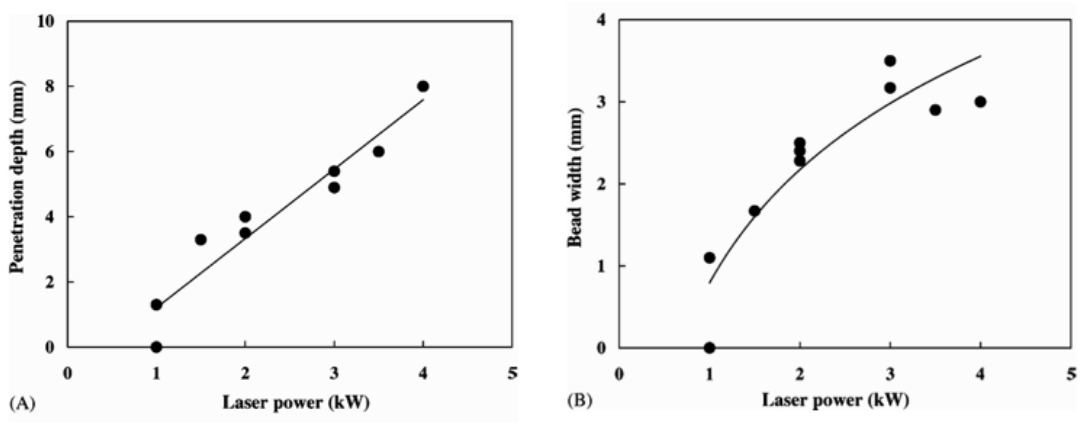

Figure 2.11: Influence of laser power on the penetration depth (A) and on the weld width (B) for WE43 alloy [18, 19].

(i.e. the threshold irradiance was 0.5 MW/cm^2). Weisheit et al. [62] investigated the laser parameters for several magnesium alloys. They reported that for thin AZ31 plates, a 1.5 kW beam power was sufficient for achieving full penetration.

Then, the optimium CO_2 laser beam power to weld 2 mm thick plates will be around 2.5kW.

2.4.3.2 Welding speed

Also based on Dhahri et al. work [19], Figure 2.12 shows that the penetration depth and weld width both increase linearly with decreasing welding speed.

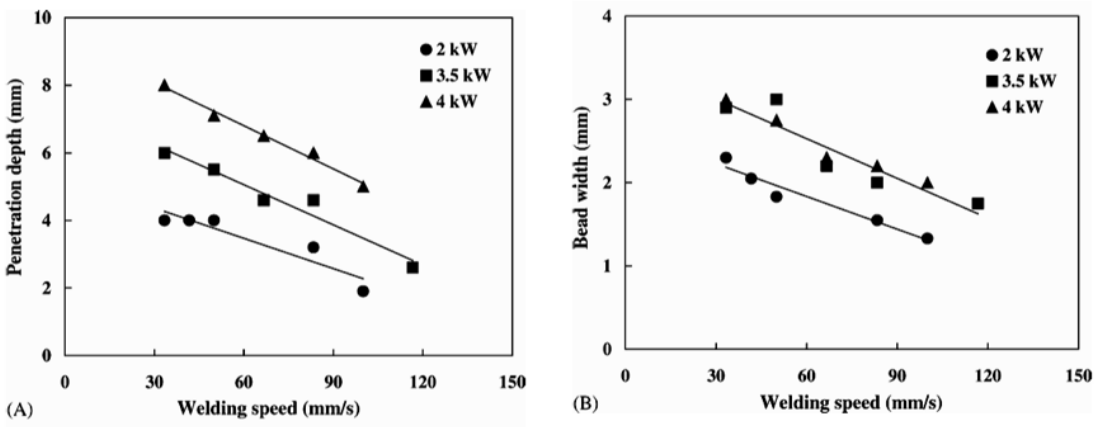

Figure 2.12: Influence of welding speed on the penetration depth (A) and on the weld width (B) for WE43 alloy [18, 19].

This is consistent with Wang et al.[20] study of AZ61. Using lower welding speeds induced

no real change in the penetration depth but wider the weld width and especially the HAZ [65]. On the other hand, using higher welding speeds reduced ripples but greatly increased crowning phenomena [63] and the fusion zone appeared to be far more brittle [57] . Weisheit et al. [62] reported that a welding speed of 2.5-3 m/min was suitable for thin plates, when using 1.5 kW laser beam. Marya et al. [61] studied the influence of the welding speed on pore formation. They found that the pore fraction goes to a maximum with increasing welding speed. At low speeds, the interaction time between molten metal and surrounding air is large enough to allow pores to nucleate in large quantity, grow and escape from the molten pool as a result of buoyancy and convection flow. At high speeds, the pores do not have enough time to nucleate. Moreover, they showed a dependency between crowning and pore content, so that crowning is actually a relevant parameter to assess the weld quality.

Therefore, welding speed above 3 m/min should be achievable during CO_2 laser welding of 2 mm thick plates.

2.4.3.3 Shielding gas

As magnesium is highly susceptible to oxidation, a protective atmosphere is required during welding. The use of shielding gas is also used to protect the optics from metal slag [19, 65]. The choice of the shielding gas influences the formation of the plasma [19, 65]. Three main types of shielding gases are used : helium, argon and nitrogen. Helium due to its high ionization potential of 24.5 eV and good thermal conductivity, has a high plasma formation threshold. Then, small plasma is produced using helium as shielding gas [18, 65, 66]. Weisheit et al. investigated [62] the effectiveness of these three shielding gases and reported that an helium gas flow was the best choice.
Hiraga et al. [66] studied 1.7 mm thick AZ31B-H24 butt joints and get some improvements using argon back shielding in addition to the helium centre shielding. Leong et al. [55] when welding 1.8 mm thick AZ31B-H4 used helium top shielding gas to protect from oxidation, combined with helium back shielding and nitrogen shielding to protect the optics. Wang et al. [20] studied the influence of gas flow rate on weld width and reported that increasing gas flow up to 20 l/min is needed to affect the susceptibility to oxidation (see Figure 2.13).

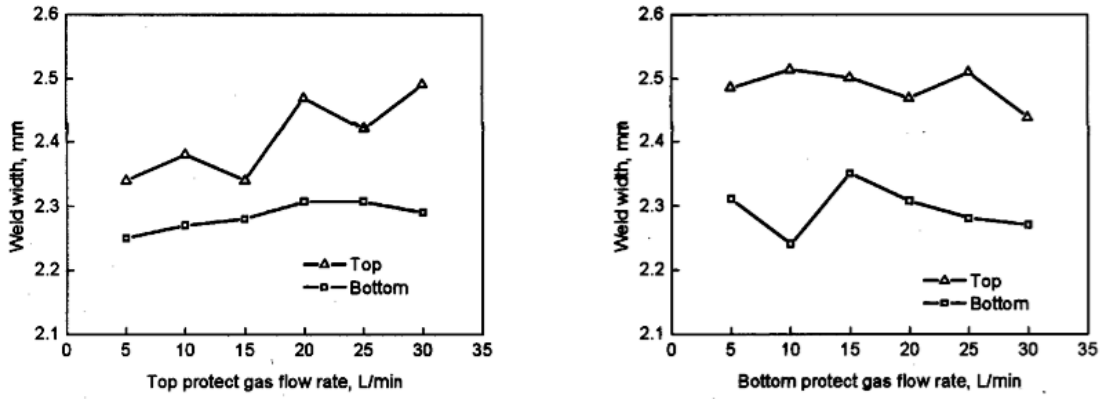

Figure 2.13: Influence of shielding gas on the weld width for AZ61 alloy [20].

Then, the optimum shielding system consists in a top helium flow superior to 20 l/min and Ar back shielding.

2.4.3.4 Focal plane position

The focal plane is influencing as well penetration depths and weld profiles. Dhahri et al. [18, 65] studied 2 kW CO_2 laser welding of 4 mm WE43-T6 alloys. They observed that, to avoid weld defects, a focal position set on the surface or 1 mm under the surface of the workpiece is needed. They also reported that moving away the focal position from the workpiece was increasing the weld width [18]. Weisheit et al. [62] achieved sound welds for thin plates (2.5 and 3 mm) when the focal point was adjusted on the surface of workpiece, whereas the focal distance had to be increased to 2 mm below the surface for thicker plates (5 and 8 mm).

Then, the optimal focal point position to weld thin plates lies on the top surface of the workpiece.

2.4.3.5 Sample preparation

The energy absorption of the beam depends on the surface condition of the material to be welded. Magnesium oxide surface layer observed on magnesium alloys increases the absorptivity for CO_2 laser beams. This will lead to the evaporation of the oxides present in the weld pool, and then to the decrease of oxide inclusions and the purification of weld metal [2]. Magnesium alloys are usually supplied with a chromate coating, which was reported to increase the absorptivity from 3 to 9 % [54, 55]. Its removal by abrasion or polishing will increase the threshold irradiance required for laser welding, reduce the surface quality of the weld, and cause increased spatter and a noisier weld monitor signal. Indeed, Leong et al. reported that, at a spot size of 420 μm and a welding speed of 127 mm/s, the threshold irradiances for CO_2 laser welding of AZ31B alloy were 4.2×10^{5} W/cm^2 with the chromate coating, 6.1×10^{5} W/cm^2 with the coating scrubbed off, and 6.9×10^{5} W/cm^2 with a polished shiny surface [54, 55]. Leong et al., also studied the influence of the sample edge preparation and could not obtain full penetration welds with shear cut edges, in spite of varying the travel speed and the beam power. They observed that improved welds were obtained by using milled edges.

2.4.3.6 Process tolerance

Important weld distortions can occur, caused by the low modulus of elasticity and the high thermal expansion coefficient of magnesium alloys. Barrallier et al. [67] studied residual stresses using neutron diffraction for 5 kW CO_2 laser welded WE43 alloy joints (3 mm thick). Tensile stresses were found in the weld, caused by the volume contraction, which occurred during solidification.

2.4.4 Nd:YAG laser welding

2.4.4.1 Laser power

The threshold irradiance to reach keyhole welding with Nd:YAG laser, has been studied for several magnesium alloys. Die cast alloys showed an optimum power between 2 and 2.5 kW [59, 58]. Indeed, the tensile strength was found to decrease with Nd:YAG laser power lower than

2 kW. Leong et al.[55] studied Nd:YAG laser welding of AZ31 wrought magnesium alloy. They reported that sound welds could be obtained at an average power of 0.8 kW (peak 1.3 kW) at 3 cm/s speed.

2.4.4.2 Welding speed

Aghion et al. [21] studied the effects of welding speed on penetration depth and weld width. Figure 2.14 shows that the penetration depth and weld width both decrease linearly with increasing welding speed.

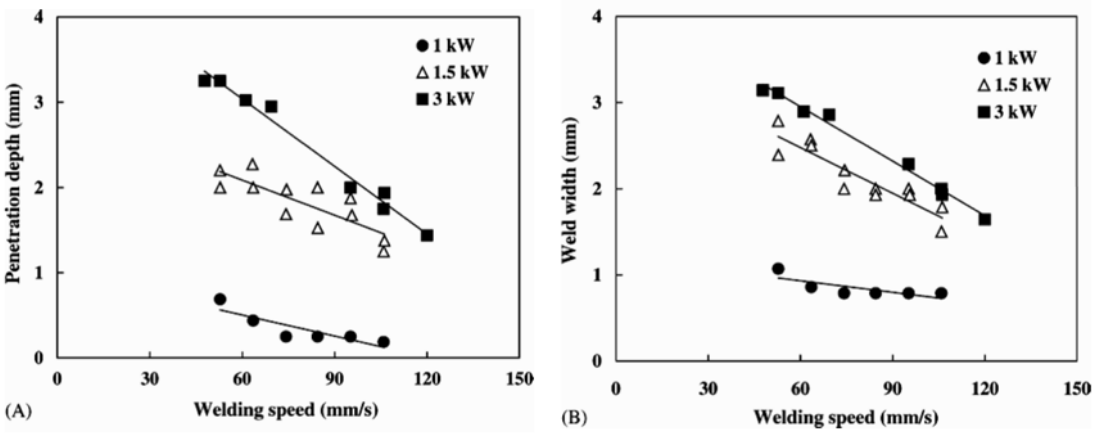

Figure 2.14: Influence of welding speed on the weld width and penetration depth [21].

Haferkamp et al. [56] observed in addition that the difference in thermophysical properties of magnesium alloys could explain the different welding performance observed. Indeed, AZ91D alloys exhibited deeper and larger welds than AZ61A alloys because its thermal conductivity (51 $W.m^{-1}.K^{-1}$) is lower than AZ61A one (139 $W.m^{-1}.K^{-1}$).

2.4.4.3 Shielding gas

With Nd:YAG laser welding, Argon centre shielding is sufficient to produce sound beads as Nd:YAG laser has less tendency to form a plasma than CO_2 laser [66]. But, the use of a back shielding gas can reduce the sag, which often occurs due to the low viscosity and surface tension of magnesium. Then, lower welding speeds can be used and a better surface quality can be obtained [58].

2.4.4.4 Focal plane position

Lehner et al. [58] studied the tolerance of focal position. They found that, for 3 mm thick AZ91 and AM50 using a 3 kW Nd:YAG laser, the best focal position is approximately 0.8 mm below the workpiece surface, with a tolerance of ± 0.5 mm. For 5 mm thick plates, the focal position has to be shifted to about 1.2 ± 0.2 mm below the surface.

2.4.4.5 Sample preparation

The MgO layer usually present on the surface of magnesium alloys should have a little influence on the energy absorption of a Nd:YAG laser beam as MgO is transparent to infrared spectra and the 1.06 μm Nd:YAG wavelength lies in the infrared region [2]. Cao et al. reported that machined surfaces would require higher power density [2]. This could imply that better surface conditions decrease the energy absorptivity for Nd:YAG laser beams.

2.4.5 Comparison between CO_2 and Nd :YAG lasers

The comparative study of CO_2 and Nd:YAG Laser Beam Welding is summarized in Table 2.3. Nd:YAG laser having a shorter wavelength than CO_2 laser, a lower threshold irradiance

Laser type	CO_2	Nd:YAG
Power (P)	high P required	sound welds achieved at low P
Welding speed (V)	high V can be reached	low V
Shielding gas	He + Ar backshielding	Ar
Focal point	on the top surface	at about 1/4 of the thickness below the top surface
Sample preparation	milled edges	cut edges

Table 2.3: Comparison between CO_2 and Nd:YAG Laser Beam Welding.

is required and then, it produces a more stable weld pool. So, the weldability of magnesium alloys appears to be improved when using Nd:YAG laser [54, 55, 57]. Moreover, Nd:YAG laser beams have a higher welding efficiency than CO_2 lasers [68, 57]. Indeed, from the literature, it can be observed that, for a 1.5 kW laser beam with a similar spot diameter and welding speed (5 m/min), a penetration depth of 2 mm was achieved for a Nd:YAG laser whereas it was only 0.7 mm deep for the CO_2 laser [68]. This is consistent with Sanders et al. [54] conclusions. They achieved to produce sound welds at a 0.8 kW beam power and a 30 mm/s travel speed with a Nd:YAG laser , whereas, for a CO_2 laser, sound welds were obtained at 2.5 kW and 127 mm/s. In addition, for CO_2 laser welding, milled edges are needed but shear cut edges can be used for Nd:YAG welding [68, 57]. This is due to the difference in beam size which makes the fit-up to become an issue for CO_2 laser [54, 55, 57]. Moreover, for Nd:YAG the presence of oxide layer is less to be concerned with, as the beam high peak power is breaking up the MgO layers better than for CO_2 laser beam. In conclusion, the weldability problems of magnesium alloys are much more easily overcome when using Nd:YAG than CO_2 laser.

2.5 Material flow and thermal histories experienced during Friction Stir Welding and Laser Beam Welding

2.5.1 Introduction

The characterisation of the mechanical and thermal processes induced during welding is required to fully understand the processes and then to optimize the process parameters for controlling microstructure and weld properties. In this section, the different methods used for the experimental characterisation of the thermal and mechanical processes will be described.

2.5.2 Metal flow visualisation in FSW

Many studies have been done, mainly on aluminium alloys, to analyse metal flow during FSW. Metal flow experimental characterisation can be performed by several techniques. For tracer techniques, a marker material which differs from the material being welded, is employed, such as:

- a metal that etches differently from the base metal [69],
- a copper foil [70, 17],
- small steel spheres [71],
- Al–SiCp and Al–W composites [72, 17].

But, with these techniques, if the marker material has different flow strength and density, the reliability of the results can be argued [17]. Flow visualization can be also studied by FSW of dissimilar materials [73, 74] but dissimilar welds may have a different structure than welds of the same alloy. FSW flow characterisation using plasticine has been performed by Liechty et al.[22]. Although plasticine is an amorphous material, which will result in a different microstructure, its stress–strain behavior at elevated strain rates and high temperatures is similar to metals. With plasticine highly contrasting colors, flow pattern and extent of mixing can be directly determined from weld sections (Figure 2.15). Metallography analysis was another method performed to

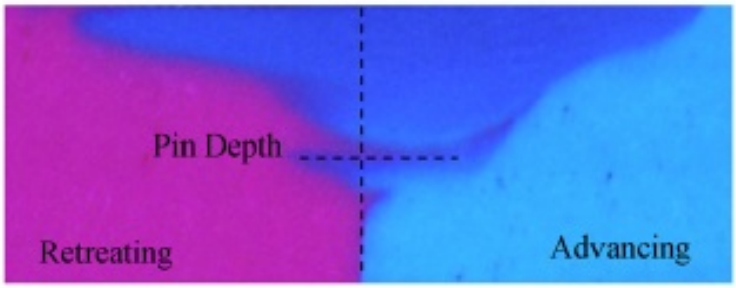

Figure 2.15: FSW flow visualisation using plasticine (W = 1500 RPM, V = 1 mm/s) [22].

study FSW material flow [75]. Kumar et al. [75] studied 4.4 mm thick 7020-T6 aluminium alloy FSW processed using a knee type vertical milling machine. The backing plate was inclinated during welding which induced a progressive increase in the applied pressure and allowed the study of shoulder and pin own influence. They have drawn the following conclusions regarding the FSWeld formation mechanism:

- The pin plunged into the base material, created a cavity and caused material to plasticize close to the pin and below the shoulder.
- The material plasticized at the leading edge and then, it flew through the retreating side to the trailing edge driven by the shoulder and by the pin.

- The shoulder-driven flow from the retreating side reached the advancing side and then, the material was forged against the advancing side base material. Meanwhile, the pin-driven flow induced material layer formation around the pin, stacking along the weld line.

- Flash creation occurred when it was easier for the material to flow out than to move forward the trailing edge of the tool.

- Sufficient temperature and pressure were needed to fill the weld cavity. Then, the material from the shoulder-driven flow, from the pin-driven flow and the base material coalesced with each other.

- The shoulder induced a sub-surface material flow which caused the weld assymmetry.

2.5.3 FSW Temperature distribution

During FSW, heat is generated by the plastic deformation occuring around the tool and the friction between the tool and workpiece. The understanding of the temperature distribution is then necessary as it influences the microstructure of the welds, and its resultant mechanical properties. Temperature measurements can be either obtained using embedded thermocouples [76] or IR thermography [77]. Tang et al. [23] embedded thermocouples in holes drilled into the back surface of the workpiece, at different distances from weld seam and different depths. They observed that the maximum peak temperature was recorded at the weld centre and decreased with increasing distance from the weld centre. The temperature distribution in the thickness was relatively uniform in the stirred area. Increasing tool rotation rate and weld pressure resulted in an increase in the weld temperature [23, 78, 79] (Figure 2.16).

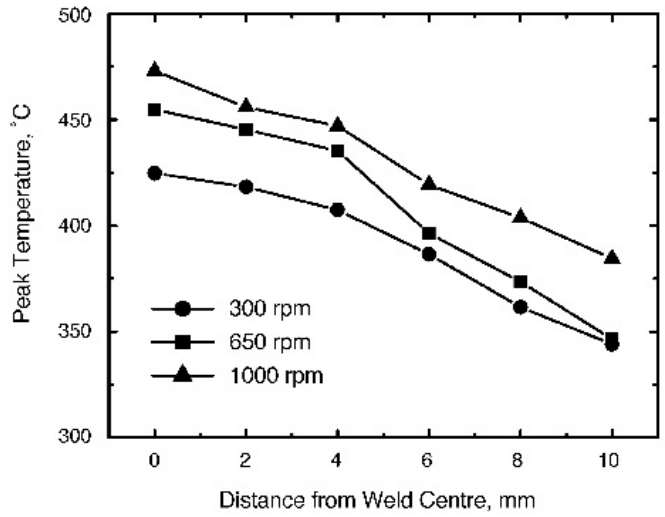

Figure 2.16: Influence of tool rotation rate on peak temperature for a 6061Al-T6 FSW (V = 120 mm/min)[23].

Tang et al.[23] study also highlighted that the heat is mainly generated by the tool shoulder (Figure 2.17). They explained that it was caused by the contact area and vertical pressure which are larger between the shoulder and workpiece than between the pin and workpiece. This was also confirmed by Colegrove and Shercliff [80]. Tang et al.[23] reported no difference in temperature distribution between the advancing and the retreating side.

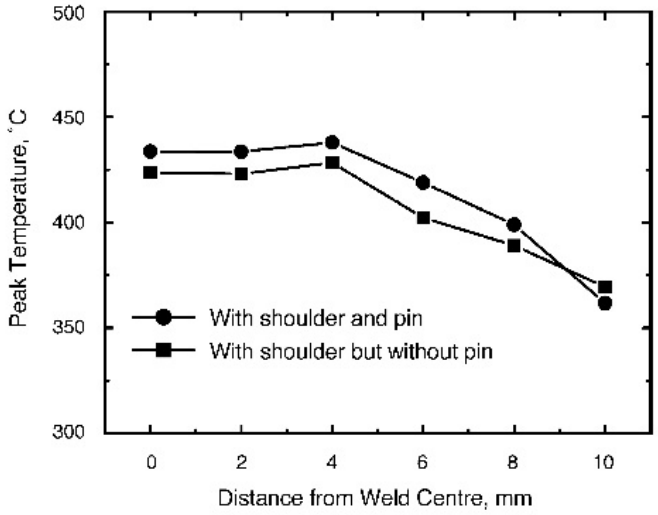

Figure 2.17: Variation of peak temperature for a 6061Al-T6 FSW weld made with and without pin (W = 400 RPM, V = 120 mm/min)[23]

Temperature measurements within the stirred zone cannot be obtained by these techniques due to the deformations induced by the tool. Therefore, the maximum process temperature could be determined by an investigation of precipitation evolution during welding [81] and comparing it with simulated weld thermal cycles [78]. The maximum temperature observed during FSW of aluminium alloys was about 450 °C which is about of 70% of the aluminium alloy melting point. The experimental temperature distribution in FSW were confirmed by several analytical and numerical modelling [82, 25, 80, 83, 77, 84, 85, 86, 87].

2.5.4 LBW Temperature distribution

During LBW, energy is absorbed at the metal surface by Fresnel absorption. If the intensity is high enough, metal ionisation occurs. The free electrons then absorb energy directly from the beam by inverse absorption, resulting in higher temperatures, increased ionisation and increased absorption. The vaporisation of the surface progressively forms a depression in the workpiece and then a keyhole, which allows the laser energy in-depth absorption. The temperature evolution during LBW can be determined using thermocouples [88] and thermo-cameras [89]. The use of IR thermography is limited by the laser reflection interferences. Indeed, the IR image is generally captured paralleling to the direction of welding seam and the laser nozzle interference shadow lies area of interest (welding seam) (Figure 2.18 (a)) preventing from a consistent measurement. Huang et al. [24] reported a method to reduce these interferences, by placing the IR thermography system perpendicularly to welding seam (Figure 2.18 (b)). The laser interference

are then transferred out of welding seam.

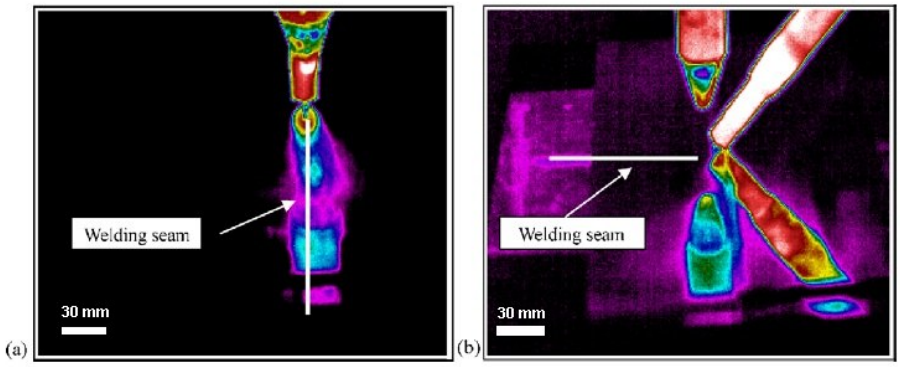

Figure 2.18: IR images captured (a) parallel and (b) perpendicular to the direction of welding seam during AZ31 hybrid laser-TIG welding process [24].

The maximum temperature observed during LBW of aluminium alloys was about 1000 ˚C [90], which is about of 155% of the aluminium alloy melting point and 100 ˚C below the magnesium boiling point. The analytical and numerical thermal modelling of LBW is reported in a review article [91].

2.6 FSW Microstructural evolution

2.6.1 Introduction

The microstructural studies of FSW revealed the formation of 3 different areas (Figure 2.19): nugget, thermo-mechanically affected zone (TMAZ), and heat-affected zone (HAZ).

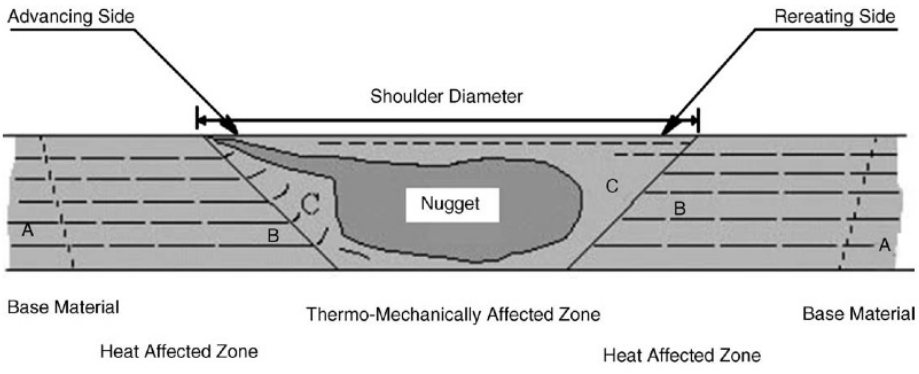

Figure 2.19: Sketch of FSW cross-section showing the different microstructural zones [25].

Each zone corresponds to various changes in microstructure and then influences the resulting weld mechanical properties.

2.6.2 FSW Nugget

Two different nugget shapes were observed, depending on processing parameters, tool geometry, temperature of workpiece, and thermal conductivity of the material: basin-shaped nugget [78, 53] and elliptical nugget [92, 93, 81] (Figure 2.20). The width of the nugget is related to the

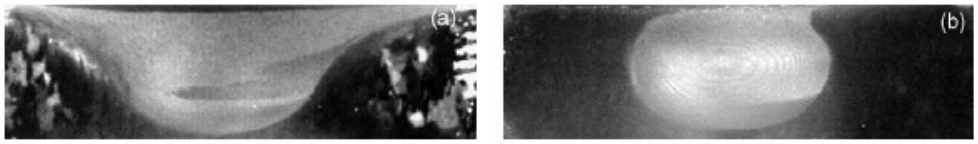

Figure 2.20: (a) basi-shaped and (b) elliptical nugget [17].

tool size [94]. The combined effects of temperature and plastic deformation in FSW produces recrystallization, precipitation [73, 93, 23] and texture evolution [73, 93, 23, 95]. The grain refinement associated with recrystallisation depends on several parameters: FSW parameters, tool geometry, temperature of the workpiece (which can be modified by cooling the workpiece during welding). Decreasing the tool rotation rate (W) at a constant welding speed (V) [73] or decreasing the W/V [96] resulted in nugget grain size reduction. Indeed, these parameters influence the temperature and the strain rate and then the recrystallised grain size. For thicker plates (6.35 mm thick [97]) grain size variation, corresponding to the temperature variation, was observed within the nugget.

Depending on the alloy composition, precipitate dissolution [78] and coarsening [98, 95, 99] can occur within the nugget due to the high temperatures involved.

The nugget usually presents low dislocation density [78] due to the recrystallisation. However, Park et al. [53] and Esparza et al. [100] found that the nugget contains a high density of dislocations respectively in AZ61 and AZ31. They explained that during the migration of recrystallization fronts, dislocations are accumulating in the unrecrystallized material but are also trapped in the recrystallized material behind the migrating front [53] leading to a high dislocation density in the recrystallised grains.

Recrystallisation occurs in FSW, especially in the nugget zone, due to the large strains and high temperature experienced in this area. The recrystallisation mechanism occuring in the nugget zone had led to several studies [99, 101, 98, 102]. The formation of fine grained structure in the nugget was attributed to dynamic recrystallisation [99, 98, 102]. The mechanisms reported in magnesium alloys are continuous and discontinuous dynamic recrystallization [103]. Discontinuous recrystallization mechanism is characterized by nucleation and nucleus growth by high angle boundary migration, whereas continuous recrystallisation consists in continuous absorption of dislocations in subgrain boundaries (low angle boundaries), resulting in high angle boundaries and then new grain formation [104]. Then, during FSW, the mechanism involved is continuous recrystallisation, as the nugget grain structure is of the order of the subgrain size [101]. Previous studies [99, 102] described the continuous dynamic recrystallisation as follows. They reported that due the high strain levels undergone in the nugget, the recrystallisation mechanism occurs by rotation of subgrains, due to the absorption of dislocations into the subgrain boundaries, until they develop high misorientations [99, 102].

2.6.3 FSW Thermo-mechanically affected zone

The TMAZ is located between the base metal-HAZ and the nugget. The strain undergone is not sufficient to promote recrystallisation but results in grain deformation. The high temperature can lead to precipitation evolution [78].

2.6.4 FSW Heat affected zone

In the HAZ, no plastic deformation occurs, only the temperature influences. The effect on the grain structure is very low, but coarsening of the strengthening precipitates and the precipitate-free zone (PFZ) increase was observed [99, 95] in aluminium alloys.

2.6.5 FSW texture evolution

Woo et al. [4] studied the texture evolution in AZ31 FSW by neutron diffraction. The results showed a significant texture variation across the FSW. Their investigation showed that the basal plane normal was parallel to the Transverse Direction (TD) in the TMAZ. In the nugget, the texture was influenced by the plastic deformation and the basal plane normal followed the pin rotation and aligned with the welding direction in the weld centre (Figure 2.21).

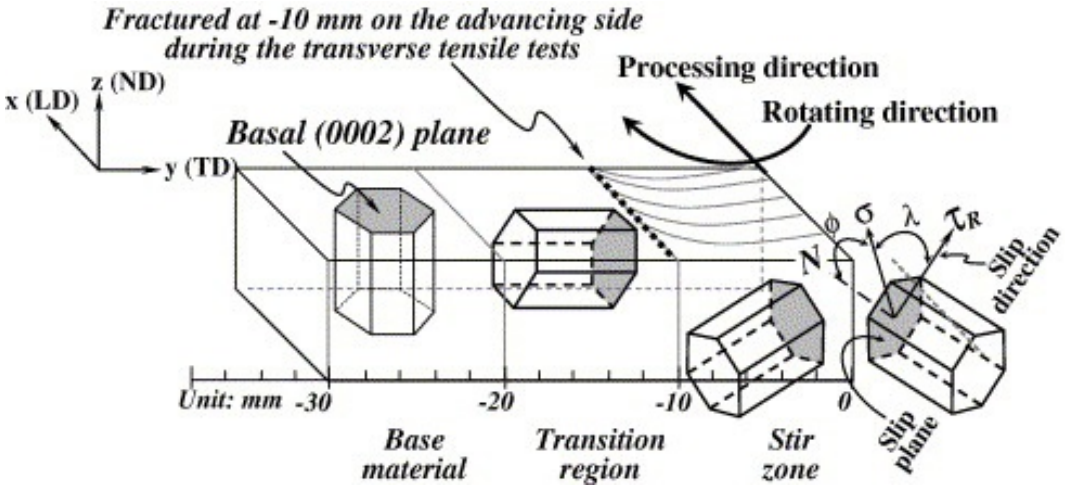

Figure 2.21: Sketch of basal plane rearrangement in the base metal, TMAZ and nugget [4] .

Similar results were found for 6061-T6 aluminium alloy [105]. The results indicated also that texture evolution is caused by the pin stirring, while heating alone from the tool shoulder has little effect [105].

2.7 LBW Microstructural evolution

In LBW, the heat input leads to the formation of 2 different areas: fusion zone and heat-affected zone (HAZ) which presents high thermal gradients. Due to the high heat dissipation, narrow fusion zone and HAZ are created. The 2 kW Nd:YAG and 6 kW CO_2 laser welding studies

of wrought AZ31B alloy indicated that the width of the HAZ was 50–60 μm and depends on the welding speed [54, 55]. The fusion zone microstructure consists in a fine equiaxed grain structure[61, 62, 59] and fine and randomly oriented equiaxed dendrites which nucleated in the fusion zone [61, 59]. Grain refinement can occur in the fusion zone caused by the rapid cooling [59, 62, 68]. Depending on the base metal, precipitation evolution and grain growth [54, 62, 55] can occur in the HAZ. A liquation of the grain boundaries adjacent to the fusion boundary was observed, caused by the melting of some low melting-point intermetallics at grain boundaries [62].

2.8 FSW Weld properties

2.8.1 Introduction

The microstructural evolution observed after welding results in the modification of the mechanical properties, and corrosion resistance. In this study the corrosion issues and the fatigue properties will not be discussed and then the literature survey was focused on hardness, tensile properties and residual stresses involved.

2.8.2 Hardness

The hardness evolution depends on the hardening mechanisms involved in the alloys studied. In cast alloys, higher hardness is reported in the nugget due to grain refinement, following the Hall–Petch relationship [26, 53, 49] (see Figure 2.22).

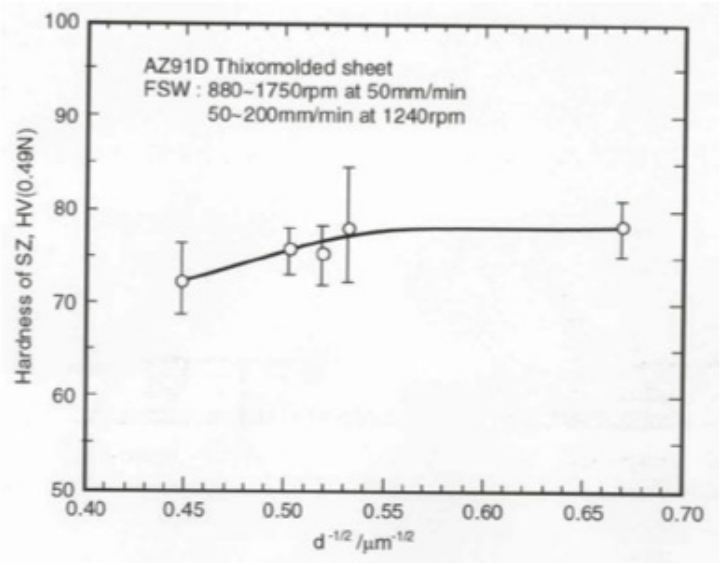

Figure 2.22: Hardness evolution in the stir zone function of the grain size[26].

In precipitation hardening alloys, the hardness decreased due to precipitate dissolution until reprecipitation occurs (e.g. in 7xxx alloys) resulting in a recovery of hardness in the nugget.

2.8.3 Tensile properties

FSW resulted in an improvement in tensile properties of cast magnesium alloys such as AZ91 [26, 53, 49], whereas a reduction in tensile properties was observed in wrought magnesium alloys AZ31B-H24 and AZ61 [53, 49]. On the other hand, Lee et al. [49] reported a reduction in tensile properties of FSW AZ31B-H24 with fracture occurring close to the stirred zone, which is attributed to significantly coarse grained structure in the stirred zone. Similar results were also observed by Park et al. [53]. Transverse tensile test revealed that FSW AZ61 weld exhibited a much lower yield strength and elongation than the base metal. Further, ultimate tensile strength of the weld is slightly lower than that of the base metal. The weld fractured in the stirred zone near the transition region.

2.8.4 Residual stress

Residual stress evolution in aluminium alloys FSW has been extensively studied [106, 107, 108, 109, 110]. X-Ray Synchrotron and Neutron Diffraction techniques were generally used to analyse residual stresses. Dalle Donne et al.[106, 17] compared several techniques such as X-ray diffraction, neutron diffraction and synchrotron radiation. They found a good agreement between these techniques (Figure 2.23).

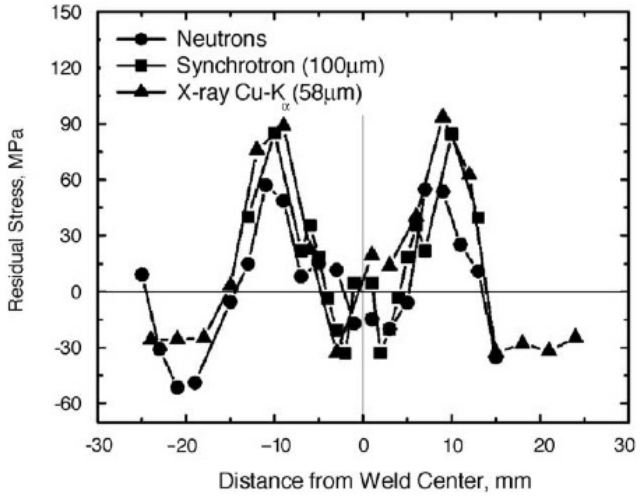

Figure 2.23: Longitudinal residual stress distribution in FSW 6013Al-T4 welds determined by different measurement methods (W = 2500 RPM, V = 1000 mm/min, tool shoulder diameter: 15 mm) [17].

Longitudinal residual stresses were higher than the transverse ones [106, 107] and this tendency was not influenced by the processing parameters (pin diameter, tool rotation rate and traverse speed). Increasing welding speed and tool rotation rate resulted in an increase in the magnitude of tensile residual stresses [106, 107] A typical "M"-shaped residual stress distribution was observed across the weld [106, 107] which widens with increasing shoulder diameter. This form of profile, with a dip in the nugget area can be caused by the higher temperature that

would lower the capacity of the material to support the generated load [107]. Another reason could be the stress relief occurring afer cutting the plate [107]. Peak tensile stresses were observed at the edge of the shoulder tool (i.e. TMAZ) and a slight assymmetry was observed with higher values on the advancing side [107, 109]. Woo et al. studied the residual stress evolution in FSW of AZ31 magnesium alloy [5] using neutron diffraction and contour method [111]. Neutron diffraction longitudinal residual stress profiles show a decrease in the nugget (Figure 2.24)

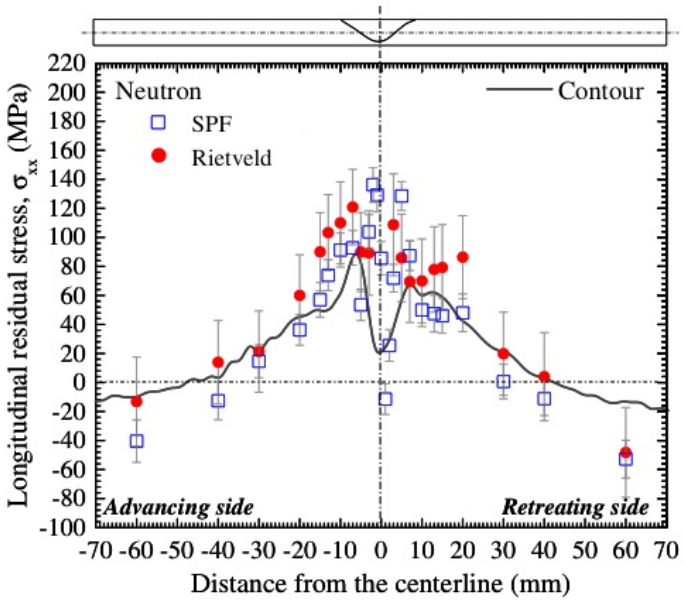

Figure 2.24: Comparison between the longitudinal residual stresses of AZ31 FSW determined using the contour method and neutron diffraction. The diffraction data include SPF (Single peak fitting method, pyramidal peak) and Rietveld results [5].

2.9 LBW weld properties

2.9.1 Hardness

The microhardness of magnesium cast alloys increased in the fusion zone due to the finer grain size [59, 61, 62] and higher precipitate volume fraction [59]. The microhardness was similar to the base metal one in the HAZ [59, 62].

For wrought alloys, little variation in hardness was observed [62, 68, 55, 54, 112]. This could be explained by the loss in work hardening which is compensated by the grain refinement. Coelho et al. [3] investigated the microhardness evolution in hot rolled AZ31 and found a slightly higher value in the fusion zone and HAZ than in the base metal; whereas Nagasawa et al. [112] found no difference in hardness between the fusion zone and AZ31 base metal. At low welding speed, the microhardness variation is small, whereas, increasing welding speed resulted in a finer grain structure in the fusion zone leading to an increase in the fusion zone hardness [59]. Inhomogeneity in the weld thickness was reported in previous studies [59, 18] of

cast alloys, whereas the study of hot rolled AZ31 did not demonstrate any significant variation between microhardness profiles made at several depths [3]. The comparison between 1.7 mm thick AZ31B-H24 butt joints produced using a Nd:YAG laser and a CO_2 laser showed that the fusion zone microhardness is higher in Nd:YAG welds than in CO_2 welds [66, 55, 54]. Indeed the cooling rate is higher with Nd:YAG laser resulting in finer grains and smaller dendrite arm spacings [66].

2.9.2 Tensile properties

The weld tensile strength was similar than the base metal one [56], whereas the ductility of the weld joints was lower than that of the base material. Tensile properties were generally determined using cross-weld specimen. Due to the inhomogeneity of the material in the sample, the elongation is not characteristic of the material but depends on the sample geometry. Haferkamp et al. [68] studied 1.36 mm thick wrought AZ31B Nd:YAG laser welds. They observed that the fracture occured in the weld zone, with a 64% reduction in fracture strain. The use of filler material (AZ61) resulted in a tensile and yield strength 90–100% of the base material and a 16% fracture strain reduction. The mechanical properties greatly depend on the weld quality (notches, porosity, oxide content) [68, 58]. Coelho et al. performed tensile tests on AZ31 CO_2 welds and observed a lower yield strength compared to the base material. They explained this reduction by the activation of different deformation mechanisms [3]. The influence of processing parameters and the heat input on the weld tensile properties was investigated by Quan et al. [113]. They observed that the UTS and elongation increased at first and then decreased when the heat input increased, with a maximum value at 24 J/mm. The maximum UTS reached was about 96.8% of the base metal whereas the maximum elongation reached was only about 50% of the base metal which was due to the change in microstructure. At low heat input, the lower mechanical properties were explained by the incomplete penetration. Increasing heat input resulted in coarser grains and precipitation occuring at the grain boundaries, which decreased the tensile properties of weld.

2.9.3 Residual stress

Coelho et al. [3] studied residual stress evolution across AZ31 CO_2 LBW by Synchrotron X-Ray diffraction (Figure 2.25). The residual stress distribution across the weld width was symmetric and the analysis on the top and bottom surface showed similar results. Higher residual stresses were observed in the longitudinal direction than in the transverse direction.

2.10 Conclusion

The literature survey has shown the specificity of magnesium alloys in terms of formability and welding conditions required. Wrought magnesium alloys exhibited a higher LBW potential than cast alloys due to their lower pore content. The processing parameters were identified. CO_2 laser welding presents some disadvantages over Nd:YAG laser welding but the manufacturing process better fits the industrial requirements. The microstructure evolutions induced by FSW and LBW will have a great influence on resulting mechanical properties. Temperature measurements and metallography examination will allow us to investigate the thermal history during LBW and FSW and metal flow during FSW.

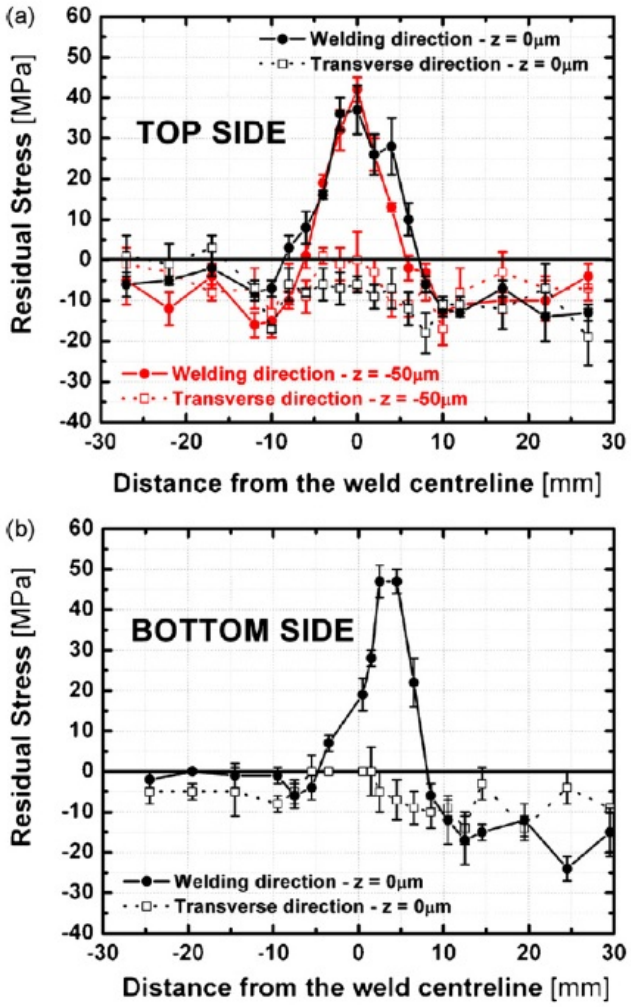

Figure 2.25: Residual stress profiles of the LBW AZ31B magnesium alloy: (a) top side and (b) bottom side of the weld, z is the distance from the surface at which the measurements were performed [3].

Chapter 3

Experimental

3.1 Materials used

3.1.1 Introduction

In the frame of this project, several magnesium alloys produced by Magnesium Elektron (MEL) were rolled by Salzgitter Magnesium Technologies GmbH to produce 2 mm thin plates. Rolling magnesium alloys is an issue and then, most plates produced are usually cast products. In this project, 100 mm ingots were hot rolled with several passes using a 4 rollers Quarto rolling mill. Strain rates between 5-20% (thickness reduction per pass) and rolling speeds between 0.5-2 m/s were used. Then the plates were hot levelled and a further heat treatment was done. A strong basal texture resulted from this process. These plates were used as raw material for welding and as samples for base material analysis.

3.1.2 AZ31 magnesium alloy

AZ31 magnesium alloy was chosen due to its good rolling capabilities. 2 mm thick plates were hot rolled by several passes and then levelled and 300°C annealed. Table 3.1 shows the chemical specification of the AZ31 magnesium alloy supplied.

Element	Al	Zn	Mn	Si	Cu	Ni	Fe	Ca	others	Mg
wt%	2.5-3.5	0.6-3.4	0.2-0.6	< 0.05	< 0.008	< 0.002	< 0.005	< 0.02	< 0.3	balance

Table 3.1: AZ31 chemical specification from MEL.

3.1.3 AZ61 magnesium alloy

AZ61 magnesium alloy was chosen because it has a higher strength than AZ31. 2 mm thick plates were hot rolled by several passes at 300-360°C, levelled and then 1 h at 250°C annealed. But rolling AZ61 is not trivial and it was first performed by Salzgitter Magnesium Technologies in the frame of this project. Table 3.2 shows the chemical specification of the AZ61 magnesium alloy supplied.

Element	Al	Zn	Mn	Si	Cu	Ni	Fe	Mg
wt%	5.8-7.2	0.4-1.5	> 0.15	< 0.1	< 0.05	< 0.005	< 0.005	balance

Table 3.2: AZ61 chemical specification from MEL.

3.1.4 WE43 magnesium alloy

WE43 magnesium alloy is a precipitate hardened alloy which was chosen for its improved corrosion resistance compared to AZ61. 2 mm thick plates were hot rolled by several passes at 460-510°C, then levelled at 350°C and then annealed during 16 h at 200°C. Rolling WE43 was first achieved during this project by Salzgitter Magnesium Technologies. Table 3.3 shows the chemical specification of the WE43 magnesium alloy supplied.

Element	Y	Nd	R.E.*	Zr	Zn	Li	Mn	Cu, Fe, Si, Ni	Mg
wt%	3.7-4.3	2.0-2.5	< 1.9	0.4-1.0	< 0.2	< 0.15	< 0.03	< 0.01	balance

Table 3.3: WE43 chemical specification from MEL. (*Rare Earth other than Nd)

3.2 Welding Process

3.2.1 Sample preparation prior to welding

Before welding, each sample was machined to remove the oxide layer and cleaned with acetone (C_3H_6O).

3.2.2 Friction Stir Welding

FSW processing was carried out with two different machines at two locations: EADS-IW-F Suresnes and EADS-IW-G Ottobrunn. Different clamping systems and 3 different steel tools (threaded pin, concave shoulder) were tested (see Table 3.4).

Facility	Pin diameter (mm)	Shoulder diameter (mm)
IW-F-ISTIR	4	10
IW-G-ESAB	5	10
IW-G-ESAB	5	13

Table 3.4: Tool designation.

Figure 3.1 shows the whole device used during FSW. The process window was determined at the IW-F by using bead on plate welds. The process parameters that have been varied are the welding speed and the tool rotation rate. Figure 3.2 highlights the processing parameters studied. Then a butt weld was produced using the optimum parameters (in terms of visual aspect and internal defects assessed using radiography). The optimum parameter criteria are defined in section 4.3. Some more butt welds were produced at the IW-G using different tools. The welding can be performed either using a position control mode (i.e. the tool advanced at a constant height and the vertical pressure was adjusted) or using load control mode (i.e. the tool

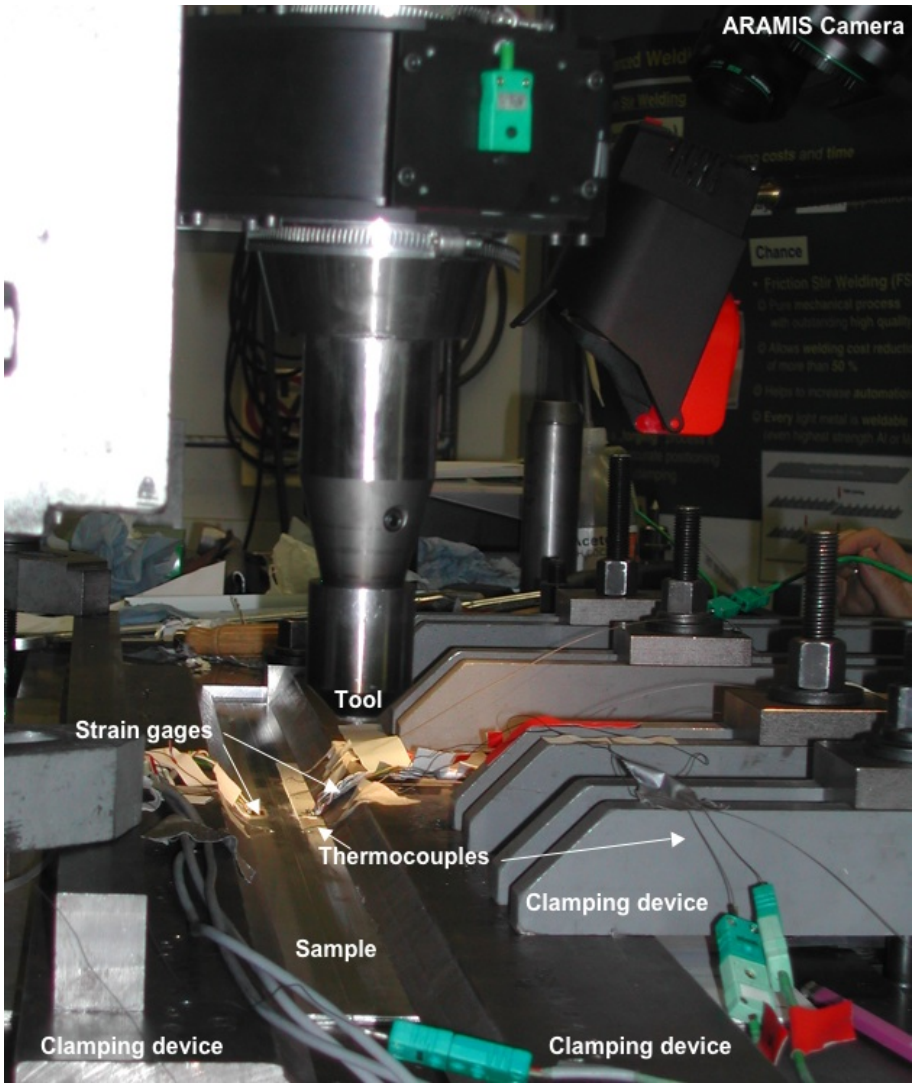

Figure 3.1: FSW Experiment.

advanced at a constant vertical pressure and the tool height was adjusted). Position control was used for bead on plate and load control for butt welding.

3.2.3 Laser Beam Welding

3.2.3.1 Nd:YAG LBW

Nd:YAG welding of AZ31 was carried out at the IW-F. Two plates were produced for analysis using 2.4 kW power and 7m/min welding speed. Argon shielding gas was used at 30 l/min.

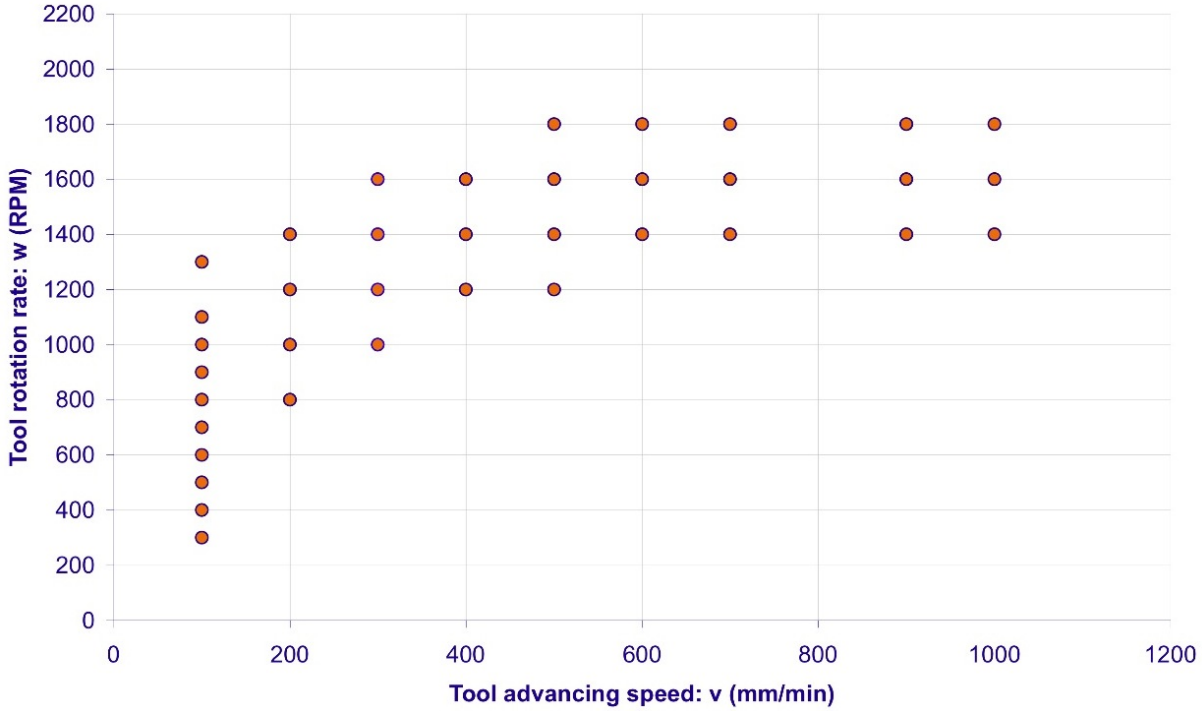

Figure 3.2: FSW Processing parameters studied, 4 mm diameter pin, 10 mm diameter shoulder.

3.2.3.2 CO_2 LBW

CO_2 welding was performed at MécaSurf Laboratory, ENSAM using a ROFIN 3kW facility (Figure 3.3). For AZ31, a 1 axis device, numerically driven by a Labview program, was used to control the weld advancing speed. For AZ61 and WE43 LBW, a computer numerical control was used. The two other axis were manually driven: Z-axis to set focal length and X-axis for positioning the laser beam. Samples were inserted in a clamping device (see Figure 3.3) which was fixed on the 1 axis device. The process window was determined by using bead on plate welds. The process parameters that have been varied are laser power (from 1.2 to 3 kW), welding speed (from 0.6 to 15 m/min), focal position to the mid-thickness (from -2 to +1 mm), and shielding gas flow (from 0 to 40 l/min). The shielding gas used were helium coaxial to the laser beam and backing Argon. Then butt welds were produced using optimum parameters (determined by stereomicroscope inspection). The optimum parameter criteria are defined in section 4.3.

3.2.4 Measurements performed during welding processes

3.2.4.1 Introduction

Temperature measurements and strain measurements were performed during welding in order to establish a relationship with the processing parameters. It will allow a better uderstanding of the thermal and thermomechanical mechanisms involved and of the resulting microstructure

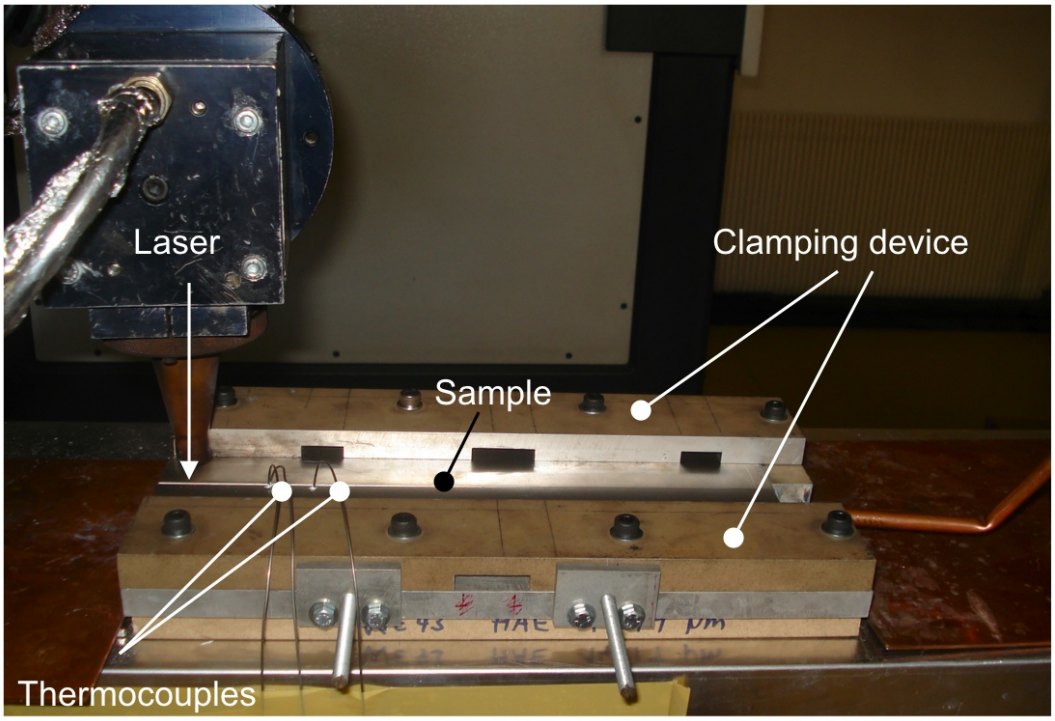

Figure 3.3: CO_2 LBW experiment.

and mechanical properties.

3.2.4.2 FSW

Thermocouples have been positionned to measure the temperature undergone during welding for 4 different processing parameters. They were fixed using silicone paste into mid-thickness drilled holes. The temperature versus the distance from the weld centre will be determined. Strain gages have been used to determine the stress state evolution during welding and to try to dissociate the clamping influence. A GOM ARAMIS CCD camera was used to get some informations of the strains that occured during the process. Although the window observed is quite small as the acquisition time limited to 2 minutes, mouchetis evolution can provide information on the strain evolution during the process [114]. The tool movements and the expelled material appeared to greatly influence the optical measurement and to prevent from obtaining accurate data with this technique. Figure 3.4 exhibits a typical picture obtained with ARAMIS.

3.2.4.3 CO_2 LBW

Thermocouples were placed to measure the temperature undergone during welding for 4 different processing parameters. They were fixed using silicone paste into mid-thickness drilled holes. Temperature data collection was done using a Labview program. The temperature versus the distance from the weld centre will be determined. The recording device could achieve a 5 Hz

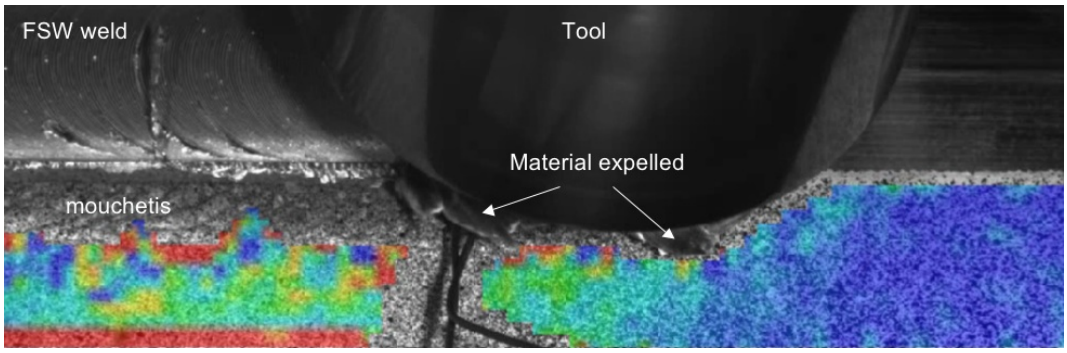

Figure 3.4: CCD measurements, the coloring corresponds to the strain level.

maximum frequency and the thermocouples had to be placed at a safe distance from the weld seam. It reduced the availability of high temperature and high temperature gradients results.

3.2.5 Weld quality control

The quality of the FSW and LBW welds produced was assessed by visual inspection and using radiography technique and used to define the optimum processing parameters. As magnesium is a very light material, 30 V and an exposition time of 25 seconds was applied to avoid over-exposed films. Figure 3.5 shows a FSW radiography, highlighting the typical features that can be observed. The bright features correspond to a lower thickness and then some lack of material and the dark features correspond to higher thickness or higher density areas.

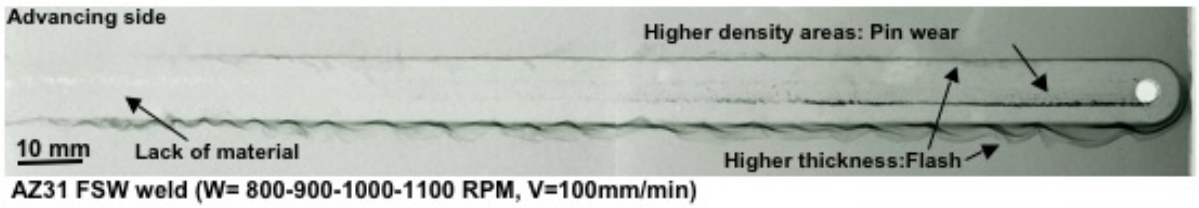

Figure 3.5: Radiography of a FSW weld

3.3 Experimental procedures

3.3.1 Introduction

In this section will be described the different experimental techniques that were used in this study. The aim of the experimental study was to characterise the microstructural and mechanical evolution of the alloys with the welding process. Optical Microscopy was performed to study the weld morphology and the evolution of the grain structure. Scanning Electronic Microscopy (SEM) was used to study the intergranular precipitation. SEM was coupled with Energy Dispersive Spectroscopy (EDS) to determine the chemical composition of the phases.

X-Ray diffraction Spectra were used to complete the analysis of the nature of the phases observed. Scanning Field Emission Gun Electron Microscopy (SFEG) and Transmission Electron Microscopy (TEM) were performed to study the evolution of the intragranular precipitation. Microhardness profile measurements were performed along the transverse axis of the welds to see the evolution of mechanical properties in the different areas. Tensile tests were done to determine the base metal strength and then speckle interferometry full field measurements were performed to investigate strain localisation after welding. Electron Back Scattered Diffraction (EBSD) was used to analyse local texture evolution.
X-ray diffraction was carried out to analyse textures and residual stresses in the welded samples and in the base material. In the welded samples, a very weak diffraction intensity was observed which is due to several phenomena:

- Low magnesium atom diffusion capabilities,
- Superficial oxide layer,
- Gage volume too small,
- Texture influence restrains the analysis along some directions.

When using X-ray diffraction, it is not possible to determine depth related variations, without matter removal. Moreover, in the welded samples, the complex thermomechanical input will induce complex stress gradients and texture evolutions. The high penetration capability of neutron diffraction technique will then allow us to determine stress profiles and the corresponding textures in a non-destructive way. This technique has been used to analyse FSW samples, but for LBW samples, the gage volume was too large compared to the weld size.

3.3.2 Optical Microscopy

3.3.2.1 Sample preparation

Due to the soft nature of magnesium, sample preparation raises difficulties in eliminating scratches. In addition, the magnesium corrosion behaviour is restricting the use of many polishing media and suspensions and it also makes sample storage impossible so that observations have to be done straight after sample preparation. The samples were first cut using an abrasive cut-off wheel, and then cold mounted in an acrylic resin. Grinding was performed using silicon carbide (SiC) grinding papers from 400 up to 2500 grit. Between each polishing, the sample was rinsed with ethanol and cleaned for several minutes using an ultrasonic cleaner. Samples were then polished with a 0.05 μm alumina suspension (Buehler MasterPrep) on a (Buehler MasterPolish) polishing cloth. Prior to the observation, the surface was chemically etched with an acetopicral solution [112, 53, 33] (0,4g picric acid $C_6H_3N_3O_7$, 13 ml ethanol C_2H_6O, 3ml boiled water H_2O, 3ml acetic acid CH_3COOH) to reveal the grain structure.

3.3.2.2 Facilities

A Leitz Aristomet and an Olympus BX41M were used for optical observations at MécaSurf laboratory. The microscopes were fitted with a Sony IRIS RGB CCD. The micrograph analysis has been performed with ImageJ software.

3.3.3 Scanning Electron Microscopy and Energy Dispersive Spectroscopy

3.3.3.1 Sample preparation

The same sample preparation as for Optical Microscopy was used. And then, the sample was removed from the mounting system because the resin was not conductive.

3.3.3.2 Facilities

A JEOL JMS 6400 scanning electron microscope (SEM) equipped with an Oxford energy dispersive spectroscope (EDS) operating at an accelerating voltage of 20 kV was used at MécaSurf laboratory. The interaction volume of the 20 kV electron beam with magnesium (see Figure 3.6) shows that EDS resolution is restricted to about 4.75 μm. EDS compositional analysis of phases smaller than 4.75 μm are therefore not reliable and can be only useful to determine what elements are present. Some complementary Secondary Electron Images have been done using

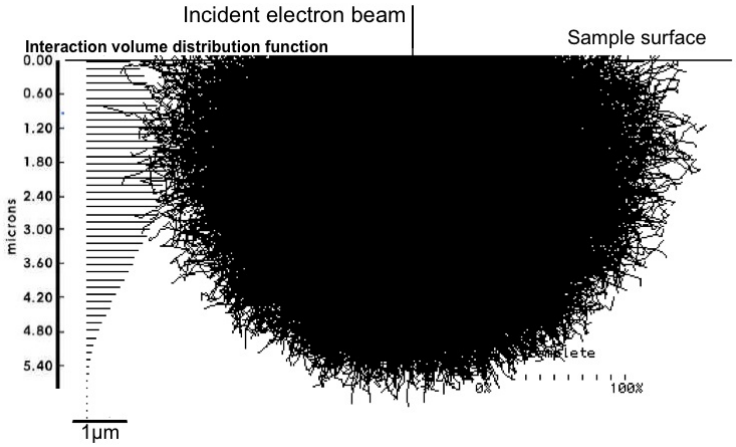

Figure 3.6: Interaction volume of 20 kV electron beam with Mg calculated using Montecarlo simulation [27].

a Philips XL305 SFEG at CP2M laboratory, Paul Cezanne University, Marseille. For these observations, the sample was not etched to avoid observation pollution. The alumina colloidal suspension prevented from a suitable sample observation because it remained on the sample surface even after ultrasonic cleaning.

3.3.4 Electron Back Scattered Diffraction

3.3.4.1 Sample preparation

The same sample preparation as for Optical Microscopy was used apart from etching. The etchant solution used for EBSD was 10 ml nitric acid HNO_3, 30 ml acetic acid CH_3COOH, 40 ml boiled water H_2O, 120 ml ethanol C_2H_6O for 10 seconds [115]. The sample preparation is one of the major issue in EBSD, especially in magnesium alloys which form oxide rapidly.

Moreover, a well prepared surface is required to get rid of the back scattered electron (BSE) tomography information and then to obtain good diffraction patterns.

3.3.4.2 Facilities

A HKL EBSD camera was coupled with the JEOL JMS 6400 SEM at MécaSurf Laboratory. A good indexation level is very difficult to obtain with magnesium alloys and 40% indexation was generally mentionned in the literature [115]. In this study, a maximum of 80% indexation was achieved. A 20 kV electron beam, 10 nA probe current and a 40 ms integration time were used.

3.3.5 Transmission Electron Microscope

3.3.5.1 Sample preparation: Electropolishing

TEM samples were made from 2 mm thick plates. 10 mm×10 mm samples were ground down to a thickness between 100 and 200 μm using grit silicon carbide polishing papers. Then, 3 mm diameter discs were cut from them using a mechanical disc cutter. The use of ultrasonic disc cutter was seen not to be necessary. The 3 mm diameter discs were electrochemically polished in a Struers Tenupol-3 jet polisher at a temperature below 10°C with a 14 V polishing voltage. The polishing solution was 10% HCl, 90% $C_4H_9OCH_2CH_2OH$ (butoxy-2-ethanol) by volume. Material removal was performed by applying a voltage and shooting a jet of an electrolyte at both sides of the sample. Large areas of the sample were then thinned without introducing any mechanical damage. The process stopped automatically when a hole is made in the specimen. On the edges of the hole, the sample is thin enough to allow TEM observations (50-200 nm). Figure 3.7 (a) shows a typical TEM sample made by this method.

3.3.5.2 Sample preparation: Focused Ion Beam

A FEI Focused Ion Beam was used at CP2M laboratory to prepare TEM specimens when it was needed to choose the exact location of interest, something which can not be achieved with electropolishing preparation. FIB system operates in a similar fashion to SEM except that, rather than a beam of electrons it uses gallium ions. It is operating at low beam currents for imaging and high beam currents for milling specific areas. Figure 3.7 (b) shows a FIB image of a typical specimen prepared for TEM.

3.3.5.3 TEM Facilities

Conventional TEM was performed using a FEI TECNAI G2 and High Resolution TEM was performed using a JEOL JEM 2010F at CP2M laboratory. EDS was used to determine the chemical composition of the features observed. SAED patterns, in case of Conventional TEM and FFT of High Resolution images were used to determine the nature of the precipitates observed.

3.3.6 X-Ray Diffraction

X-Ray diffraction has been performed using a SEIFERT MZ6TS diffractometer with Cr and Cu anodes at MécaSurf laboratory. No sample preparation is needed. Measurements were done at several depths. The different weld areas were characterised. XRD spectra were collected to

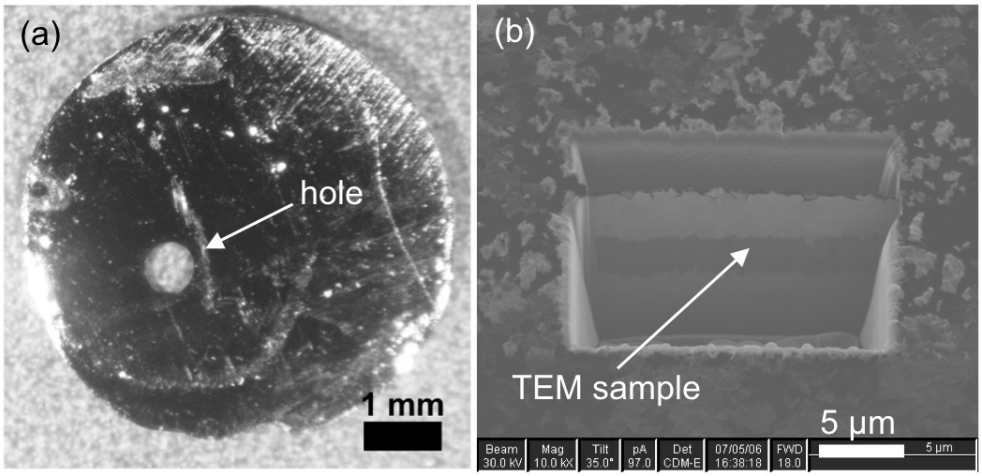

Figure 3.7: (a) Electropolished TEM sample and (b) Sample prepared using FIB.

determine the phase evolution. Indeed the 2θ (or d_{hkl}) position of each peak is characteristic of the phase analysed. Texture and residual stress profiles were analysed. Pole figures were built using the intensity distribution of each peak studied. 5 pole figures are needed to analyse the hcp symmetry texture. For the stress analysis, the $\sin^2\psi$ analysis method was used [116]. The peaks studied (2θ constant, varying ψ, ϕ) were fitted using PROFILE software and then the peak shifts were analysed and the stress tensor calculated using STRESS software from Siemens (Brücker).

Residual stress determination using $\sin^2\psi$ method The stress state influences the interplanar distance d_{hkl} and $\epsilon_\perp$ can be expressed as:

$$\epsilon_\perp = \frac{\Delta d_{hkl}}{d_{hkl0}} \tag{3.1}$$

From Bragg's law the following equation can be determined:

$$\Delta 2\theta = -\tan\theta \frac{\Delta d_{hkl}}{d_{hkl0}} \tag{3.2}$$

Then, from $\Delta\theta$, $\epsilon_\perp$ can be determined, and a better precision is obtained using high 2θ angles. The basis assumption is that the deformation in the observation direction $\epsilon_{\phi\psi}$ is directly related to the lattice deformation $\epsilon_\perp$. The relationship used to link deformation and stress comes from continuum mechanics and can be written in the major directions:

$$\epsilon_i = \frac{1+\nu}{E}\sigma_i - \frac{\nu}{E}(\sigma_1+\sigma_2+\sigma_3) \text{ for i=1,2,3} \tag{3.3}$$

becomes then in ϕ, ψ direction:

$$\epsilon_{\phi\psi} = \frac{1+\nu}{E}(a_1^2\sigma_1 + a_2^2\sigma_2 + a_3^2\sigma_3) - \frac{\nu}{E}(\sigma_1+\sigma_2+\sigma_3) \tag{3.4}$$

using director cosines $a_1 = \sin\psi\cos\phi$, $a_2 = \sin\psi\sin\phi$ and $a_2 = \cos\psi$. The major directions are considered to be the weld longitudinal, transverse and normal direction (see Figure 3.8). Due to the low penetration of X-rays, the plane stress assumption is made ($\sigma_3 = 0$), which leads to the $\sin^2\psi$ law:

$$\epsilon_{\phi\psi} = \frac{1+\nu}{E}\sigma_\phi \sin^2\psi - \frac{\nu}{E}(\sigma_1 + \sigma_2) \tag{3.5}$$

and,

$$\epsilon_{\phi\psi} \sim \epsilon_\perp = -\cot\theta(\theta - \theta_0) \tag{3.6}$$

with θ_0 the diffraction angle of the unstrained metal. hence:

$$2\theta = \frac{\sigma_\psi}{K_1}\sin^2\psi + \frac{\sigma_1 + \sigma_2}{K2} + 2\theta_0 \tag{3.7}$$

Then from the $2\theta = \mathrm{f}(\sin^2\psi)$ plot and least square method σ_ϕ can be determined:

$$\sigma_\phi = \text{slope } (2\theta = f(\sin^2\psi)).K_1 \tag{3.8}$$

K_1 and K_2 are related to the X-rays elastic constants: $K_1 = \frac{-E_{hkl}}{2(1+\nu_{hkl})}\cot\theta = \frac{-1}{1/2S_{2\,hkl}}\cot\theta$ $K_2 = \frac{E_{hkl}}{2\nu_{hkl}}\cot\theta = \frac{1}{S_{1\,hkl}}\cot\theta$ The uncertainties are calculated using the difference between the measurements and the fitting curve. If the material is anisotropic, this relationship must take into account the textures. K_1 and K_2 will then depend on ϕ and ψ.

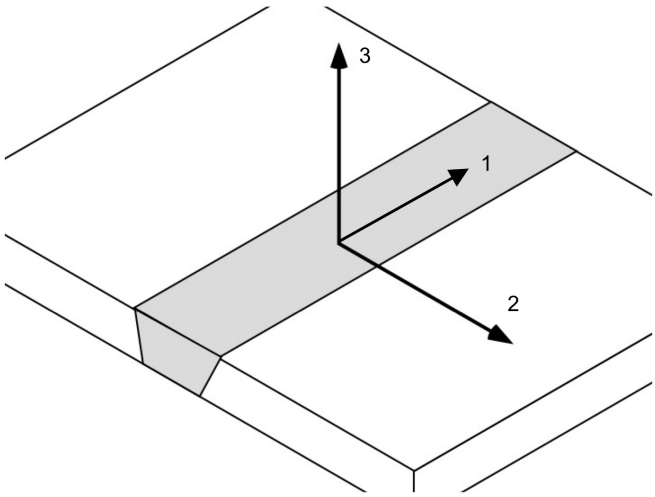

Figure 3.8: Major direction considered in the welds studied.

3.3.7 Neutron diffraction

When using X-Ray diffraction, it is not possible to determine depth related variations, without matter removal. Moreover, the complex thermomechanical input will induce complex stress gradients and texture evolutions. The high penetration capability of neutron diffraction technique

will then allow us to determine stress profiles and the corresponding textures in a non-destructive way. Neutron diffraction experiments have been carried out at the Hahn Meitner Institute in Berlin (HMI, called Berlin Helmholzt Centre for Materials and Energy since 4th July 2008), at the Laboratoire Léon Brillouin in Saclay (LLB) and at the Institut Laüe Langevin in Grenoble (ILL).Figure 3.9 shows 2 of the experiments carried out.

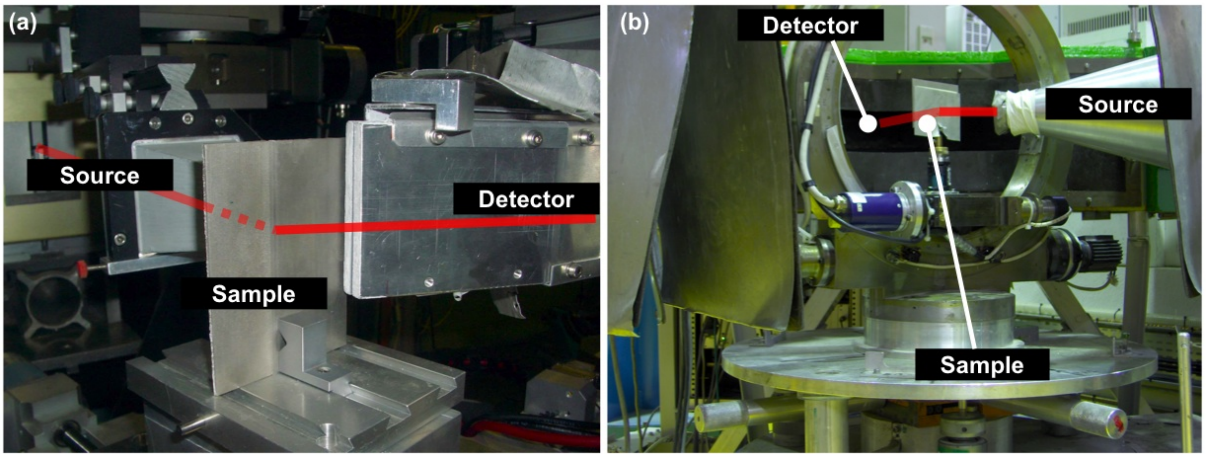

Figure 3.9: (a) HMI-E3 experiment (b) ILL-D1B experiment.

Stress profile analysis has been performed using HMI E3 instrument with 0.137 nm monochromator wavelength and 1×1×40 mm slits. Measurements were done for the $\{22\bar{4}1\}$, $\{11\bar{2}4\}$, $\{21\bar{3}2\}$ crystallographic planes, along the weld width and within its thickness at $\phi = 0^{\circ}$, $\psi = 30^{\circ}$, -60°, 90°, 0°. The specimens were 2 mm thick and the welded zone was 10 mm wide.

Several peaks were observed in the analysis window which led to difficulties in data treatment. LLB G5-2 instrument with 0.35 nm monochromator wavelength and 0.5×0.5×20 mm slits has been used to perform measurements for the {0002} crystallographic planes along the weld width and within its thickness at $\phi = 0^{\circ}$, ψ = -30°, 60°, 90°, 10°, 50°. The detector exhibited a large noise due to electronic failure. It resulted in difficulties in determining the background and then in getting an accurate analysis of the peaks. Longitudinal and transverse measurements have been done with ILL SALSA instrument to build stress maps of the sample using a 0.16457 nm monochromator wavelength, 0.6×0.6×10 mm slit for the transverse direction, 0.6×0.6×1 mm slit for the longitudinal direction and 0.6×0.6×20 mm slit for the normal direction. The slit height depends on the resolution nedeed to reduce stress gradients in the gage volume analysed. Measurements have been done for the $\{20\bar{2}0\}$ $\{11\bar{2}2\}$, $\{21\bar{3}0\}$ crystallographic planes.
Measurements at the same locations have been done with ILL D1B instrument to get the corresponding textures. Measurements were done using 3.8 mm diameter slits and 0.252 nm monochromator wavelength. Texture measurements were done averaging through thickness and data treatment was performed using MAUD software [117]. The $\sin^2\psi$ analysis method has been used [116]. The plane stress assumption used is not fully suited to characterise welds. The weak peak intensity due to the low neutron flux is restricting the number of ψ angles that can be studied and a few peaks can be observed because of the textured nature of the material analysed. As the gage volume width is larger than the 2 mm sample thickness, a simulation of

the whole experiment, depending on reactor and instrument parameters, is needed to determine accurately the gage volume location whithin the sample at each measurement. A simulation program developped at MécaSurf Laboratory [118, 119, 120] was used. It allows to determine the shift whithin the thickness (Z shift) (Figure 3.10), the simulated intensities and the simulated 2θ angles (Figure 3.11), versus the gage volume barycenter (which corresponds to the gage volume centroid). The measured intensities and 2θ angles (Figure 3.12) can then be corrected and the stress profiles are calculated.

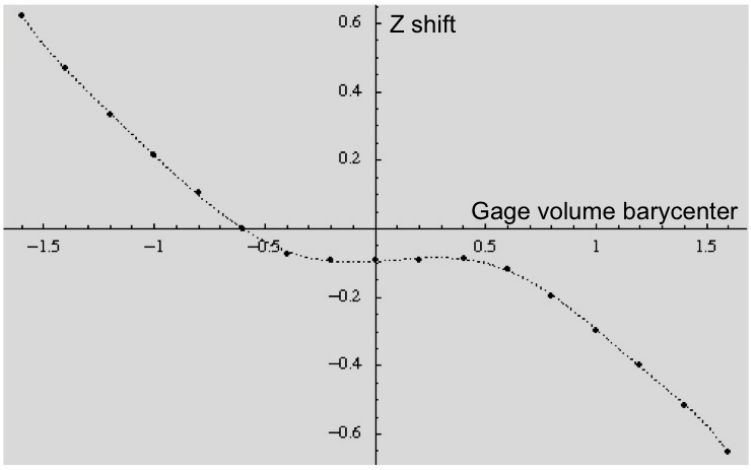

Figure 3.10: Z shift versus the gage volume barycenter.

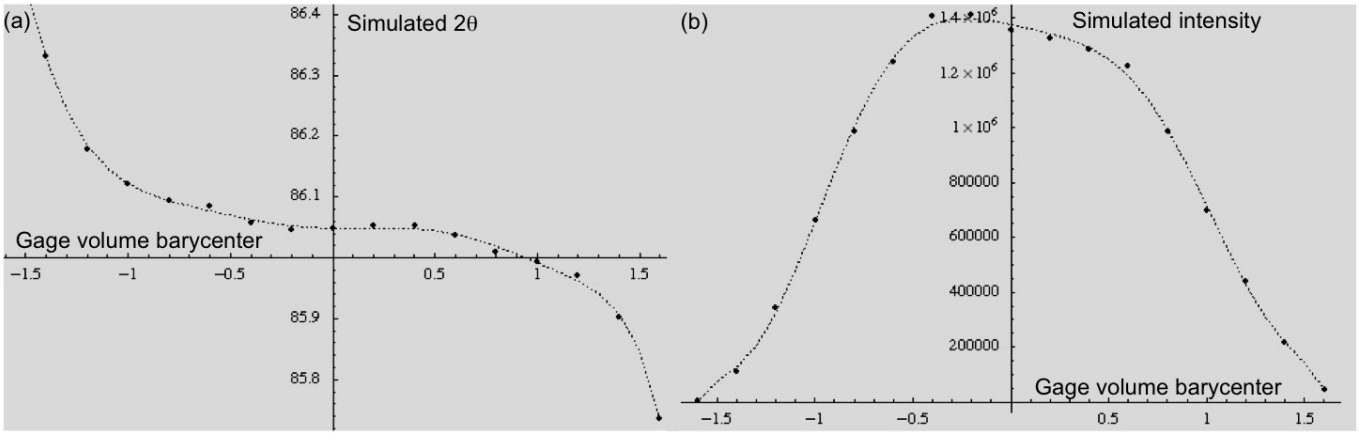

Figure 3.11: (a) Simulated intensities and (b) simulated 2 θ angles, versus the gage volume barycenter.

The Neutron diffraction experiments performed during this study and the experimental parameters are summarized in Table 3.5.

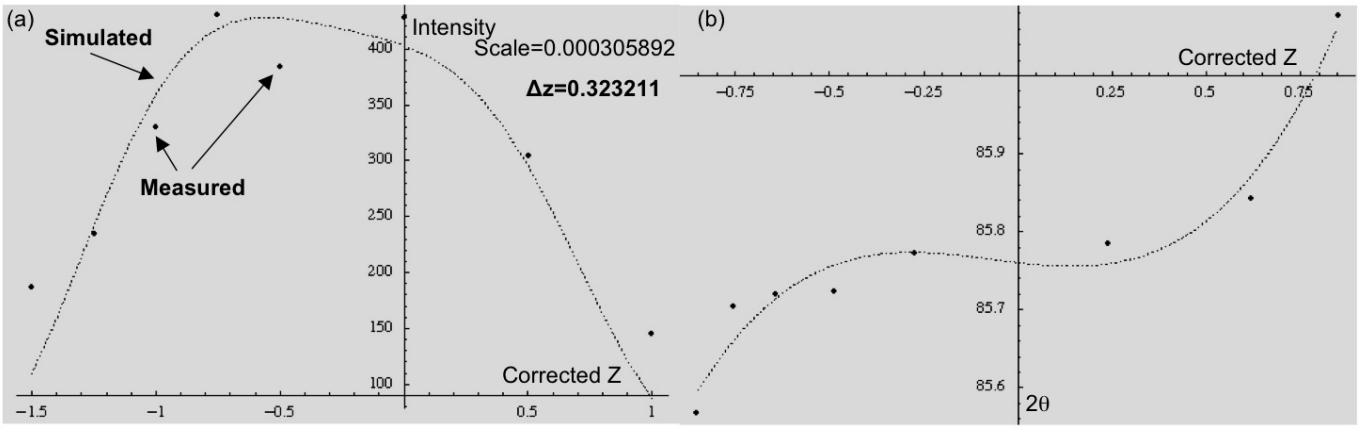

Figure 3.12: Correction of (a) measured intensities and (b) 2 θ angles.

Instrument	HMI-E3	LLB-G5-2	ILL-SALSA	ILL-D1B
Analysis method	$\sin^2\psi$	$\sin^2\psi$	triaxial stresses	$\sin^2\psi$
Results	Residual stresses	Residual stresses	Residual stresses	Textures
Wavelenght (nm)	0.137	0.35	0.16457	0.252
Slit size (mm)	1	0.5	0.6	3.8
Crystallographic planes studied	$\{22\bar{4}1\}$, $\{11\bar{2}4\}$, $\{21\bar{3}2\}$	$\{0002\}$	$\{11\bar{2}2\}$, $\{21\bar{3}0\}$ $\{20\bar{2}0\}$	$\{10\bar{1}0\}$, $\{0002\}$, $\{10\bar{1}$ $\{10\bar{1}2\}$, $\{11\bar{2}0\}$, $\{10\bar{1}$

Table 3.5: Overview of the Neutron diffraction experiments performed.

3.3.8 Microhardness tests

Microhardness tests were performed using a Leica VMHT coupled with Sony IRIS CCD. Sample preparation method was the same as the one used for optical micrographs at MécaSurf laboratory. The influence of the load applied was studied (see Figure 3.13) and showed that the dispersion observed is whithin the repeatability range. Then, for each further indentation, a 0.98 N load was applied during 15 seconds[112].

3.3.9 Tensile tests

Dumbell specimen preparation was performed using water jet cutting (see Figure 3.14). A sketch of dumbell specimen dimension is exhibited in Figure 3.15. The lateral section were then polished to avoid crack initiation during tensile test. An Instron 1185 machine with mechanical grips and a 100 kN load cell was used and tensile tests were performed at 4 mm/min strain rate at MécaSurf laboratory. Complementary analysis was performed in LMPF laboratory, Arts et Métiers Paristech, Chalons en Champagne using Dantec Dynamics Q-300 speckle interferometry system coupled with tensile test to investigate the strain localisation. Speckle interferometry is a full field method using laser light which enables to measure the surface deformations.

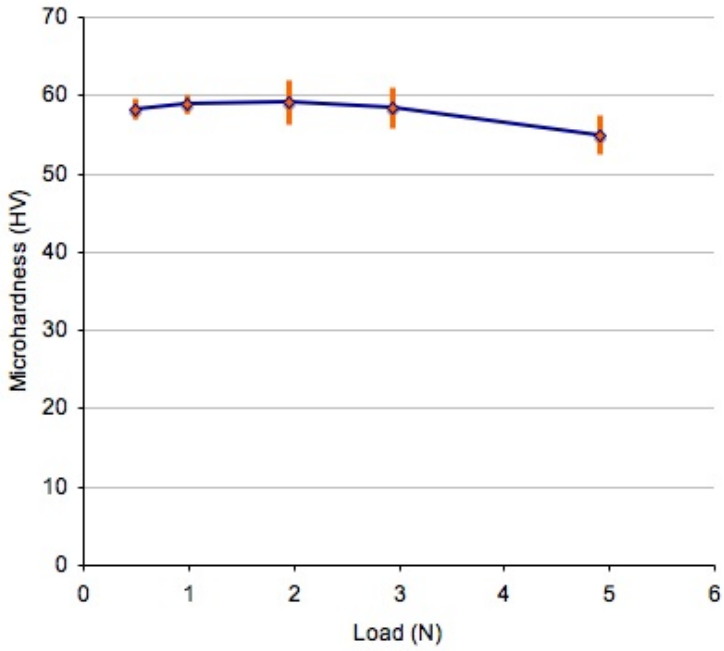

Figure 3.13: Evolution of microhardness with load applied.

Figure 3.14: Waterjet cutting dumbell preparation.

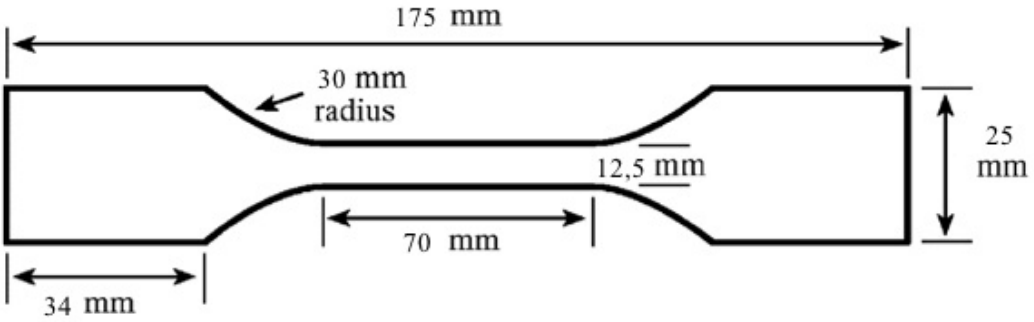

Figure 3.15: Dumbell specimen dimensions.

Chapter 4

Welding processes

4.1 Introduction

In order to optimize magnesium alloy welding process, the identification of the critical welding parameters and their influence is required. From this knowledge, the process window for each welding process and each magnesium alloy studied can be determined. FSW and LBW involve respectively thermomechanical and thermal input, which will influence the resulting microstructure and mechanical properties. Then the knowledge of the thermal and thermo-mechanical mechanisms is required for the better understanding of these processes. In this section will be described the FSW and CO_2 LBW process window determination and the influence of welding parameters. The AZ31, AZ61 and WE43 magnesium alloys will be studied. Nd:YAG LBW processing parameter analysis was not performed during this study. The Nd:YAG samples analysis was performed in the next section in order to characterise the weld microstructure and properties and to compare with the other welding processes. Then, the experimental analysis of the temperature distribution (for FSW and LBW) and of the material flow (for FSW) will be performed.

4.2 Description of the Friction Stir Welds and of the Laser Beam Welds

A typical FSWeld morphology can be described by the Figure 4.1. From the top surface, the advancing and retreating sides can be differentiated, because of the features left behind the tool and the higher flash on the reatreating side.

A typical LBWeld morphology is exhibited in Figure 4.2. From the cooling isotherms, the welding direction can be determined.

4.3 Weld quality

The analysis of the welds produced revealed the presence of several defects: for Friction Stir Welding (see Figure 4.3):

- Porosity, Tunneling (inner voids located in the nugget area all along the weld),

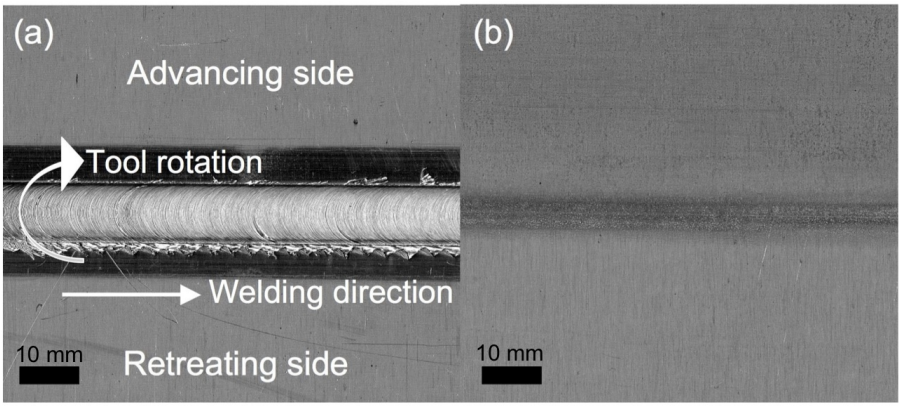

Figure 4.1: Macrographs of AZ31 FSWeld structure (a) top surface and (b) bottom surface.

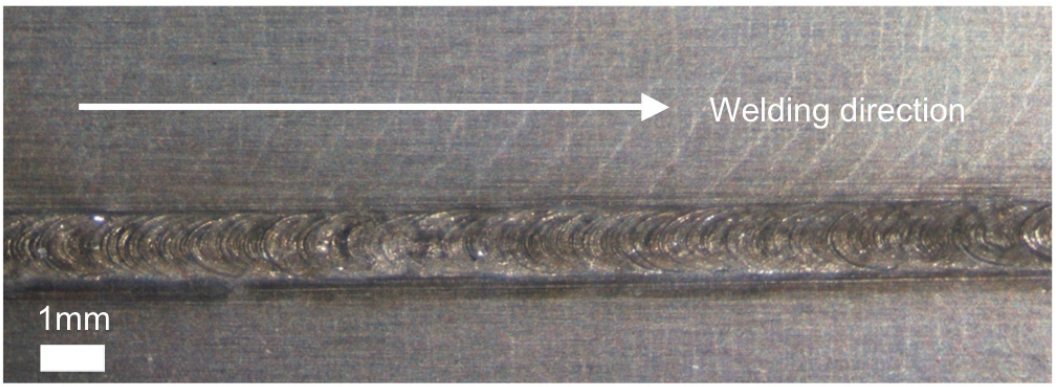

Figure 4.2: Macrograph of AZ31 LBWeld.

- Cracks,
- Flash (excedent material at the weld edges),
- Surface corrosion occuring preferentially in the weld area than in the base metal during weld storage,
- Pin wear, which was identified by higher density areas in FSW radiographies. It was further confirmed by the presence of steel inclusions in these areas using EDS-SEM analysis (see Figure 4.4).

and, for Laser Beam Welding (see Figure 4.5):

- Porosity,
- Laser cutting,
- Lack of penetration,

- Sag of the weld pool.

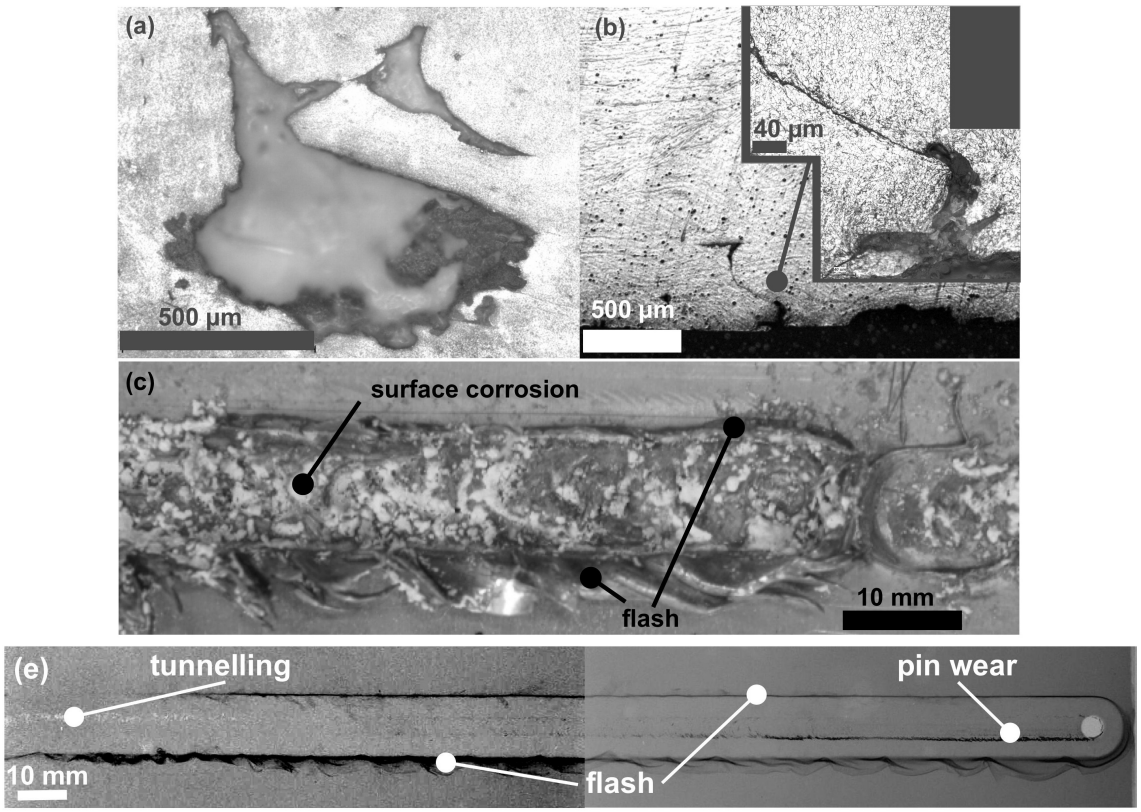

Figure 4.3: Defects observed in AZ31 FSW: Optical micrograph of (a) porosity in FSW (W = 800 RPM, V = 100 mm/min), and (b) crack in FSW (W = 1800 RPM, V = 1000 mm/min), macrograph of (c) flash and surface corrosion in FSW (W = 400 RPM, V = 100 mm/min), (e) Radiography of FSW (W = 800-1100 RPM, V = 100 mm/min) exhibiting tunneling, flash and pin wear.

The weld quality depends on the amount of these defects within the weld produced. Oxide inclusions which are often described in magnesium alloys LBW [2], were not observed in the alloys studied.

FSW that did not present any porosity, any crack, any pin wear, any surface corrosion and a flash size inferior to 2 mm were defined as sound welds. LBW with full penetration, stable weld pool, and an amount of porosity inferior to 5% [121] were defined as sound welds.

4.4 Influence of processing parameters on weld quality

The processing parameters influencing the weld quality were studied. The visual aspect of the FSWelds was improved with increasing the load applied (F), welding speed (V) and tool rotation rate (W) with a smaller flash, less surface corrosion and less tunnelling phenomena occurring (see Figure 4.6). These results are consistent with the literature [17, 49, 26, 122].

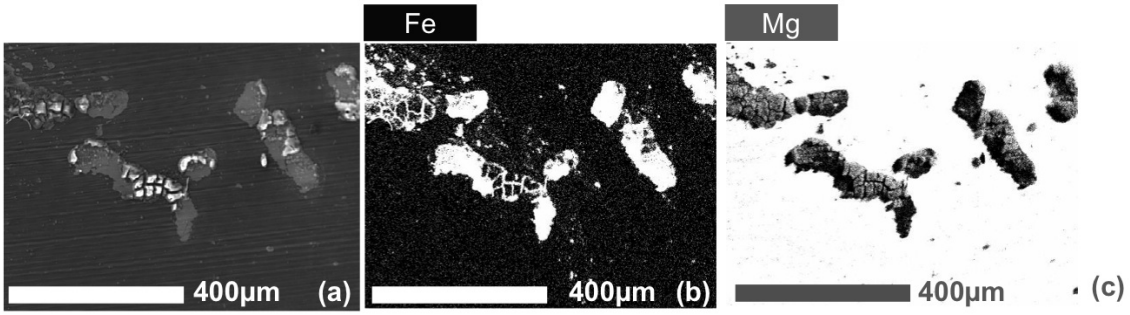

Figure 4.4: EDS-SEM analysis of AZ31 FSW (W = 1100 RPM, V = 100 mm/min), white zones are typical of a high element content. (a) SE image, (b) Fe EDS map showing higher Fe content in the particles and (c) Mg EDS map showing lower Mg content in the particles.

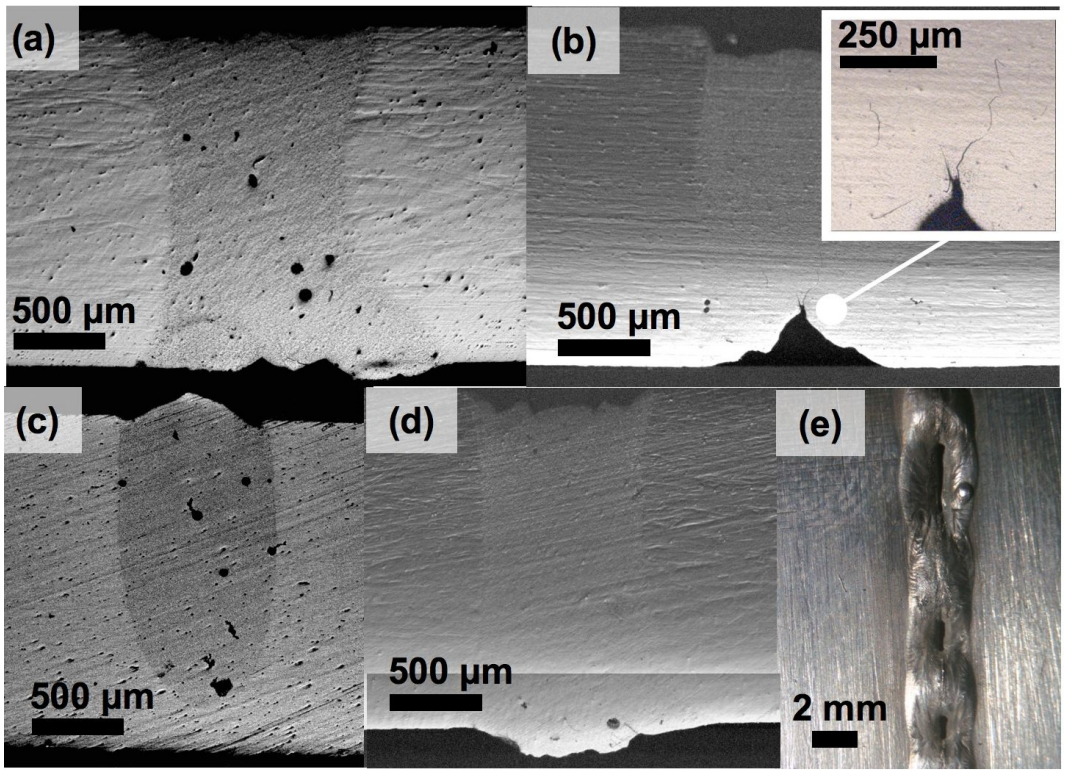

Figure 4.5: Defects observed in AZ31 LBW: Optical micrograph of (a) porosity in CO_2 LBW (P = 2 kW, V = 2.76 m/min, f = -2 mmm, gas flux = 40 l/min), (b) weld cracking in CO_2 LBW (P = 3 kW, V = 3.6 m/min, f = 0 mmm, gas flux = 40 l/min), (c) lack of penetration in CO_2 LBW (P = 2.4 kW, V = 12 m/min, f = 16 mmm, gas flux = 40 l/min), (d) sag of weld pool in CO_2 LBW (P = 3kW, V = 4.2 m/min, f = 0 mmm, gas flux = 40 l/min) (e) Macrograph of laser cutting in CO_2 LBW (P = 3 kW, V = 1.2 m/min, f = 0 mmm, gas flux = 40 l/min).

Concerning LBW, increasing the laser power (P) and decreasing the welding speed (V) resulted in an increase of the power density. A good balance had to be found to avoid laser cutting when the power density was too high and lack of penetration when the power density was too low. This tendency is consistent with all the previous studies on laser welding [2, 55, 19]

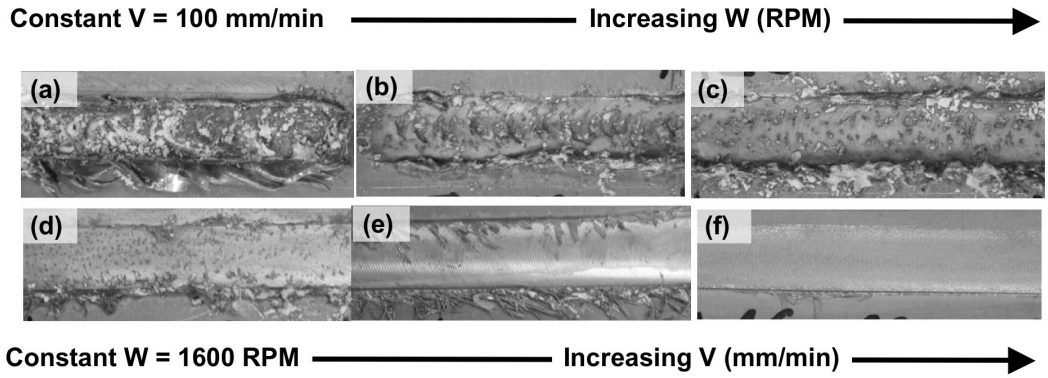

Figure 4.6: Digital images of the superficial aspect of several "bead on plate" AZ31 welds (a) W= 400 RPM V=100 mm/min, (b) W= 700 RPM V=100 mm/min, (c) W= 900 RPM V=100 mm/min, (d) W= 1600 RPM V=400 mm/min, (e) W= 1600 RPM V=600 mm/min, (f) W= 1600 RPM V=1000 mm/min.

4.4.1 FSW rotation rate, W (RPM)

Figure 4.6 shows the visual aspect of AZ31 FSWelds with increasing W. Increasing tool rotation rate (W) results in a better visual aspect and less surface corrosion in the weld zone. The FSWelds analysis revealed an influence of W on the defects observed (see Figure 4.7). Tunneling phenomenon is reduced with increasing W due to a better material flow, until a limit where a further increase in W produces surface crack formation. This is consistent with previous studies on FSW [17, 49, 26, 122].

4.4.2 FSW welding speed, V (mm/min)

Increasing welding speed (V) also produces a better visual aspect as shown in Figure 4.6, with an improved surface corrosion resistance in the weld zone and a reduced flash size. The flash size evolution versus welding speed was analysed in more details and showed than increasing V results in a smaller amount of material expelled to the tool rotation and then, a smaller flash (see Figure 4.8). But, the defects analysis versus processing parameters showed that a further increase in V results in inner void formation (see Figure 4.7). This is consistent with previous studies on FSW [17, 49, 26, 122].

4.4.3 FSW applied pressure, F (kN)

The influence of applied load for given tool rotation rate and welding speed was studied. The temperature produced by friction increases with increasing applied load leading to better mate-

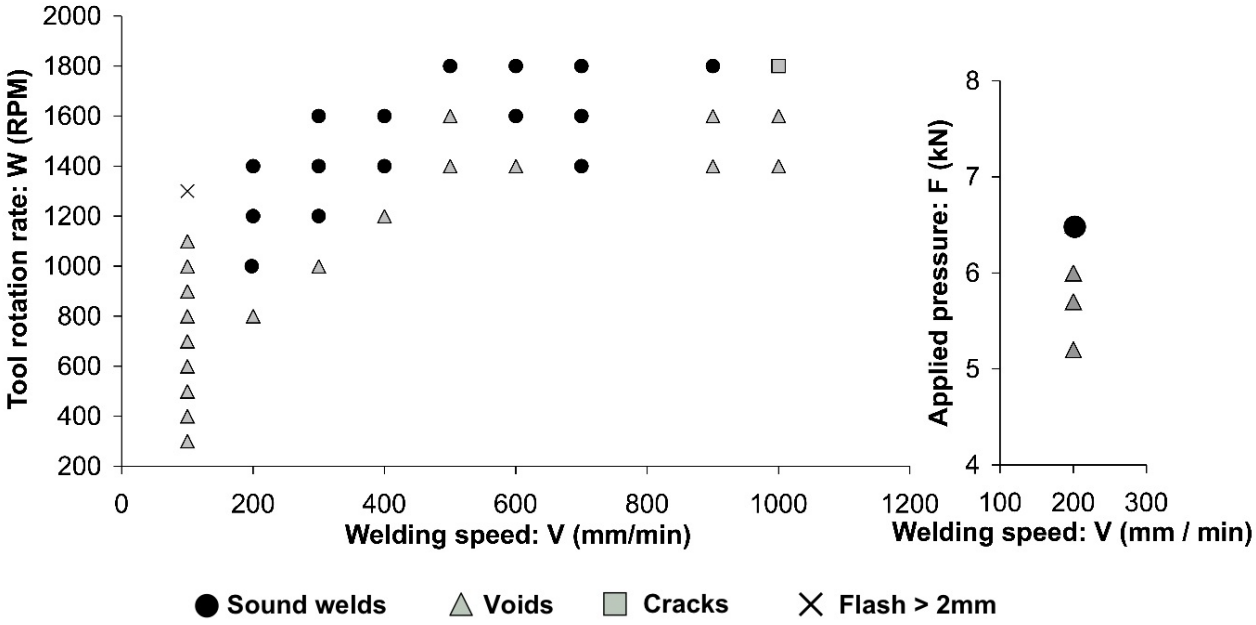

Figure 4.7: Influence of processing parameters on AZ31 FSW quality.

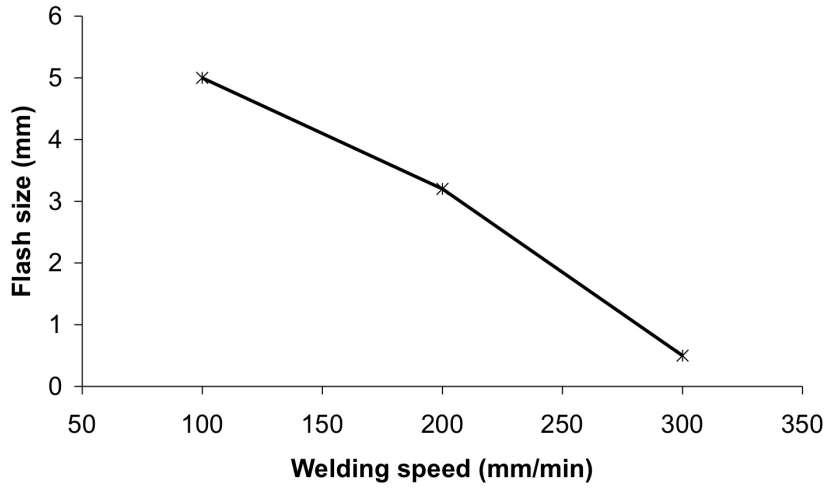

Figure 4.8: Influence of the welding speed on the flash size for AZ31 FSW (W = 1000 RPM).

rial flow and less void created (see Figure 4.7 and Figure 4.9). This is consistent with Zhang et al. study [51].

Figure 4.9: Digital image showing the influence of the applied pressure (from 5.2 to 6.5 kN) on the weld quality for AZ31 FSW (W = 1000 RPM, V = 200 mm/min).

4.4.4 LBW laser power, P (kW)

The penetration depth and weld width increased with increasing laser power due to higher power density. Then, when laser power was too low, lack of penetration was observed (see Figure 4.10), whereas high laser power produced laser cutting. This is consistent with the LBW literature [2].

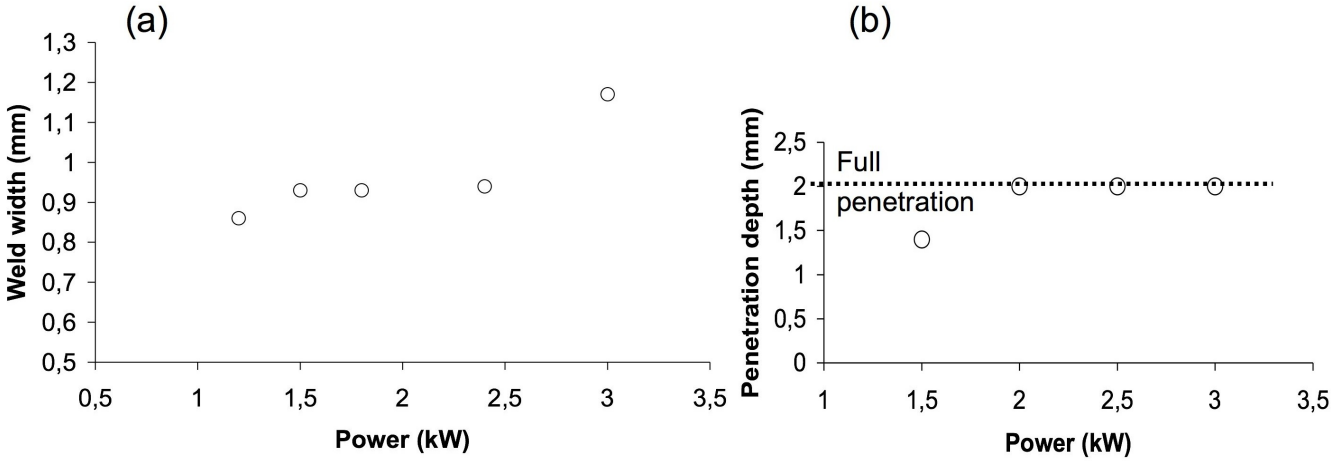

Figure 4.10: Influence of the laser power on (a) the weld width for AZ31 LBW (V = 3600 mm/min) (b) the penetration depth for AZ61 LBW (V = 7200 mm/min).

4.4.5 LBW welding speed, V (mm/min)

The power density increases with decreasing welding speed. Then, when welding speed was too high, lack of penetration was observed, whereas low welding speed produced laser cutting (see Figure 4.11). This is consistent with the previous studies [2].

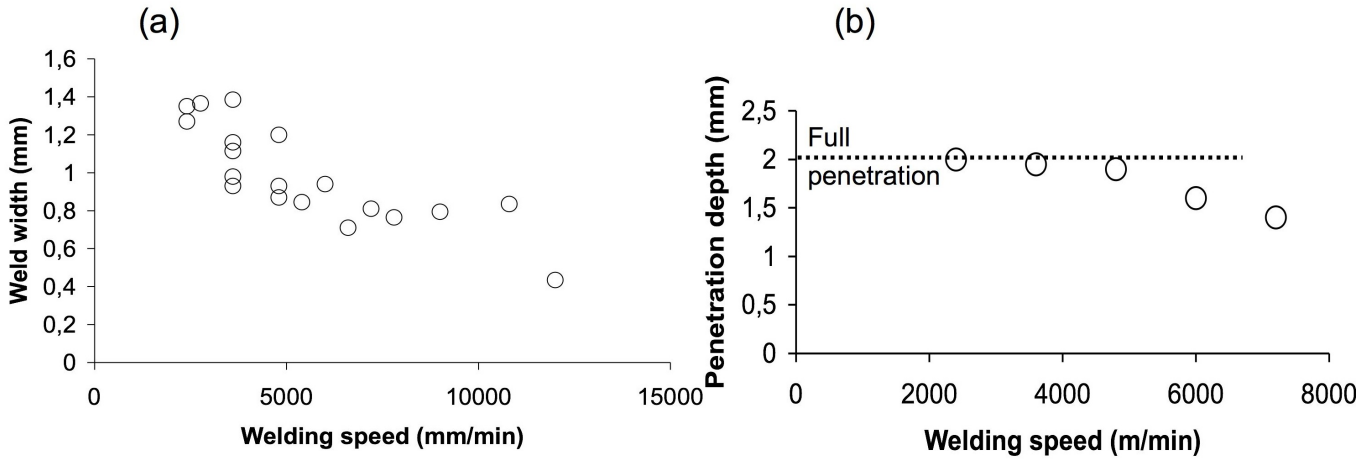

Figure 4.11: Influence of the welding speed on (a) the weld width for AZ31 LBW (P = 2.4 kW) (b) the penetration depth for AZ61 LBW (P = 1.5 kW).

4.4.6 LBW focal distance, f (mm)

For the sake of simplicity, the focal distance will be defined as the distance between the focal point and the top surface of the sample. Sound welds were achieved with a focal point on the surface (see Figure 4.12), which is consistent with what Weisheit et al. [62] found for thin plates. The weld width increases with moving the focal point away from the surface (i.e. increasing focal distance) (see Figure 4.13) which was also observed by Dhahri et al [65].

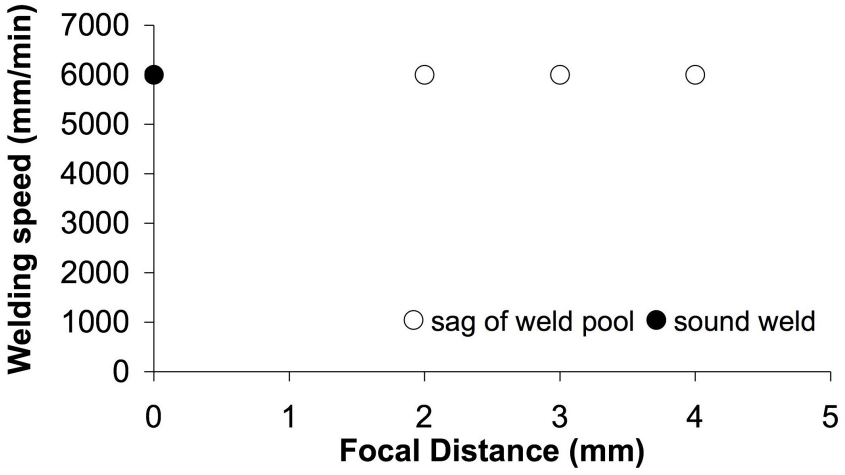

Figure 4.12: Influence of the focal distance on the weld quality for WE43 LBW (P = 3 kW).

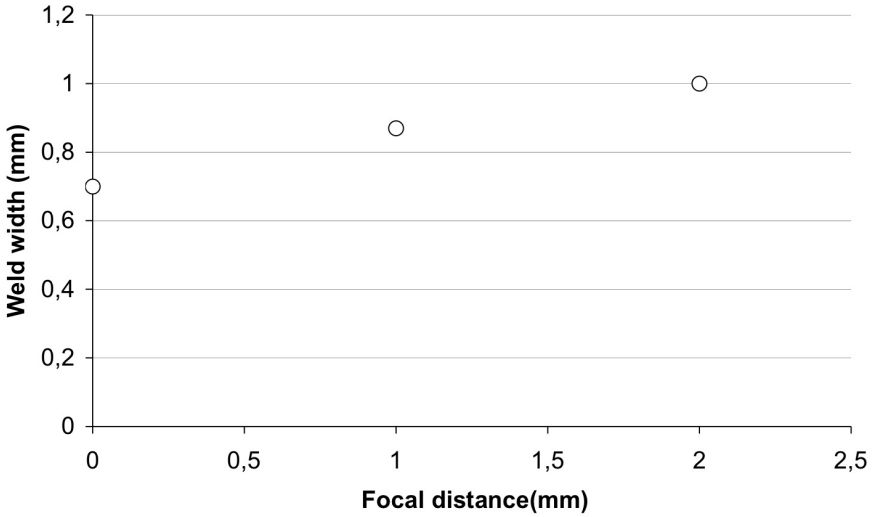

Figure 4.13: Influence of the focal distance on the weld width for AZ61 LBW (P = 3 kW, V = 7200 mm/min).

4.4.7 LBW shielding gas flow, V (l/min)

Shielding gas selection to produce the best weld quality was previously studied by Weisheit et al. and Hiraga et al. for magnesium alloys [62, 66]. Our study led to the same conclusions and sound welds were produced with He shielding gas. Surface cracking leading to laser cutting was observed without gas protection. This is due to the oxide formation during welding. A higher porosity content was observed for He gas flow higher than 60 l/min (see Figure 4.14). Using Ar back shielding gas allowed us to produce sound welds at lower welding speed, reducing sag of the weld pool (see Figure 4.15). This effect was also observed by Lehner et al. [58].

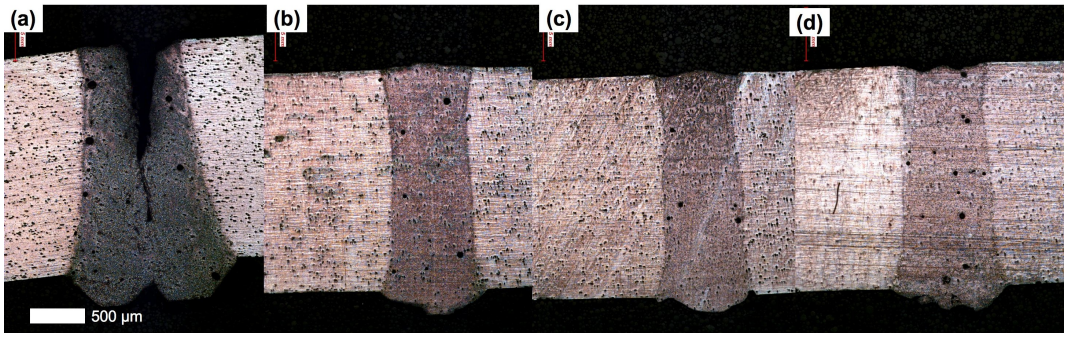

Figure 4.14: Influence of the shielding gas (a) 0 l/min, (b) 40 l/min, (c) 60 l/min, (d) >60 l/min for AZ61 LBW (P = 3 kW, V = 7200 mm/min).

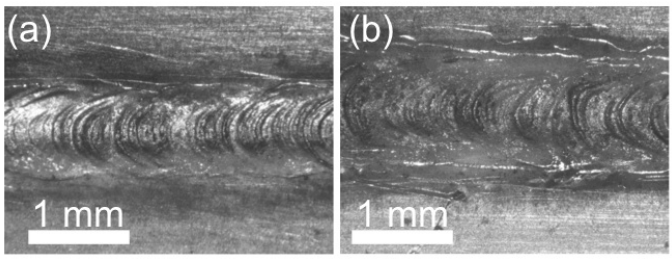

Figure 4.15: Macrograph of sound welds produced using back shielding gas for (a) AZ61 LBW (P = 3 kW, V = 2200 mm/min) and (b) WE43 LBW (P = 3 kW, V = 2200 mm/min).

4.4.8 Influence of alloy conductivity on weld quality

The magnesium alloys studied exhibited different thermal conductivity (Table 4.1). The influence of the alloy thermal conductivity on LBW weld pool area was investigated (Figure 4.16). The penetration depth and bead width evolution versus the thermal conductivity was plotted. The weld width slightly decreases with increasing thermal conductivity due to easier temperature dissipation. The penetration depth variation observed is only due to variation in the plate initial thickness, then no influence of the thermal conductivity on the penetration depth could be determined.

Alloy	Thermal conductivity ($Wm^{-1}K^{-1}$)
AZ31	96
AZ61	70
WE43	51

Table 4.1: Magnesium alloy thermal conductivity.

4.4.9 Process windows

From these results, a process window for each welding process and each alloy studied could be determined (see Figure 4.7, Figure 4.17). AZ31 sound welds could be obtained at lower laser power and the process window is wider for AZ31. This is partly due to the higher thermal conductivity of AZ31 which induced an easier temperature propagation than in AZ61 for a given power density. This leads to a AZ61 process window shift to higher laser power range.

4.5 Thermal history determination

4.5.1 Introduction

AZ31 FSW and LBW butt welds were instrumented with K-type thermocouples embedded in the sample at mid-thickness.The thermocouples were placed at several distances from the weld centre and several processing parameters were used to study the influence of the process on the temperature distribution during welding (Figure 4.18 and 4.19).

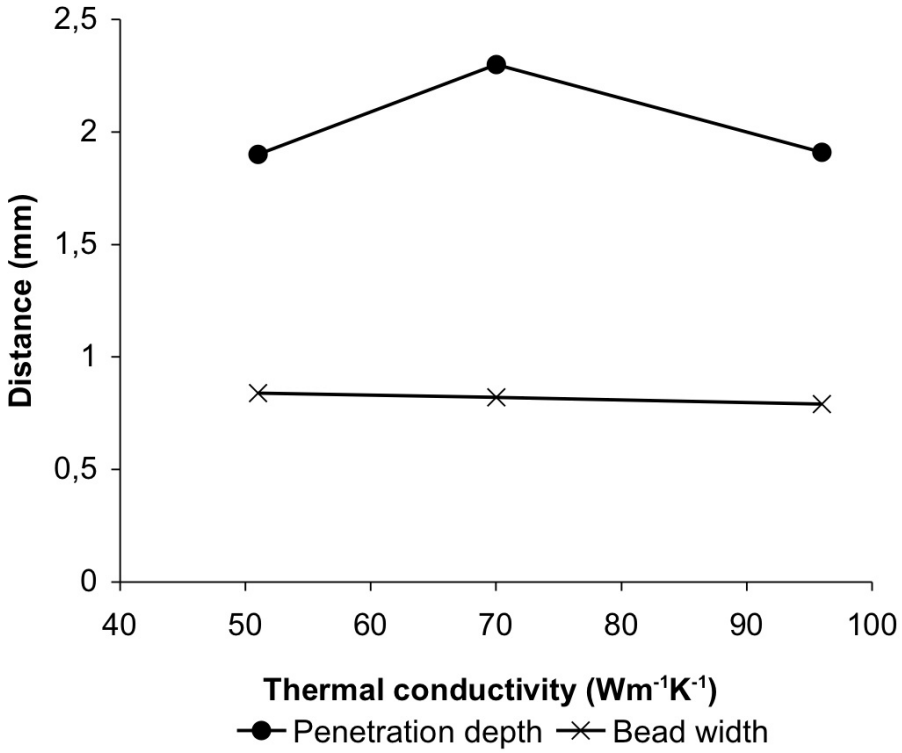

Figure 4.16: Influence of the alloy conductivity on the penetration depth and bead width.

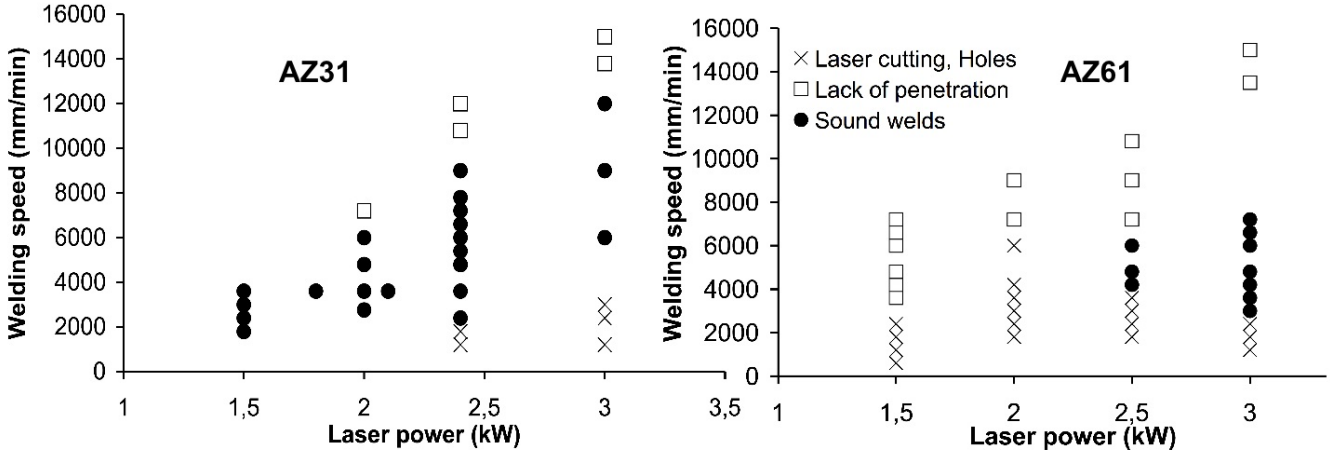

Figure 4.17: LBW Process window (f=0 mm, He gas flow = 40 l/min) for (a) AZ31, (b) AZ61.

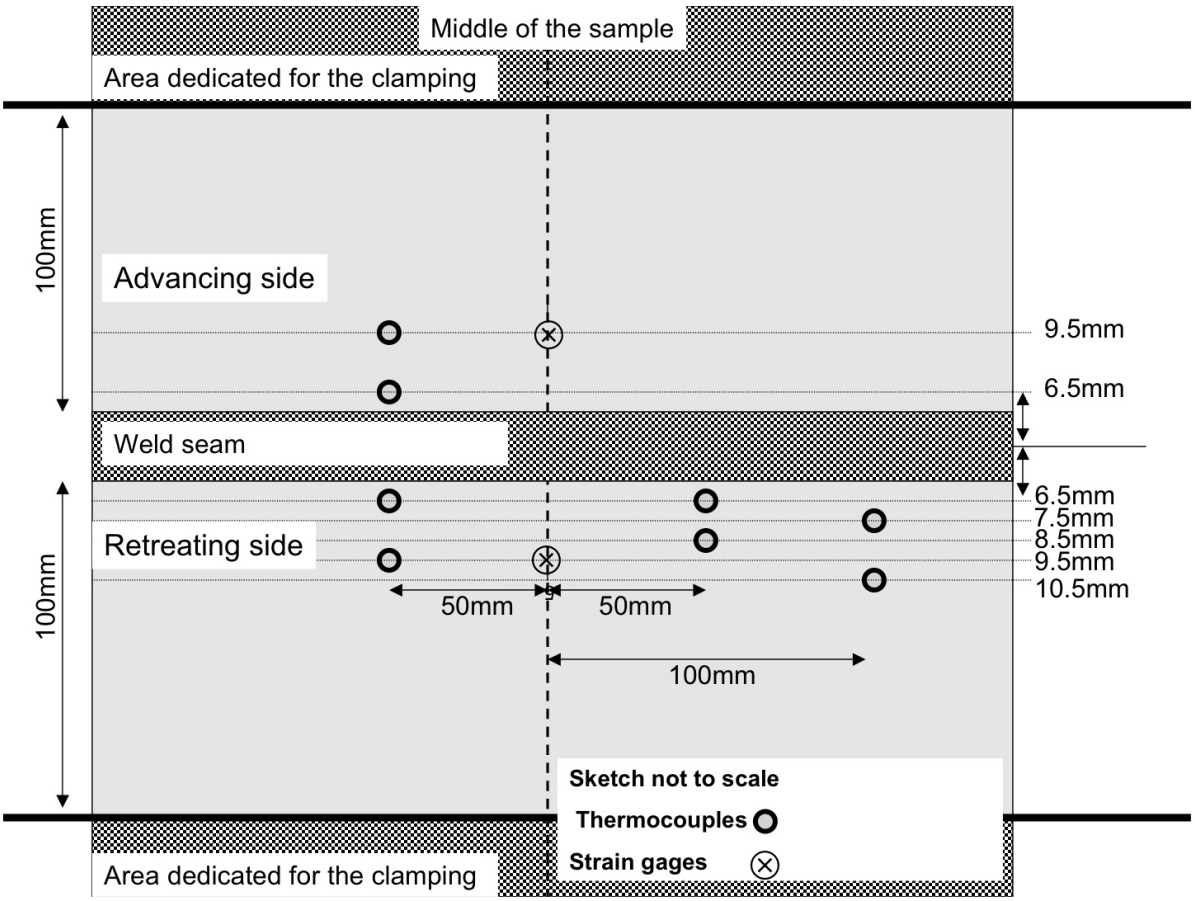

Figure 4.18: Location of the thermocouples during FSW processing.

4.5.2 Experimental data

The typical temperature evolution curves obtained at each measurement location during FSW and LBW are shown in Figure 4.20 and Figure 4.21. For each butt welding parameter studied, similar curves were obtained. The peak temperature shift is due to the fact that the thermocouples were not embedded at the same location along the weld length. The peak temperature determined for each curve was taken into account for the further analysis. The peak temperature was plotted versus the measurement location for each welding parameter investigated (Figure 4.22). Zone III represents the area where temperature measurement could not be obtained because thermocouples would have been destroyed by the pin for FSW and by the laser in LBW. Zone II is located under the shoulder for FSW. So temperature measurements could only be performed in Zone I. For FSW, the temperature is uniform along the weld length and the temperatures measured on the advancing side and on the retreating side were different. This is due to the heat input generated by the plastic deformation. For LBW, the temperature variations observed for the same locations is mainly due to the fit-up. The welding speeds are higher in LBW than in FSW, which explains the easier heat dissipation and then the lower temperatures

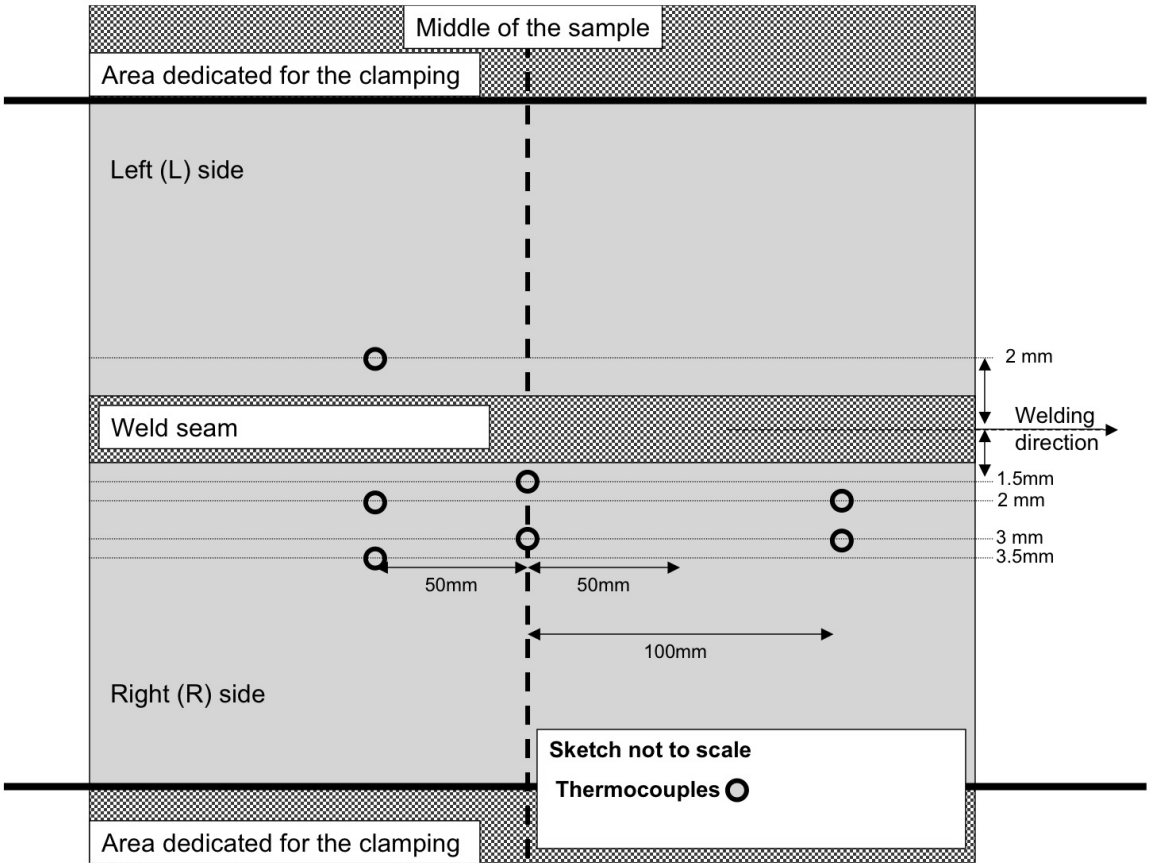

Figure 4.19: Location of the thermocouples during LBW processing.

observed in LBW.

4.6 Material flow in FSW

4.6.1 FSW hole

The microstructure study showed that the Al_8Mn_5 particles did not dissolve during FSW. Then, they can be used to observe the material flow during FSW. The area around the hole left by the pin at the end of the weld indicates the transition between welded and non-welded material (Figure 4.23). Then, the analysis of this area can give some informations about the material flow.

Optical micrograph of the FSW section were made without etching the surface. The material flow can be observed and the weld zone can be clearly distinguished. Several phenomena were occuring: the material was pushed from the surface downwards and in the same time flowed around the tool.

SEM analysis was performed in the FSW hole area (see Figure 4.25). The magnified areas show that the Al_8Mn_5 intergranular precipitates aligned with the tool rotation.

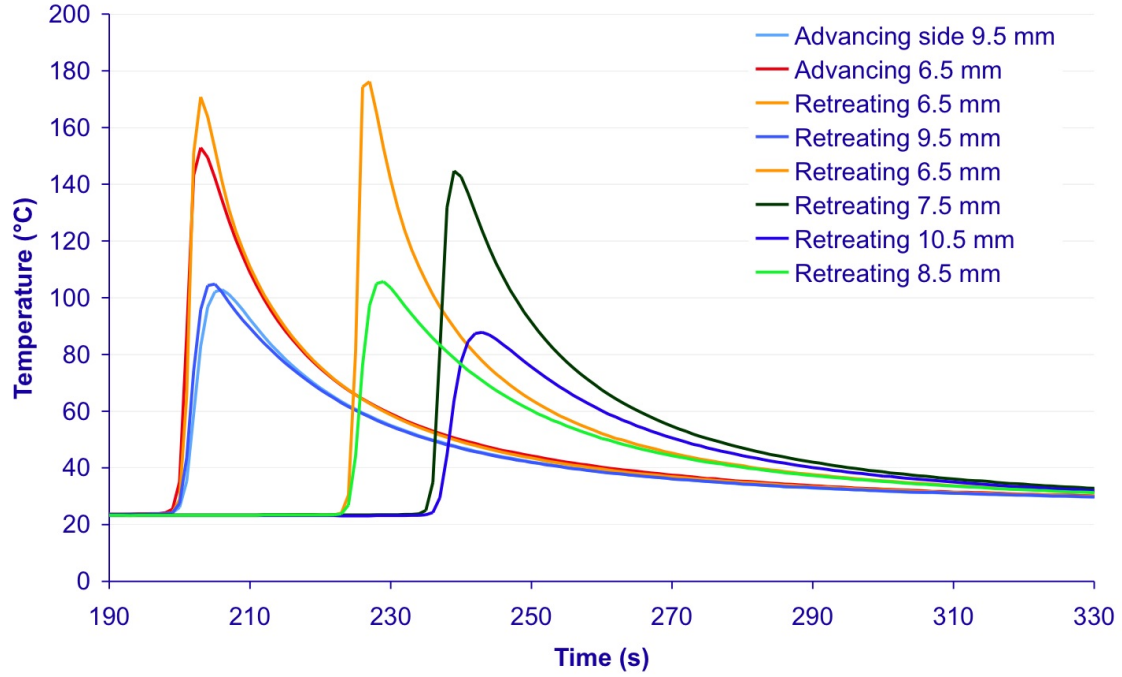

Figure 4.20: Temperature measurement during FSW (W = 600 RPM, V = 2000 mm/min).

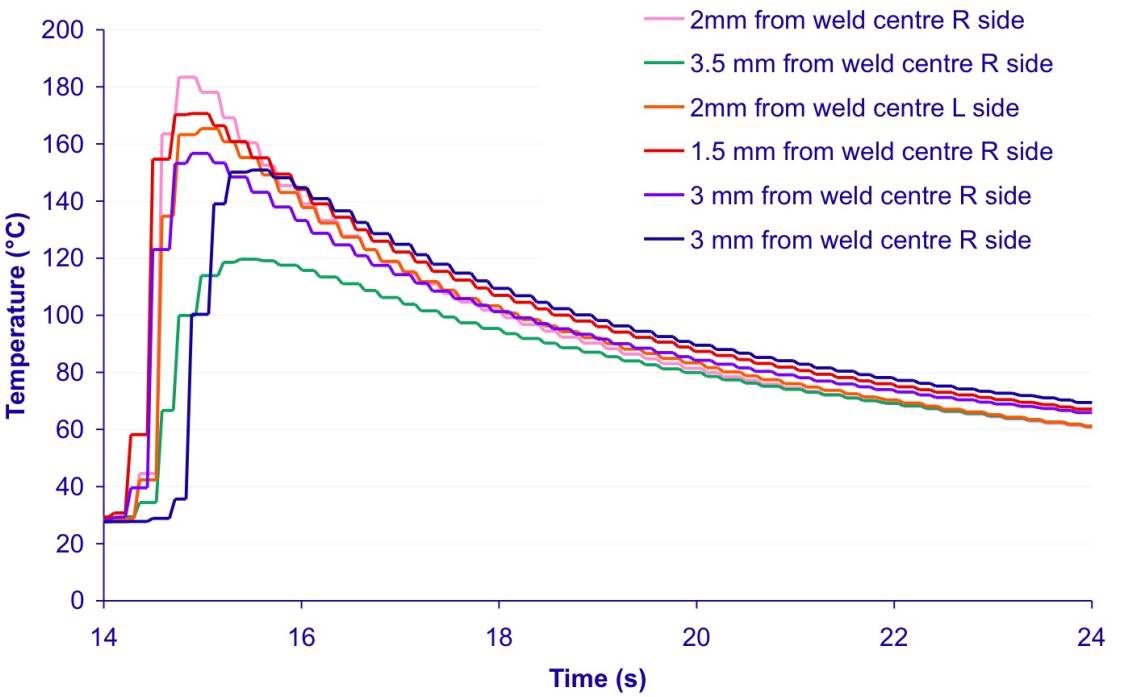

Figure 4.21: Temperature measurement during LBW (P = 2 kW, V = 4600 mm/min).

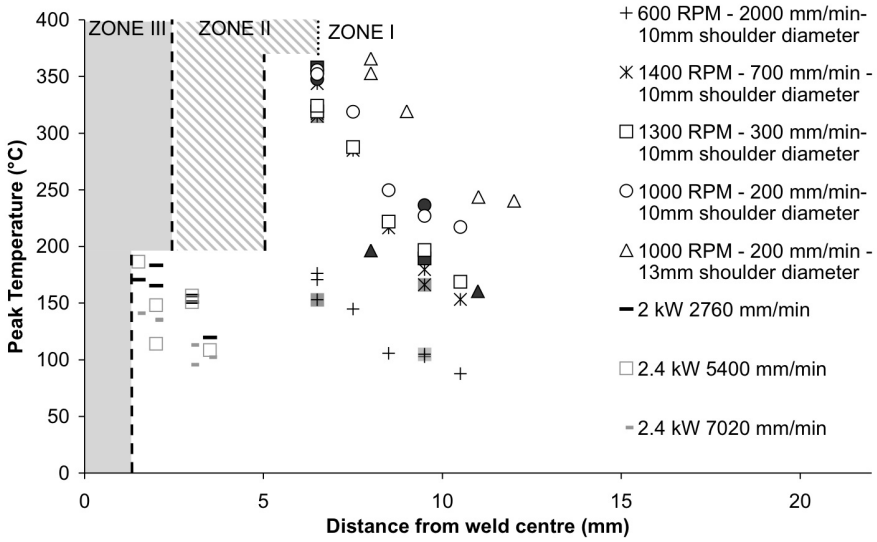

Figure 4.22: Peak temperature measured versus distance from weld centre during FSW and LBW. The filled features correspond to the advancing side data.

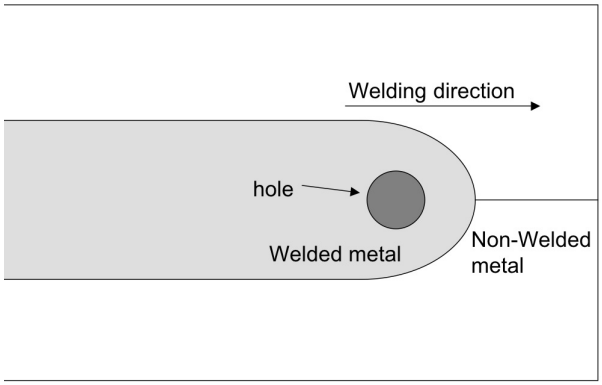

Figure 4.23: Sketch of the FSW hole location.

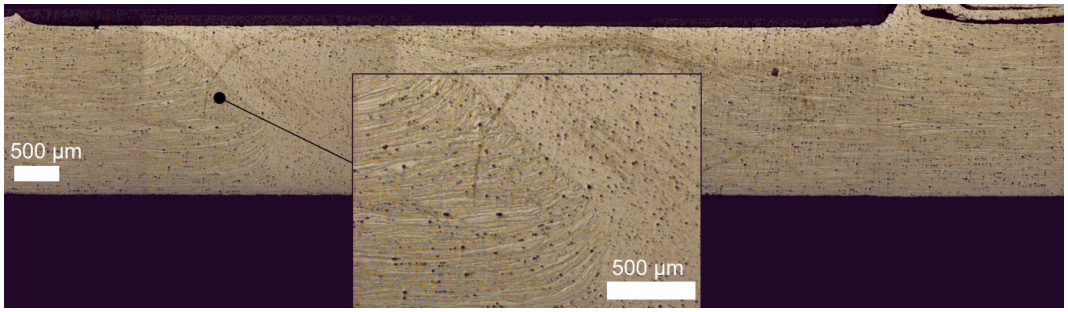

Figure 4.24: Optical micrograph of the FSW section showing material flow.

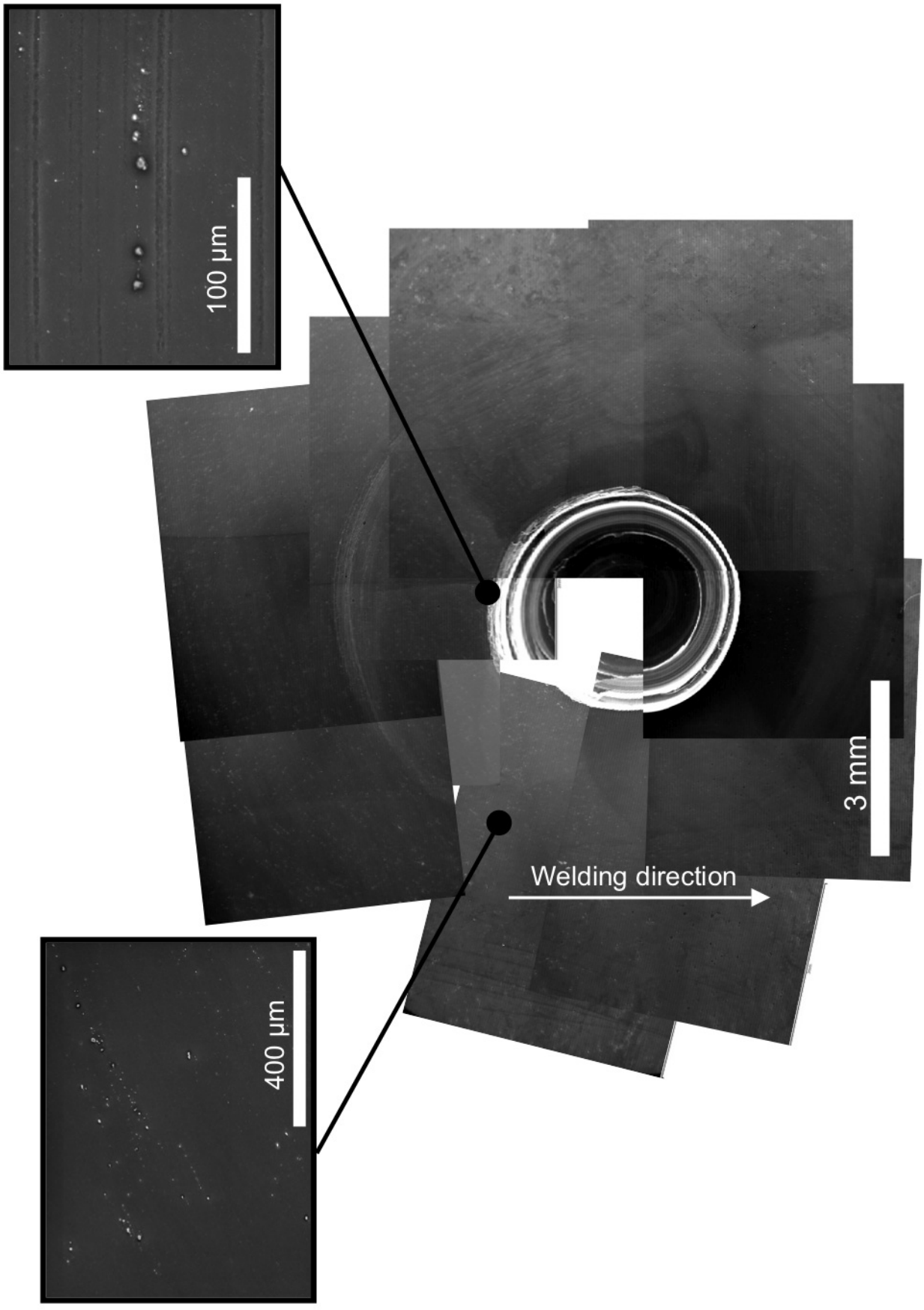

Figure 4.25: SE images of the FSW hole and the intergranular precipitation aligning with the material flow.

Figure 4.26 shows the microstructure of the FSW hole. The grain refinement is clearly visible under the tool.The hole corresponds to the pin location, then the fine grained area observed is located under the shoulder. This is due to the large strains undergone under the shoulder contact area that led to a thin fine grained layer on the surface of the weld. Behind the pin (i.e. the hole), some very fine grained lines following the tool rotation were observed. It was formed of several lines following the tool rotation and alterning very small grains and larger ones. This indicates the strain inhomogeneity undergone in this area. This may be caused by the influence of different flows involved resulting in different strains and by the grain orientation before recrystallisation. Indeed, the influence of the initial orientation of the parent grain which causes refinement to occur at different rates was reported in a previous study [101].

After the hole, at the end of the weld line, a crack was observed. It created at the plate junction, at the end of the weld line (see Figure 4.27), moved forward the weld line and, when arriving at the tool edge, followed the tool rotation in the nugget area along Al_8Mn_5 intergranular precipitate cluster (see Figure 4.26). The small grains observed on the edge of the crack/plate junction were caused by the milling process prior welding. The crack observation indicated then that during FSW, the material ahead of the tool moved to the retreating side of the pin, and then filled in the cavities. When observing the bottom surface of the weld, the crack was still visible, indicating that it passed through the plate (see Figure 4.26). Then the crack may be caused by some lack of material during welding.

EBSD analysis was performed at the end of the crack to check if the fracture occured within the grains. Indeed, if the grain orientation from both sides of the crack is the same, it can be concluded that there was only one grain before fracture . Figure 4.28 shows different grain orientations across the crack, then the fracture occured in an intergranular manner.

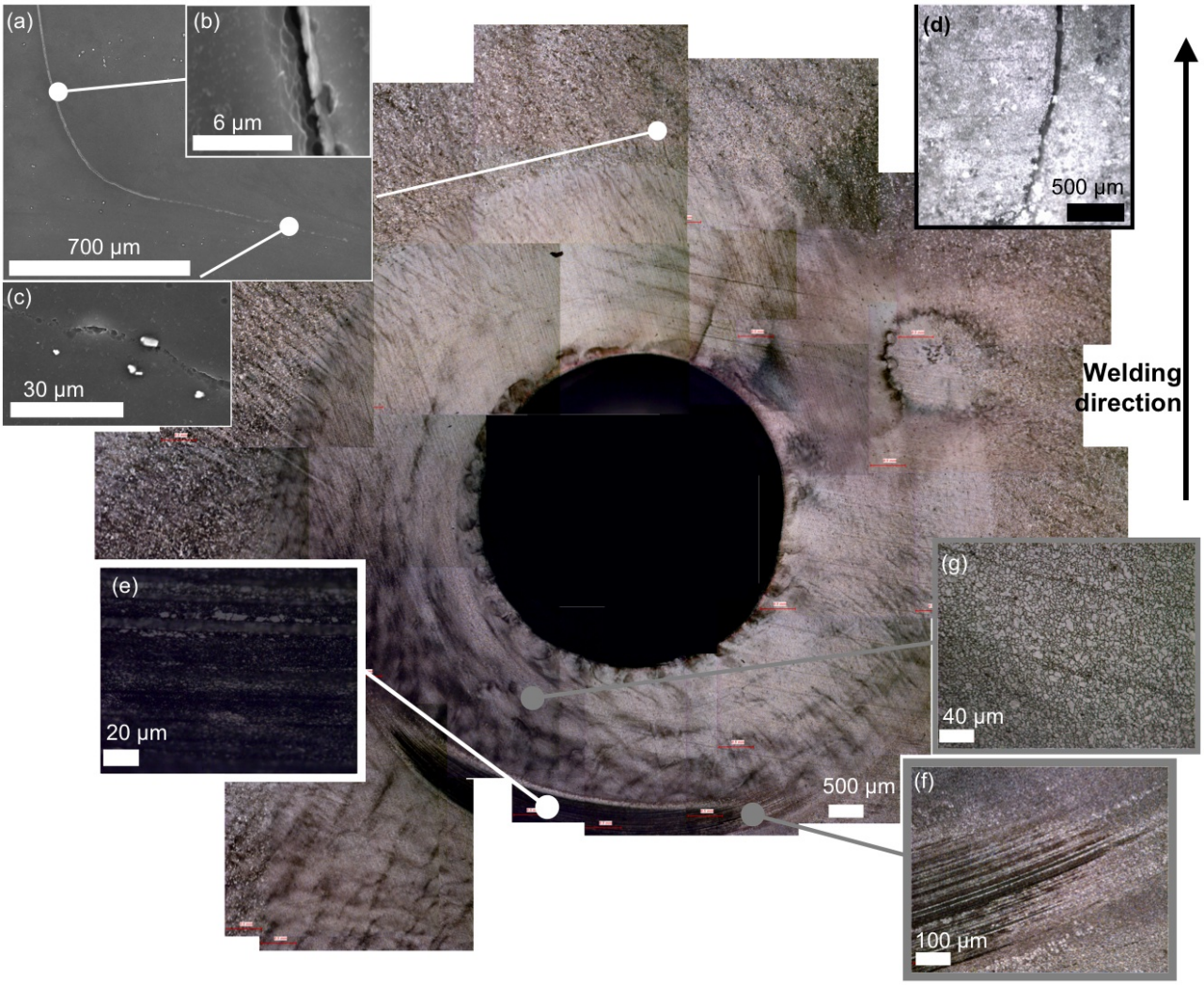

Figure 4.26: FSW hole micrographs: (a-b) SE images of the crack observed at the end of the weld line, (c) SE image of the Al_8Mn_5 precipitates observed along the crack, (d) Optical micrograph of crack on the bottom surface of the weld, (e-f) Microstructure at the shoulder edge, (g) Microstructure behind the pin.

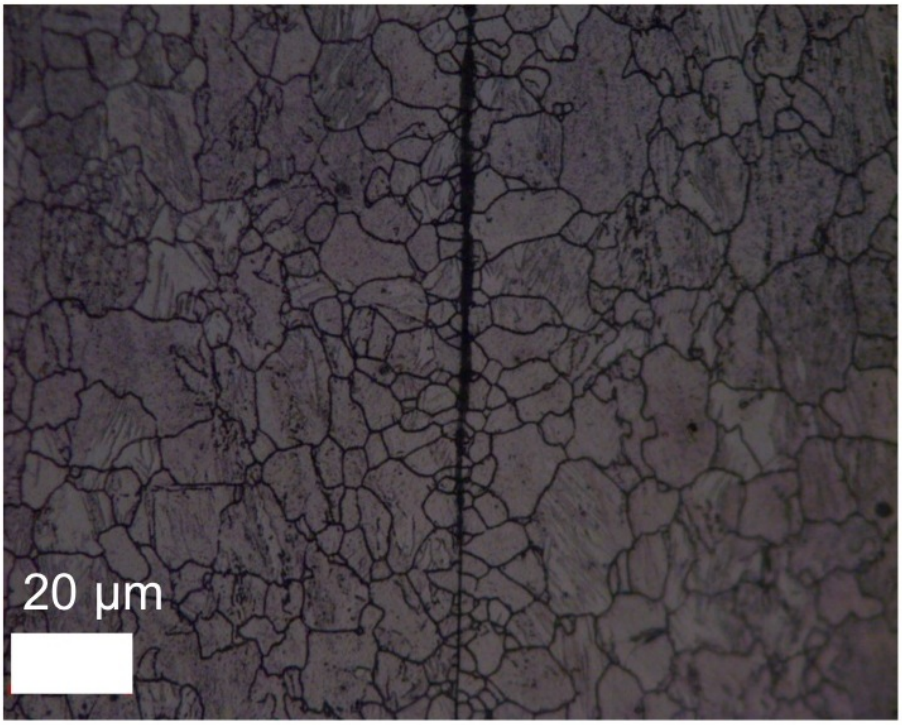

Figure 4.27: Optical micrograph of the plate junction where originated the crack.

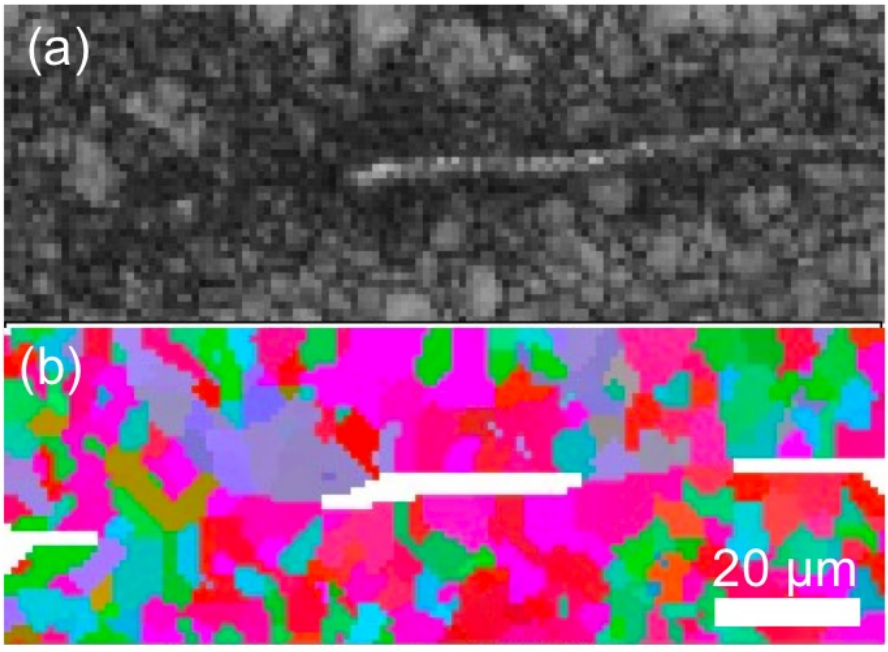

Figure 4.28: EBSD map of the end of the crack (a) Band contrast colouring, (b) All Euler colouring.

4.6.2 FSW flash

Micrographs were performed in the FSW flash to study the microstructure evolution in this area which was highly deformed. Full recrystallisation and grain growth occured in the curved area whereas, highly twinned microstructure is observed in the folded area (see Figure 4.29). This shows that several deformation mechanisms can occur and that recrystallisation process activation is quite sensitive.

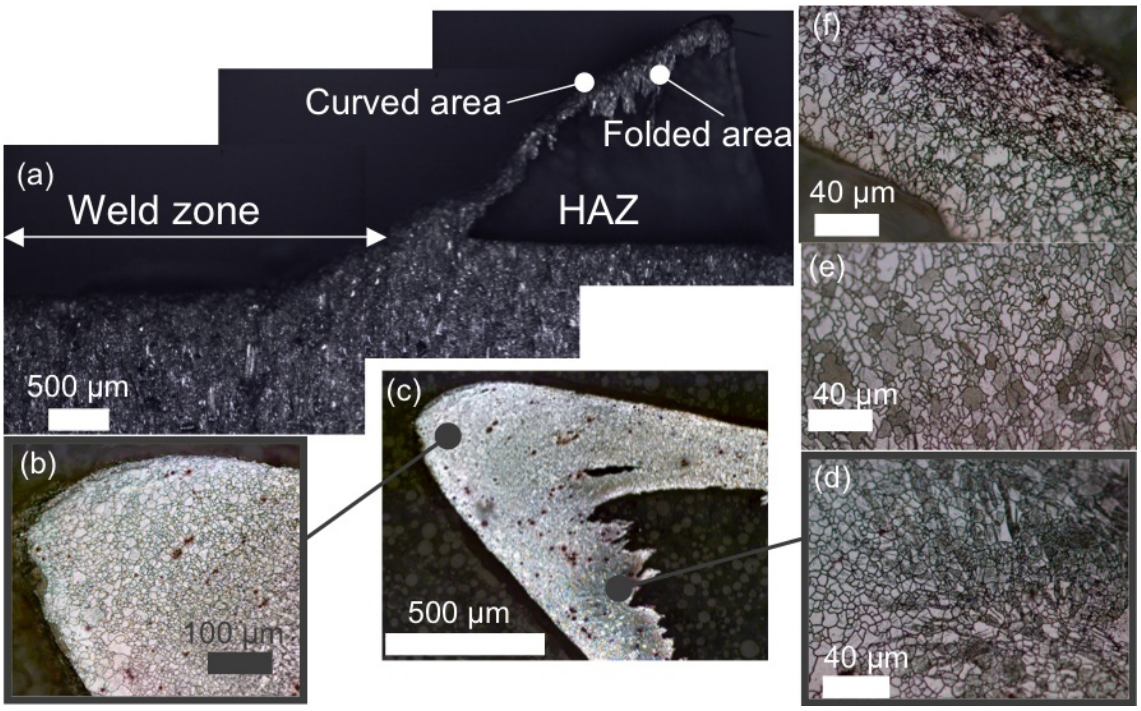

Figure 4.29: Optical micrographs of (a) FSW flash, (b) grain growth in the curved area, (c) microstructure gradients, (d) twinned microstructure in the folded area, (e) recrystallised microstructure, (f) microstructure gradient in a narrow flash area.

4.7 Conclusion

The process windows for FSW and LBW were established and the influence of the processing parameters were characterized. The temperature distribution in FSW and LBW was determined using thermocouples measurements. The analysis of the area surrounding the FSW hole allowed us to describe the material flow and FSWeld formation. The analysis of the FSW flash microstructure showed the sensitivity of the activation of recrystallisation and deformation mechanisms.

Chapter 5

Characterization of AZ31 optimized welds

5.1 Introduction

The determination of the process window described in the previous section led to the production of optimized butt welds. The optimized weld analysis, in terms of microstructure and mechanical properties, was focused on AZ31 alloy. In this section, will be described the experimental results obtained during this study to characterize AZ31 optimized welds (i.e. for FSW: W = 1000 RPM, V = 200 mm/min and for LBW: P = 2.4 kW, V = 7000 mm/min). The methodologies used being the same, the study of FSW and LBW will not be splitted in this section. Indeed FSW and LBW are both thermal processes, completed by a mechanical input in FSW. The main differences are then the processing temperature range and the cooling speed.

5.2 Microstructure evolution

5.2.1 AZ31-O base metal

5.2.1.1 Grain structure

AZ31 Mg alloy hot rolled plates were received for this study in annealed condition. There were used as base metal to produce FSW and LBW welds. Micrograph analysis was performed using optical microscopy in the 3 directions (Figure 5.1):

- on the top surface,
- parallel to the rolling direction,
- parallel to the transverse direction.

The AZ31 base metal revealed a fine equiaxed grain structure, with very few deformation twins. Two grain size populations could be observed (5μm and 15μm) and the average grain size is 10 μm .

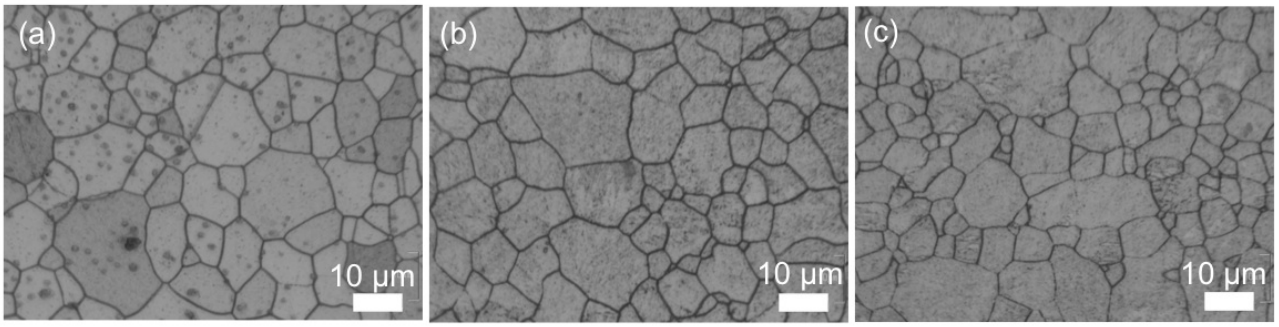

Figure 5.1: Optical micrograph of AZ31 observed along (a) the top surface, (b) the rolling direction and (c) the transverse direction.

5.2.1.2 Precipitation

The equilibrium phases at room temperature in magnesium alloys with 2 to 9 wt.% aluminium and less than 1 wt.% manganese are alpha-Mg solid solution, $Mg_{17}Al_{12}$ and Al_8 Mn_5 [123, 124]. The $Mg_{17}Al_{12}$ and the Al_8 Mn_5 could not be observed using XRD phase analysis, due to their small size and volume fraction. Only the α-Mg phase diffracted.

AZ31 optical micrograph study showed that the microstructure consisted in only an α-Mg phase structure. Using this technique, the $Mg_{17}Al_{12}$ structure, which is usually present in Mg alloys containing more than 2 wt% Al [123], was not observed. 3-10 μm precipitates aligned in the rolling directions were observed Figure 5.2. Using SEM, these precipitates were identified as very bright particles (Figure 5.2). Energy Dispersive Spectroscopy (EDS) analysis showed that theses inclusions were Al and Mn-rich phases and that there was a loss in Mg content in these areas (see Figure 5.2).

Further microstructural analysis using TEM and HR-TEM revealed the presence of intragranular nanoscale precipitates (Figure 5.3). These features were not observed previously in the literature in this magnesium alloy.

Two different particle sizes can be observed:

- Few large 200 nm×500 nm particles
- Smaller particles uniformly distributed in the α-Mg matrix, representing 1.15% volume fraction. They have a mean size of 35 nm (standard deviation 10 nm), which was determined by image analysis using ImageJ software (Figure 5.4).

EDX was used to analyse the chemical composition of theses two particle types. They were both identified as Aluminium-Manganese rich particles (Figure 5.5). The relative proportion of Aluminium and Manganese in these particles indicated that the larger one corresponds to Al_8Mn_5 (1.6) whereas the Al/Mn ratio in the smaller particle corresponds to 1, suggesting that it is a AlMn precipitate.

Figure 5.6 shows the SAED patterns taken along [0001] zone axis, with a substructure. From the reflection indexation, the presence of Al_8Mn_5 can be confirmed.

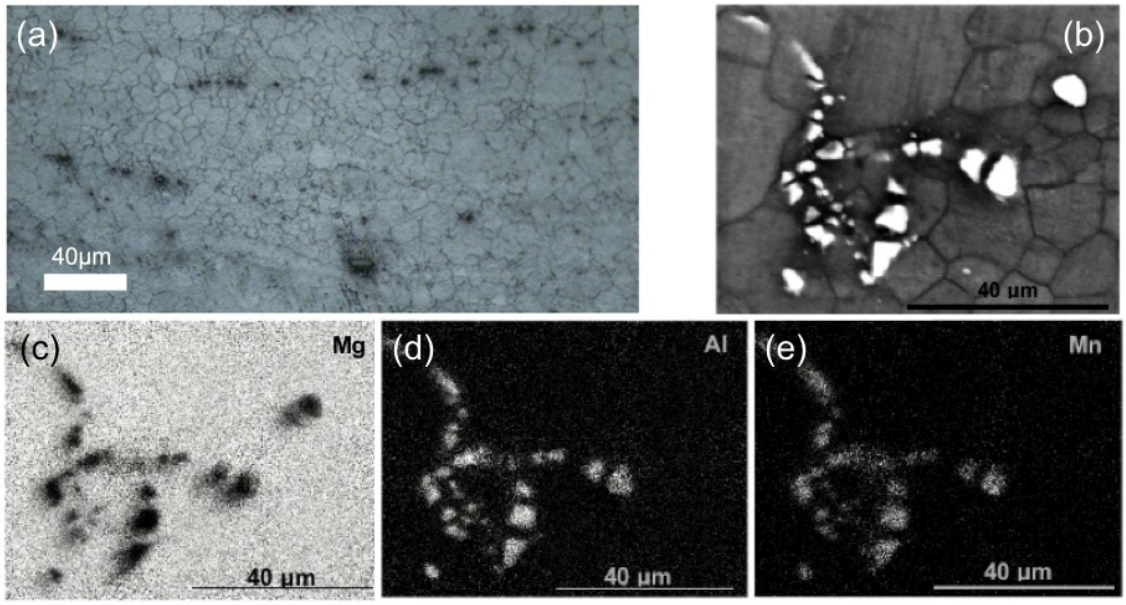

Figure 5.2: (a) Optical micrograph of Aluminium Manganese particles aligned along the rolling direction in AZ31 base metal, (b) SE images of Aluminium Manganese particles, (c) corresponding Mg EDS map (d) Al EDS map and (e) Mn EDS map, white zones are typical of a high element content.

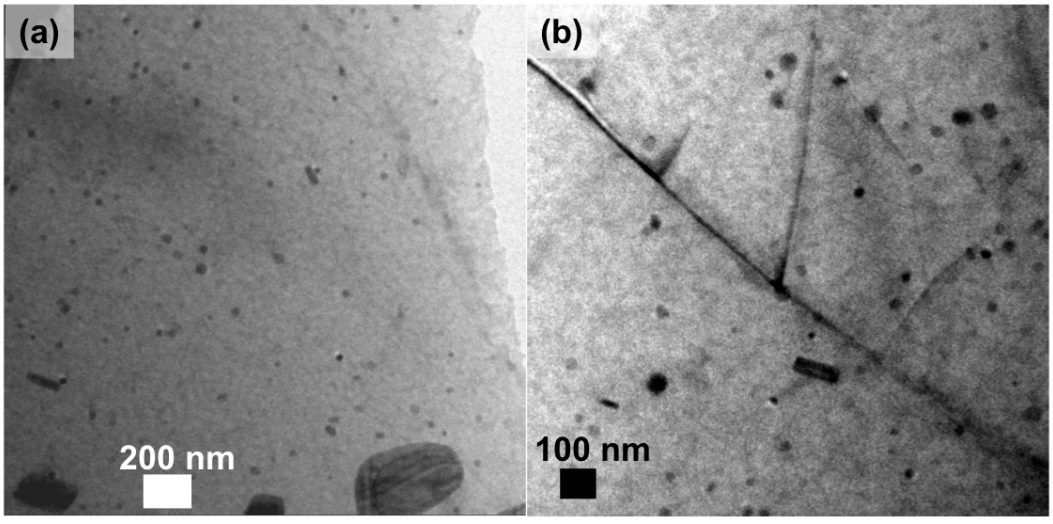

Figure 5.3: Nanoprecipitates in AZ31 base metal.

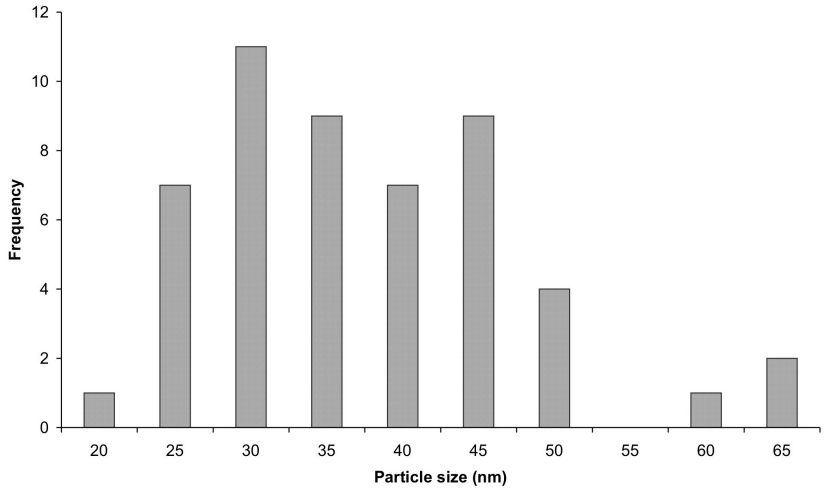

Figure 5.4: Nanoprecipitate size distribution.

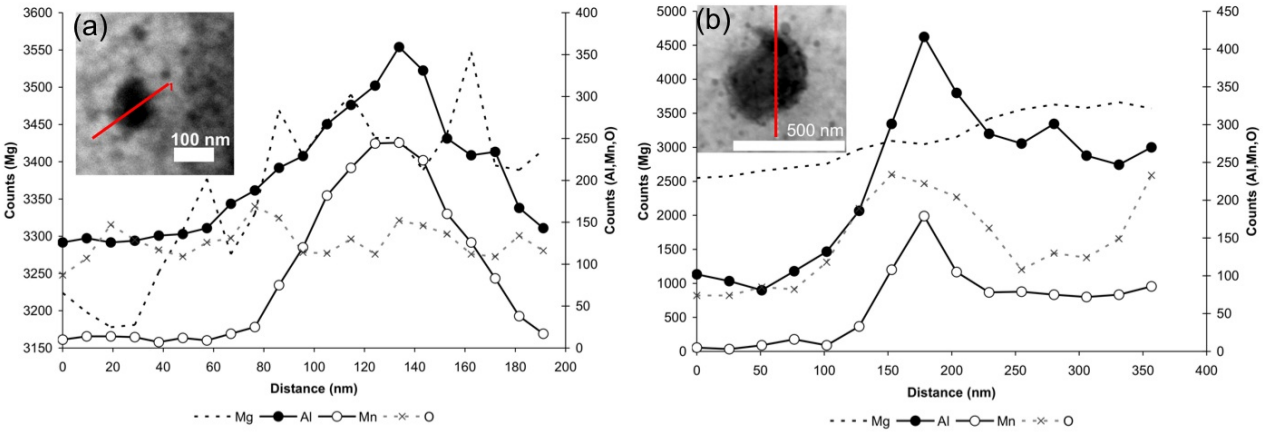

Figure 5.5: EDX-TEM chemical analysis of (a) smaller and (b) larger nanoprecipitates in AZ31 base metal. Analysis was performed along the red line which can be seen on the Bright Field image.

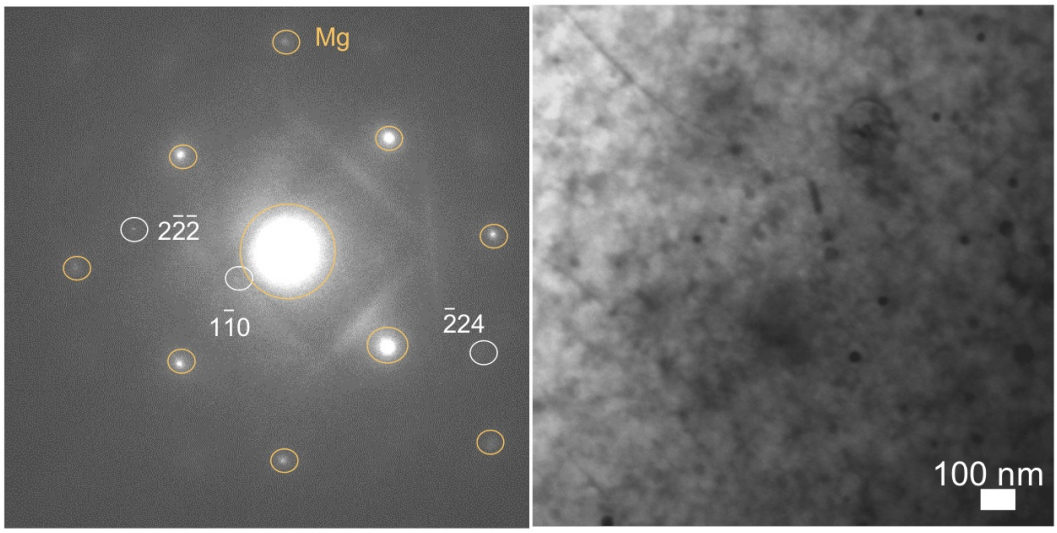

Figure 5.6: Identification of substructure in SAED pattern corresponding to Al_8Mn_5 in $[11\bar{2}0]$ zone axis (white) with α-Mg [0001] zone axis matrix (orange).

5.2.2 Microstructure observed after heat treatments

Heat treatments were performed on AZ31 base metal samples to study the influence of the temperature on the microstructure. The microstructure of samples heated at 550 °C during 1h and then air-quenched is shown in Figure 5.7. A substantial grain growth is observed. SEM analysis showed that the intergranular Al_8Mn_5 are still present and then that they did not dissolve until 550 °C. Intragranular nanoscale features can be observed ranging from about 600 nm down to 20 nm. EDX analysis revealed that the precipitates observed were Al-Mn compounds. No $Mg_{17}Al_{12}$ phase could be identified from EDX analysis.

5.2.3 Weld structure

The FSW microstructure consists in 4 different areas: Base Metal (BM), Heat Affected Zone (HAZ), Themo-Mechanical Affected Zone (TMAZ) and Nugget (Figure 5.8) as described in previous studies [17].

The LBW microstructure consisted in 3 different areas: Base Metal (BM), Heat Affected Zone (HAZ) and Fusion Zone (FZ) (Figure 5.9).

5.2.4 HAZ

From the microstructure analysis, any difference could not be observed between the Heat Affected Zone (HAZ) and the Base Metal (BM).This is consistent with the thermal history of AZ31 base metal which has undergone a 300°C heat treatment. Then the microstructure should not be modified until 300°C. In FSW, the HAZ could undergo temperature higher than 300°C but the cooling rate was high enough to prevent from grain growth. Then, even if we know that a HAZ exists, as FSW and LBW are thermal processes, this zone could not be identified and

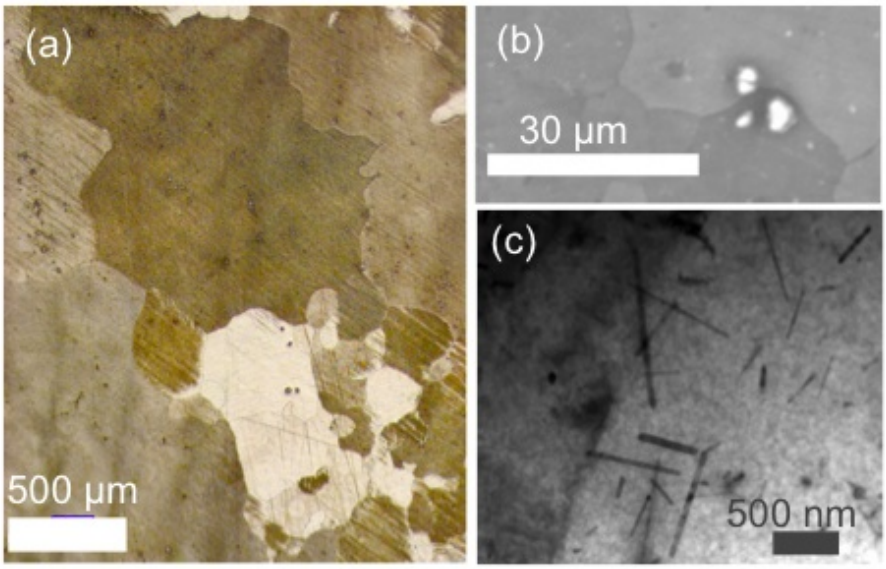

Figure 5.7: (a) Grain structure and precipitation observed by (b) SEM and (c) TEM of 550 ˚C heat treated sample.

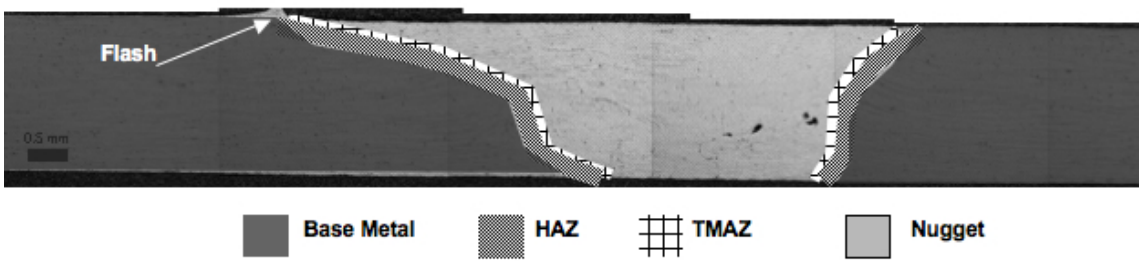

Figure 5.8: Microstructure of FSWeld section.

characterised during this study. At least, we can say that this zone was very narrow in the case of hot rolled AZ31 for both FSW and LBW.

5.2.4.1 Shear bands

The observation of LBW and FSW surfaces revealed the presence of band features at 45˚from the weld line (Figure 5.10 and 5.11). These band features started in the TMAZ/HAZ boundary of the weld, and propagated in the base metal direction. They were observed on both plate sides (top and bottom of the weld) and both weld sides (advancing and retreating for FSW). These band features were identified in each butt weld produced (Figure 5.10 and 5.11) and also on bead on plate welds. The sample preparation prior welding was performed by milling the sample edges. The observation of the edges after milling process did not show the presence of shear bands. Then, these features are caused by the welding process.

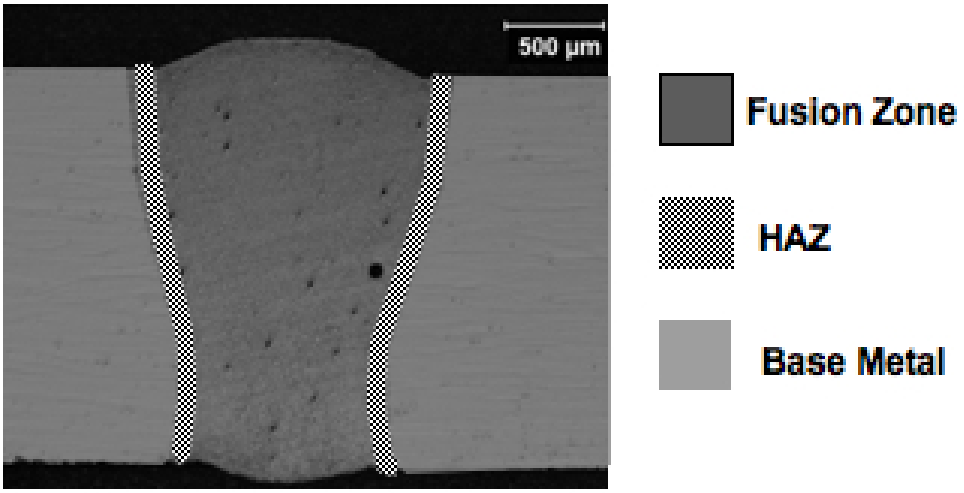

Figure 5.9: Microstructure of LBWeld section.

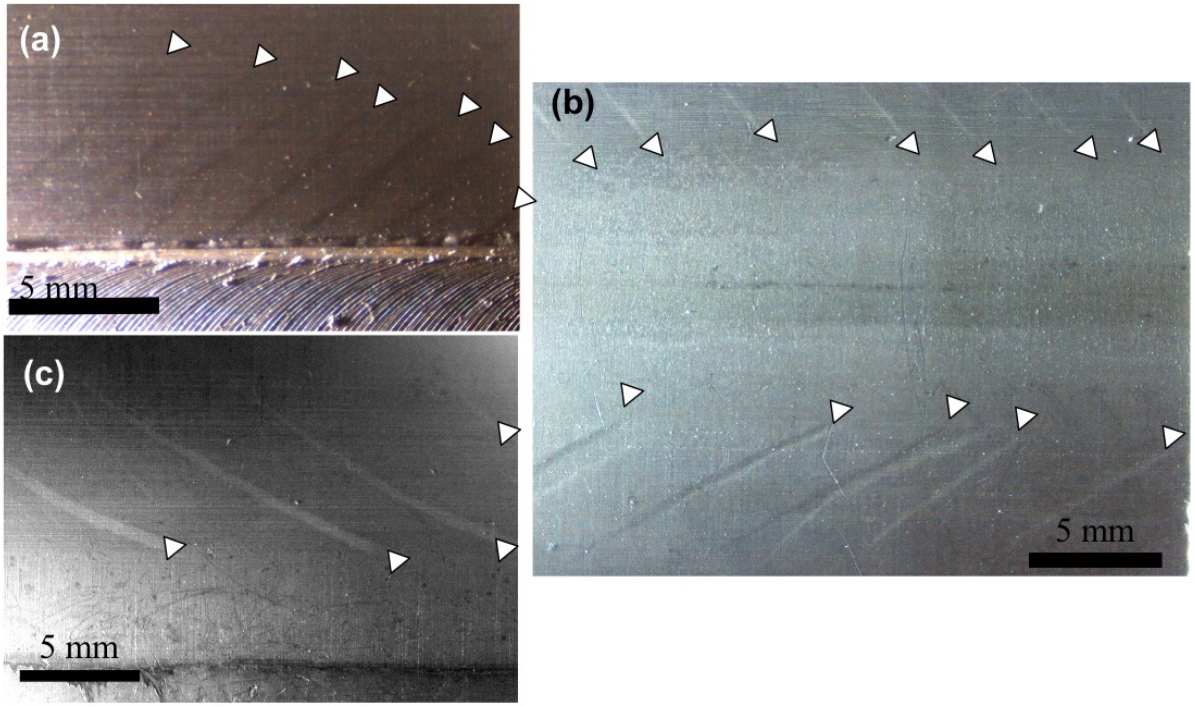

Figure 5.10: Macrographs of shear band features in FSW butt welds (a) W = 1000 RPM, V = 2000 mm/min top surface (b) W = 1300 RPM, V = 300 mm/min bottom surface, (c) W = 1000 RPM, V = 200 mm/min (13 mm shoulder diameter) bottom surface, the white arrows help to visualize the shear bands.

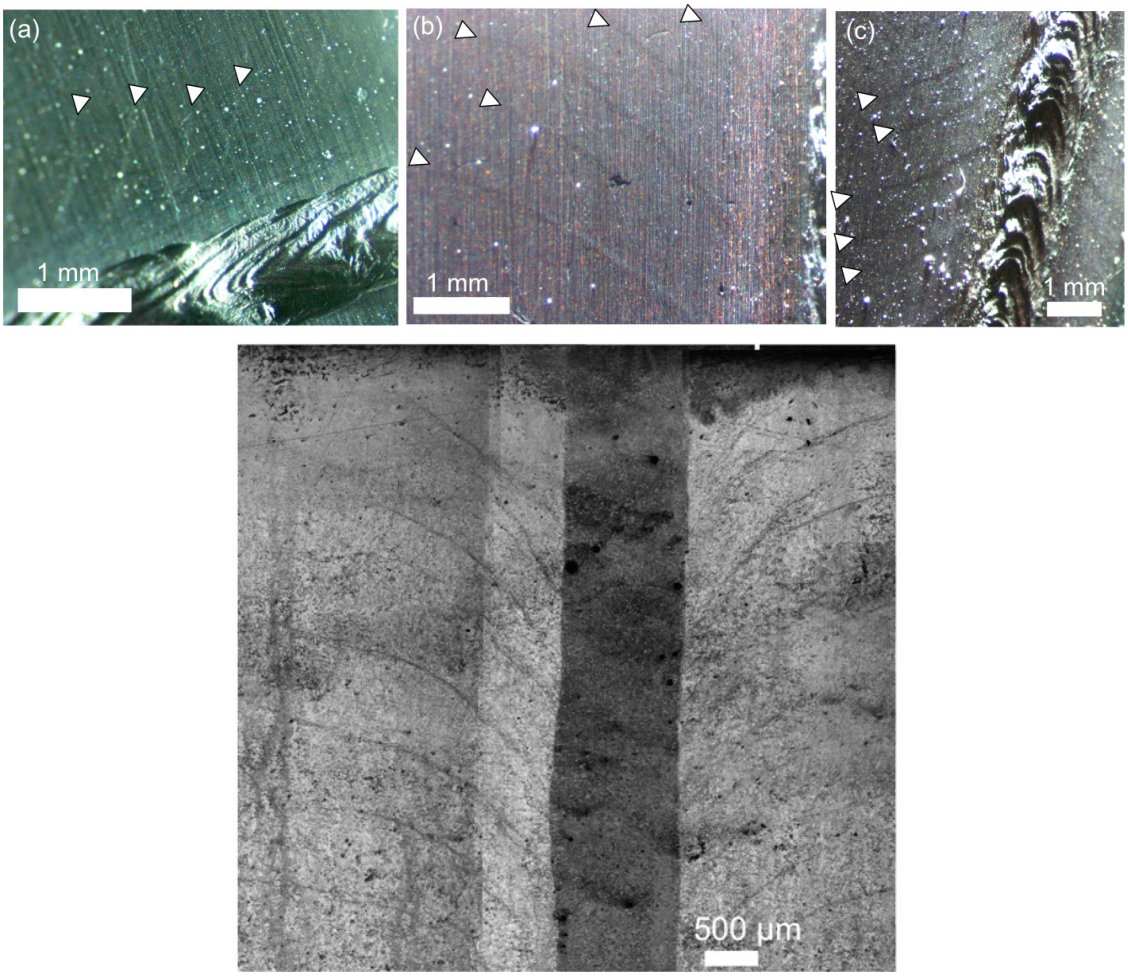

Figure 5.11: Macrographs of shear band features in LBW butt welds (a) Nd:YAG 2.4 kW, 7 m/min, (b) CO_2 2 kW, 3 m/min, (c) CO_2 2.5 kW, 3.5 m/min, and optical micrograph of shear bands in Nd:YAG (2.4 kW, 7 m/min).

An adiabatic shear band is a narrow region of intense shearing which sometimes occurs in metal which experienced high strain rates [125]. It can reach a very high aspect ratio (few microns wide, and millimeters or even centimeters in length). The thickness is perpendicular to the maximum shearing direction. The bands generally cut straight through the material, but branching can also be observed. They can affect the mechanical behaviour, acting as damage sites. Shear bands are usually produced after ballistic impact, forging and in machining chips [125]. Figure 5.12 shows the microstructure of adiabatic shear bands [28].

In this study, shear bands were identified as darker area with optical microscopy (Figure 5.13, Figure 5.11), and then, using a higher magnification revealed that this was due to impressive larger amount of twins in these areas (Figure 5.13, Figure 5.14) whereas AZ31 HAZ/base metal microstructure and even TMAZ and nugget microstructures do not exhibit twinning. Mechanical twins and a large amount of annealing twins were observed. Indeed mechanical twins formed

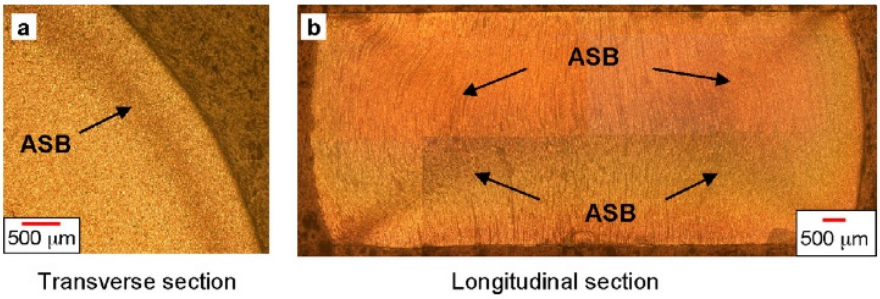

Figure 5.12: Optical microstructure showing adiabatic shear bands (ASB) in an impacted dual-phase steel [28].

due to a large strain energy and then they present sharp edges. Annealing twin microstructure consists in broader edges associated with the accommodation of interfacial energy. Then, the formation of shear bands is not only due to the strain induced by the stiffness heterogeneity at the boundary between the solid-state base metal and the liquid (for LBW) or soft-solid (for FSW) weld. The thermal input caused also twin formation. The influence of the hcp crystal structure of magnesium and the initial strong basal texture which affect the deformation mechanisms must also be taken into account to explain the formation of shear bands.

The shear bands are observed all along the weld length with a constant spacing. The periodic character of this phenomenon is caused by the strain rate due to material flow in FSW and convective flow in LBW. The welding conditions influenced the band size and band spacing (Figure 5.15).

A complementary study was done using EBSD to confirm the twinning microstructure in these areas (Figure 5.16). The pole figures calculated from the EBSD analysis showed the conservation of the base metal basal texture.

Microhardness analysis did not show any hardening that would be caused by twinning in the shear band (Figure 5.17).

Such features were not cited in previous studies and the literature survey did not mention the formation of shear bands with FSW and LBW. Shear bands are usually produced after ballistic impact, forging and in machining chips [125]. The band spacing depends on the thermal conductivity, the strain rate and increases with thermal softening component when work hardening can be neglected [126]. During plastic deformation, competing mechanisms are acting: the flow stress increases with work hardening and strain rate hardening but lowers with thermal softening. Thermal softening wins over other hardening mechanisms so that the material can softens with increasing strain. When this strain softening increases the ability of the material to transmit shear forces decreases and then shear bands are formed [125].

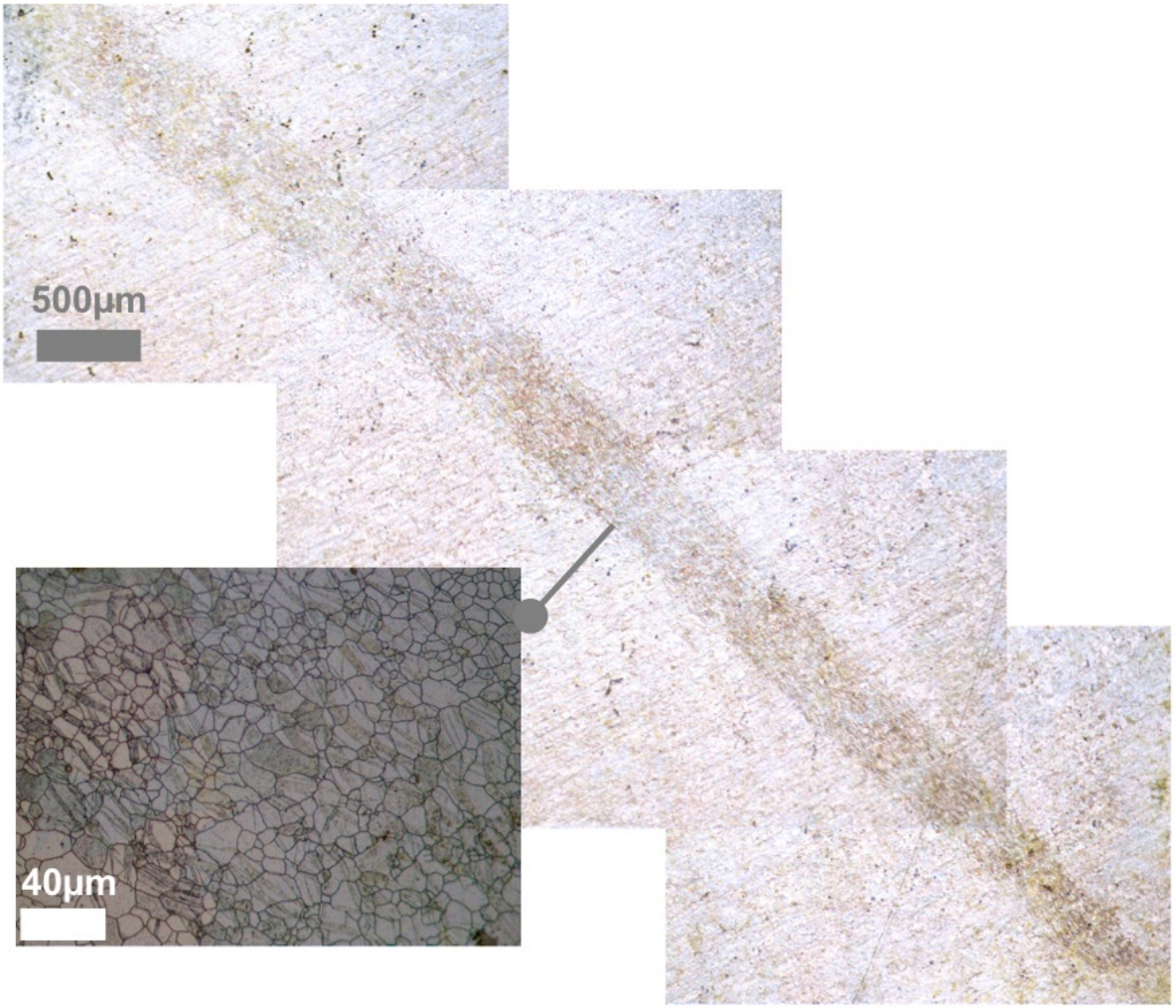

Figure 5.13: Optical micrograph of one shear band in FSW (13 mm shoulder diameter, W = 1000 RPM, V = 200 mm/min).

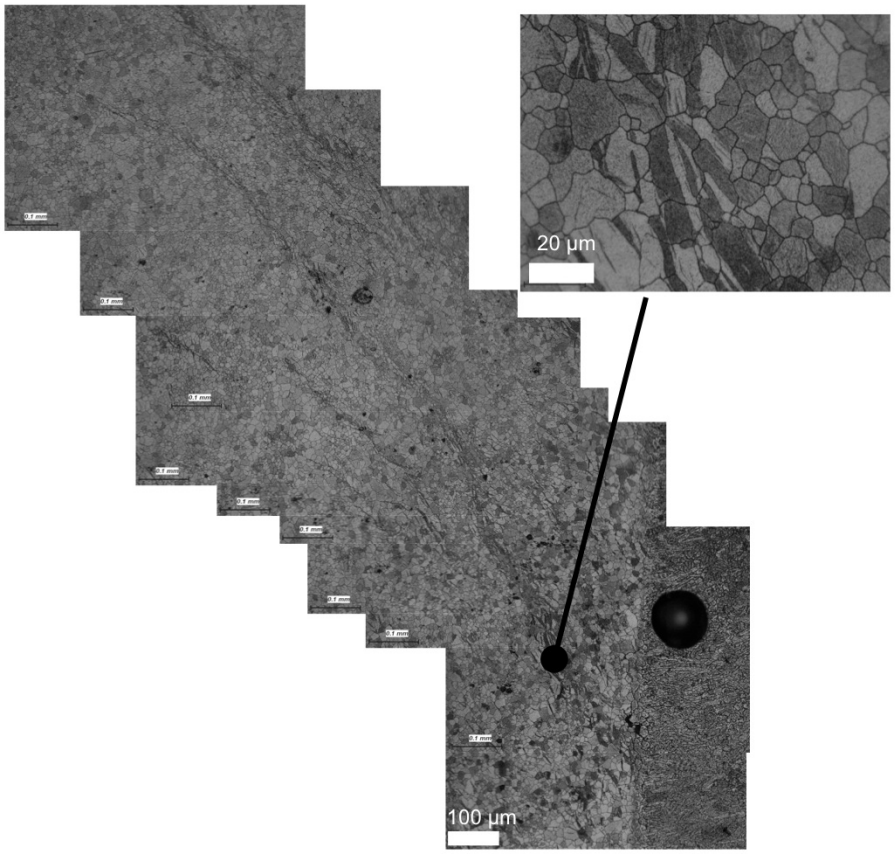

Figure 5.14: Optical micrograph of shear band in Nd:YAG (2.4 kW, 7 m/min).

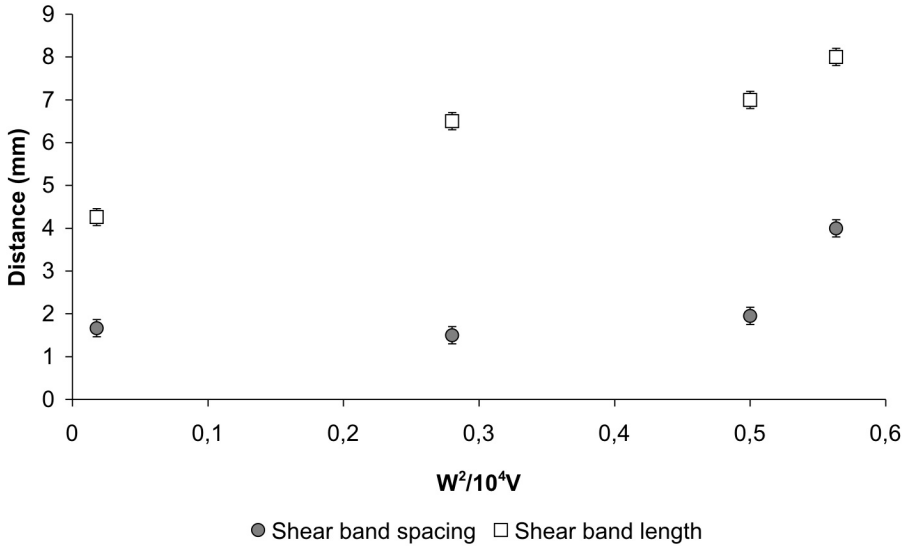

Figure 5.15: Influence of the FSW processing parameters on shear band spacing and shear band length.

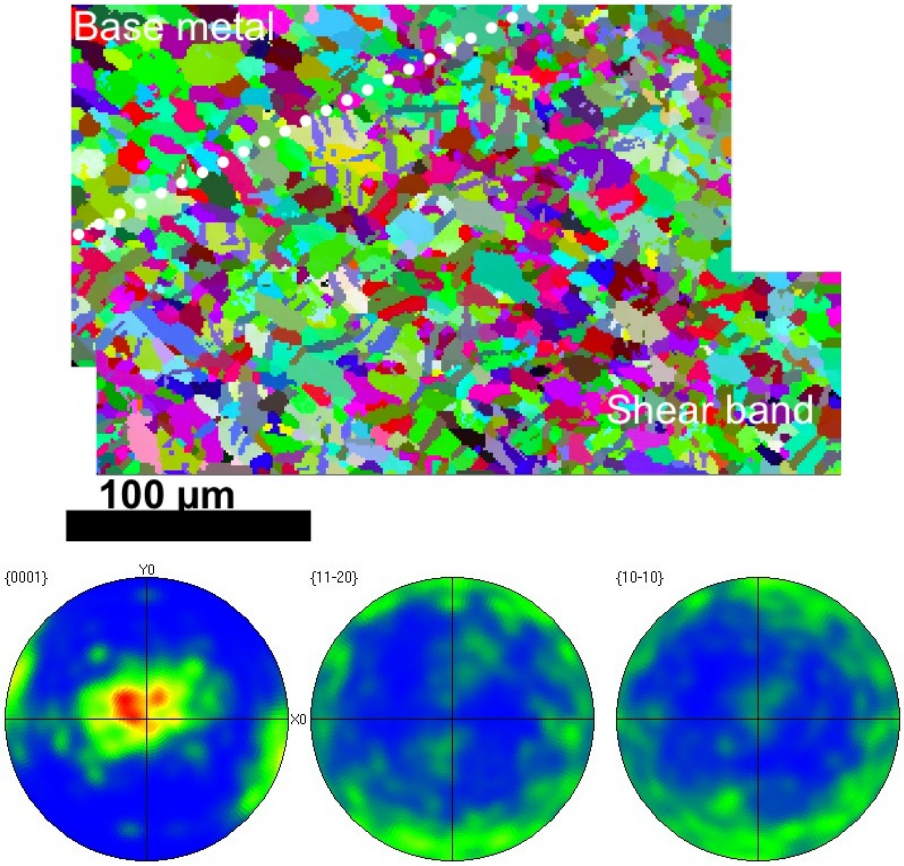

Figure 5.16: All-Euler EBSD map of a shear band and associated pole figures in FSW (13 mm shoulder, W = 1000 RPM, V = 200 mm/min).

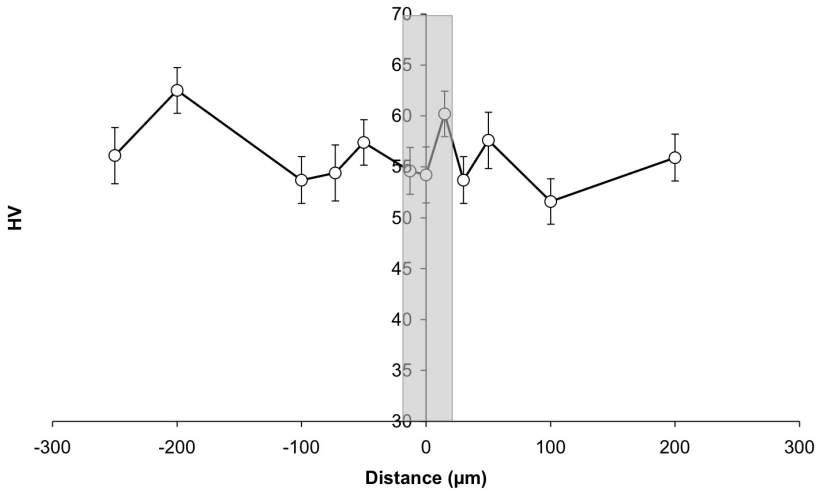

Figure 5.17: Microhardness evolution across a shear band in FSW (13 mm shoulder, W = 1000 RPM, V = 200 mm/min), the shaded area corresponds to the shear band.

5.2.5 Friction Stir Welding TMAZ

The FSW TMAZ microstructure consists in not fully recrystallised grains. The TMAZ grain size ranges between 2 to 15 μm. A large microstructure gradient is obtained in the TMAZ at low (W, V) values, whereas this gradient is smoother at high (W, V) values (Figure 5.18).

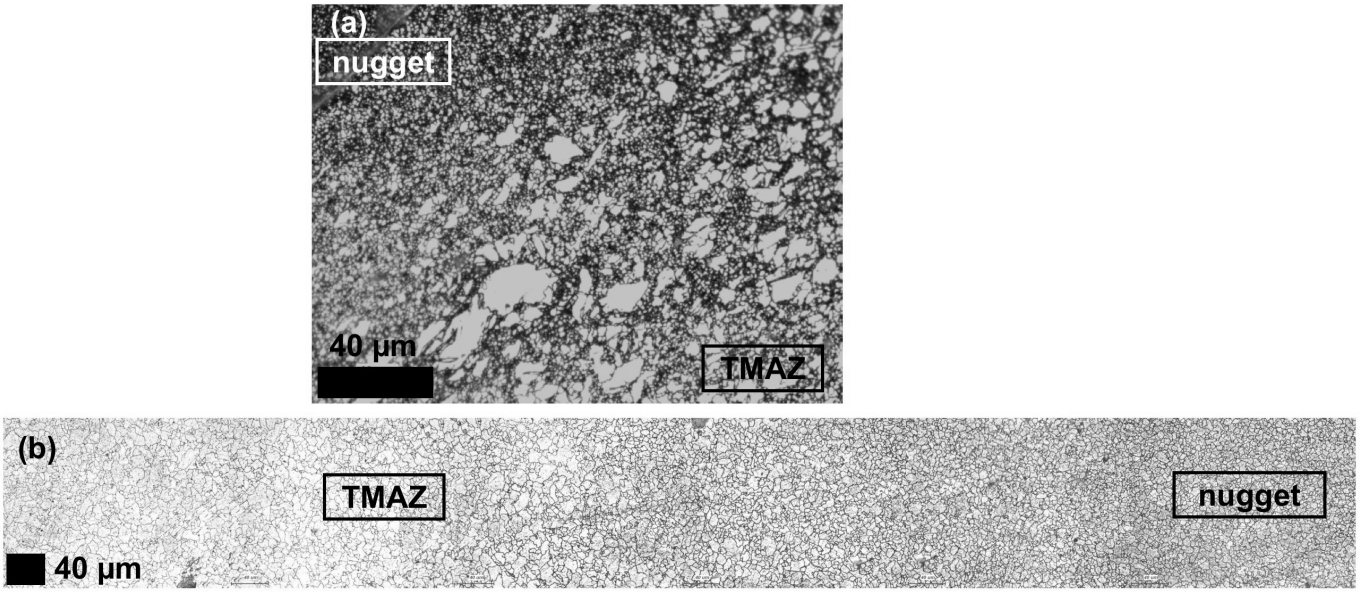

Figure 5.18: Grain size evolution in the TMAZ for FSW (tool 4mm pin / 10mm shoulder): (a) 600 RPM, 100 mm/min and (b) 1800 RPM, 1000 mm/min.

The precipitation analysis was performed using SEM and TEM. The 2-10 μm (Figure 5.19) and the nanosized Aluminium Manganese precipitates (Figure 5.20) were still observed in the TMAZ and remained unchanged. This indicated that there was no precipitation evolution in this area.

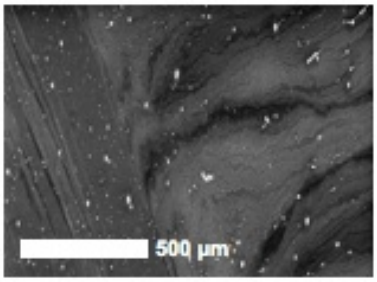

Figure 5.19: SEM analysis of precipitation in the TMAZ for 4 mm pin, 10 mm shoulder diameter FSW W = 1000 RPM, V = 200 mm/min.

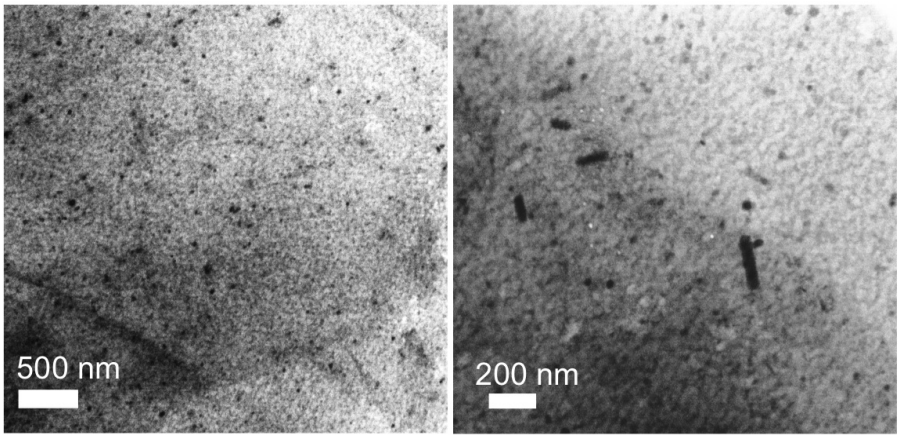

Figure 5.20: TEM analysis of precipitation in the TMAZ for 5 mm pin, 10 mm shoulder diameter FSW W = 1000 RPM, V = 200 mm/min.

5.2.6 Friction Stir Welding nugget

Dynamic recrystallisation occurs in the FSW nugget, leading to a fine grain size structure. Increasing W leads to an increase in grain size and in grain size dispersion (Figure 5.21(f)). Increasing V induces a decrease in grain size. At high W, there is no more influence of the welding speed on the grain size (Figure 5.21). Then, increasing the shoulder diameter induced an increase in the grain size (Figure 5.22). This is mainly due to the relationship between welding parameters and the temperature undergone during welding. Indeed increasing the shoulder diameter, the tool rotation speed (W) or decreasing the welding speed (V) produces an increase in the heat generated during the process and then promotes grain growth.

The intergranular precipitation was not modified in the nugget (Figure 5.23). The nanoscale precipitates identified as Al_8Mn_5 using Energy Dispersive Spectroscopy, did not dissolve in the nugget and were not modified by changing the welding parameters (Figure 5.24). Indeed, FSW is a solid-state process, and then the maximum temperature undergone does not exceed the melting temperature which is 610 °C for this alloy. This is consistent with the phase diagram [127] which indicates that Al_8Mn_5 phase dissolves above 610 °C for this alloy chemical composition. Moreover, they do not evolve in size as observed during heat treatments at 550 °C (see section 5.2.2), as the high temperature excursion very short.

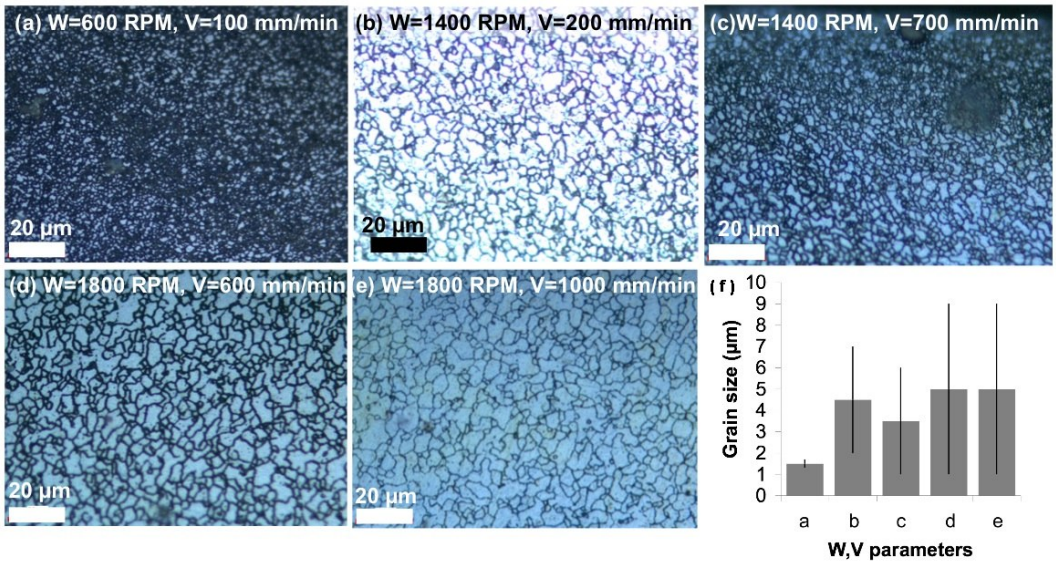

Figure 5.21: Nugget grain size evolution with W and V parameters for 4 mm pin, 10 mm shoulder diameter FSW (a) W = 600 RPM, V = 100 mm/min, (b) W = 1400 RPM, V = 200 mm/min, (c) W = 1400 RPM, V = 700 mm/min, (d) W = 1800 RPM, V = 600 mm/min, (e) W = 1800 RPM, V = 1000 mm/min and (f) grain size dispersion.

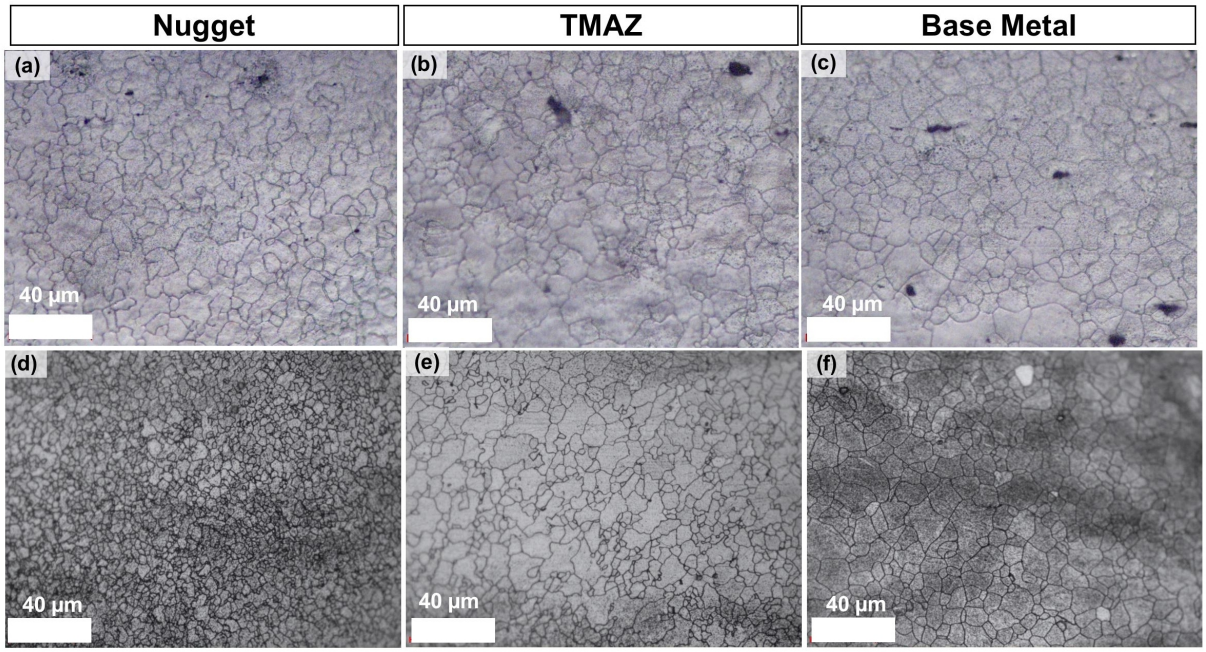

Figure 5.22: Grain size evolution with shoulder diameter for 1000 RPM, 200 mm/min butt FSW (a-c) 13mm shoulder diameter, (d-f) 10mm shoulder diameter.

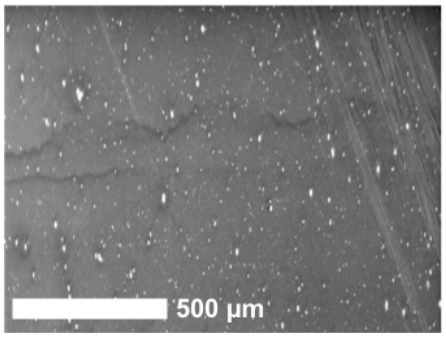

Figure 5.23: SEM analysis of precipitation in the nugget for 4 mm pin, 10 mm shoulder diameter FSW W = 1000 RPM, V = 200 mm/min.

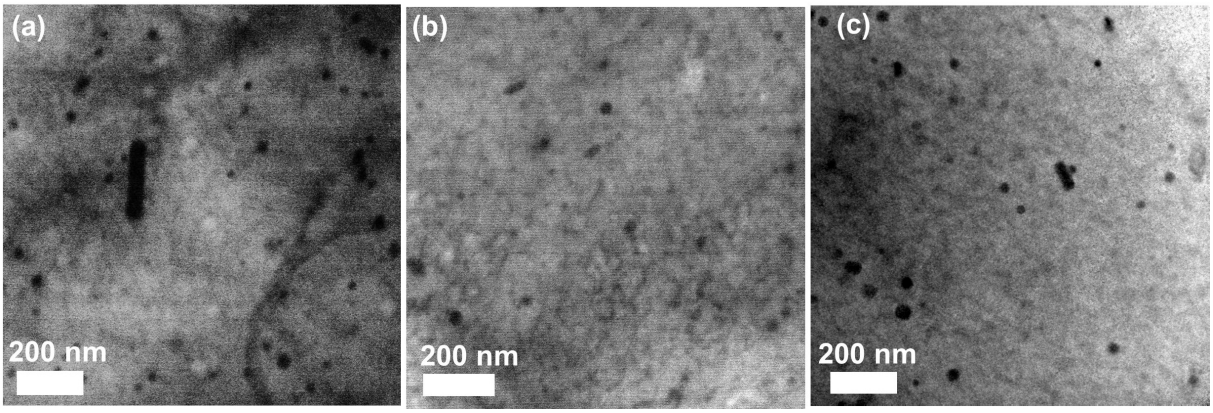

Figure 5.24: Intragranular precipitation evolution in the butt weld nugget (tool 5 mm pin / 10 mm shoulder): (a) (600 RPM, 2000 mm/min), (b) (1000 RPM, 200 mm/min) and (c) base metal.

5.2.7 Laser fusion zone

The microstructure in the LBW fusion zone consists in 2 different phases (Figure 5.25):α-Mg phase and a second phase with a dendritic structure. The dendrites were symmetric in the areas which last solidified, whereas, columnar dendrite structure is observed where the temperature gradient are higher (Figure 5.25).

SEM and SFEG observations were used to study the precipitation evolution in the LBW fusion zone (Figure 5.26). The intergranular Aluminium-Manganese precipitation was not modified (Figure 5.26), indicating that these precipitates could have not dissolved during LBW. Then, if this was confirmed, the maximum temperature undergone during LBW would lie between the AZ31 melting temperature and the Al_8Mn_5 dissolution temperature (i.e. between 610-665 $^{\circ}$C [127]). The second phase morphology consisted in small bright particle agglomerates distributed along the α-Mg grain boundaries but also within the α-Mg phase.The EDS analysis showed that this second phase presented an increase in Aluminium content and a loss in

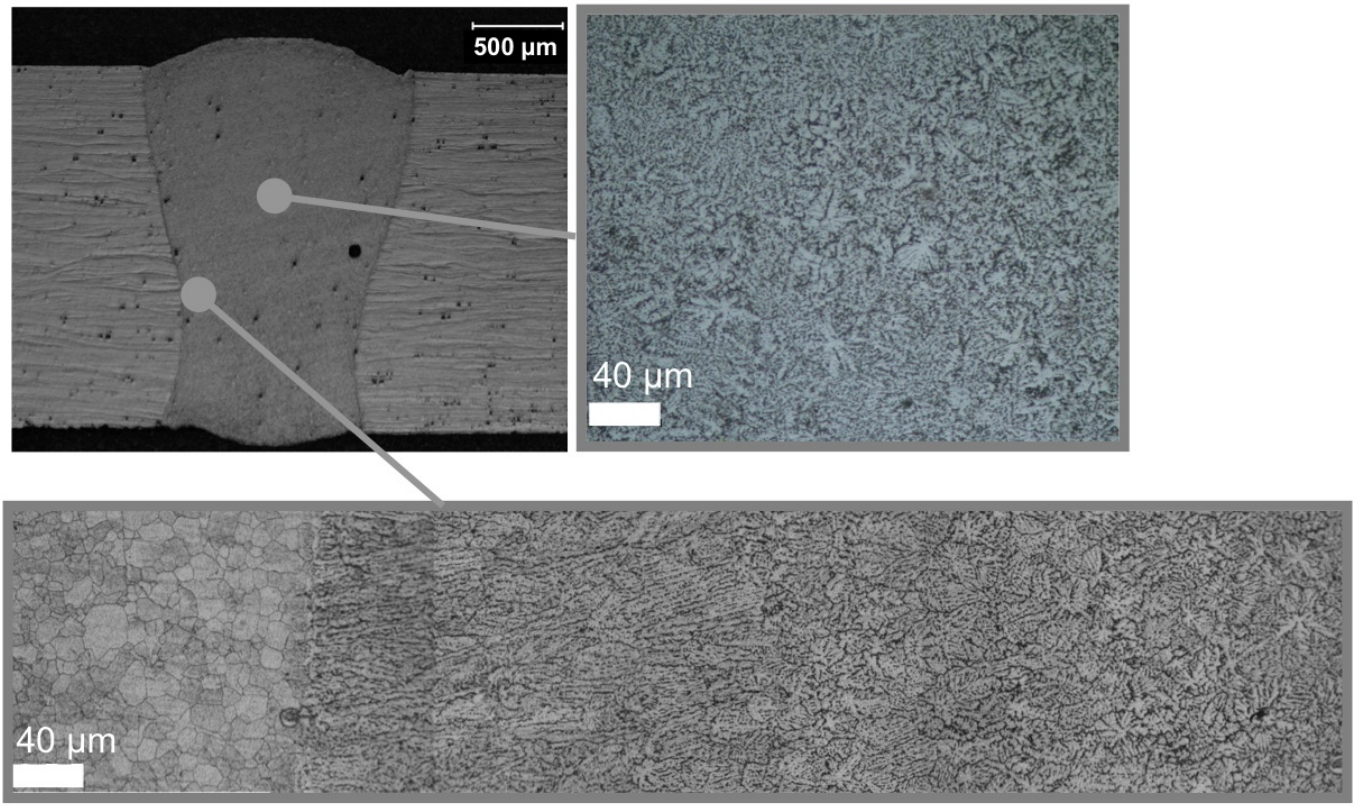

Figure 5.25: Optical micrograph of Nd:YAG LBW section (2.4 kW, 7000 mm/min).

Magnesium content.

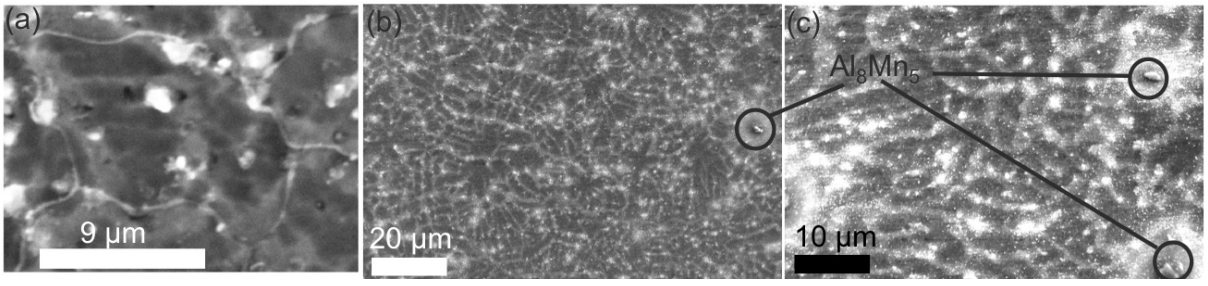

Figure 5.26: Intergranular Al_8Mn_5 precipitation and Al-rich second phase in Nd:YAG LBW fusion zone (2.4 kW, 7000 mm/min) (a) SEM observation, (b) and (c) SFEG observations.

As the final polishing was performed using an 0.05 μm Alumina suspension, the Aluminium rich areas could be attributed to the residual Alumina. So further EDS-SEM analysis was performed using a SiO_2 colloidal suspension final polishing (Figure 5.27). Aluminium rich areas were still observed in the fusion zone. The second phase is then characteristic of the LBW fusion

zone.

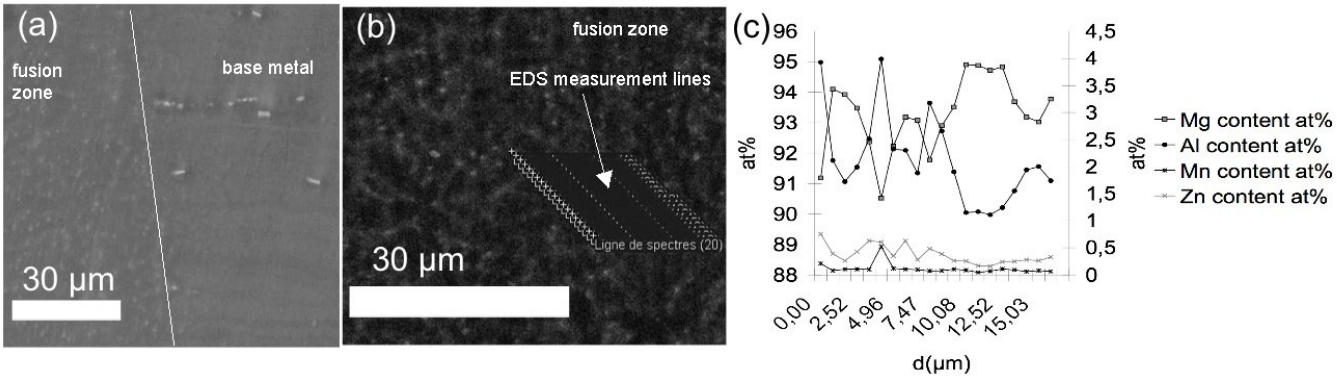

Figure 5.27: EDS-SEM analysis of Nd:YAG LBW after SiO_2 polishing (2.4 kW, 7000 mm/min) (a) BSE image, EDS measurement location in the fusion zone and (c) EDS analysis results.

The microstructure observed in the LBW fusion zone is consistent with previous studies [113] and it is similar to the one observed in Rapid Soldified AZ31 [128]. It consists in α-Mg phase with Al-rich solid solution and β-$Mg_{17}Al_{12}$ eutectic structure concentrated in the centre of Al-rich solid solution. During LBW, rapid solidification occured and the maximum solubility of aluminium decreased quickly, causing the precipitation of remaining aluminium in β phase. XRD phase analysis confirmed the presence of $Mg_{17}Al_{12}$ and magnesium oxides in addition to α-Mg in the LBW fusion zone (Figure 5.28).

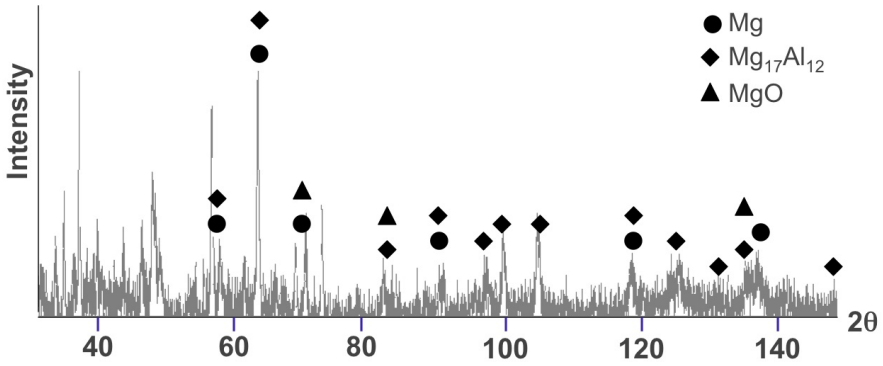

Figure 5.28: XRD Phase analysis of Nd:YAG LBW fusion zone (2.4 kW, 7000 mm/min).

TEM analysis was performed and large particles were observed (Figure 5.29) with a size ranging from 500 to 1500 nm. They were containing smaller 50-150 nm particles. EDS was used to identify the nature of these precipitates. Figure 5.29 shows the EDS profiles obtained. The profile taken through a large particle and a small one indicated that there was an increase in Aluminium and Manganese content in the small particle, surrounded by a Aluminium-Magnesium-Zinc rich area. The diffusivity of Zinc in Magnesium is higher than the diffusivity of Aluminium

in Magnesium [129]. During $Mg_{17}Al_{12}$ solidification , some Al atoms can be replaced by Zn atoms, then leading to $Mg_{17}(Al\text{-}Zn)_{12}$ compound [130, 129]. Then, the large particles can be identified as β precipitates. The profile taken through a large particle, but avoiding the small one confirmed the presence of $Mg_{17}(Al\text{-}Zn)_{12}$. The 50-150 nm particles could be identified as Al_8Mn_5, which indicated that the nanosized precipitates initially observed in the AZ31 base metal did not dissolve during LBW. They initiated the nucleation of the $Mg_{17}(Al\text{-}Zn)_{12}$ during solidification.This is consistent with Tamura study [129], which found that β precipitates preferentially formed in the Mn-rich areas.

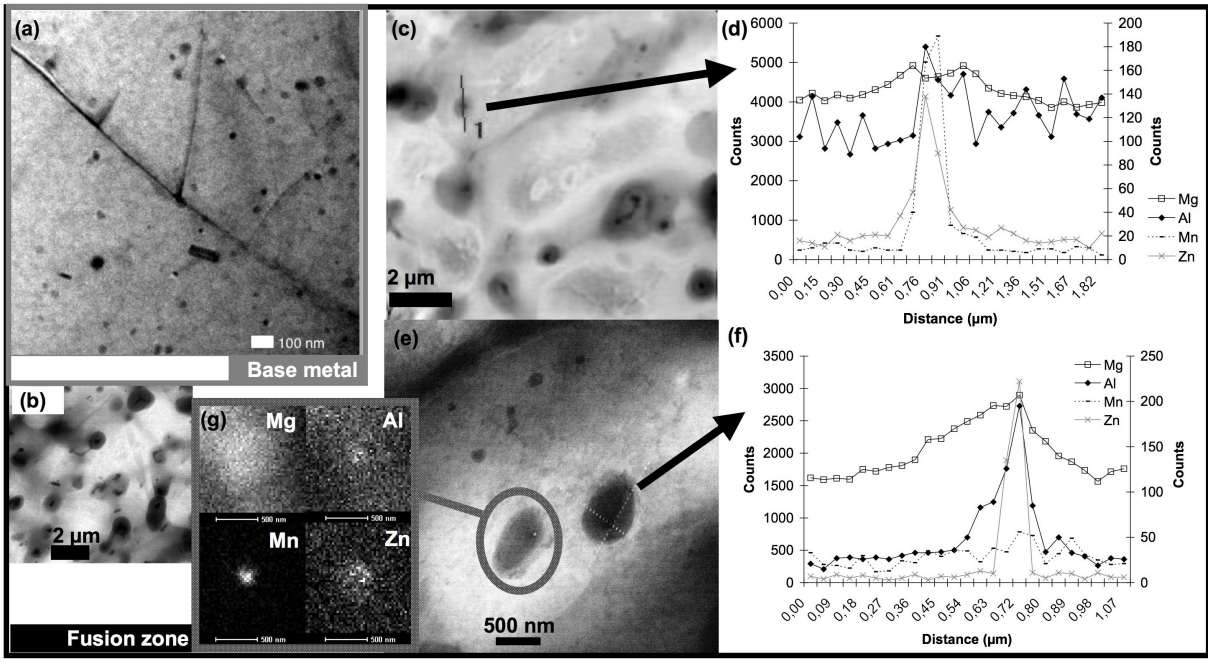

Figure 5.29: TEM analysis of Nd:YAG LBW fusion zone precipitation (2.4 kW, 7000 mm/min) (b) Brigth field image, (c) Brigth field image of the profile analysis location across a large precipitate and a small one, (d) the corresponding EDS profile, (e) Brigth field image of the profile analysis location across a large precipitate and without any small one, (f) the corresponding EDS profile, (g) the EDS maps of a large particle with a small one inside, compared to (a) base metal.

TEM analysis revealed a FCC sub-structure with 0.4186 nm lattice parameter corresponding to MgO structure (Figure 5.30).

The presence of the second phase prevented from grain observation using conventional microscopy (Figure 5.31). Indeed, the second phase etched differently and exhibited a different topography (Figure 5.32 (b) and (c)).

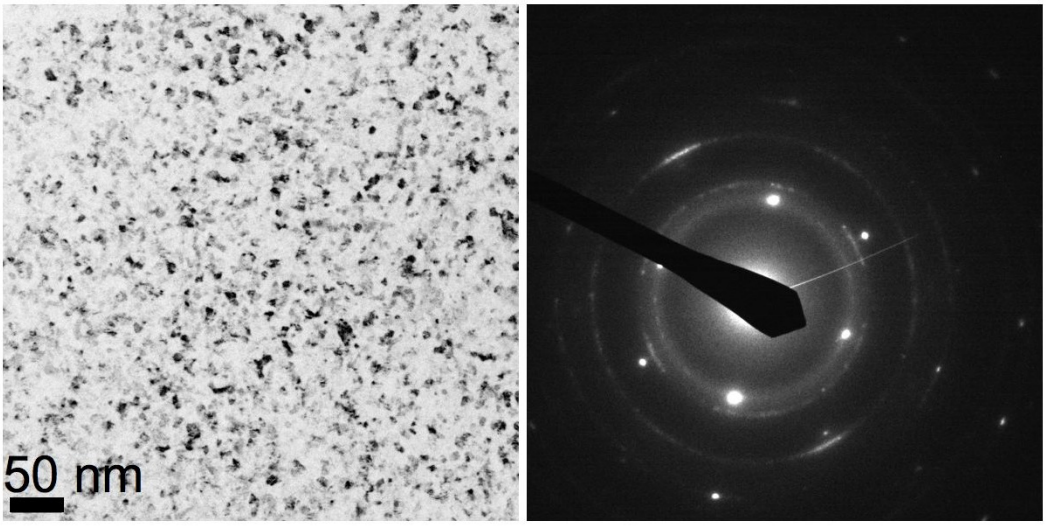

Figure 5.30: TEM Bright field image of MgO in Nd:YAG LBW fusion zone (2.4 kW, 7000 mm/min) and corresponding SAED pattern of α-Mg [001] zone axis matrix with MgO rings substructure.

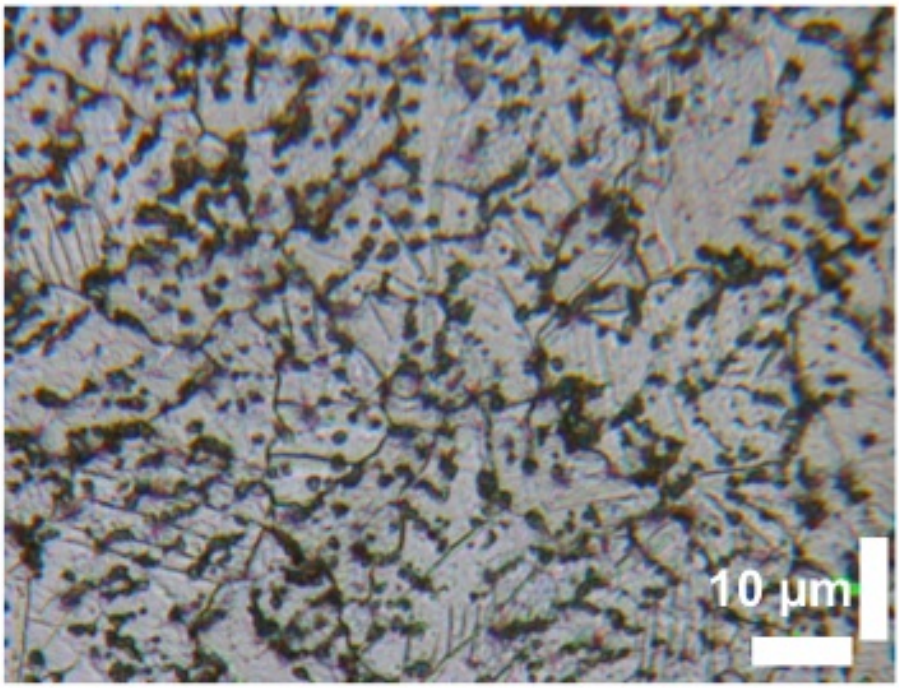

Figure 5.31: Optical micrograph of Nd:YAG LBW fusion zone (2.4 kW, 7000 mm/min).

The grain size evolution was then studied using Electron Back Scattered Diffraction (EBSD) (Figure 5.32).The grain size in the fusion zone is similar to the base metal one for the optimized welding parameters.

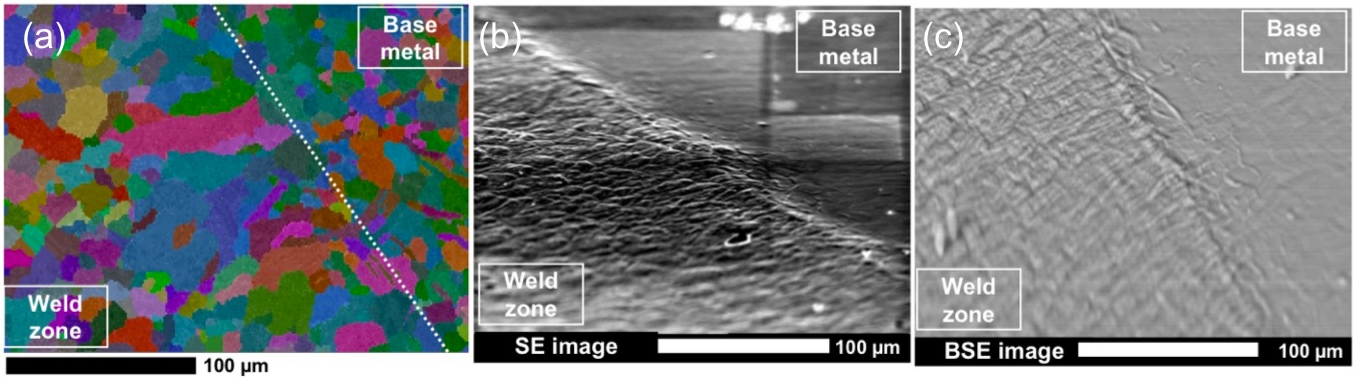

Figure 5.32: Grain size determination using EBSD of Nd:YAG LBW fusion zone (2.4 kW, 7000 mm/min): (a) All Euler EBSD map, (b) SE image and (c) BSE image of the analysed area.

The grain size in the fusion zone increased with increasing heat input (Figure 5.33). Indeed, increasing heat input will reduce the cooling rate, then allowing grain growth. Quan et al.[113] reported that, increasing heat input will also influence the precipitation, causing the $Mg_{17}(Al-Zn)_{12}$ location to change from being intragranularly scattered to intergranularly segregated. This was not observed in this study (Figure 5.34). As CO_2 laser presents a larger power density than Nd:YAG laser, some microstructural differences should arise between weld microstructures using these processes. A similar 10 μm grain size was observed in both fusion zones of LBW produced using CO_2 and Nd:YAG laser for a heat input of 20 J/mm. This is in contradiction with previous work [66] which found coarser grains in CO_2 laser welds compared to Nd:YAG laser welds of 1.7 mm thick wrought AZ31B-H24 butt joints.

5.2.8 Conclusion

The microstructure observed for each zone is summarized in Table 5.1.

5.3 Texture evolution

5.3.1 Introduction

The AZ31 base metal was in hot rolled condition. Using this deformation process, highly textured resulting material was expected. FSW and LBW induced high temperature and deformation gradients which may cause changes in crystalline orientations. The study of the texture evolution is then required to understand the anisotropic characteristic of the welds and its influence on mechanical properties. The texture of the base metal and the texture evolution in FSWelds and LBWelds was studied using several techniques: XRD, EBSD and Neutron Diffraction.

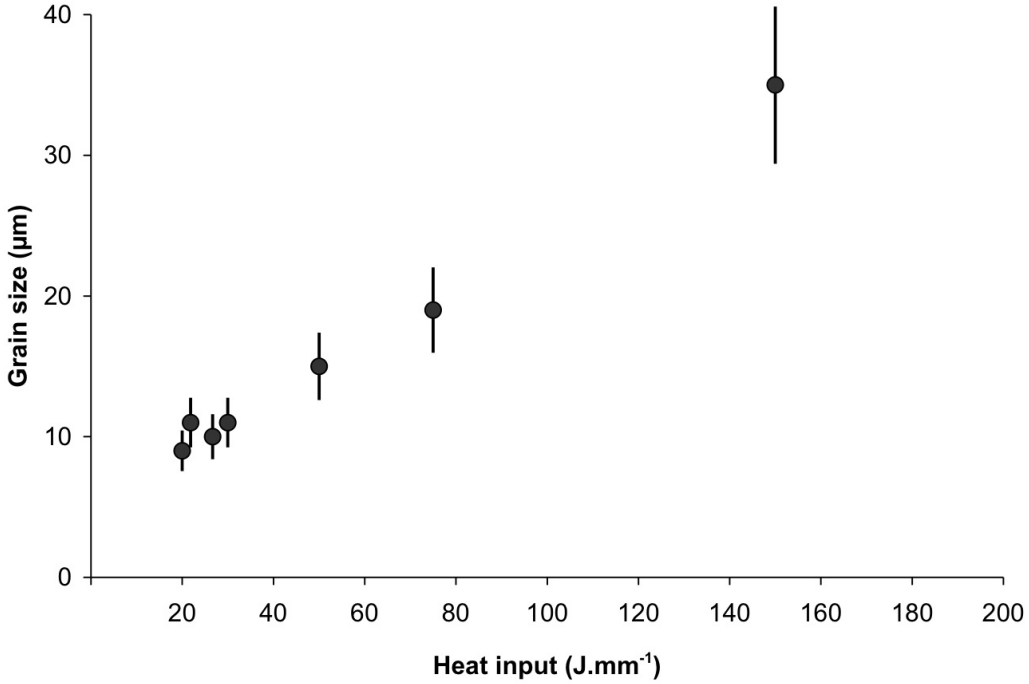

Figure 5.33: Evolution of CO_2 LBW fusion zone grain size with heat input.

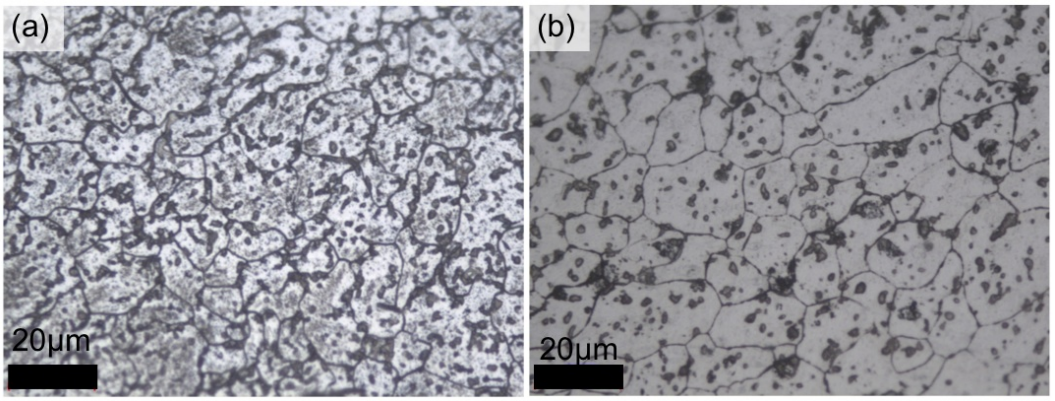

Figure 5.34: Optical Micrograph of CO_2 LBW fusion zone grain size processed at several heat input: (a) H=50 J/mm (P=1.5 kW,V=1800 mm/min), (b) H=150 J/mm (P=1.5 kW,V=600 mm/min).

Zone	Grain microstructure	Precipitation	Tmax (°C)
Base metal	10 μm equiaxed grains, few twins	3-10 μm intergranular Al_8Mn_5, nanosized intragranular Al_8Mn_5	300°C annealing
Heat treated sample 550°C 1h	2 mm large grains, 10 μm recrystallised grains, few twins	3-10 μm intergranular Al_8Mn_5, needle shaped 500 nm nanosized intragranular Al_8Mn_5	550°C
HAZ	10 μm equiaxed grains, few twins shear bands	3-10 μm intergranular Al_8Mn_5, 3-10 μm nanosized intragranular Al_8Mn_5	200-400°C
FSW TMAZ	10 μm not fully recrystallised grains, few twins	3-10 μm intergranular Al_8Mn_5, nanosized intragranular Al_8Mn_5	500°C
FSW nugget	fine equiaxed grains, few twins	3-10 μm intergranular Al_8Mn_5, nanosized intragranular Al_8Mn_5	500°C
LBW fusion zone	10 μm equiaxed grains, few twins	3-10 μm intergranular Al_8Mn_5, nanosized intragranular Al_8Mn_5 β $Mg_{17}(Al,Zn)_{12}$	665°C

Table 5.1: Microstructure observed.

5.3.2 Base metal texture

In-depth XRD analysis was performed from top surface to mid-thickness (Figure 5.35). The base metal pole figures showed a strong texture, with the {0002} basal plane normals parallel to the normal direction (ND), which is the typical hot rolling texture of magnesium alloys [53, 4]. The in-depth texture variation showed that the orientation was similar but sligthly elongated fiber pattern was found close to the surface.

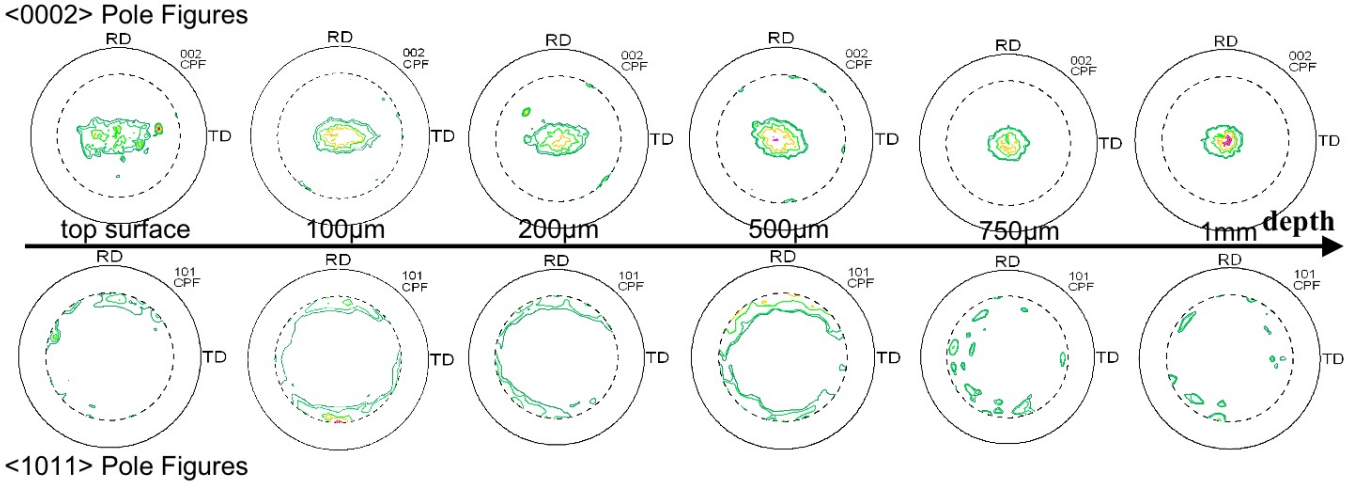

Figure 5.35: XRD Pole figures of AZ31 base metal.

5.3.3 FSW texture evolution

During FSW, the heat input and plastic deformations caused by the tool are influencing the texture of the material.

5.3.3.1 Neutron diffraction

Texture analysis was performed using ILL-D1B instrument. The welded zone is 10 mm wide. Measurements were made in the nugget, in the HAZ (TMAZ/base metal boundary) and in the base metal. Average through thickness textures were obtained for each zone studied. The {0002} strong basal texture was still prevalent within the weld zone and did not seem to be strongly affected by the mechanical and heat input induced by the FSW process (Figure 5.36). The measurements were done averaging through thickness, then the texture and the microstructure is assumed to be the same within the thickness. But texture gradients and microstructural zone changes (nugget on the top surface to base metal on the bottom surface and TMAZ in between) can occur in the areas studied, which were not taken into account. This could explain the uniformity of the results obtained. Neutron diffraction analysis was also performed using ILL-SALSA

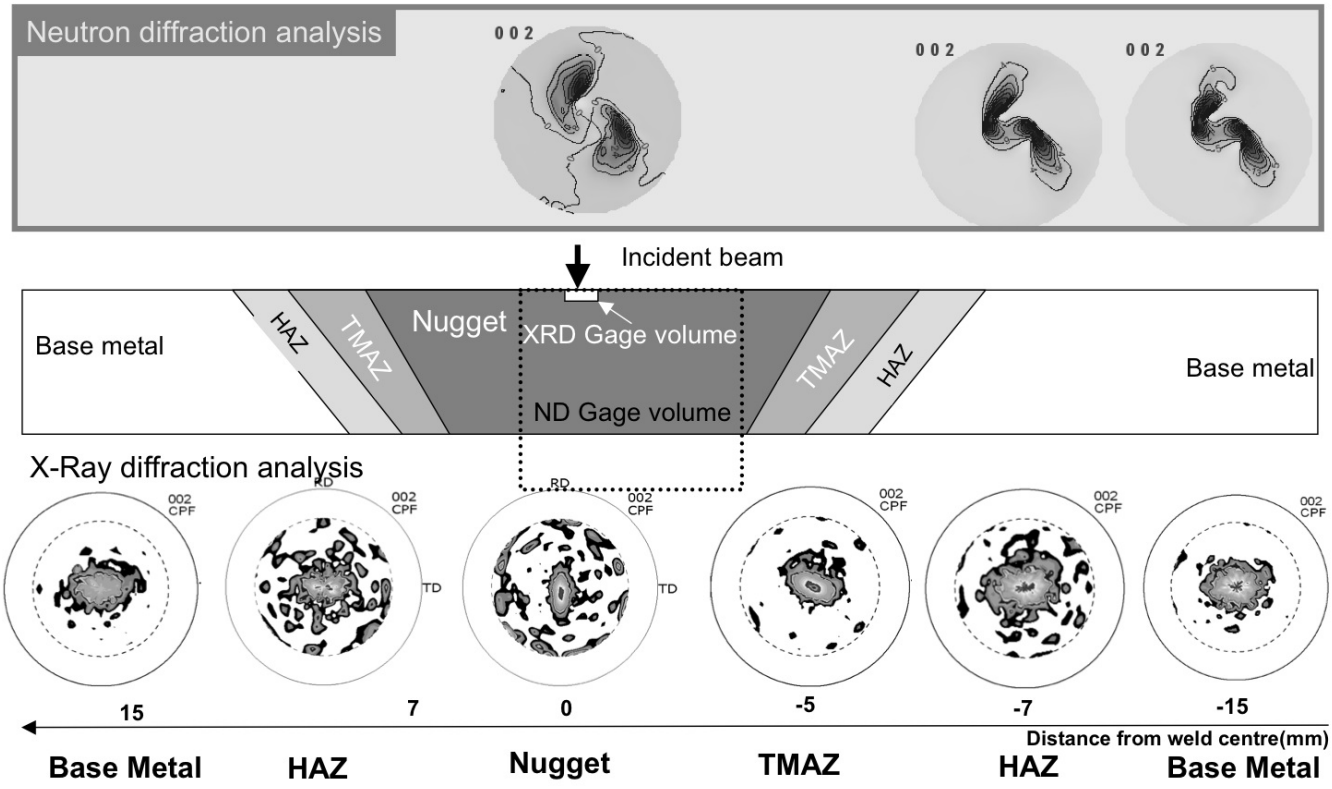

Figure 5.36: Neutron diffraction and XRD Pole figures of FSW.

instrument through a mid-thickness profile across the FSWeld. The intensity of a diffraction peak is related to the texture. The analysis of $\{11\bar{2}2\}$ and {201} diffraction peaks exhibited an

evolution of the intensity across the weld whereas the intensity of each peak remained constant in the base metal (Figure 5.37). This showed that there was a high texture change across the weld.

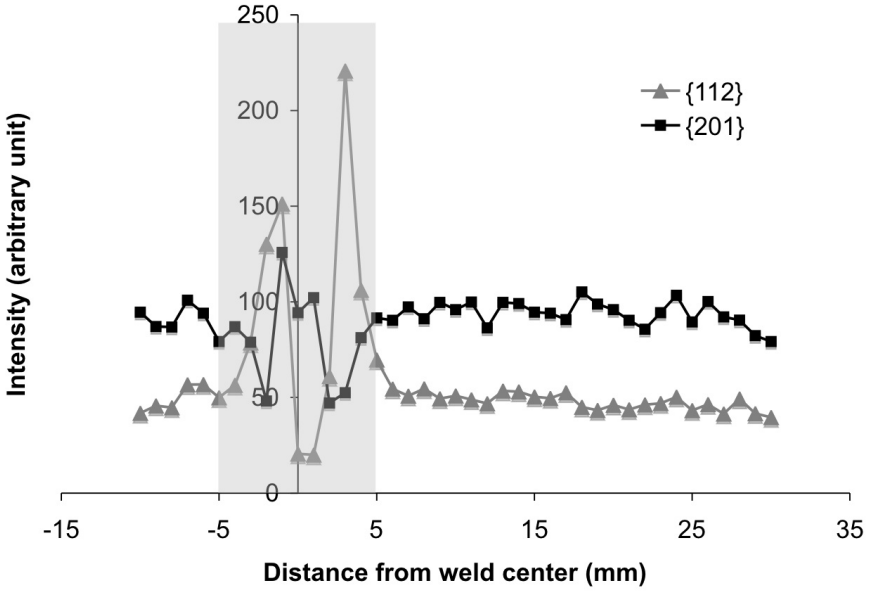

Figure 5.37: Evolution of diffracted intensity across FSW, the shaded area corresponds to the weld zone.

This is consistent with Woo et al. [4] who observed a texture evolution within FSW AZ31 hot rolled sheet (see section 2.6.5). Their investigation showed that the basal plane normal was parallel to the transverse direction (TD) in the TMAZ. In the nugget, the texture was influenced by the plastic deformation and the basal plane normal followed the pin rotation and aligned with the welding direction in the weld centre.

5.3.3.2 X-ray diffraction (XRD)

Superficial texture analysis was performed using laboratory XRD. No change in crystalline orientations between the FSW zones was observed (Figure 5.36). As the analysis was performed on the FSW top surface, this texture is characteristic of the shoulder effect. Indeed, the basal texture observed on the weld top surface might be caused by the mechanical and thermal input of the shoulder. Al-Samman et al. [103] reported that using macrotexture analysis to study recrystallization texture in magnesium is quite difficult, due to the sixfold rotation symmetry in the basal plane especially in the case of a strong basal fiber texture, which is the case in this study. Indeed, depending on the activation of slip systems in the basal plane ($<11\bar{2}0>$ RD or $<10\bar{1}0>$RD) texture component will form, both of which are related by a $30^{\circ}<0001>$ rotation. When having a basal fiber texture, i.e. the two main deformation components $\{0001\}<11\bar{2}0>$ and $\{0001\}<10\bar{1}0>$ and their scatter generating a $\{0001\}$ fiber texture, it is not possible to recognize any texture change even in a $<10\bar{1}0>$ pole figure.

5.3.3.3 Electron Back Scattered Diffraction (EBSD)

EBSD was used to study the local texture evolution. The analysis was performed 100 μm below the top surface (mechanical polishing removal) and then the microstructure observed was characteristic of the FSW and not of the special microstructure underlaying the soulder. This could explain the different results obtained between XRD and EBSD analysis. EBSD maps with 72% indexation was reached. Previous studies published on AZ31 EBSD could only reach 40% indexation [115]. Figure 5.38 shows the IPF (inverse pole figure) map of FSW from base metal to nugget. In the base metal area all the grains exhibited a green to blue colouring which confirmed that the {0002} basal plane normals was parallel to the sample normal direction. In the TMAZ, some grains with a red colouring were progressively appearing and then, all the grains exhibited a red colouring in the nugget. This demonstrated that the grain {0002} basal plane normals aligned to the welding direction with FSW. These results are consistent with Woo et al. study [4]. The temperature gradient and the mechanical input induced by the tool pin motion were then influencing the texture after FSW.

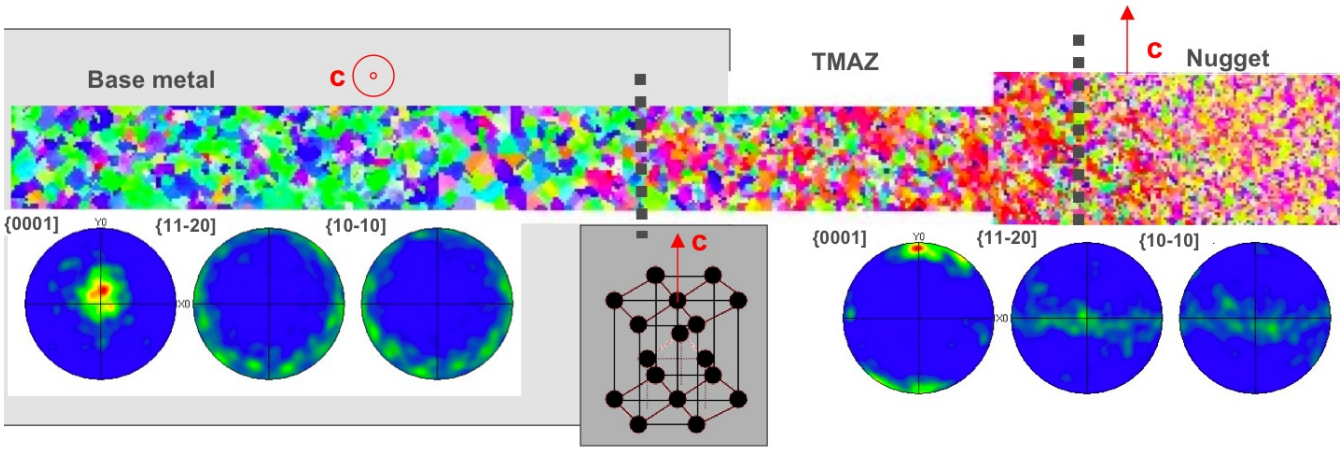

Figure 5.38: EBSD maps of FSW top surface and corresponding calculated pole figures.

5.3.4 LBW texture evolution

During LBW, the temperature gradients during solidification are influencing the texture of the material. Neutron diffraction techniques could not be used because the fusion zone was too narrow for the slits available, then the base metal would also have diffracted, making the results useless. XRD and EBSD were used to analyse the texture evolution in LBW. A 70% indexation was reached to build the EBSD maps. IPF (inverse pole figure) colouring was used. XRD and EBSD results showed that the material in the fusion zone is not textured (Figure 5.39). The grains in the base metal area exhibit a red colouring, then the {0002} basal plane normals was parallel to the sample normal direction, as the analysis was performed in the sample section. Then, a random colouring is obtained in the fusion zone characterizing a random orientation of equiaxed grains which was consecutive to the new grain formation during solidification. This is consistent with Coelho et al. study [3].

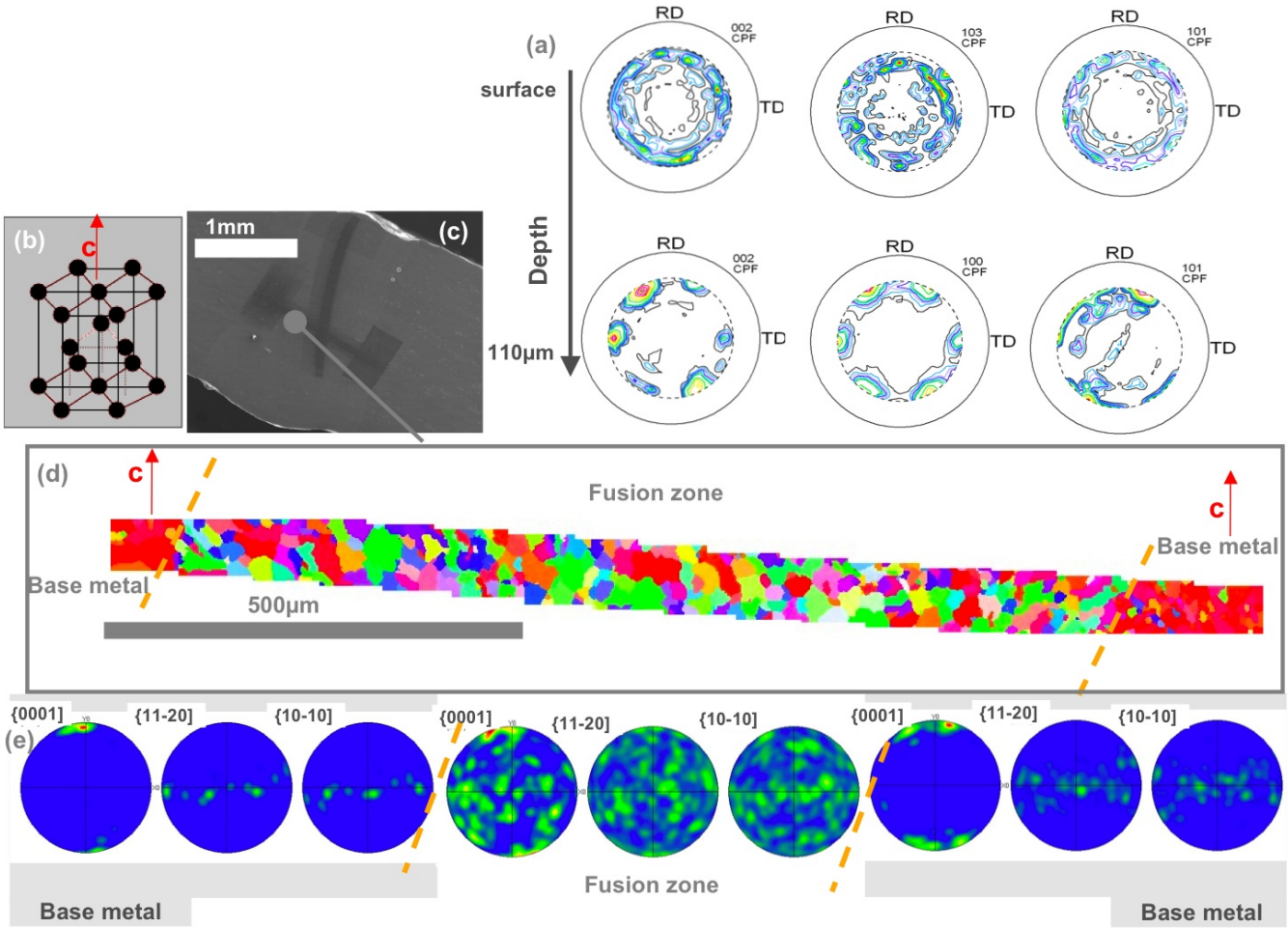

Figure 5.39: (a) XRD Pole figures of LBW fusion zone, (b) sketch of the hcp crystal (c) EBSD analysis location in the mid-thickness weld section, through the weld width, (d) EBSD maps of LBW section (IPF colouring) and (e) corresponding pole figures.

5.3.5 Grain misorientations in FSW

During FSW due to the high strains and temperatures undergone, dynamic recrystallisation occurs. The nugget grain size suggested that subgrain formation occured and then that this was rather due to a continuous dynamic recrystallisation than to a discontinuous recrystallisation process [8, 101]. The increase in grain misorientation angles is related to dislocation absorption by subgrain boundaries [101] and then to the deformation undergone. The misorientation profiles in the nugget area and in the base metal area were calculated using EBSD (Figure 5.40). Misorientation angles lower than 1.5°were considered as orientation noise and then they were not taken into account. High Angle Grain Boundaries (HAGB) were defined as being superior to 15°[101]. The amount of HAGB increased with increasing deformation from the Base metal area to the TMAZ. The nugget presented a majority of low angle boundaries, as the grains are re-

cystallised. The misorientation angle did not significantly increase with increasing deformation. The migration of HAGB with increasing dislocation density resulting in subgrains formation which is characteristic of continuous dynamic recrystallisation is not obviously observed in this case.

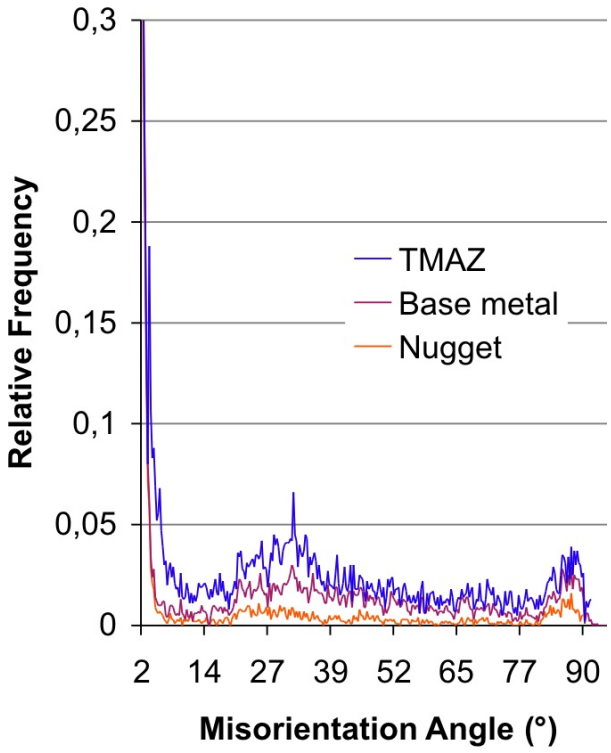

Figure 5.40: Misorientation angle distribution in FSW.

5.3.6 Conclusion

A strong {0002} fiber texture was observed in base metal caused by the hot rolling process. The texture was influenced by the welding process. FSW resulted in aligning the {0002} fiber texture with the welding direction whereas LBW produced randomly oriented grains in the fusion zone.

5.4 Residual stress evolution

5.4.1 Introduction

Residual stress analysis was performed on the AZ31 base metal and then, the influence of the welding process on residual stresses was studied.

5.4.2 Influence of the material anisotropy

Texture analysis has shown that AZ31 base metal presented a strong {0002} basal texture (see previous section). The elastic anisotropy of AZ31 alloy was investigated to determine the influence of specific orientations on the residual stresses in magnesium alloy polycrystalline structures. Magnesium alloys exhibit a hexagonal close packed structure, with an orthotropic symmetry. In the generalized case, the Hooke's law may be expressed as:

$$\sigma_{ij} = C_{ijkl}\epsilon_{kl} \tag{5.1}$$

$$\epsilon_{ij} = S_{ijkl}\sigma_{kl} \tag{5.2}$$

The elastic constants tensor in the orthotropic case can be represented by

$$C_{ij} = \begin{pmatrix} C_{11} & C_{12} & C_{13} & 0 & 0 & 0 \\ C_{12} & C_{22} & C_{23} & 0 & 0 & 0 \\ C_{13} & C_{23} & C_{33} & 0 & 0 & 0 \\ 0 & 0 & 0 & C_{44} & 0 & 0 \\ 0 & 0 & 0 & 0 & C_{55} & 0 \\ 0 & 0 & 0 & 0 & 0 & C_{66} \end{pmatrix} \tag{5.3}$$

The Young Modulus can be expressed in cartesian coordinates by:

$$1/E_n = S_{11} - ((S_{11} - S_{33})a_3^2 + (2S_{11} - 2S_{13} - S_{44})(a_1^2 + a_2^2))a_3^2 \tag{5.4}$$

with a_1, a_2 and a_3 the director cosines. For the magnesium singlecrystal, the elastic constant tensor at 295K is given by [131]:

$$C_{ij} = \begin{pmatrix} 0.597 & 0.262 & 0.217 & 0 & 0 & 0 \\ 0.262 & 0.597 & 0.217 & 0 & 0 & 0 \\ 0.217 & 0.217 & 0.617 & 0 & 0 & 0 \\ 0 & 0 & 0 & 0.164 & 0 & 0 \\ 0 & 0 & 0 & 0 & 0.164 & 0 \\ 0 & 0 & 0 & 0 & 0 & 0.1675 \end{pmatrix} \tag{5.5}$$

Calculating with Contex software [132] the elastic constant tensor for the isotropic polycrystal with Kroner Eshelby using 3000 crystallites, we get:

$$C_{ij} = \begin{pmatrix} 0.74876 & 0.41798 & 0.41798 & 0 & 0 & 0 \\ 0.41798 & 0.74876 & 0.41798 & 0 & 0 & 0 \\ 0.41798 & 0.41798 & 0.74876 & 0 & 0 & 0 \\ 0 & 0 & 0 & 0.16539 & 0 & 0 \\ 0 & 0 & 0 & 0 & 0.16539 & 0 \\ 0 & 0 & 0 & 0 & 0 & 0.16539 \end{pmatrix} \tag{5.6}$$

Then taking into account the Orientation Distribution Functions (ODF) mesured experimentally, the elastic constant tensor of AZ31 can be calculated:

$$C_{ij} = \begin{pmatrix} 0.6286 & 0.2438 & 0.2357 & 0.0002 & -0.0001 & -0.0001 \\ 0.2438 & 0.74876 & 0.2357 & 0.0002 & 0.0001 & 0.0001 \\ 0.2438 & 0.2357 & 0.6333 & -0.0003 & 0.0001 & 0 \\ 0.0002 & 0.0002 & -0.0003 & 0.1935 & 0 & 0.0001 \\ -0.0001 & 0.0001 & 0.0001 & 0 & 0.1906 & 0.001 \\ -0.0001 & 0.0001 & 0 & 0.0001 & 0.0001 & 0.1918 \end{pmatrix} \tag{5.7}$$

If the Young Modulus is plotted in the cartesian coordinates, the elastic anisotropy can be illustrated. Figure 5.41 shows the Young Modulus anisotropy for the magnesium singlecrystal, for the magnesium isotropic polycrystal and for hot rolled AZ31. These results show that

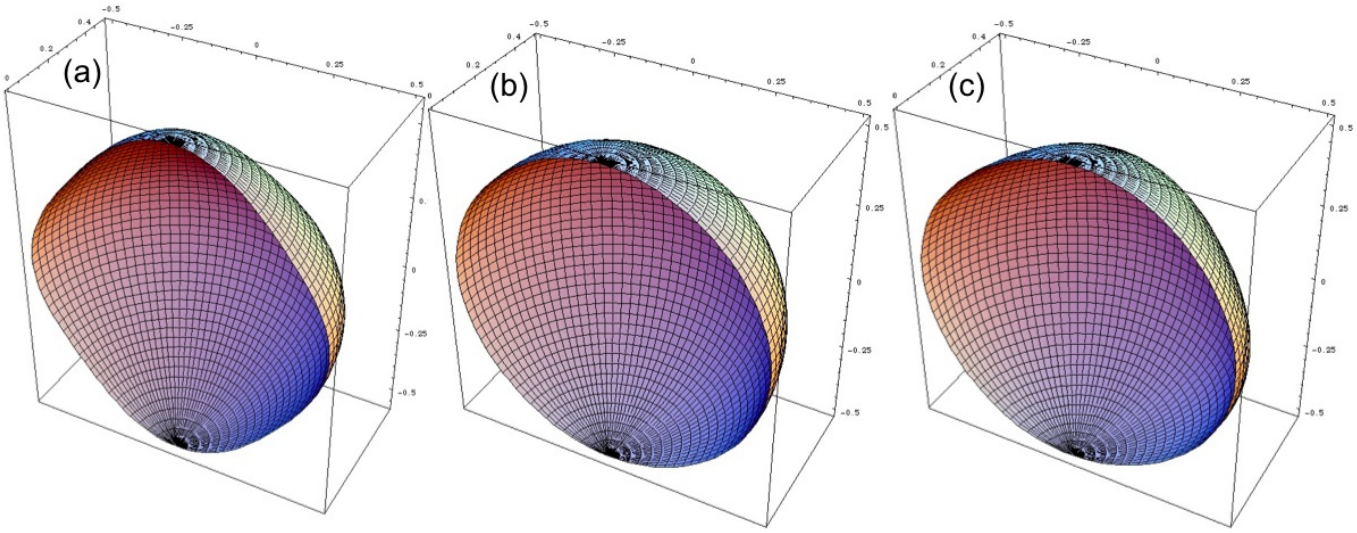

Figure 5.41: Young's modulus of (a) Magnesium singlecrystal, (b) Magnesium isotropic polycristal and (c) hot rolled AZ31.

although the Mg singlecrystal is anisotropic, polycrystalline AZ31 alloy exhibits a relatively weak anisotropy. Then, besides magnesium alloy can exhibit a strong texture, its effect on the residual stress determination is limited.

5.4.3 Residual stresses in AZ31 base metal

AZ31 base metal residual stresses were determined experimentally using X-Ray Diffraction. Residual stresses were calculated using the $\sin^2\Psi$ method on the {104} plane. In-depth measurements were made from top surface to 500 μm below the surface. The stress tensors were calculated with and without taking into account the Orientation Distribution Functions (ODF) determined by the texture analysis. Figure 5.42 shows each stress component versus the measurement depth. Low compressive residual stresses are observed in the longitudinal and transverse direction and the variation between surface and in-depth results is very low. It can be observed that the difference between the isotropic calculation and the anisotropic calculation is within

the error bar. This result illustrates the limited influence of elastic anisotropy determined in the previous section.

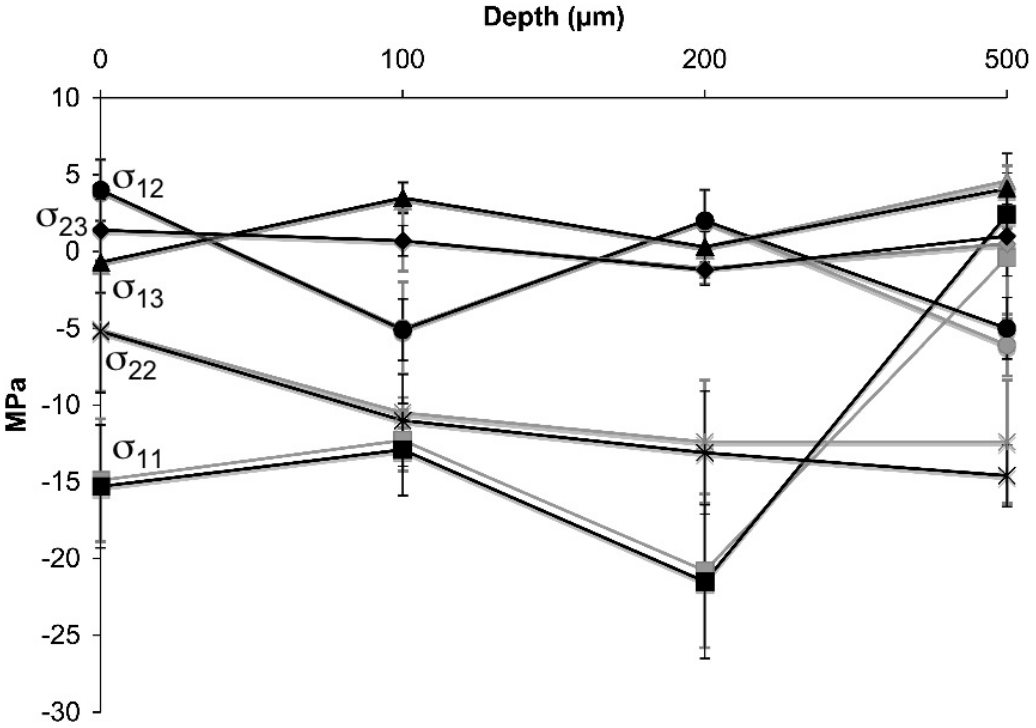

Figure 5.42: Base metal residual stress tensor components versus measurement depth, in grey the calculation without taking into account the ODF and in black the calculation taking into account the ODF.

Then, for the further residual stress analysis, the influence of the anisotropy will be neglected and stress calculations will be done without taking into account the ODF.

5.4.4 Residual stresses induced by FSW

5.4.4.1 Strain gages

In situ strain measurements were performed during the FSW processing using strain gages. If the material underneath the strain gages does not undergo plastic deformation, there is only an elastic part of the deformation which is measured and that can be directly linked to residual stresses. Then, residual stress analysis was performed using the strain gage data recorded during welding and by XRD after welding. Figure 5.43 shows the evolution of the equivalent stress and the hydrostatic stress during welding. The strain gages overcharged (peak values) when the tool passed across, and then, they reached a constant residual stress level. XRD was carried out after welding at the same measurement locations (± 4 mm from weld seam). XRD and strain gage results gave the same tendancy (Figure 5.43). The differences can be explained by the fact that they are both superficial analysis but the gage volume is much smaller in XRD. Then there is

a relative good agreement between the XRD and strain gage results, both showing that higher stress levels are induced on the retreating side.

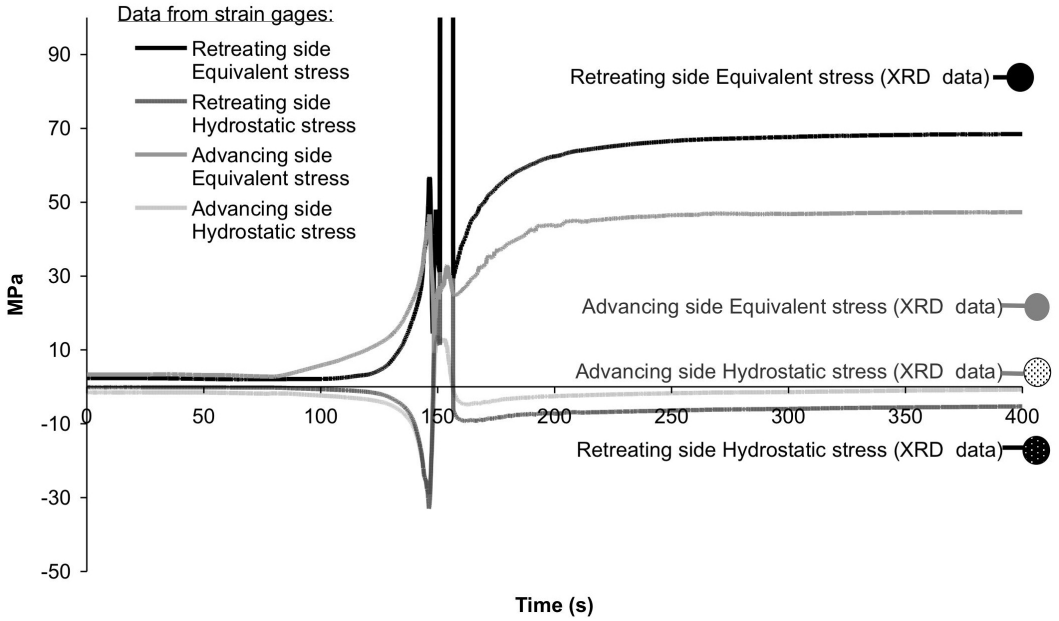

Figure 5.43: Comparison between the stress evolutions during welding (strain gages) with the XRD results for FSW (1000 RPM, 200 mm/min, tool 5 mm pin / 13 mm shoulder).

5.4.4.2 X-ray diffraction (XRD)

The residual stress evolution across the FSW was studied using XRD and the measurements were performed on the top surface, on the bottom surface and in the mid-thickness. For mid-thickness measurements, material removal using electro-chemical polishing was performed. Figure 5.44 shows the evolution of equivalent and hydrostatic stresses. The superficial residual stresses are higher than the residual stresses in the bulk material and the highest residual stresses were obtained in the TMAZ.

The residual stress values reached in AZ31 using FSW are higher than the ones that would be obtained using laser welding process [3]. Due to the low temperature gradients observed in FSW compared to fusion welding processes, such as laser welding, lower residual stresses would be expected. But, FSW requires a far more rigid clamping, which causes the residual stress generation during cooling. In comparison to aluminium alloys, the residual stress level obtained after FSW is in the same range (below 100 MPa [106, 107]), but it corresponds to 30-60% of FSW yield stress and 20-50% of base metal yield stress [106] in the case of aluminium alloys, whereas in AZ31 it corresponds to 66-76% of FSW yield stress and 46% of base metal yield stress.

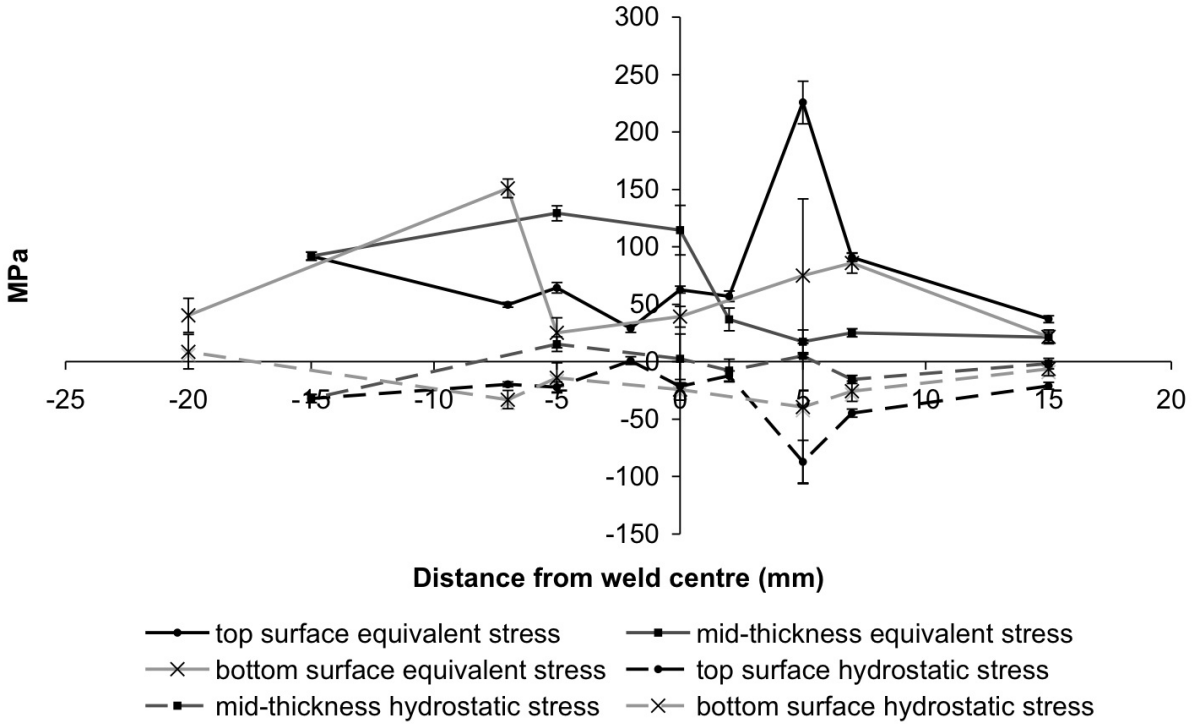

Figure 5.44: XRD Equivalent stress and Hydrostatic stress evolution across FSWeld (1000 RPM, 200 mm/min, tool 5 mm pin / 10 mm shoulder).

5.4.4.3 Neutron Diffraction

When using XRD, it was not possible to determine depth related variations, without matter removal. Moreover, it was observed that the complex thermomechanical input induced complex stress gradients. Then the high penetration capability of neutron diffraction technique was used to determine stress profiles through the thickness and along the weld width. Residual stress analysis was performed with HMI-E3 instrument with a 0.135 nm wavelength and 1×1×40 mm slits. Measurements were then performed in the transverse direction. The longitudinal direction measurements could not be performed in the beam time allowed, because the neutron flux would have been too low using the 1×1×1 mm slits needed to reduce stress gradients in the gage volume. Stress map across the weld width and within the weld thickness was built using $\{11\bar{2}4\}$ plane. The gage volume is very large compared to the sample dimension (2 mm thick) and then the results obtained are averaged. The stress gradients could be determined by the extrapolation of the measurements. Figure 5.45 shows the contour plot of the stress map. The grey areas are the locations where the fitting operation could not be correctly fulfilled. High compressive stresses are observed in the middle of the nugget and slightly tensile stresses are observed in the TMAZ area.

Residual stress analysis was performed with ILL-SALSA instrument with a 0.16457 nm wavelength and 0.6 mm slits to get a better resolution. Analysis was performed in the mid-

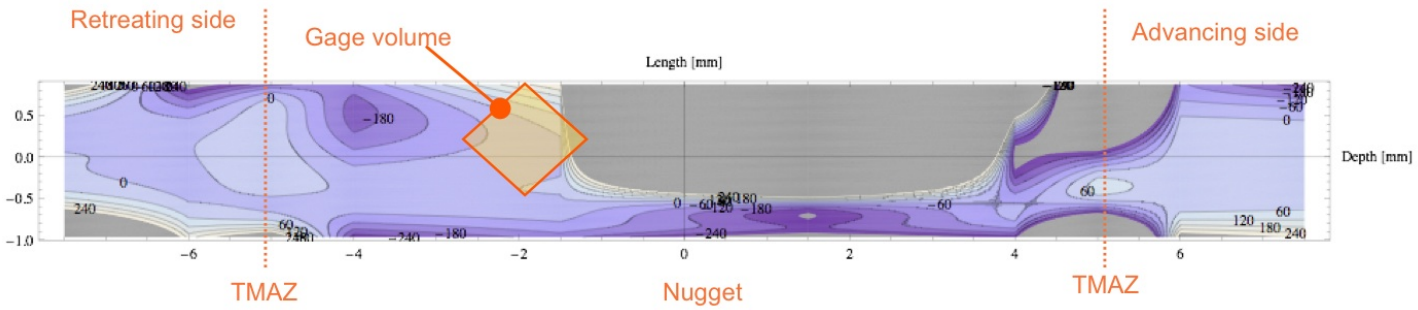

Figure 5.45: Stress map across FSWeld.

thickness across the weld. The 2θ window allowed the analysis of both $\{11\bar{2}2\}$ and $\{21\bar{3}0\}$ planes. Longitudinal and transverse stresses were determined and the normal stresses were assumed to be 0. The stresses calculation was performed using the (3.3) equation (see Experimental section). Figure 5.46 shows the results obtained. A good agreement is observed between the two plane results. The mean value of the results for the two planes was taken into account (Figure 5.47). A large variation is observed in longitudinal stresses. Low longitudinal compressive stresses are observed in the base metal and in the center of FSW, whereas tensile stresses are observed in the TMAZ. This is the well known "M" shape generally described in FSW longitudinal residual stresses [17]. An increase in the compressive transverse stresses is observed in the FSW nugget. Higher stresses were observed on the advancing side than on the retreating side. This is due to the lower temperature generated on the advancing side, leading to a temperature gradient occuring in a narrower zone and then higher residual stresses generated. This is consistent with previous studies [17, 106, 107].

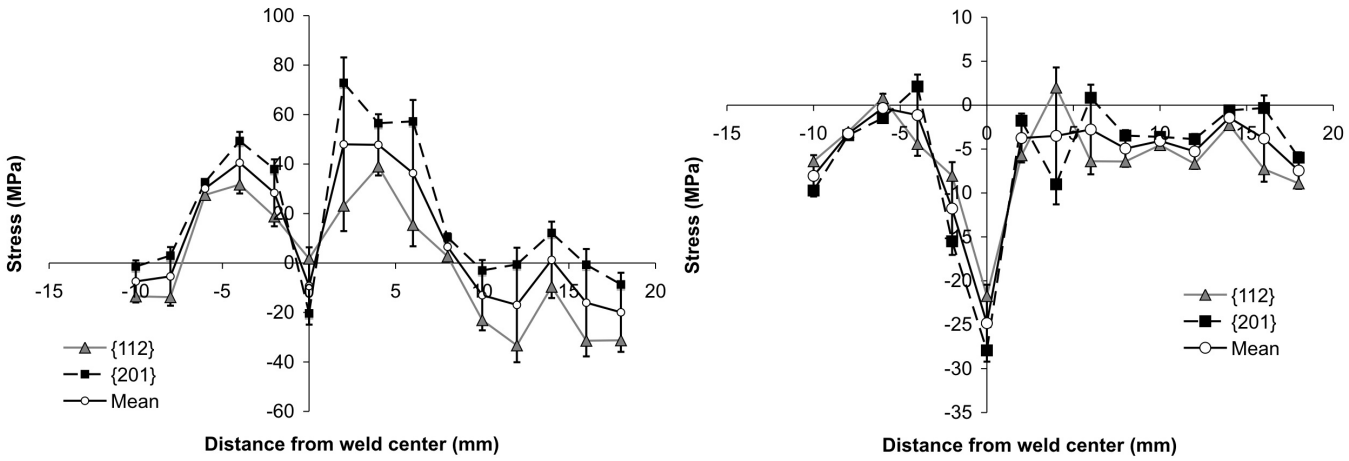

Figure 5.46: Longitudinal stress evolution and transverse stress evolution across FSWelds.

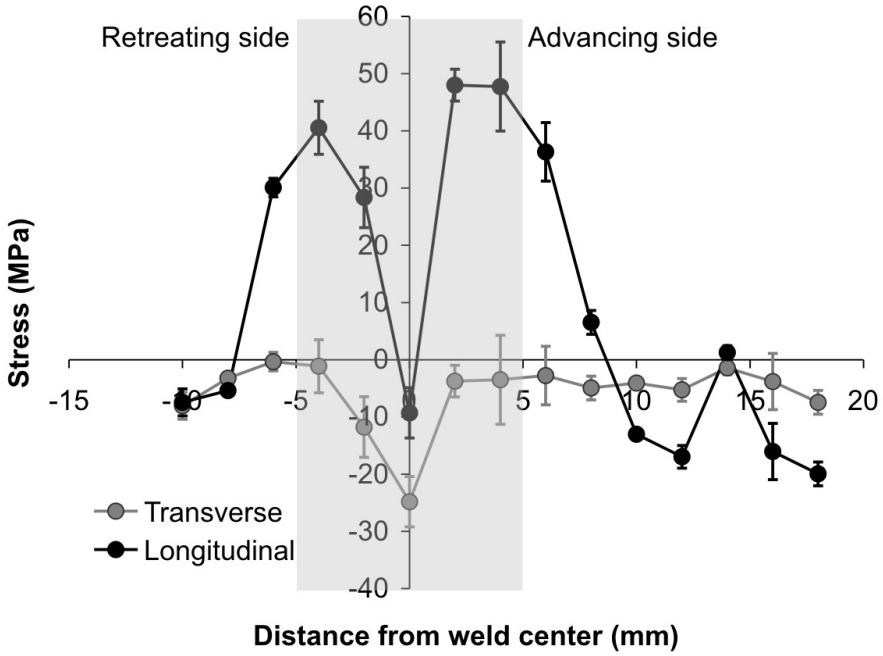

Figure 5.47: Residual stress evolution across FSWelds, the shaded area corresponds to the weld zone.

5.4.5 Comparison between the methods used

The FSW residual stresses were determined using several experimental techniques and the results showed the same tendancies. The results obtained using $\sin^2\psi$ methods (HMI-E3) and triaxial method (ILL-SALSA) were in good agreement. XRD results revealed higher residual stress values. The residual stress analysis is a mean value among a gage volume which is far smaller in XRD than in neutron diffraction. Moreover, the XRD experiments were performed on the weld top surface, exhibiting then also the shoulder contribution.

5.4.6 Residual stresses induced by LBW

LBW residual stress analysis was performed using a tape mask to define the gage volume. As the fusion zone is very narrow, the gage volume was too small to use neutron diffraction technique. Previous studies showed that in-depth residual stresses obtained in the fusion zone were similar to the ones obtained on the surface [3]. Then, superficial X-Ray diffraction analysis was performed. The residual stress determination in the fusion zone was quite difficult because the diffracted signal was very weak. This was due to the very small gage volume size (use of a tape mask) and the poor diffusion of Mg atoms. Figure 5.48 shows that whereas compressive stresses were observed in the base metal, tensile stresses were obtained in the fusion zone. This was attributed to the shrinkage during rapid cooling. These results are consistent with AZ31 LBW Coelho et al. study [3] which observed 40 MPa tensile residual stresses in the fusion zone.

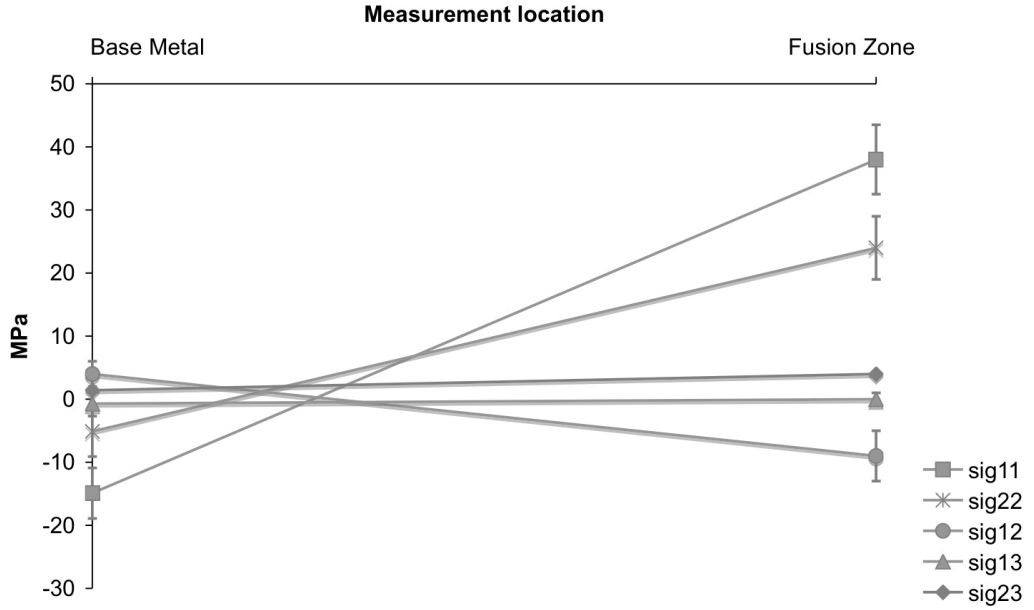

Figure 5.48: Residual stress evolution between base metal and LBW fusion zone.

5.4.7 Conclusion

The welding processes influenced the residual stress distribution. Whereas compressive stresses are obtained in the base metal, tensile stresses are obtained in the LBWelds due to thermal gradients and high residual stresses are observed in the FSW TMAZ. An assymmetry between the advancing side and the retreating side is observed in FSW. The higher residual stresses in FSW are attributed to the clamping.

5.5 Evolution of mechanical properties

5.5.1 Introduction

The evolution of microhardness and tensile properties was studied for LBW and FSW. Then, several post-weld heat treatments were performed to get an improvement of mechanical properties.

5.5.2 FSW microhardness evolution

The influence of FSW and its welding parameters on the microhardness evolution is characterised in Figure 5.49. Using high (W/V) a very low variation in microhardness values compared to the base metal ones, whereas, using low (W/V) induced an increase in the weld zone. As the hardening effect of the nanosized precipitates is not modified during FSW, the hardness evolution is mainly related to the grain size evolution observed. At high (W/V), the grain size was smaller in the nugget than in the base metal, but no variation in microhardness occurred,

but with a further decrease in grain size (obtained at low W/V), higher microhardness values were obtained. From the microstructure and microhardness experimental analysis, we can study the hardening effect due to grain size evolution across the weld. The mean values of grain size and microhardness in each weld zone and the corresponding standard deviation were used. In aluminium alloys FSW, the Hall Petch relationship is generally followed [6, 133]. In this study we can observe that the grain size influence on hardness and then on the yield strength does not follow the Hall-Petch relationship as the correlation factor is very low (Figure 5.50). This is due to the influence of the dislocation density [100] and residual stress variations within the weld.

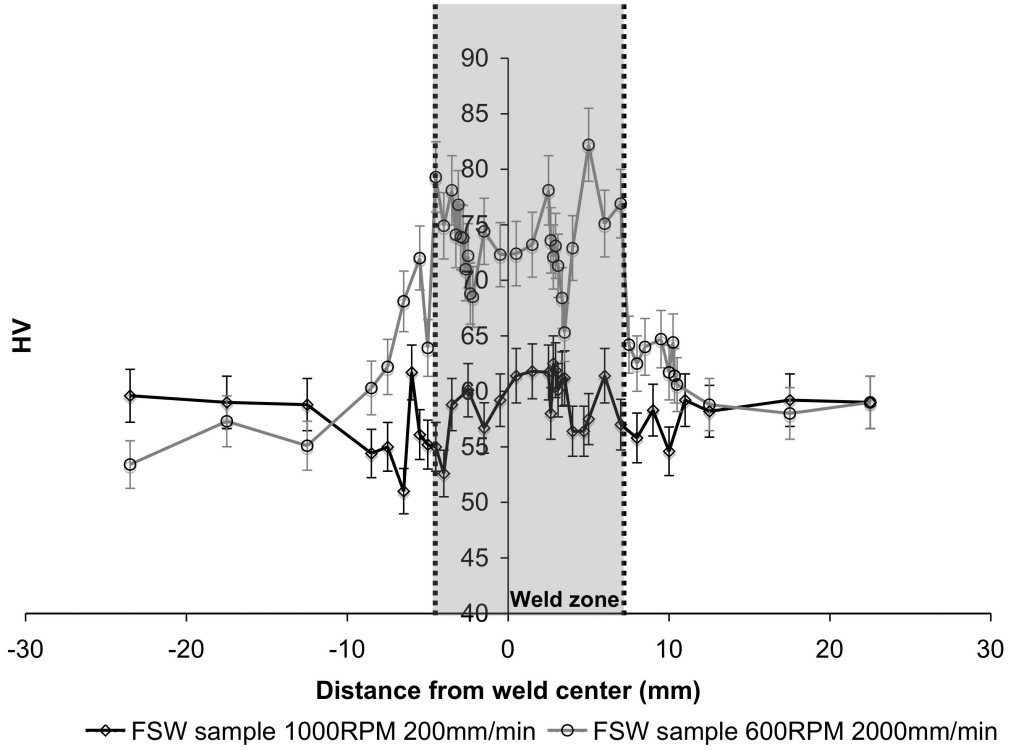

Figure 5.49: Microhardness evolution across FSWelds.

5.5.3 LBW microhardness evolution

Microhardness measurements showed a slight increase in the LBW fusion zone as observed on the HV profiles along the weld in Figure 5.51, which is consistent with previous studies on AZ31 alloy [55, 54, 68] . Microstructure study of the fusion zone (see section 5.2.7) revealed a grain size in the fusion zone similar to the base metal one. So the strengthening in the fusion zone can not be attributed to the grain size. The nanosized Al_8Mn_5 precipitation is not modified. The $Mg_{17}(Al,Zn)_{12}$ precipitation and the twinning occuring in the fusion zone are acting as the hardening mechanisms and could explain the microhardness values in the fusion zone.

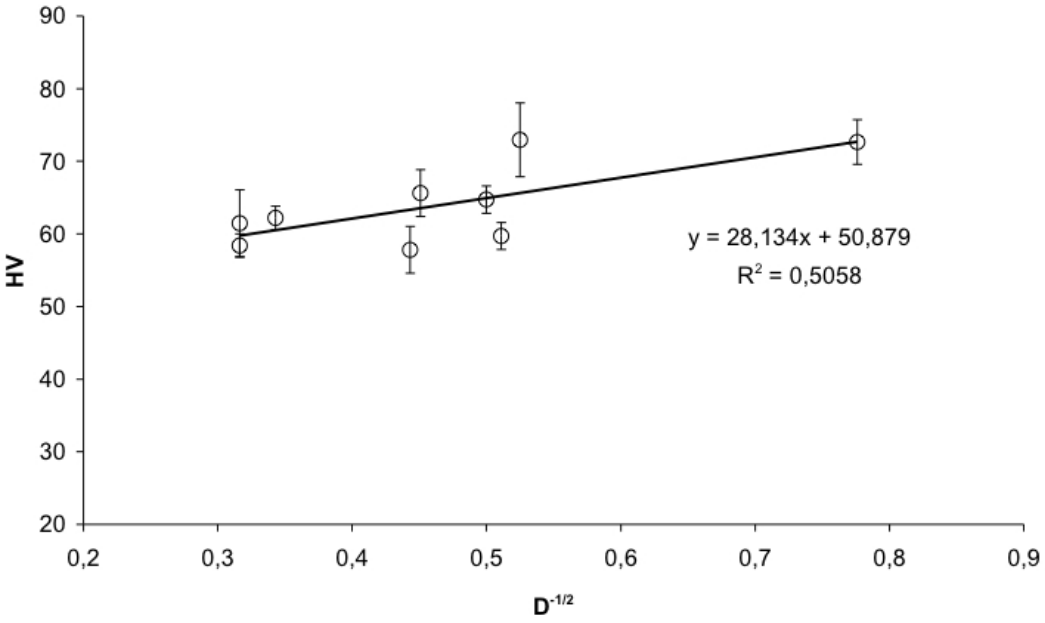

Figure 5.50: Microhardness evolution with grain size in FSWelds.

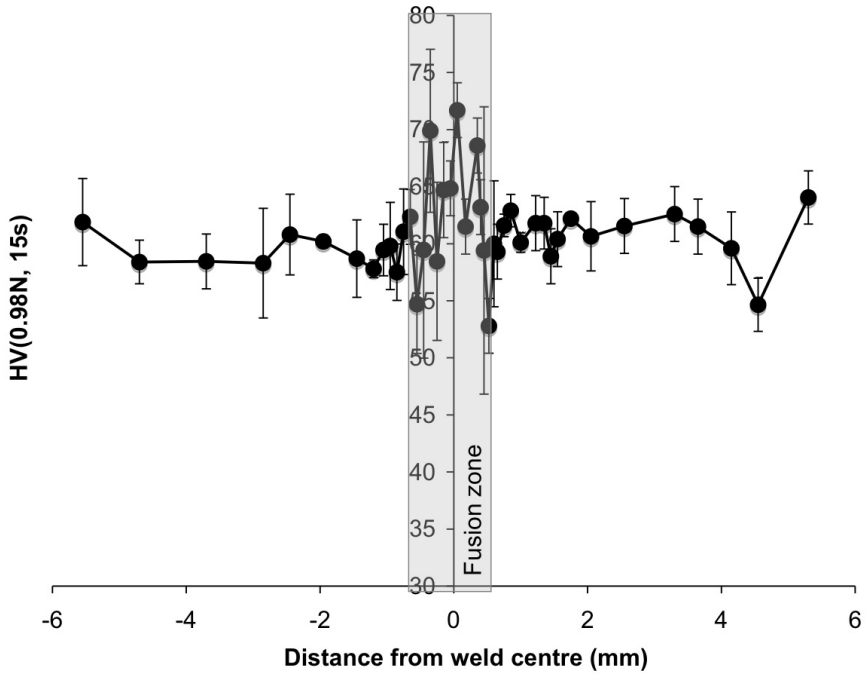

Figure 5.51: Microhardness evolution across LBWelds.

5.5.4 Conventional tensile tests

Tensile test were performed on FSW and LBW butt welds, and base metal AZ31 samples. Figure 5.52 shows the base metal properties. Higher yield stress and ultimate tensile stress are observed when moving away from the rolling direction (RD). Then, an anisotropy of the mechanical properties is observed resulting from the rolling process. FSW resulted in a dramatic loss in all

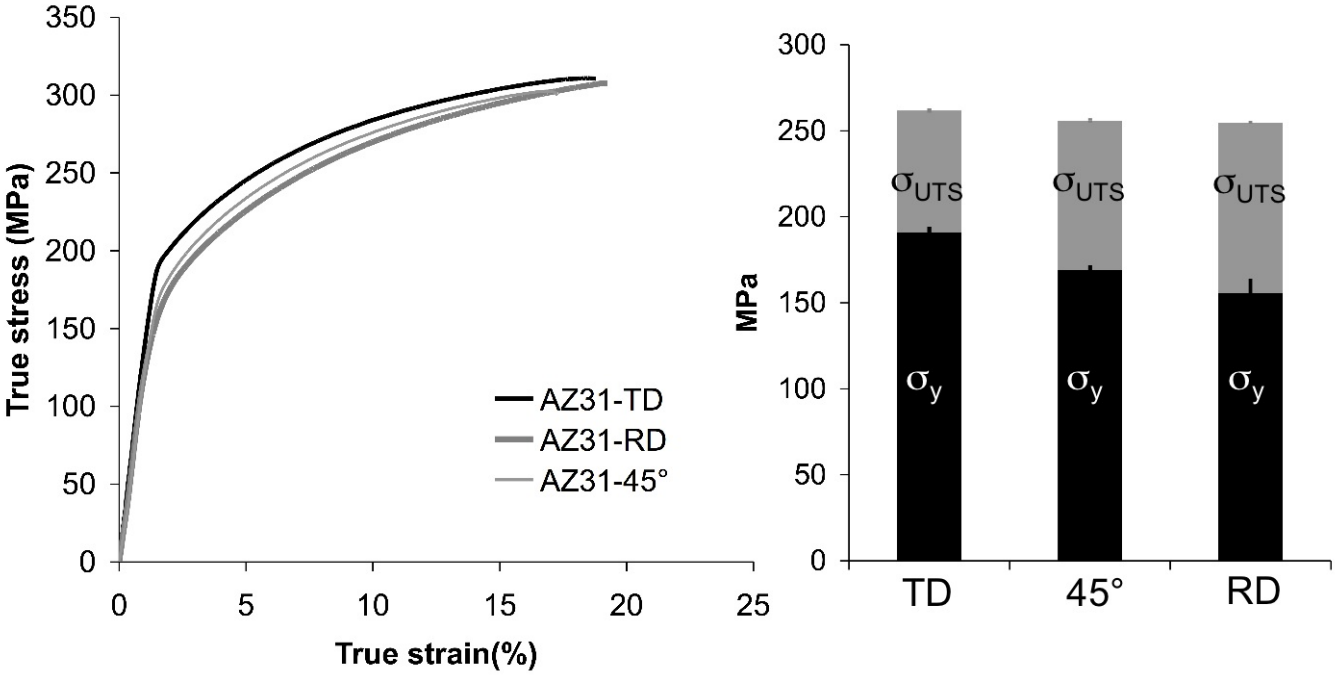

Figure 5.52: Tensile properties of AZ31 base metal in rolling direction, Transverse Direction and 45 °Direction.

the tensile properties (Yield Strength, Ultimate Tensile Strength and Strain to failure) (Figure 5.53), whereas LBW showed similar UTS but lower YS and strain to failure (Figure 5.53). These results are consistent with previous studies on FSW [134] and LBW [68, 3]. For LBW and FSW, the welds tensile mechanical properties were not influenced by the welding parameters used (Figure 5.53). This is consistent with Lim study, which also observed no significant influence of the FSW welding parameters [134]. It was observed in the literature [113] that LBW tensile properties were reduced when increasing heat input because grain growth and intergranular β phase occured . In this study, the process window is quite narrow and then, the welding parameters to produce sound welds led to a quite similar heat input (40-44 J/mmm).Then, the influence of the heat input on tensile properties could not be observed.

For the FSW butt welds, the failure occurred systematically in the TMAZ/nugget transition on the advancing side (see Figure 5.54) except for the (1400 RPM, 700 mm/min) butt weld, which failed on the retreating side of the weld. An additional crack was created on the back surface of the opposite TMAZ/nugget transition. The fracture surface exhibited 3 different zones (Figure 5.55) presenting ductile and brittle fracture features. Brittle fracture occurred on the

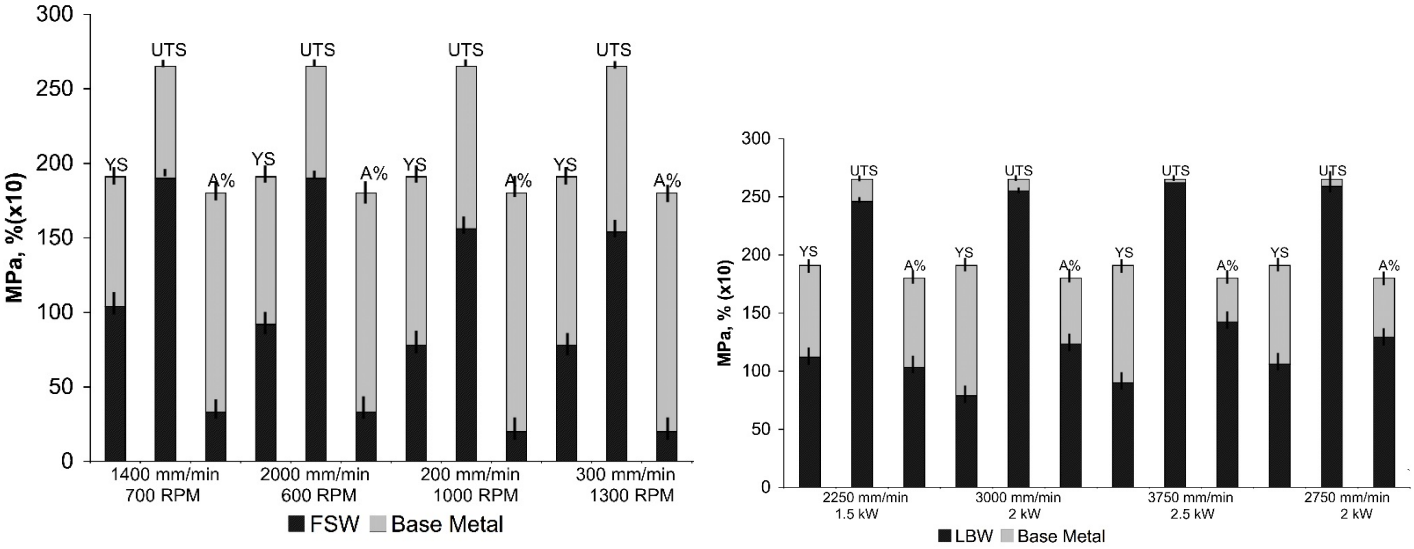

Figure 5.53: Tensile properties of AZ31 FSW and LBW butt welds.

top surface of the weld. This fracture pattern is consistent with other studies and characteristic of AZ31 friction stir welds [134, 135].

For the LBW butt welds the fracture occured in the base metal (Figure 5.56). SEM analysis of the fractographies showed ductile and brittle pattern (Figure 5.57) which is consistent with the fractographies obtained for the base metal tensile tests. The base metal fractographies are exhibited in Figure 5.58 and showed brittle and ductile failure mechanisms.

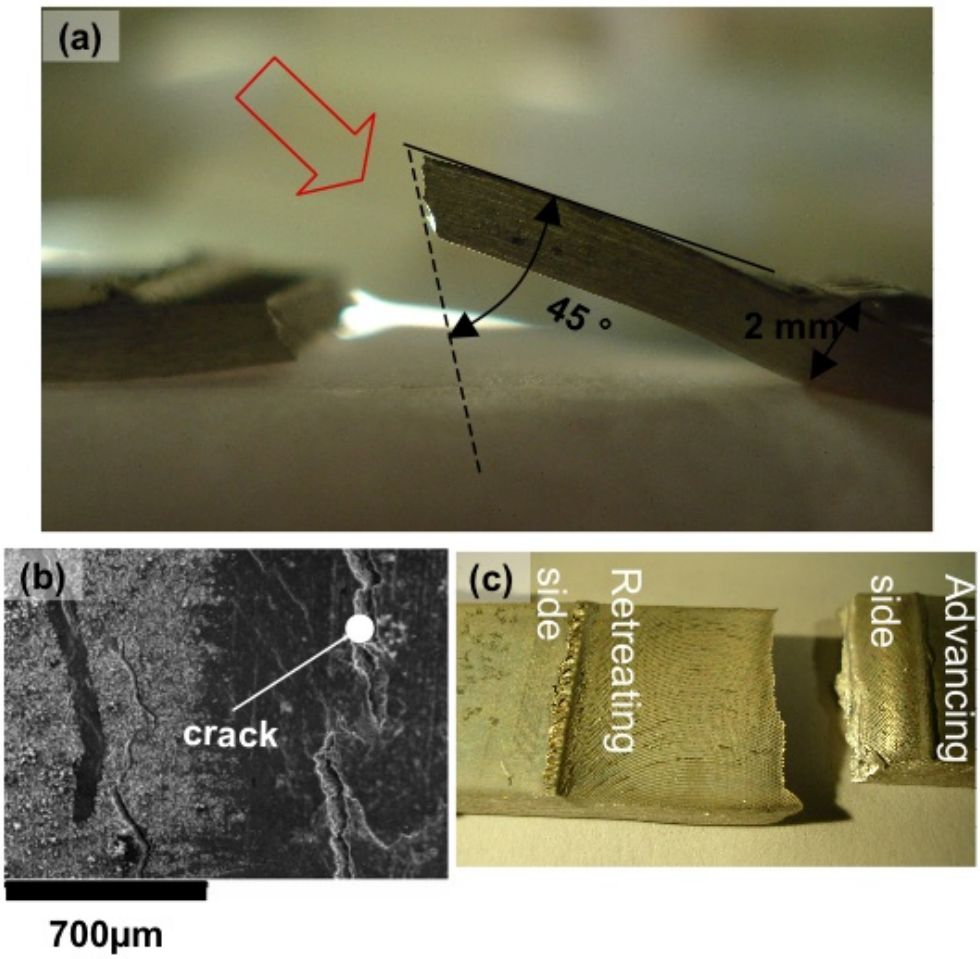

Figure 5.54: Fracture location in AZ31 FSW butt welds: (a) 45˚fracture, (b) crack on the bottom surface and (c) fracture in the advancing side TMAZ.

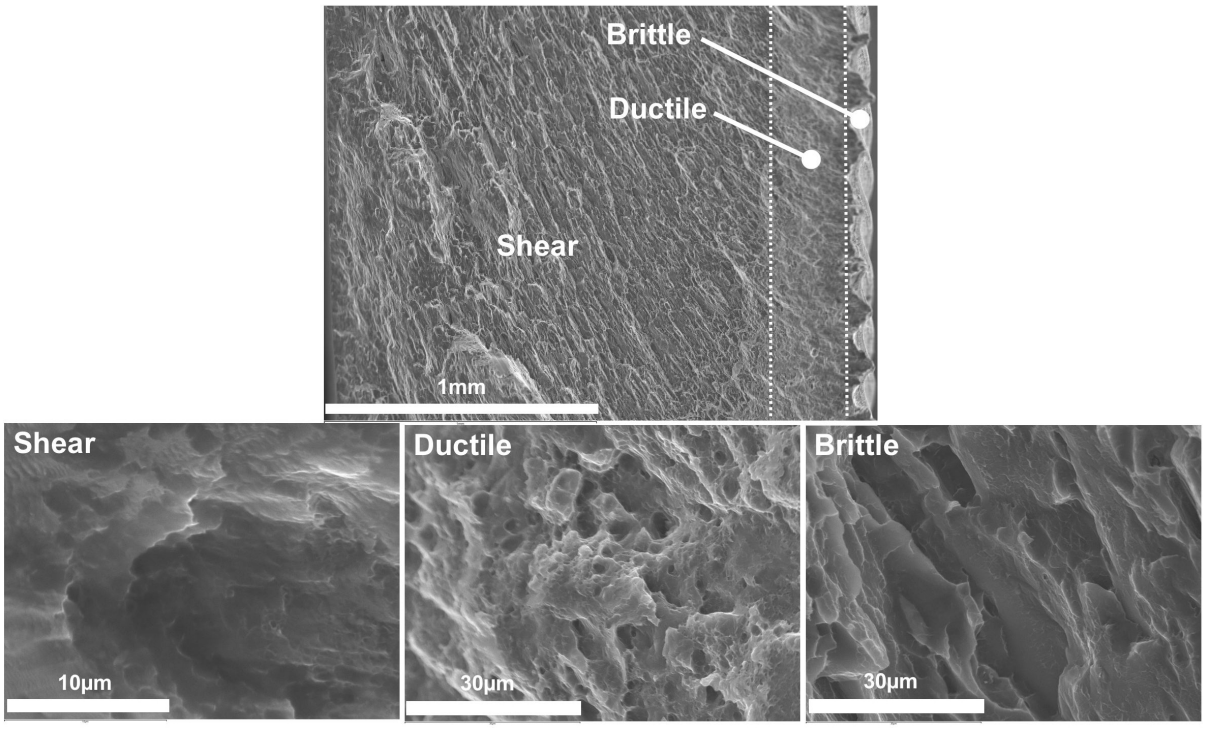

Figure 5.55: Tensile fractographies of FSW butt welds.

Figure 5.56: Fracture location in AZ31 LBW butt welds.

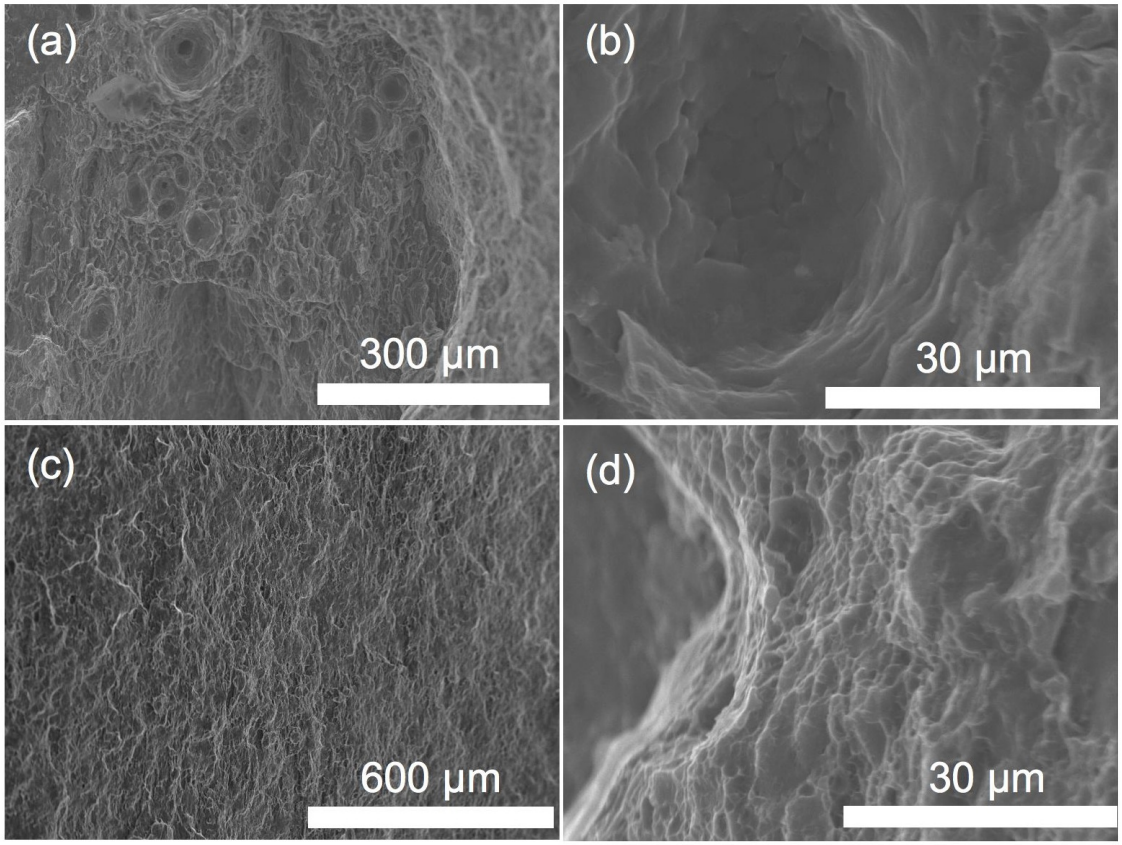

Figure 5.57: Tensile fractographies of AZ31 LBW butt welds: (a), (b) ductile pattern and (c), (d) partly brittle pattern.

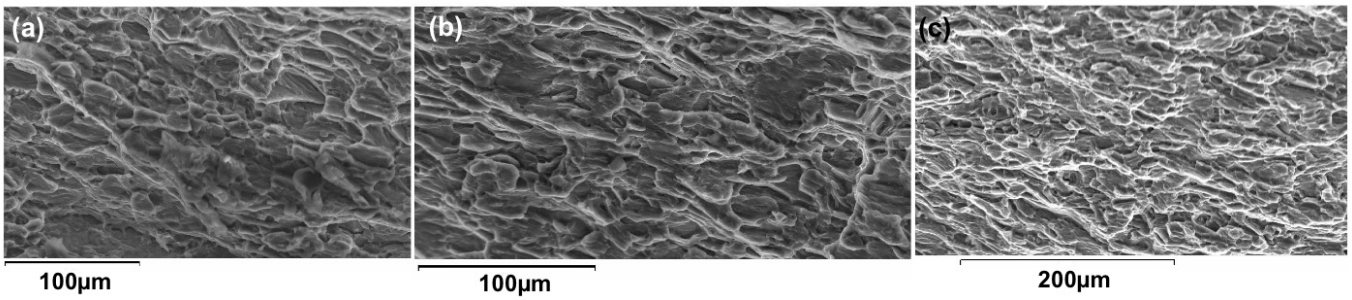

Figure 5.58: Tensile fractographies of AZ31 base metal in (a) Rolling direction, (b) 45 ˚direction and (c) Transverse direction.

5.5.5 Speckle interferometry coupled tensile tests

Speckle interferometry was used to study the local deformations in FSW during tensile test (x: loading direction, y: transverse direction, z:normal direction). The analysis was performed until the load reached 3.44 kN (i.e. 123 MPa). The ϵ_{xx} evolution showed that the strain localisation occured in the TMAZ area, with higher strains on the advancing side, and in the shear bands. The material has almost undergone no strain in the other areas (Figure 5.59). The ϵ_{yy} evolution confirmed the ϵ_{xx} results. Negative strains are observed in the localisation areas (Figure 5.59). The ϵ_{xy} evolution showed shear occuring in the boundary between the areas where the material had undergone deformation and where it had not. This corresponds to the TMAZ/HAZ transition areas and to the shear band initiation zones (Figure 5.59). The shear bands appeared at 2000 N and then their propagation along the sample width occured till 2500 N to reach their full length. Afterwards shear band broadening was observed. The influence of the weld thickness assymmetry was observed in the U_z evolution (Figure 5.59). The rotation of the sample around the tensile direction was observed.

5.5.6 Conclusion

The tensile properties of AZ31 dramatically decreased after welding especially with FSW . The ductility of AZ31 reduced after LBW and FSW. The fracture occurred in the TMAZ for FSW whereas it occured in base metal for LBW. After FSW welding, plastic deformation occured very quickly with high localisation area and 3D component was observed due to the microstructure inhomogeneity in the weld thickness.

5.6 Post-weld heat treatments

5.6.1 Introduction

Several post-weld heat treatments were performed to remove the residual stresses in FSW and homogenize the microstructure in LBW and then to try to improve the weld mechanical properties:

- Solution treatment: 1 h at 530°C for FSW.
- Annealing:
  - 16 h at 180°C for FSW.
  - 1 h at 300°C for LBW.
- Solution treatments + Annealing: 1 h at 530°C followed by 19 h at 180°C for FSW.

The temperature and time of heat treatment were chosen from the literature [136, 128] and the supplier (Magnesium Elektron) data.

5.6.2 Mechanical properties after post-weld heat treatments

The tensile properties of FSW samples after post-weld heat treatments are exhibited in Figure 5.60. Annealing treatment resulted in higher UTS but the yield stress and elongation was still very low and the fracture occured in the weld zone. After solution treatment, a higher strain

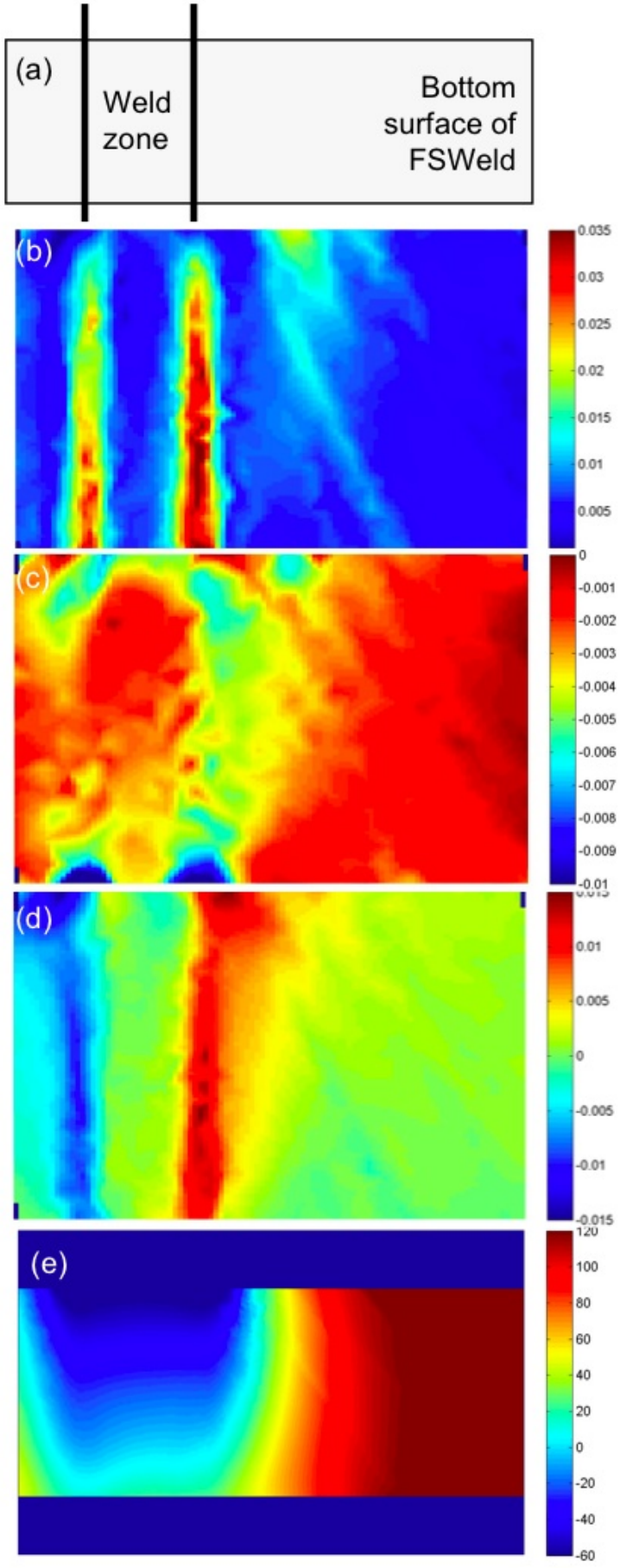

Figure 5.59: (a) Speckle interferometry analysis localtion, (b) Evolution of ϵ_{xx}, (c) Evolution of ϵ_{yy}, (d) Evolution of ϵ_{xy} and (e) Evolution of U_z.

to failure is observed and the fracture occured in the base metal. Then, a solution treatment followed by annealing treatment would result in higher UTS and elongation than "as welded" samples. But this improvement is mainly caused by a decrease in base metal properties after heat treatment. Indeed, the hardening effect of the rolling process is lost after heat treatment. This is consistent with Elangovan et al. [137] who studied the influence of various post-weld heat treatments on FSW of rolled aluminium alloys and Xu et al. [136] who showed that post-weld heat treatment can improve the mechanical properties only in the case of precipitation hardened alloys.
For LBW, annealing heat treatment restored the loss in elongation observed with "as LBW welded" samples (Figure 5.60). After heat treatment, the fracture still occured in the base metal. When observing the microstructure after heat treatment, the fusion zone can no longer be distinguished, because the microstructure has changed (Figure 5.61).The $Mg_{17}(Al,Zn)_{12}$ and the Al-rich solid solution dissolved in the α-Mg matrix. This was also described by Ju et al. after heat treating Rapid Soldified AZ31 [128] . They reported also that the mechanical properties would not be further improved by increasing the annealing temperature and time. These results are consistent with the fact that the lower strain to failure after LBW was attributed to the microstructure change in the fusion zone. A lower yield stress is observed for the LBW samples "as welded" and after heat treatment. This is due to the loss of the hardening provided by the rolling process.

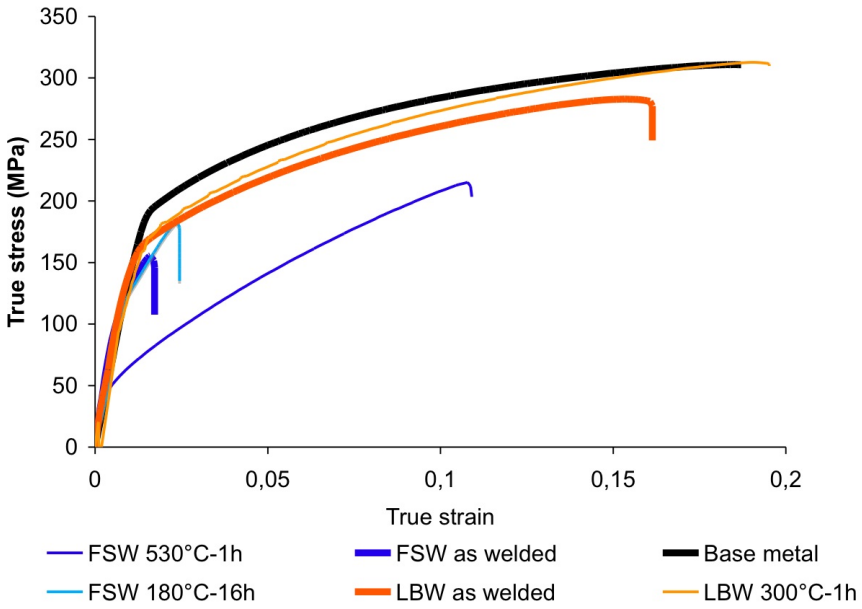

Figure 5.60: Tensile curves of heat treated samples compared to AZ31 base metal and samples as welded.

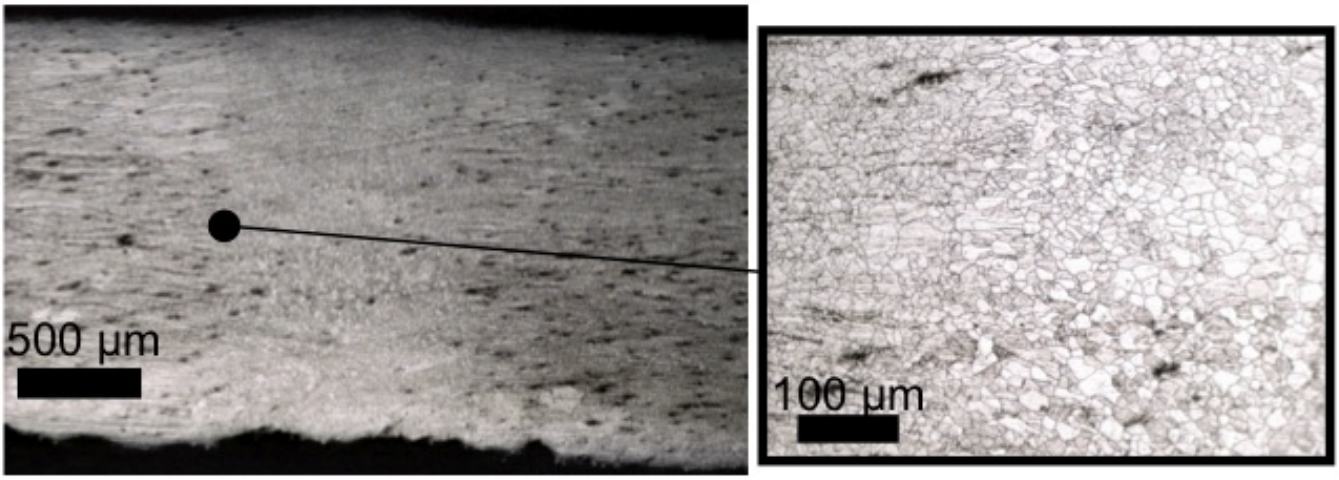

Figure 5.61: Optical micrographs of grain structure in heat treated LBW.

5.6.3 Conclusion

Post-weld heat treatment showed that the mechanical properties of the weld can be improved. In the case of FSW, mechanical properties cannot be restored. After annealing treatment, the base metal properties were also modified and resulting properties are far away from the requirements. In the case of LBW, post-weld heat treatments are promising since a recovery of elongation and UTS can be achieved by a 300°C/1h heat treatment.

5.7 Conclusions

The characterization of FSW and LBW AZ31 optimised joints resulted in the following conclusions. The microstructure and the resulting mechanical properties were investigated. In FSW, an evolution in grain size and texture was observed whereas no precipitation evolution occured. In LBW, the precipitation and textures were modified whereas no change was observed in the grain size. Besides the high grain refinement resulting from FSW, the Hall-Petch relationship which is generally followed [6, 135] was not applicable for hot rolled AZ31. No grain size evolution was observed in the LBWelds studied, then the grain size hardening can be neglected. No precipitation evolution, neither solute modification was observed during FSW, then the precipitation hardening and the solution hardening effects can be neglected. In LBW fusion zone, the $Mg_{17}(Al,Zn)_{12}$ precipitation induces an hardening effect. The AZ31 hot rolled Magnesium alloys get its properties from the rolling process. Then, the grain refinement observed in the FSW nugget and the precipitation hardening in LBW fusion zone must be compensated by the loss of initial rolling hardening in these areas, resulting in microhardness values similar to the base metal ones. The tensile properties of LBW, FSW and base metal are compared in Figure 5.62. LBW showed better mechanical properties than FSW. Post-weld heat treatment resulted in mechanical properties recovery for FSW whereas the FSW mechanical properties remained very low.

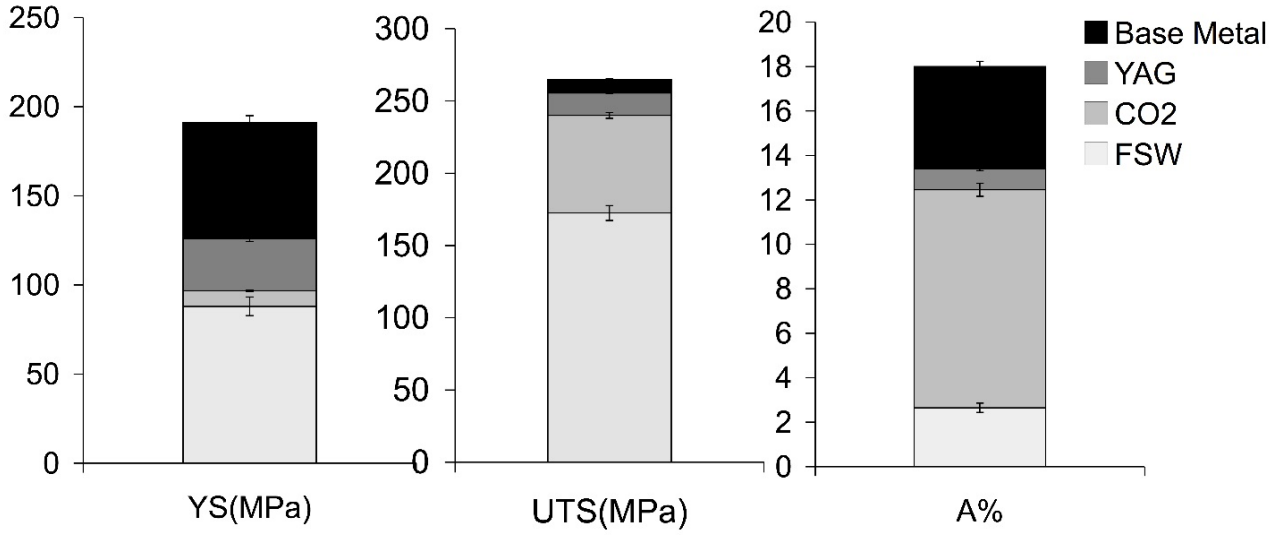

Figure 5.62: Comparison of tensile properties of butt welds resulting from different welding process to base metal ones.

Chapter 6

General discussion

6.1 Introduction

The results obtained during this study led to a better understanding of the relationship between the welding process (FSW or LBW) and the resulting weld quality, microstructure and mechanical properties. Then, FSW and LBW AZ31 alloy will be discussed and compared to the other magnesium alloys studied (AZ61 and WE43). Finally, comparison between FSW and LBW and the aeronautic industry requirements will lead to the determination of the efficiency of these processes to join magnesium alloys.

6.2 Relationship between Processing parameters, Processing temperature, Microstructure and Weld Quality

From the thermocouples measurements, the weld temperature distribution could be determined (see section 4.5). Fitting each curve was performed using: erfc function which is commonly used for diffusion laws [138] (Figure 6.1).

$$T = RT + T_{x0}\ \mathrm{erfc}\left(\frac{x}{2\sqrt{\frac{Kt}{\rho C}}}\right) \tag{6.1}$$

with RT = Room Temperature,T_{x0}= Temperature of heat source, x = distance from heat source, K the thermal conductivity = 96 $\mathrm{Wm^{-1}K^{-1}}$, ρ the alloy density = 1.78 $\mathrm{g.cm^{-3}}$, C the specific heat = 1040 $\mathrm{J.kg^{-1}K^{-1}}$, t the time. The temperature values obtained are valid in Zone I for FSW and LBW. The temperature distribution below the shoulder (Zone II) cannot be described by this behaviour, as it does not take into account the shoulder extra contribution to heat generation. Tang et al. [23] study demonstrated that temperature distribution within the stirred zone is relatively uniform. Then, we can assume that the temperature in Zone III is uniform.

6.2.1 Determination of the FSW nugget temperature (i.e. FSW maximum temperature) from the grain microstructure

In the literature relative to AZ31 Friction Stir Processing [139, 36], empirical relationships were established to calculate the maximum processing temperature (that we will call from now "nugget temperature") from the grain size obtained in the nugget. Chang et al study [139, 37] developed a model for ultra fine grained structure (submicron grains) and Watanabe [36] developed a model for 3-100 μm range grain size.

Watanabe model:

$$10^3.Z^{-1/3} = \left(\frac{D_{\text{nugget}}}{D_{\text{initial}}}\right) \tag{6.2}$$

Chang model:

$$lnD_{\text{nugget}} = 9.0 - 0.27 \ln Z \tag{6.3}$$

with D_{nugget} the grain size in the nugget, D_{initial}, the base metal grain size and Z the Zener-Hollomon parameter The Zener-Hollomon parameter can be described by:

$$Z = \dot{\epsilon} \exp\left(\frac{Q}{RT}\right) \tag{6.4}$$

where Q is the activation energy for lattice diffusion (135 kJ.mol^{-1} [140]), R the gas constant, T the nugget temperature and the strain rate [37]:

$$\dot{\epsilon} = \frac{W.\pi.R_{\text{nugget}}}{d_{\text{nugget}}} \tag{6.5}$$

where R_{nugget} and d_{nugget} are the effective radius and depth of the recrystallized zone. The grain size in the nugget was determined for each (W, V) parameter studied (Table 6.1). The nugget temperatures were then calculated using Chang and Watanabe models (Table 6.1). The temperature at the shoulder edge (ZoneI/ZoneII junction) was determined from experimental data using the fitting function described above. The experimental data grain sizes are in the 1.5-5 μm range, then in between the application range of Chang and Watanabe models. A better description is given in our case with Chang model, with temperature values closer to the measured ones and always below AZ31 melting point. If we compare the nugget temperatures calculated using Chang model and the corresponding Experimental temperature at the shoulder edge for each welding parameter studied, we can calculate the mean difference between these temperatures. The nugget temperature is then about 232.5 $\pm$ 57.6 $^{\circ}$C higher than the temperature at the edge of the shoulder.

6.2.2 Determination of the LBW maximum temperature from the microstructure

Microstructural study of LBW fusion zone showed the presence of Al_8Mn_5 precipitates. Therefore, the maximum temperature undergone in the fusion zone lies in the Liquid + Al_8Mn_5 area of the AZ31/Mn phase diagram, for a Manganese content between 0.2 and 0.6 % [127] (i.e. in the 610-660 $^{\circ}$C range). This corresponds to the LBW Zone I data point indicated in the Figure 6.1.

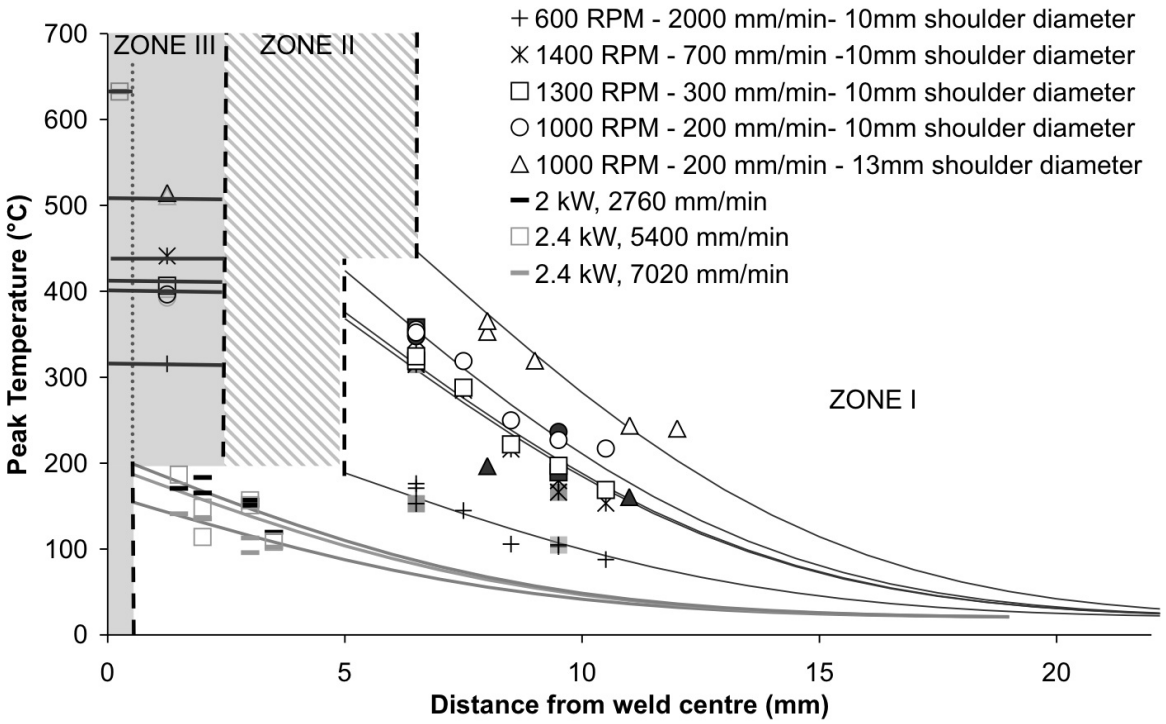

Figure 6.1: Temperature evolution in FSW and LBW. The filled features correspond to the FSW advancing side data. The data in Zone III correspond to the nugget temperatures calculated using Chang model for FSW and to fusion zone temperatures for LBW.

Process	Processing parameters	Tmax (Zone I) (°C)	T_{nugget}(Chang model) $T_{fusion\ zone}$ (°C)
FSW	W=600 RPM, V=2000 mm/min	188.5	315.6
FSW	W=1000 RPM, V=200 mm/min	375.6	396.5
FSW	W=1300 RPM, V=300 mm/min	368.3	406.5
FSW	W=1400 RPM, V=700 mm/min	424.0	441.2
LBW	P=2.4 RPM, V=7020 mm/min	155.1	630
LBW	P=2.4 RPM, V=5400 mm/min	187.4	630
LBW	P=2 RPM, V=2760 mm/min	199.7	630

Table 6.1: Thermal history of welds.

6.2.3 Relationship between processing parameters and heat generation.

6.2.3.1 FSW

The welding parameters have a major influence on the heat generated. Indeed, increasing the tool shoulder diameter, increasing the rotation rate and decreasing the welding speed contribute to increase the process heat generation. From the temperature measurement performed during welding, the influence of processing parameters, such as welding speed, tool rotation rate and shoulder diameter, was investigated. Increasing the W/V ratio leads to an increase in the nugget temperature as found in previous studies [23, 79]. Arbegast and Hartley [82] established a relationship for aluminium alloys between the nugget temperature and the processing parameters (W, V):

$$\frac{T_{\text{nugget}}}{Tm} = K.\left(\frac{W^2}{V.10^4}\right)^{\alpha} \tag{6.6}$$

with Tm the alloy melting point, and the constants α, K varying respectively between 0.04-0.06 and 0.65-0.75. Using this relationship for AZ31 alloy a good agreement was found with the following parameters (Figure 6.2): Tm = 610 °C the alloy melting point, and the constants α = 0.0442 and K = 0.8052

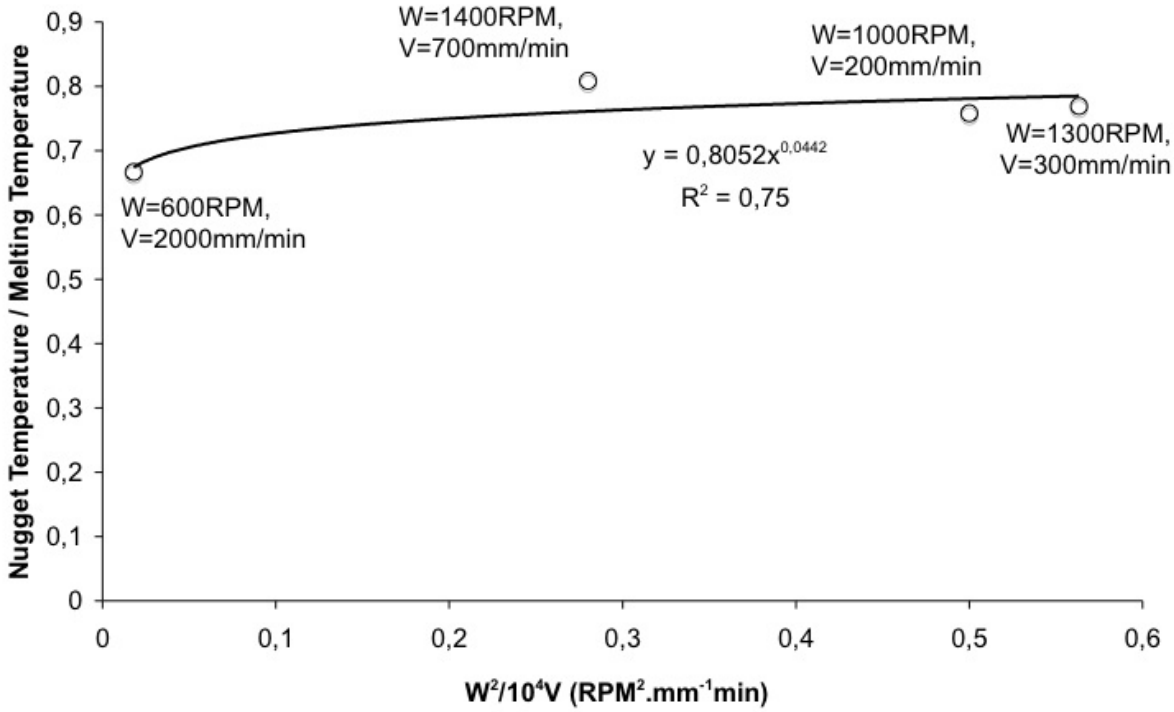

Figure 6.2: Nugget temperature versus W^2/V ratio.

Increasing the shoulder diameter led to an increase in the maximum temperature observed (Figure 6.1) and a modification in the heat dissipation. Indeed, the area which had undergone

friction is larger with increasing shoulder diameter. Then, the heat generated is larger for the same W and V parameters.

6.2.3.2 Relationship with weld quality

The AZ31 FSW process window determination revealed that there was a minimum welding speed (200 mm/min) to achieve sound welds. At low welding speed, the intense stirring causes an increase in the trapped particles content, which can be responsible for the weld defects. Then, above this threshold value, when using low rotation rates, the frictional heat generated is not sufficient to promote material flow and then inner voids all along the weld are created (tunnelling phenomenon). But an excessive increase in rotation rate results in cracks apparition due to the expelling of material. These results are consistent with Nakata study [14], which described the same phenomena for AZ61 alloys. For each "bead on plate" weld of the process window, the nugget temperature can be calculated from the welding parameters (see Figure 6.3). This shows that there is a minimum temperature of about 410°C (i.e. $W^2/V > 4000$ RPM^2min/mm) needed to achieve sound welds. During FSW butt welding, sound welds were achieved at 315°C, then this indicates that a different relationship is required to characterize "bead on plate" welds and that the processing temperature may not be the only one parameter to consider.

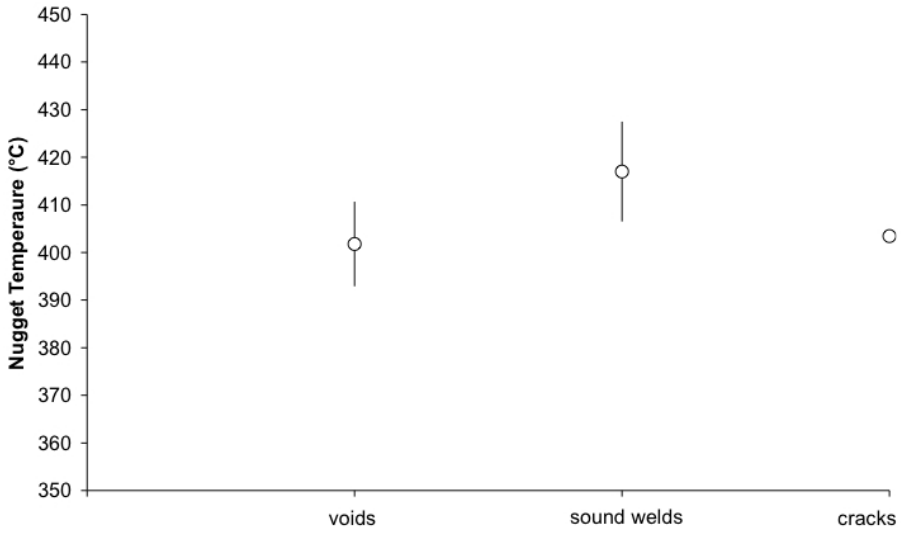

Figure 6.3: Nugget temperature versus weld quality for FSW bead on plate (tool 4mm pin / 10mm shoulder).

For LBW, the laser power (P) and weld speed (V) directly influence the heat input. This relationship was used to determine the heat input for each AZ31 and AZ61 LBW bead on plate of the process window (Figure 6.4). A similar heat input is needed for getting sound welds for each alloy studied. It was then determined that the heat input must be in the 20-45 J/mm range to produce sound welds. Below these values, the heat input is too low and full penetration can not be reached, and above these values, the heat input is too important and then laser cutting is produced.

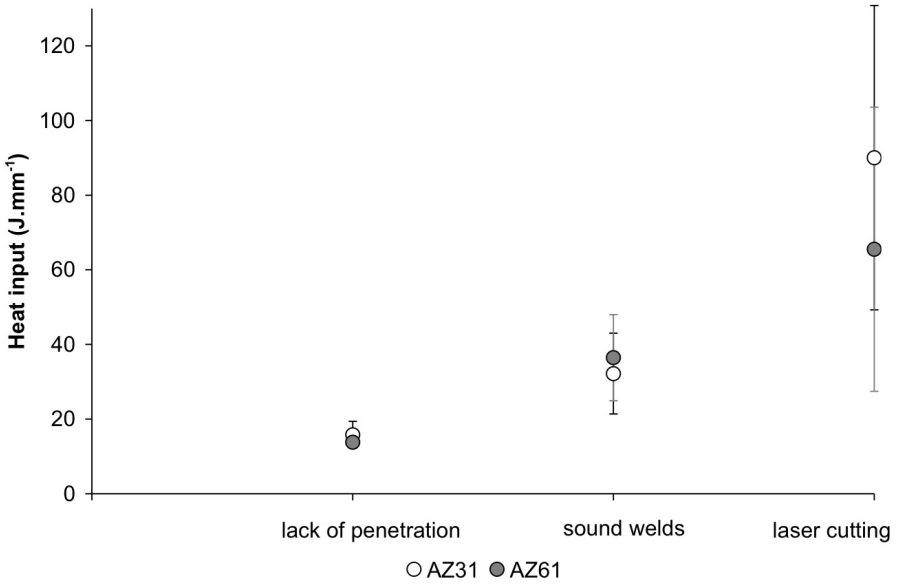

Figure 6.4: Heat input versus weld quality for LBW bead on plate.

6.3 Efficiency of LBW and FSW for joining AZ31 magnesium alloys

The several tensile tests performed on base metal, after LBW, FSW, heat treatments and post-weld heat treatments showed that the base metal properties could not be recovered once the material was welded. The Yield Strength, Ultimate Tensile Strength and Strain to failure were decreased by the welding processes, even more with FSW compared to LBW. The differences between the process performance lie in the different factors influencing the strenghtening mechanisms.

6.3.1 Influence of microstructure evolution

The grain and precipitation evolution did not influence the mechanical properties in FSW whereas it was of major influence in the loss of ductility in LBW. In FSW, the fracture location and the evolution of mechanical properties are generally attributed to microstructure gradients across FSW [17, 141, 135]. In AZ31 the precipitation was not modified during FSW, then the grain size evolution is considered. During the tensile tests performed in this study, the fracture occurred in the area where the microstructural heterogeneity is high (i.e. TMAZ). But, when comparing the mechanical properties of butt welds presenting low grain size gradients (e.g. processed using a higher W/V ratio or a larger shoulder tool) to those presenting high grain size gradients, the following observations can be made: The mechanical properties were similar (or even slightly higher for the higher grain size gradient welds) (see Figure 6.5). This indicates that the grain microstructure heterogeneity is not the prevailing factor for FSW failure.

For LBW, the lower elongation may be caused by the change in microstructure. Microstructure study revealed that the fusion zone had a rapid solidification structure, which presents

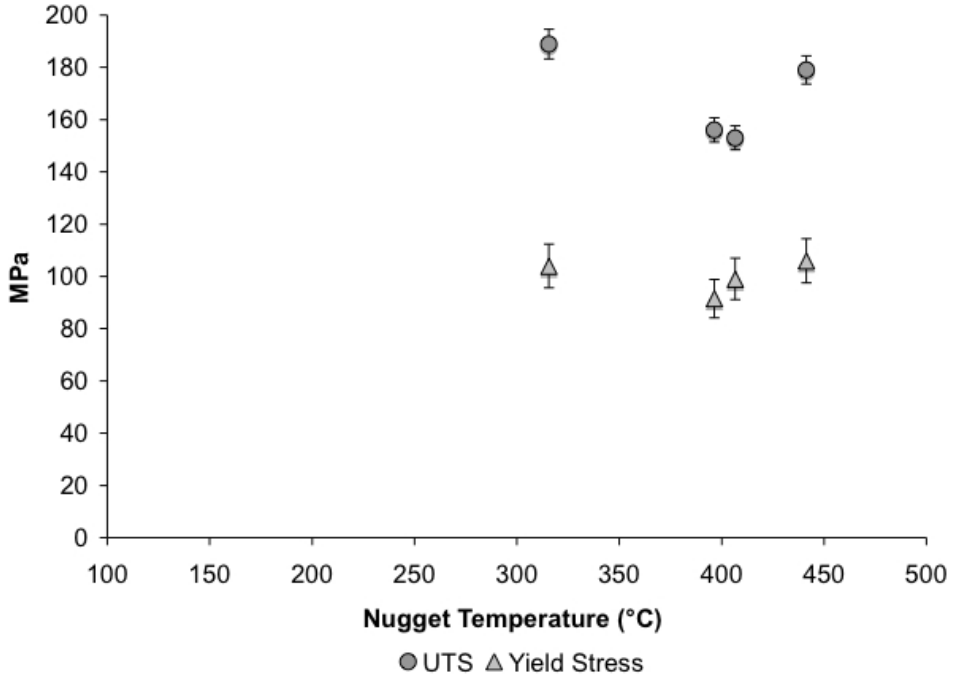

Figure 6.5: Evolution of UTS and Yield Stress with the nugget temperature during FSW butt welding.

lower elongation than the rolled base metal.

6.3.2 Influence of texture evolution

The texture evolution observed in FSW and LBW influences the mechanical properties. Indeed, in FSW, as the texture change occurs in the TMAZ, the fracture will occur in this area. This is consistent with Woo et al. study [4] and Park et al. study [53] which indicated that the large texture variation influenced the tensile properties of FSW and that the fracture was caused by the incompatible boundary between the TMAZ and the nugget.

The texture change observed during LBW could lead to the activation of different deformation mechanisms (non-basal slip and twinning). This was also observed in a previous study on hot rolled AZ31 Nd:YAG welding [3].

6.3.3 Influence of shear bands

The accommodation of plastic deformation in FSW and LBW will be influenced by the shear bands located in the TMAZ. Strain localisation was observed in these areas (Figure 6.6). The highly textured base material could be the main factor generating the shear band formation, as these features were not mentionned in previous studies.

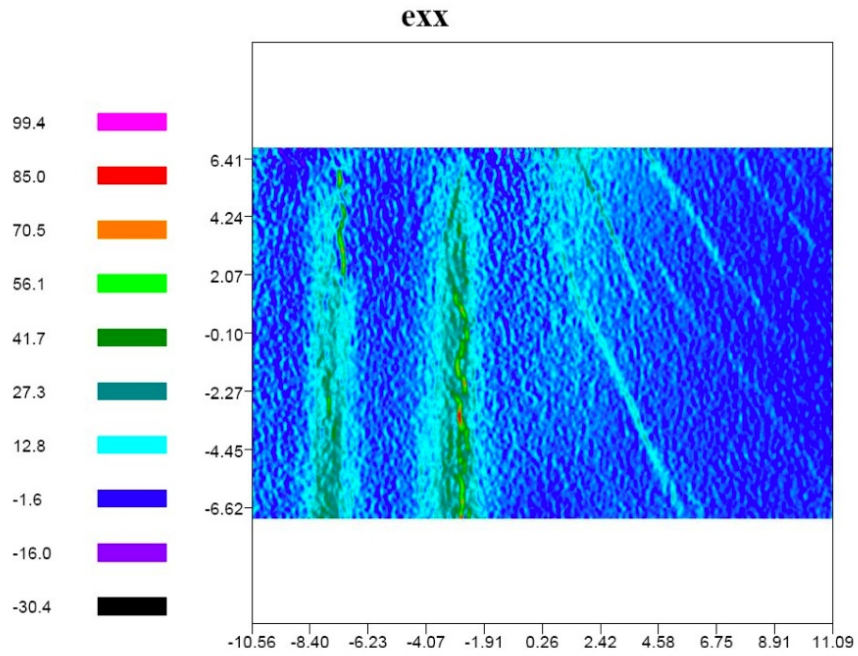

Figure 6.6: Speckle analysis during tensile test showing the strain localisation in the FSW shear bands (ϵ_{xx} analysis with a better resolution (less pixels fitting) than in the Figure 5.59 (a)).

6.3.4 Influence of residual stresses

The major contribution of this study is the characterisation of the residual stress influence on the mechanical properties of FSW and LBW. It must be noted however that the sectionning of the weld to produce test specimens might result in a relaxation of the residual stress field [142].

Adding a tensile stress component which corresponds to the mean butt weld yield strength, to the residual stress tensor was performed: $\sigma_{22}^{\text{True}} = \sigma_{22}^{\text{Residual}} + \sigma_{y}^{\text{Weld}}$ with the loading direction being the weld transverse direction, labelled direction 2. Then, the resulting equivalent stress and hydrostatic stress were calculated and compared to the yield stress of the base material.

Figure 6.7 shows the resulting equivalent stress and hydrostatic stress calculated with applying tensile loading, using the residual stresses obtained by XRD. This analysis was performed across two different FSWelds, processed using two different shoulder diameters (10 mm and 13 mm diameter shoulders). For each FSWeld studied an extremely large increase of the equivalent stress, higher than AZ31 yield stress was observed at the advancing side TMAZ. This corresponds to the fracture location observed during FSW tensile tests.

Figure 6.8 shows the same analysis applied to LBW. The values are far below the AZ31 yield stress (74% of AZ31 YS), then the influence of residual stresses on strength properties can be neglected.

Then, the residual stresses had a major influence on the mechanical properties of FSW, whereas their influence on LBW tensile properties was limited.

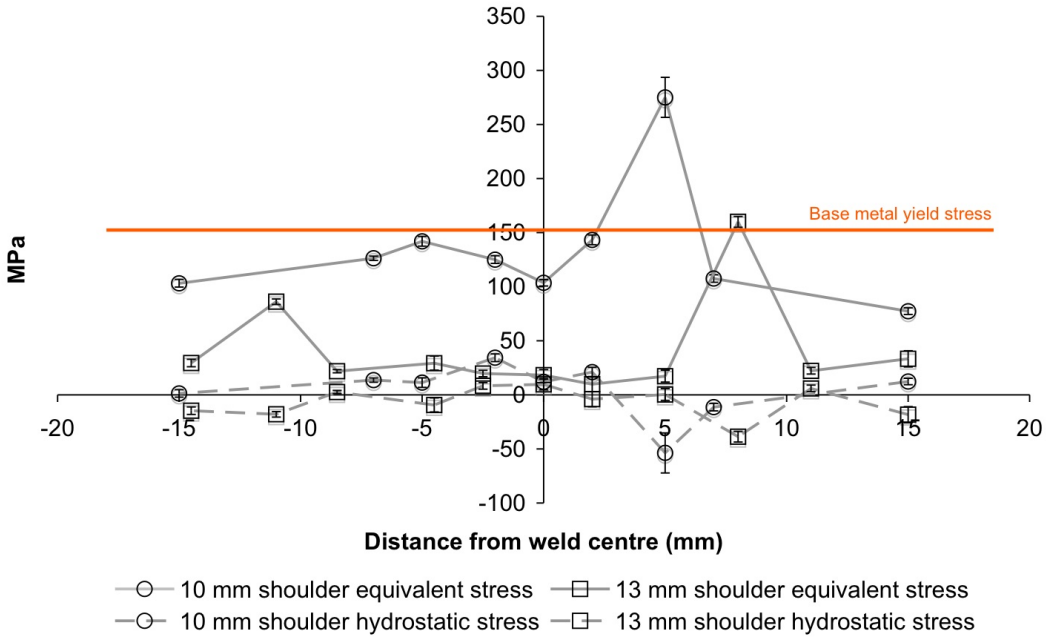

Figure 6.7: Equivalent stress and Hydrostatic stress evolution after tensile loading across FSWelds (1000 RPM, 200 mm/min, tool 5mm pin / 10mm shoulder) and (1000 RPM, 200 mm/min, tool 5 mm pin / 13 mm shoulder).

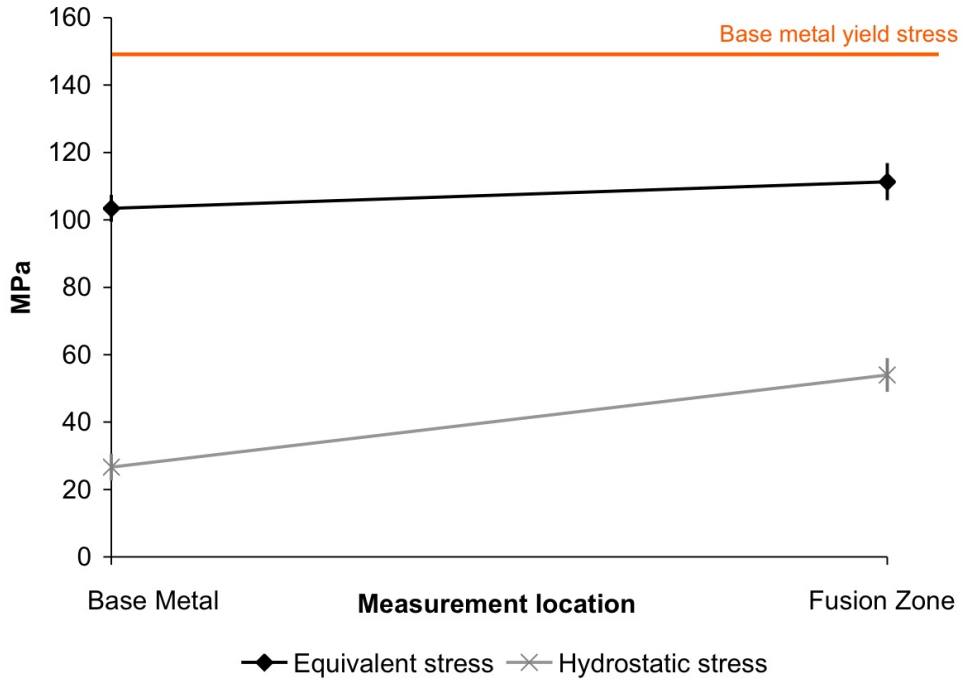

Figure 6.8: Equivalent stress and Hydrostatic stress evolution after tensile loading across LB-Welds (2.4 kW, 7000 mm/min).

The base metal properties could not be recovered even after post-weld heat treatments. It must be noted that AZ31 base metal properties reached in this study are caused by the rolling process. Then, after welding the loss of hardening induced a dramatic loss in mechanical properties which could not be compensated. The same conclusions were drawn by a recent study on Al-Mg-Sc alloys [143]. The FSW properties, apart from the ductility were not strongly affected by post-welding heat treatment. Then, LBW was seen to be more suitable to join AZ31 as the ductility and UTS of the base material were reached after post-weld heat treatments.

6.4 Comparison with precipitation hardened Magnesium alloys

AZ31 magnesium alloy is not a precipitate hardened alloy. The other magnesium alloys that were CO_2 LBW welded during this project were AZ61 and WE43 hot rolled alloys. AZ61 and WE43 base metal microstructure is described in Figure 6.9. It consisted for AZ61 in fine equiaxed $10 \pm 3\mu$m grains with intergranular Al_8Mn_5 and $Mg_{17}Al_{12}$ precipitates located at the grain boundaries. The microstructure was similar in the 3 directions. WE43 presented large variation in grain size ranging between 20 to 80 μm. A large amount of twins and intergranular $Mg_{12}NdY$ precipitates were observed.

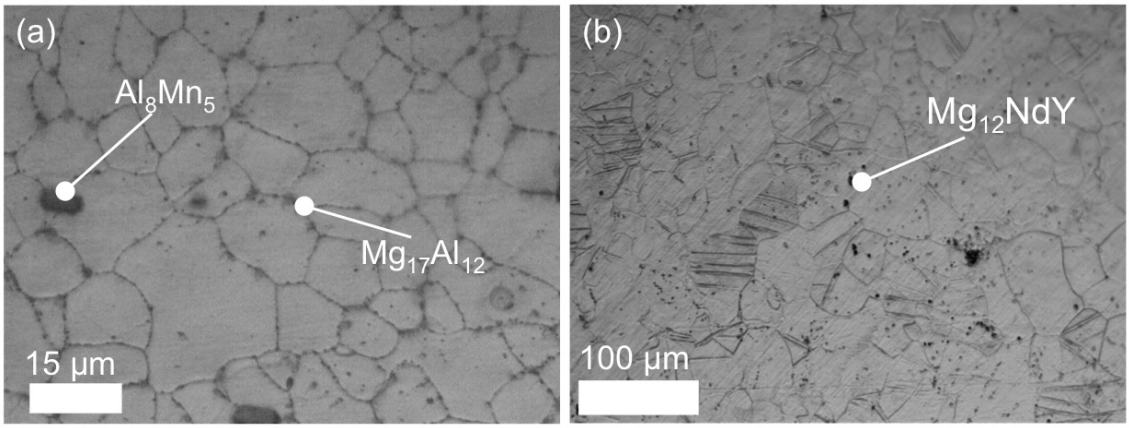

Figure 6.9: Optical micrographs of hot rolled (a) AZ61 and (b) WE43 base metals.

The grain size was seen not to have a strong influence during this study. Then, the main difference in AZ61 and WE43 alloys compared to AZ31 alloy lies in the precipitation. Indeed, especially in WE43 magnesium alloys, precipitation plays a major role in the hardening mechanisms, thus the comparison with AZ31 may show interesting differences and leads to a further interpretation of the results . The comparative study will then focus on the precipitation evolution influence on mechanical properties. After LBW, the microstructure in AZ61 welds consisted in fusion zone containing $Mg_{17}Al_{12}$ dendritic structure and intergranular Al_8Mn_5, similar to AZ31 alloy fusion zone. Then, a dissolution of $Mg_{17}Al_{12}$ was observed in the HAZ (see Figure 6.10). In WE43, the $Mg_{12}NdY$ precipitates were still present in the fusion zone (see Figure 6.10). For AZ61, the microhardness was higher in the fusion zone consecutive to the $Mg_{17}Al_{12}$ formation. A lower microhardness was observed in the HAZ due to the $Mg_{17}Al_{12}$ dissolution (see Figure 6.11).For WE43, a decrease of the microhardness was observed in the fusion zone. Indeed the

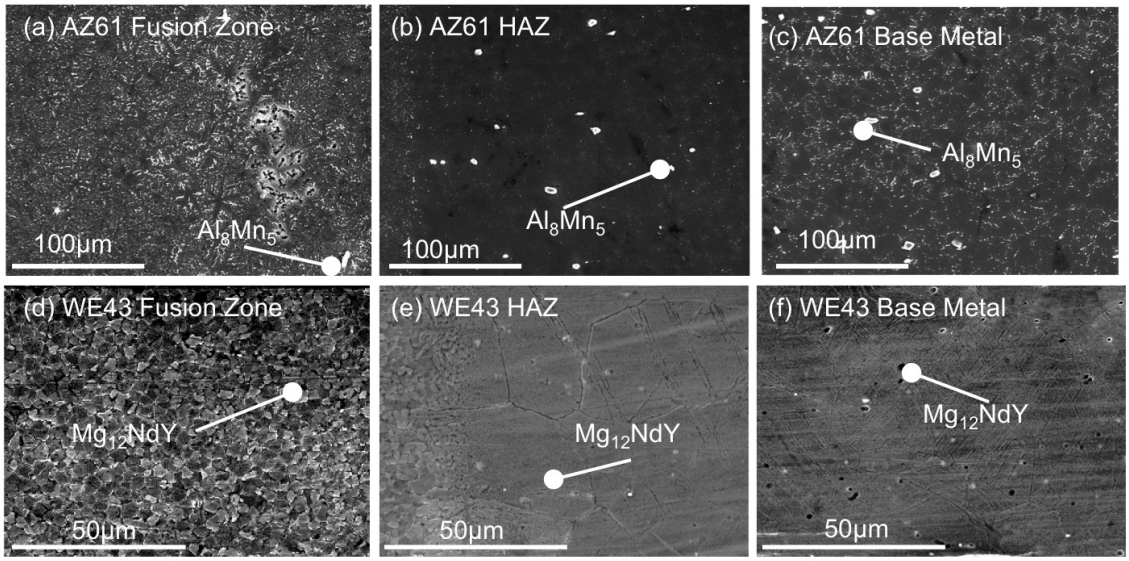

Figure 6.10: SE images of (a) AZ61 Fusion zone, (b) AZ61 HAZ, (c) AZ61 base metal, (d) WE43 Fusion zone, (e) WE43 HAZ and (f) WE43 base metal.

precipitation was not modified, and the amount of twins decreased. The grain refinement did not compensate the microhardness loss (see Figure 6.11).

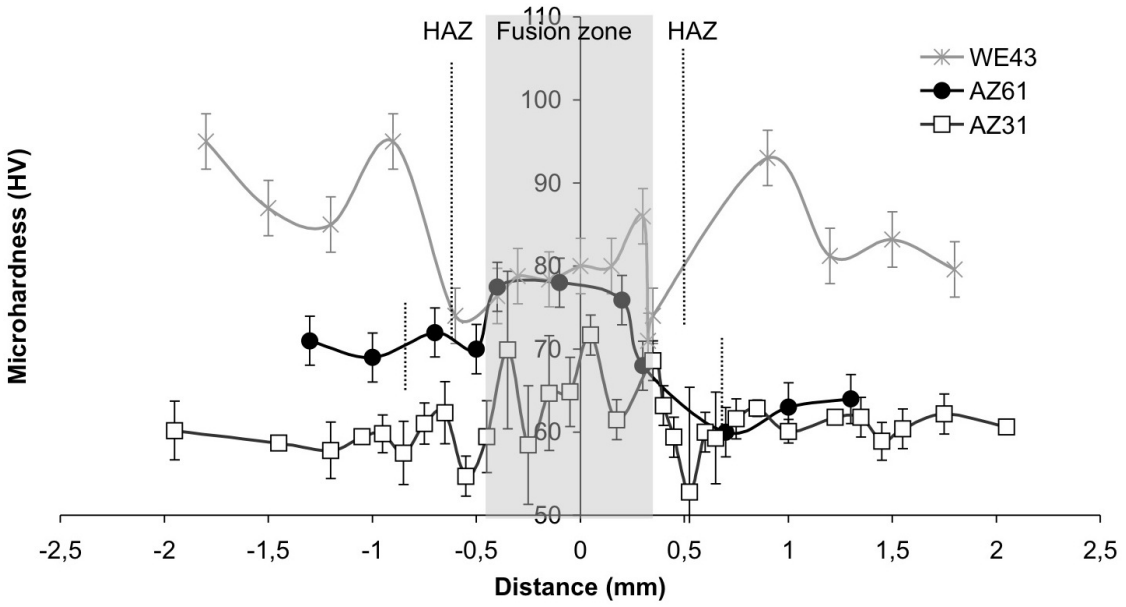

Figure 6.11: Microhardness profiles across AZ31, AZ61 and WE43 LBW processed at P = 3kW, V = 7 m/min.

Tensile tests were performed on base metals, as welded LBW, 1 h at 250 °C heat treated AZ61 LBW and 16 h at 200 °C heat treated WE43 LBW (see Figure 6.12). The loss in mechanical

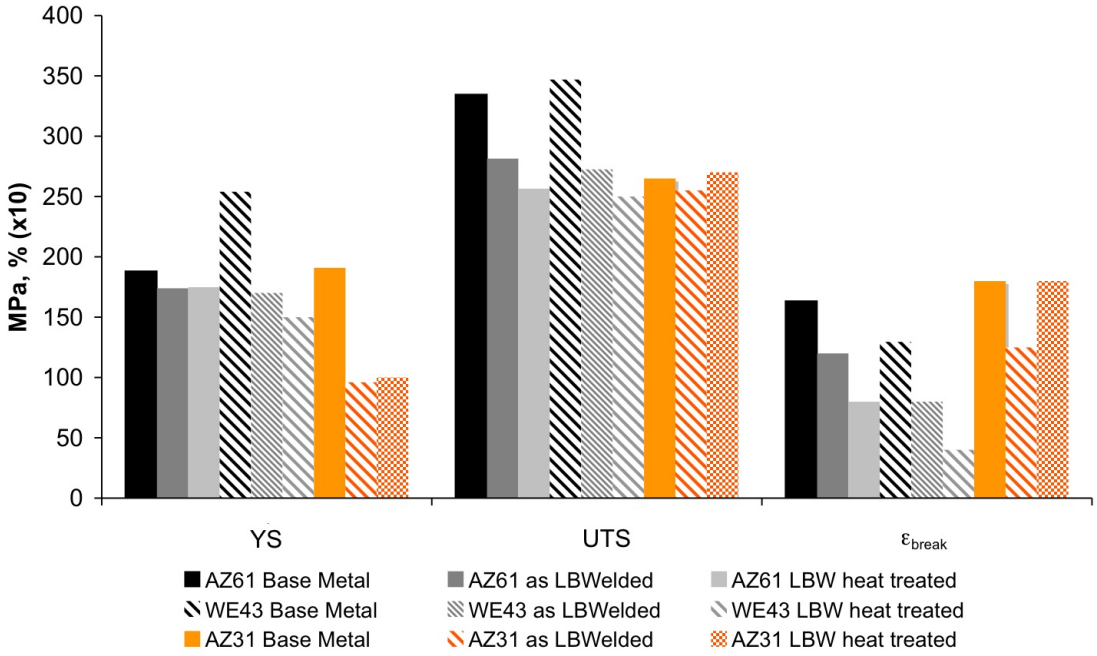

Figure 6.12: Comparison between AZ31, AZ61 and WE43 mechanical properties after LBW.

properties could not be compensated by post-weld heat treatments.

6.5 Comparison with the aeronautic industry requirements

The magnesium alloys investigated in this study are aimed at replacing AA5083 for non-structural applications and AA2024 for secondary structural applications. Table 6.2 shows the density of each alloy. The comparison of the specific properties of the magnesium alloys inves-

Alloy	AA5083	AA2024	AZ31	AZ61	WE43
Density ($g.cm^{-3}$)	2.66	2.78	1.78	1.8	1.84

Table 6.2: Aluminium and magnesium alloys density.

tigated in this study and aluminium alloy specific properties from the literature [6, 7, 8, 9] are shown in Figure 6.13. Concerning the non-structural applications (AA5083), all the magnesium alloys studied are good alternatives as base metal. But when joining is needed, AZ31 LBW with the appropriate post-weld heat treatment is the best suited to reach the same ductility. AZ61 and WE43 could replace AA2024-T3 in secondary structural applications, if used as sheet material. When joining will be necessary, the loss in yield strength of WE43 after LBW will be too important and then, AZ61 will be more appropriate.

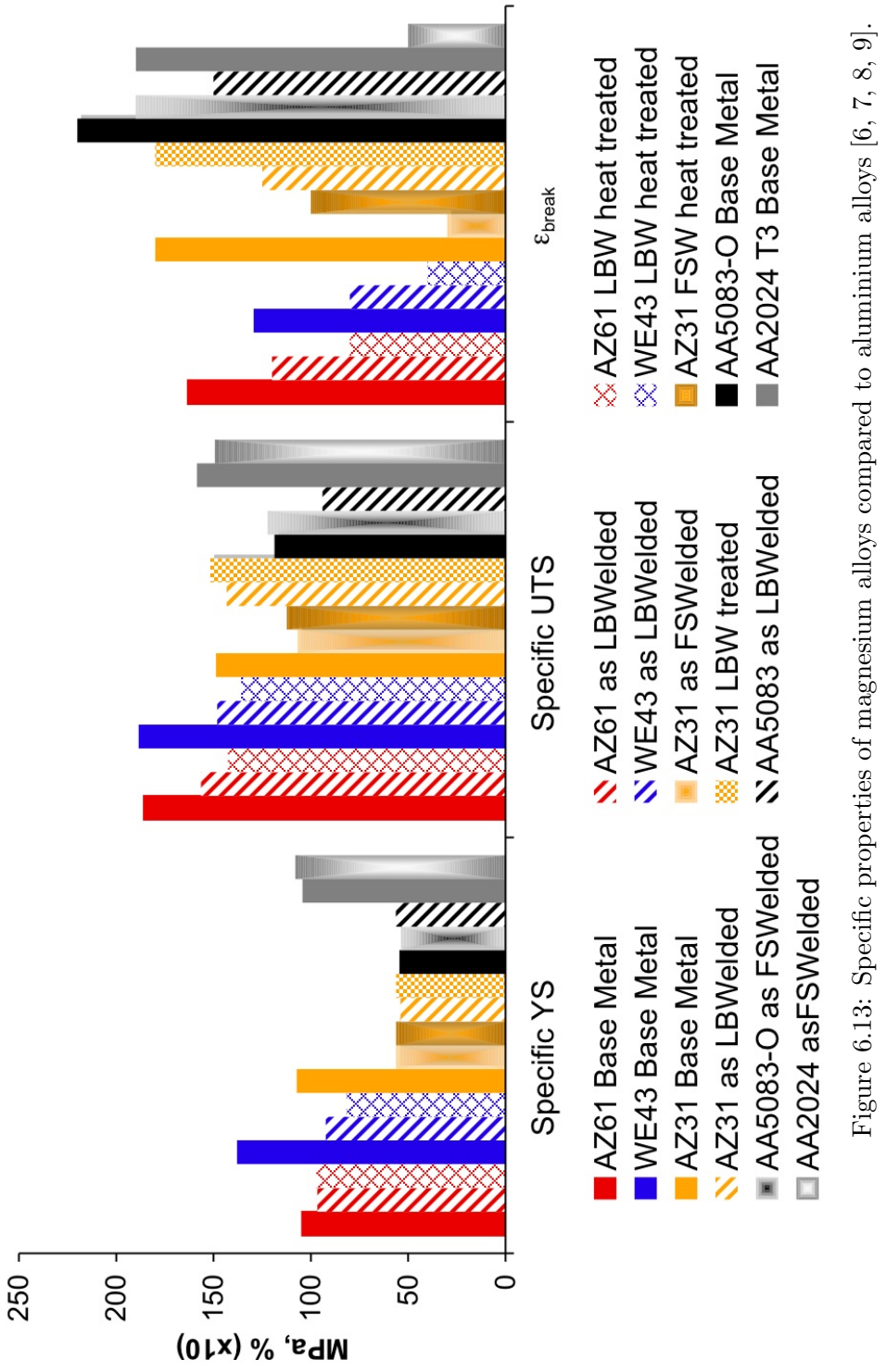

Figure 6.13: Specific properties of magnesium alloys compared to aluminium alloys [6, 7, 8, 9].

Chapter 7

Conclusions

This work is an experimental study aimed at investigating the potentiality of FSW and LBW techniques to join wrought magnesium alloys for aeronautic applications. It was part of AERO-MAG european project, which involved european universities, magnesium and aerospace industries, in order to develop the use of wrought magnesium alloys in aeronautic. The magnesium alloys studied are wrought AZ31, AZ61 and WE43. The main results obtained will be summarized in this section.

Results outline

Welding process FSW and LBW are widely used in aluminium alloys. Their application to wrought magnesium alloy was studied. This led to the following conclusions:

- 2 mm thick plates hot rolled magnesium alloys can be joined using either Laser Beam Welding and Friction Stir Welding, and the process window were determined: a minimum W^2/V ratio of 4000 $RPM^2.min.mm^{-1}$ in FSW and a heat input between 20 and 45 J/mm in LBW were needed to achieve sound welds.

- The processing parameters which affect the weld quality (load applied, weld speed and tool rotation rate for FSW; laser power, welding speed, focal distance and shielding gas for LBW) were identified and their respective influence was analysed.

- Temperature measurements during FSW and LBW welding processes could be performed using embedded thermocouples. The temperature distribution across the welds showed high temperature gradients in LBW and that the temperature did not exceed 450 °C in FSW. Assymmetry in the temperature distribution was observed between FSW advancing and retreating sides.

AZ31 Optimised Welds Characterisation Once the AZ31 optimum welding parameters defined (1000 RPM, 200 mm/min for FSW and 2.4 kW, 7000 mm/min for LBW), the weld characterisation was performed.

- The hot rolled AZ31 base metal consists in fine equiaxed grains, Al_8Mn_5 precipitates and a strong basal texture.

- The FSW microstructure resulted in grain refinement in the nugget area depending on the processing parameters, no precipitation evolution and an important texture evolution.
- The LBW microstructure resulted in the formation of $Mg_{17}(Al,Zn)_{12}$ secondary phase in the fusion zone, in grain size conservation depending on the processing parameters and an important texture evolution.
- High residual stresses are induced by welding processes, in particular by FSW in the TMAZ which involves the ruin of the mechanical properties of AZ31 FSWelds.
- Good mechanical properties can be recovered after post-weld heat treatments in the case of AZ31 LBWelds.

General conclusion

The magnesium alloys studied here are wrought alloys, then they present distinctive properties compared to the magnesium cast alloys which are generally used. They show a strong basal texture consecutive to the rolling process.

This particular base metal condition was not favourable to FSW. Indeed texture evolution, shear band formation and high residual stresses were induced by the FSW process, resulting in a dramatic loss of the mechanical properties. Post-weld heat treatments could not overcome the loss in mechanical properties after FSW. On the contrary, wrought alloys are better suited to LBW than cast alloys because they contain less porosity. The ductility was reduced after LBW due to the fusion zone cast microstructure, but it could be restaured after heat treatment. Contrary to FSW, residual stresses in LBWelds have not a significant influence on final mechanical properties

Then LBW is more appropriate to weld wrought magnesium alloy than FSW and has given promising results in the frame of this project for joining AZ31 hot rolled sheets.

When comparing with LBW of wrought precipitate hardened magnesium alloys (AZ61 and WE43), the precipitation evolution could not compensate the loss in hardening and then a decrease of the mechanical properties was observed. In this case, appropriate heat treatments allowing a good recovery of base metal mechanical properties were not obtained. The AZ61 and WE43 base metal mechanical properties are far higher than AZ31 ones and then they were still higher after LBW, but the loss induced by LBW was higher in WE43 than in AZ61 and AZ31.

Perspectives and future developments

A first development arising from my work would be to investigating the application to real manufacturing parts for aeronautic industry and other transportation industries. The issues of developing process industrialisation would also be worth to take into account. It must also be noted that due to the high suceptibility of magnesium alloys, post-welding corrosion resistance treatments should be investigated. Joining magnesium alloys to other materials, such as alluminium will be needed for an industrial application. Therefore, it would be worth studying dissimilar weld behaviour. A direct development of my work would be to develop modeling aspects, especially concerning FSW, taking into account residual stress and texture evolution.

The study of the shear band formation mechanisms during welding would also be an interesting continuation.

Bibliography

[1] AEROMAG Project AST4-CT-2005-516152. Annex 1 description of work, September 2004.

[2] X. Cao, M. Jahazi, J.P. Immarigeon, and W. Wallace. A review of laser welding techniques for magnesium alloys. *Journal of Materials Processing Technology*, 171:188–204, 2006.

[3] R.S. Coelho, A. Kostka, H. Pinto, S. Riekehr, M. Koçak, and A.R. Pyzalla. Microstructure and mechanical properties of magnesium alloy AZ31B laser beam welds. *Materials Science and Engineering: A*, 485(1-2):20–30, 2008.

[4] W. Woo, H. Choo, D.W. Brown, P.K. Liaw, and Z. Feng. Texture variation and its influence on the tensile behavior of a friction-stir processed magnesium alloy. *Scripta Materialia*, 54:1859–1864, 2006.

[5] W. Woo, H. Choo, M.B. Prime, Z. Feng, and B. Clausend. Microstructure, texture and residual stress in a friction-stir-processed AZ31B magnesium alloy. *Acta Materialia*, 56(8):1701–1711, 2008.

[6] T. Hirata, T. Oguri, H. Hagino, T. Tanaka, S.W. Chung, Y. Takigawa, and K. Higashi. Influence of friction stir welding parameters on grain size and formability in 5083 aluminum alloy. *Material Science and engineering A*, 2007.

[7] A. Ancona, P.M Lugara, D. Sorgente, and L. Tricarico. Mechanical characterization of CO2 laser beam butt welds of AA5083. *Journal of materials processing technology*, 191:573–583, 2007.

[8] C. Genevois. *Genèse des microstructures lors du soudage par friction malaxage d'alliages d'aluminium de la série 2000 et 5000 et comportement mécanique résultant.* PhD thesis, INPG, 2004.

[9] C. Genevois, A. Deschamps, and P. Vacher. Comparative study on local and global mechanical properties of 2024-T351, 2024-T6 and 5251-O friction stir welds. *Materials Science and Engineering A*, 415:162–170, 2006.

[10] ASM International. Aluminium-magnesium binary diagram, 2006.

[11] S. R. Agnew and O. Duygulu. Plastic anisotropy and the role of non-basal slip in magnesium alloy AZ31B. *International Journal of Plasticity*, 21:1161–1193, 2005.

[12] C.E.D. Rowe and W.M. Thomas. Advances in tooling materials for friction stir welding. Technical report, TWI Ltd Cambridge, UK.

[13] W.M. Thomas, E.D. Nicholas, and S.D. Smith. In *Proceedings of the TMS 2001 Aluminium automotive joining sessions*, page 213, 2001.

[14] K. Nakata, Y.G. Kim, and M. Ushio. Friction stir welding of Mg-Al-Zn alloys. *Transactions of the Joining Welding Research Institute*, 31(2):141–146, 2002.

[15] X. Wang and K. Wang. Microstructure and properties of friction stir butt- welded AZ31 magnesium alloy. *Materials science and engineering A*, 431:114–117, 2006.

[16] M.A. Gharacheh, A.H. Kokabi, G.H. Daneshi, and R. Shalchi, B. Sarrafi. The influence of the ratio of "rotational speed / transverse speed (w/v) on mechanical properties of AZ31 friction stir welds. *International journal of machine tool and manufacture*, 3:333–338, 2001.

[17] R.S. Mishraa and Z.Y. Ma. Friction stir welding and processing. *Materials Science and Engineering Reports*, 50(1-78), 2005.

[18] M. Dhahri, J.E. Masse, J.F. Mathieu, G. Barreau, and M. Autric. Laser weldability of WE43 magnesium alloys for aeronautic industry. In *Third LANE 2001: Laser Assisted Net Shape Engineering*, pages 297–310, 28-31 August 2001.

[19] M. Dhahri, J.E. Masse, J.F. Mathieu, G. Barreau, and M. Autric. Laser welding of AZ91 and WE43 magnesium alloys for automotive and aerospace industries. *Advanced engineering materials*, 3(7):504–507, 2001.

[20] H.Y. Wang and Z.J. Li. Investigation of laser beam welding process of AZ61 magnesium-based alloy. *Acta metallurgica sinica (english letters)*, 19(4):287–294, 2006.

[21] E. Aghion and B. Bronfin. Magnesium alloys development towards the 21st century. *Material Science Forum*, 2000.

[22] B.C. Liechty and B.W. Webb. The use of plasticine as an analog to explore material flow in friction stir welding. *Journal of Materials Processing Technology*, 184(1-3):240–250, 2007.

[23] W. Tang, X. Guo, J.C. McClure, and L.E. Murr. Heat input and temperature distribution in friction stir welding. *Journal of Materials Processing and Manufacturing Science*, 7:163–172, 1998.

[24] R.S. Huang, L.M. Liu, and G. Song. Infrared temperature measurement and interference analysis of magnesium alloys in hybrid laser- TIG welding process. *Materials Science and Engineering: A*, 447:239–243, 2007.

[25] P. Vilaça, L. Quintino, and J. F. dos Santos. iSTIR-analytical thermal model for friction stir welding. *Journal of Materials Processing Technology*, 169:452–469, 2005.

[26] K. Nakata, S. Inoki, Y. Nagano, T. Hashimoto, S. Johgan, and M. Ushio. Friction stir welding of AZ91 thixomolded sheet. In *Proceedings of the Third International Symposium on Friction Stir Welding, Kobe, Japan, September 27–28*, 2001.

[27] D. C. Joy. *Monte Carlo Modeling for Electron Microscopy and Microanalysis.* Oxford University press, 1995.

[28] A.G. Odeshi and M.N. Bassim. Evolution of adiabatic shear bands in a dual-phase steel at very high strain rates. *Materials Science and Engineering: A*, 488:235–240, 2008.

[29] M.M. Avedesian and H. Baker. *Magnesium and magnesium alloys.* ASM Specialty Handbook, 1999.

[30] G.V. Raynor. *The Physical metallurgy of Magnesium and its alloys.* New York Pergamon Press, 1959.

[31] C.S. Roberts. *The deformation of magnesium. Magnesium and Its Alloys.* Wiley, New York, 1964.

[32] B.C Wonsiewicz and W.A. Backofen. *Plasticity of magnesium crystals*, chapter 239, pages 1422– 1431. Trans. TMS-AIME, 1967.

[33] M.T. Perez-Prado, J.A. del Valle, and O.A. Ruano. Effect of sheet thickness on the microstructural evolution of an Mg AZ61 alloy during large strain hot rolling. *Scripta Materialia*, 50:667–671, 2004.

[34] J.A. del Valle, M.T. Perez-Prado, and O.A. Ruano. Texture evolution during large-strain hot rolling of the mg AZ61 alloy. *Materials Science and Engineering A*, 355:68–78, 2003.

[35] R. Gehrmann, M.M. Frommert, and G. Gottstein. Texture effects on plastic deformation of magnesium. *Materials Science and Engineering A*, 395:338–349, 2005.

[36] H. Watanabe, H. Tsutsui, T. Mukai, H. Ishikawa, Y. Okanda, M. Kohzu, and K. Higashi. Grain size control of commercial wrought Mg-Al-Zn alloys utilizing dynamic recrystallization. *Materials Transansactions*, 42:1200–1205, 2001.

[37] C.I. Chang, C.J. Lee, and J.C. Huang. Relationship between grain size and zener–holloman parameter during friction stir processing in AZ31 Mg alloys. *Scripta Materialia*, 51(6):509–514, 2004.

[38] L. Boehm. New engineering processes in aircraft construction: Application of laser-beam and friction stir welding. In *Glass Physics and Chemistry, Proceedings of the 3rd Russian–Israeli bi-national Workshop 2004 "The optimization of the composition, structure and propoerties of metals, oxides, composites, nanomaterials and amorphous materials " St. Petersburg, Russia, June 13–23, 2004*, volume 33, pages 27–29, 2005.

[39] W.M. Thomas, E.D. Nicholas, J.C. Needham, M.G. Murch, P. Templesmith, and C.J. Dawes. G.B. patent application materials N°. 9125978.8. Technical report, TWI, 1991.

[40] Z. Li and S. L. Gobbi. Laser welding for lightweight structures. *Journal of Materials Processing Technology*, 70:137–144, 1997.

[41] K. Behler, J. Berkmanns, A. Ehrhardt, and W. Frohn. Laser beam welding of low weight materials and structures. *Materials and Design*, 18:261–267, 1997.

[42] E. Schubert, M. Klassen, I. Zerner, C. Walz, and G. Sepold. Light-weight structures produced by laser beam joining for future applications in automobile and aerospace industry. *Journal of Materials Processing Technology*, 115(1):2–8, 2001.

[43] C.J. Dawes and W.M. Thomas. *TWI Bulletin*, 6:124, November/December 1995.

[44] J.C. Mc Clure, E. Coronado, S. Aloor, B.M. Nowak, L.E. Murr, and A.C. Nunes. Effect of pin tool shape on metal flow during friction stir welding. In ASM International 2003, editor, *6th international trends in welding research conference proceedings, 15-19 April 2002*, 2002.

[45] M. Boz and A. Kurt. The influence of stirrer geometry on bonding and mechanical properties in friction stir welding process. *Materials and design*, 25:343–347, 2004.

[46] K. Wang, J. Liu, K. Xu, and Y. Shen. The influence of the stirrer's shape and process parameter on friction stir welded MB3 magnesium joining. *Materials Science Forum*, 475-479:485–488, 2005.

[47] S.W. Kalee, W.M. Thomas, and E.D. Nicholas. Friction stir welding of lightweight materials. *Magnesium alloys and their applications*, pages 175–190, 2000.

[48] R. Zettler, A.C. Blanco, J.F. dos Santos, and S. Marya. The effect of process parameters and tool geometry on thermal field development and weld formation in friction stir welding of the alloys AZ31 and AZ61. *Magnesium technology*, pages 409–423, 2005.

[49] W.B. Lee, Y.M. Yeon, K.K. Shae, Y.J Kim, and S.B. Jung. Microstructure and mechanical properties of friction stir welded AZ31 magnesium alloy. *Magnesium technology*, pages 309–312, 2002.

[50] S. Lin, Zhang H., Wu L., Feng J., and Dai H. Friction stir welding of AZ31 magnesium alloy. *China welding*, 12(2):137–141, 2003.

[51] H. Zhang, S.B. Lin, L. Wu, J.C. Feng, and S.L. Ma. Defects formation procedure and mathematic model for defect free friction stir welding of magnesium alloy. *Materials and design*, 2005.

[52] J. Yan, Z. Xu, Z. Li, and L. Li. Microstructure and mechanical performance of friction stir welded joints of AZ31 magnesium alloy. *Trans. Nonferrous Met. Soc. China*, 15(2):21–24, 2005.

[53] S. H. C. Park, Y.S. Sato, and H. Kokawa. Effect of micro-texture on fracture location in friction stir weld of Mg alloy AZ61 during tensile test. *Scripta Materialia*, 49:161–166, 2003.

[54] P.G. Sanders, J.S. Keske, K.H. Leong, and G. Kornecki. High power Nd:YAG and CO2 laser welding of magnesium. *Journal of Laser Applications*, 11(2):96–103, 1999.

[55] K.H. Leong, P.G. Sanders, J.S. Keske, and G. Kornecki. Laser beam welding of AZ31B-H24 alloy. *ICALEO 98: Laser Material processing conference, Orlando, FL*, pages 28–36, 16-19 November 1998.

[56] H. Haferkamp, M. Goede, A. Bormann, and P. Cordini. Laser beam welding of magnesium alloys-new posiibilities using filler wire and arc welding. In *LANE: Laser Assited Net Shape Eng.*, volume 3, pages 333–338, 2001.

[57] K.G. Watkins. Laser welding of magnesium alloys. In H.I. Kaplan, editor, *Magnesium Technology, TMS Annual Meeting and Exhibition, San Diego, CA*, pages 153–156, 2003.

[58] C. Lehner, G. Reinhart, and L. Schaller. Welding of die cast magnesium alloys for production. *Journal of Laser applications*, 11(5):206–210, 1999.

[59] M. Pastor, H. Zhao, and T. DebRoy. Continuous wave Nd:YAG laser welding of AM60B magnesium alloy. *Journal of laser apllications*, 12(3):91–100, 2000.

[60] Z. Zhao and T. DebRoy. Pore formation during laser beam welding of die cast magnesium alloy AM60B -mechanism and remedy. *Welding journal*, 80(8):204S–210S, 2001.

[61] M. Marya and G.R. Edwards. The laser welding of magnesium alloy AZ91. *Weld. world*, 44(2):31–37, 2000.

[62] A. Weisheit, R. Galun, and B.L. Mordike. Weldability of various magnesium alloys using a CO2 laser. *IIW seminar, Trends Weld. Lightweight automobile railroad vehicles*, pages 28–41, 1997.

[63] M. Marya and G.R. Edwards. Factors controlling the magnesium weld morphology in deep penetration welding by a CO2 laser. *Journal of Materials Engineering and Performance*, 10(4):435–443, 2001.

[64] A. T. D'Annessa. Sources and effects of growth rate fluctuation during weld metal solidification. *Welding Journal*, 49(2):41–45, 1970.

[65] M. Dhahri, J.E. Masse, J.F. Mathieu, G. Barreau, and M. Autric. CO2 laser welding of magnesium alloys. In *Proceedings of the SPIE: High power lasers in manufacturing*, pages 725–732, 2000.

[66] H. Hiraga, T. Inoue, S. Kamado, and Y. Kojima. Effect of the shielding gas and laser wavelenght in laser welding magnesium alloy sheet. *Quart J Jpn WeldSoc*, 19(4):591–599, 2001.

[67] L. Barrallier, A. Fabre, J.E. Masse, and M. Ceretti. Residual stress measurements using neutron diffraction in magnesium alloy laser welded joints. *Material Science Forum*, pages 404–407, 2002.

[68] H. Haferkamp, I. Burmester, and M. Niemeyer. Laser beam welding of magnesium alloys technological developments and advances for australian industry. In *Proceedings of the 1997 International welding and joining research conference, WTIA 45th annual conference, Vic.*, pages 333–338, 10-12 November 1997.

[69] T. U. Seidel and A. P. Reynolds. Visualization of material flow in AA2195 friction stir welds using a marker insert technique. *Metallurgical and Materials Transactions*, 32A:2879–2884, 2001.

[70] M. Guerra, J.C. McClure, L.E. Murr, and A.C. Nunes. Metal flow. during friction stir welding. In R.S. Mishra S.L. Semiatin D.P. Filed (Eds.) K.V. Jata, M.W. Mahoney, editor, *n:Friction Stir Welding and Processing, TMS, Warrendale, PA, USA*, page 25, 2001.

[71] K. Colligan. Material flow behavior during friction stir welds of aluminium. *Welding Journal*, 78:229S–237S, 1999.

[72] B. London, M. Mahoney, W. Bingel, M. Calabrese, R.H. Bossi, and D. Waldron. In R.S. Mishra S.L. Semiatin T. Lienert (Eds.) K.V. Jata, M.W. Mahoney, editor, *Friction Stir Welding and Processing II, TMS*, page 3, 2003.

[73] Y. Li, L.E. Murr, and J.C. McClure. Flow visualization and residual microstructures associated with the friction-stir welding of 2024 aluminum to 6061 aluminum. *Materials Science and Engineering A*, pages 213–223, 1999.

[74] J.H. Ouyang and R.Kovacevic. Material flow and microstructure in the friction stir butt welds of the same and dissimilar aluminum alloys. *Journal of Materials engineering performance*, 11:51–63, 2002.

[75] K. Kumar and S. V. Kailas. The role of friction stir welding tool on material flow and weld formation. *Materials Science and Engineering A*, 485:367–374, 2008.

[76] K. S. Vecchio D. C. Hofmann. Thermal history analysis of friction stir processed and submerged friction stir processed aluminum. *Materials Science and Engineering A*, 465:165–175, 2007.

[77] M. Song and R. Kovacevic. Thermal modeling of friction stir welding in a moving coordinate system and its validation. *International Journal of Machine Tools and Manufacture*, 43:605–615, 2003.

[78] Y.S. Sato, H. Kokawa, M. Enmoto, and S. Jogan. Microstructural evolution of 6063 aluminum during friction-stir welding. *Metallurgical and Materials Transaction A*, 30:2429–2437, 1999.

[79] T. Hashimoto, S. Jyogan, K. Nakata, Y.G. Kim, and M. Ushio. Fsw joints of high strenght aluminium alloy. In *Proceedings of the First International Symposium on Friction Stir Welding, Thousand Oaks, CA, USA, June 14–16, 1999*, 1999.

[80] P. A. Colegrove and H. R. Shercliff. 3-dimensional CFD modelling of flow round a threaded friction stir welding tool profile. *Journal of Materials Processing Technology*, 169(2):320–327, 2005.

[81] C.G. Rhodes, M.W. Mahoney, W.H. Bingel, R.A. Spurling, and C.C. Bampton. Effects of friction stir welding on microstructure of 7075 aluminum. *Scripta Materialia*, 36(1):69–75, 1997.

[82] W.J. Arbegast and P.J. Hartley. Friction stir weld technology development at Lockheed Martin Michoud space systems-an overview. In *Proceedings of the Fifth International Conference on Trends in Welding Research, Pine Mountain, GA, USA, June 1-5,*, 1998.

[83] R. Nandan, G. G. Roy, T. J. Lienert, and T. DebRoy. Numerical modelling of 3D plastic flow and heat transfer during friction stir welding of stainless steel. *Science and Technology of Welding and Joining*, 11:526–537, 2006.

[84] Y.J. Chao, X. Qi, and W. Tang. Heat transfer in friction stir welding-experimental and numerical studies. *Journal of Manufacturing Science and Engineering*, 125:138–146, 2003.

[85] H.B. Schmidt and J.H. Hattel. Thermal modelling of friction stir welding. *Scripta Materialia*, 58:332–337, 2008.

[86] K.J. Colligan and R.S. Mishrab. A conceptual model for the process variables related to heat generation in friction stir welding of aluminum. *Scripta Materialia*, 58:327–331, 2008.

[87] P. A. Colegrove, H. R. Shercliff, and R. Zettler. Model for predicting heat generation and temperature in friction stir welding from the material properties. *Science and Technology of Welding and Joining*, 12:284–297, 2007.

[88] X.F. Wang, X.D. Lu, G.N. Chen, Sh.G. Hu, and Y.P. Su. Research on the temperature field in laser hardening. *Optics and Laser Technology*, 38:8–13, 2006.

[89] G. Brüggemann, A. Mahrle, and T. Benziger. Comparison of experimental determined and numerical simulated temperature fields for quality assurance at laser beam welding of steels and aluminium alloyings. *NDT.E International*, 33:453–463, 2000.

[90] W. Chen and P. Molian. Dual-beam laser welding of ultra-thin AA 5052-H19 aluminum. *The International Journal of Advanced Manufacturing Technology*, 2007.

[91] A.P. Mackwood and R.C.Crafer. Thermal modelling of laser welding and related processes: a literature review. *Optics and Laser Technology*, 37:99–115, 2005.

[92] C. Zhou, X. Yang, and G. Luan. Investigation of microstructures and fatigue properties of friction stir welded Al-Mg alloy. *Materials Chemistry and Physics*, 98:285–290, 2006.

[93] M.W. Mahoney, C.G. Rhodes, J.G. Flintoff, R.A. Spurling, and W.H. Bingel. Properties of. friction-stir-welded 7075 T651 aluminum. *Metallugical Materials Transaction A*, 29:1955, 1998.

[94] A.P. Reynolds. Visualisation of material flow in an autogenous friction stir weld. *Science and Technology of Welding and Joining*, 5:120, 2000.

[95] B. Heinz and B. Skrotzki. Characterization of a friction-stir-welded aluminum alloy 6013. *Metallurgical Materials Transaction B*, 33(6):489, 2002.

[96] Z.Y. Ma, R.S. Mishra, and M.W. Mahoney. Superplastic deformation behaviour of friction stir processed 7075Al alloy. *Acta Materialia*, 50:4419–4430, 2002.

[97] M. Mahoney, R.S. Mishra, T. Nelson, J. Flintoff, R. Islamgaliev, and Y. Hovansky. In R.S. Mishra S.L. Semiatin D.P. Filed (Eds.) K.V. Jata, M.W. Mahoney, editor, *Friction Stir Welding and Processing, TMS, Warrendale, PA, USA*, 2001.

[98] G. Liu, L.E. Murr, C.S. Niou, J.C. McClure, and F.R. Vega. Microstructural aspects of the friction-stir welding of 6061-T6 aluminum. *Scripta Materialia*, 37:355–361, 1997.

[99] K. V. Jata and S. L. Semiatin. Continuous dynamic recrystallization during friction stir welding of high strength aluminum alloys. *Scripta materialia*, 43:743–749, 2000.

[100] J. A. Esparza, W. C. Davis, E. A. Trillo, and L.E. Murr. Friction-stir welding of magnesium alloy AZ31B. *Journal of materials science letters*, 21(12):917–920, 2002.

[101] P.B. Prangnell and C.P. Heason. Grain structure formation during friction stir welding observed by the 'stop action technique'. *Acta Materialia*, 53:3179–3192, 2005.

[102] J. Q. Su, T. W. Nelson, R. Mishra, and M. Mahoney. Microstructural investigation of friction stir welded 7050-T651 aluminium. *Acta Materialia*, 51:713–729, 2003.

[103] T. Al-Samman and G. Gottstein. Dynamic recrystallization during high temperature deformation of magnesium. *Materials Science and Engineering A*, 490:411–420, 2008.

[104] S. E. Ion, F. J. Humphreys, and S. H. White. Dynamic recrystallisation and the development of microstructure during the high temperature deformation of magnesium. *Acta Metallurgica*, 30:1909–1919, 1982.

[105] W. Woo, H. Choo, D.W. Brown, S.C. Vogel, P.K. Liaw, and Z. Feng. Texture analysis of a friction stir processed 6061-T6 aluminum alloy using neutron diffraction. *Acta Materialia*, 54:3871–3882, 2006.

[106] C.Dalle Donne, E. Lima, J. Wegener, A. Pyzalla, and T. Buslaps. Investigations on residual stresses in friction stir welds. In *in: Proceedings of the Third International Symposium on Friction Stir Welding, Kobe, Japan, September 27–28, 2001.*, 2001.

[107] M. Peel, A. Steuwer, M. Preuss, and P. J. Withers. Microstructure, mechanical properties and residual stresses as a function of welding speed in aluminium AA5083 friction stir welds. *Acta Materialia*, 51(16):4791–4801, 2003.

[108] R.V. Preston, H.R. Shercliff, P.J. Withers, and S. Smith. Physically-based constitutive modelling of residual stress development in welding of aluminium alloy 2024. *Acta materialia*, 52:4973–4983, 2004.

[109] A. Steuwer, M.J. Peel, and P.J. Withers. Dissimilar friction stir welds in AA5083-AA6082: The effect of process parameters on residual stress. *Materials Science and Engineering: A*, 441:187–196, 2006.

[110] A. Steuwer, M. Dumont, M. Peel, M. Preuss, and P.J. Withers. The variation of the unstrained lattice parameter in an AA7010 friction stir weld. *Acta Materialia*, 55:4111–4120, 2007.

[111] M. B. Prime, T. Gnäupel-Herold, J. A. Baumann, R. J. Lederich, D. M. Bowden, and R. J. Sebring. Residual stress measurements in a thick, dissimilar aluminum alloy friction stir weld. *Acta Materialia*, 54:4013–4021, 2006.

[112] T. Nagasawa, M. Otsuka, T. Yokota, and T. Ueki. *Structure and mechanical properties of friction stir welded joints of magnesium alloy AZ31*, chapter Magnesium Technology 2000, pages 383–387. The Mineral, Metals and Materials society, 2000.

[113] Y.J. Quan, Z.H. Chen, X.S. Gong, and Z.H. Yu. Effects of heat input on microstructure and tensile properties of laser welded magnesium alloyAZ31. *Materials Characterization*, 2008.

[114] F. Lagattu, J. Brillaud, and M.-C. Lafarie-Frenot. High strain gradient measurements by using digital image correlation technique. *Materials characterization*, 53(1):17–28, 2004.

[115] Z.Keshavarz and M. R. Barnett. EBSD analysis of deformation modes in Mg-3Al–1Zn. *Scripta Materialia*, 55:915–918, 2006.

[116] L. Castex, J.L. Lebrun, G. Maeder, and J.M. Sprauel. *Détermination des contraintes résiduelles par diffraction X*, volume 22. Publications Scientifiques et Techniques, ENSAM, 1981.

[117] L. Lutterotti, S. Matthies, and H.R. Wenk. Maud (material analysis using diffraction): a user friendly java program for rietveld texture analysis and more. In *Proceeding of the Twelfth International Conference on Textures of Materials (ICOTOM-12)*, volume 1, page 1599, 1999.

[118] E. Pluyette, J.M. Sprauel, A. Lodini, M. Perrin, and 1996 P. Todeschini pp. 153-163. Residual stresses evaluation near interfaces by means of neutron diffraction : modelling a spectrometer. In *Proceedings of ECRS4*, pages pp. 153–163, 1996.

[119] E. Pluyette, J.M. Sprauel, M. Cerretti, and P. Todeschiniand A. Lodini. Neutron diffraction residual stress evaluation around a bimetal welded joint. In A. Anderson Ed. T. Ericson, M. Oden, editor, *Proceedings of ICRS5, Institute of technology, Linköping's University, 16-18 juin 1997*, pages pp. 604–609, 1997.

[120] E. Pluyette. *Évaluation par diffraction de neutrons, des contraintes résiduelles dans les liaisons bi-métalliques.* PhD thesis, ENSAM, 1997.

[121] D. Peng and P. Molian. Q-switch Nd:YAG laser welding of AISI 304 stainless steel foils. *Materials Science and Engineering: A*, 486(1-2):680–685, 2008.

[122] M. Jariyaboon, A.J. Davenport, R. Ambat, B.J. Connolly, S.W. Williams, and D.A. Price. The effect of welding parameters on the corrosion behaviour of friction stir welded AA2024–T351. *Corrosion Science*, 49(2):877–909, 2007.

[123] S. Kleiner, O. Beffort, A. Wahlen, and P.J. Uggowitzer. Microstructure and mechanical properties of squeeze cast and semi-solid cast Mg-Al alloys. *Journal of Light Metals*, 2:277–280, 2002.

[124] V.Y. Gertsman. Microstructure and second phase particles in low and high pressure die-cast magnesium alloy AM50. *Metallurgical and materials transaction A*, 36A:1989–1997, 2005.

[125] T.W. Wright. *The physics and mathematics of adaibatic shear bands*. Cambridge University Press, 2002.

[126] L. Chen and R.C. Batra. Effect of material parameters on shear band spacing in work-hardening gradient dependent thermoviscoplastic materials. *International Journal of plasticity*, 15:551–574, 1999.

[127] T. Laser, M.R. Nürnberg, A. Janz, C. Hartig, D. Leitzig, R. Schmid-Fetzer, and R. Bormann. The influence of manganese on the microstructure and mechanical properties of AZ31 gravity die cast alloys. *Acta Materialia*, 54(11):3033–3041, 2006.

[128] D.Y Ju and X.D Hu. Effect of casting parameters and deformation on microstructure evolution of twin-roll casting magnesium alloy AZ31. *Transactions of Non ferrous Metals Society of China*, 16:874–877, 2006.

[129] Y. Tamura, Y. Kida, H. Tamehiro, N. Kono, H. Soda, and A. McLean. The effect of manganese on the precipitation of Mg17Al12 phase in magnesium alloy AZ91. *Journal of Materials Science*, 43:1249–1258, 2008.

[130] F. Czerwinski. The oxidation behaviour of an AZ91D magnesium alloy at high temperatures. *Acta Materialia*, 50:2639–2654, 2002.

[131] T. R. Long and C. S. Smith. Single-crystal elastic constants of magnesium and magnesium alloys. *Acta Metallurgica*, 5(4):200–207, 1957.

[132] M. Francois. *Detemination de contraintes residuelles sur des fils d'acier eutectoïde de faible diametre par diffraction de rayons* X. PhD thesis, ENSAM, 1991.

[133] M.J. Jones, P. Heurtier, C. Desrayaud, F. Montheillet, D. Allehaux, and J.H. Driver. Correlation between microstructure and microhardness in a friction stir welded 2024 aluminium alloy. *Scripta Materialia*, 52(8):693–697, 2005.

[134] S. Lim, S. Kim, C.G. Lee, C.D. Yim, and S.J. Kim. Tensile behavior of friction-stir-welded AZ31-H24 Mg alloy. *Metallurgical and Materials Transactions A*, 36:1609, 2005.

[135] N. Afrin, D.L. Chena, X. Cao, and M. Jahazi. Microstructure and tensile properties of friction stir welded AZ31B magnesium alloy. *Materials Science and Engineering A*, 2008.

[136] D.K. Xu, L. Liu, and Y.B. Xu. The effect of precipitates on the mechanical properties of ZK60-Y alloy. *Materials Science and Engineering A*, 420:322–332, 2006.

[137] K. Elangovan and V. Balasubramanian. Influences of post-weld heat treatment on tensile properties of friction stir-welded AA6061 aluminum alloy joints. *Materials characterization*, 2008.

[138] Y. Adda and J. Philibert. *La diffusion des solides*. Presses universitaires de France, 1966.

[139] C.I. Chang, X.H. Du, and J.C. Huang. Achieving ultrafine grain size in Mg–Al–Zn alloy by friction stir processing. *Scripta Materialia*, 57(3):209–212, 2007.

[140] H.J. Forst and M.F. Ashby. Pergamon Press, Oxford, 1982.

[141] A.H. Feng and Z.Y. Ma. Enhanced mechanical properties of Mg–Al–Zn cast alloy via friction stir processing. *Scripta Materialia*, 56:397–400, 2007.

[142] J. Altenkirch, A. Steuwer, M. Peel, D.G. Richards, and P.J. Withers. The effect of tensioning and sectioning on residual stresses in aluminium AA7749 friction stir welds. *Materials science and engineering A*, 488:16–24, 2008.

[143] A. Cabello Munoz, G. Ruckert, B. Huneau, X. Sauvage, and S. Marya. Comparison of TIG welded and friction stir welded Al–4.5Mg–0.26Sc alloy. *Journal of Materials Processing Technology*, 197:337–343, 2008.

ASSEMBLAGE DES ALLIAGES DE MAGNÉSIUM LAMINÉS À CHAUD PAR SOUDAGE FRICTION MALAXAGE ET SOUDAGE LASER - APPROCHE EXPERIMENTALE VERS UNE COMPRÉHENSION DES PROPRIÉTÉS MÉCANIQUES -

RÉSUMÉ *: En raison de la faible densité des alliages de magnésium, un intérêt grandissant est apparu pour leur application dans l'industrie aéronautique. De ce fait, il s'est avéré nécessaire de développer l'assemblage de ces matériaux, notamment par des procédés de soudage innovants, tels le soudage par Friction malaxage (FSW) et le soudage laser. Le but de ce projet est d'étudier les relations entre les paramètres de soudage, les températures et les déformations générées et enfin la microstructure et le comportement mécanique des joints soudés. Ce projet fait partie du projet européen AEROMAG qui a pour objectif de promouvoir l'utilisation des alliages de magnésium corroyés dans l'industrie aéronautique. Les alliages étudiés sont l'AZ31, l'AZ61 et le WE43 sous forme de tôles de 2mm d'épaisseur. Le matériau de base présente une forte texture de fibre par rapport au plan basal. Les soudures ont été effectuées par FSW par laser Nd:YAG et par laser CO_2. Le domaine de soudabilité opérationnel (DSO) a été déterminé pour chacun des procédés. Ensuite, l'analyse des joints soudés s'est plus spécialement focalisée sur les soudures optimisées d'AZ31. Une relation entre les paramètres de soudage et la microstructure des joints soudés a pu être trouvée. Le procédé de FSW entraîne une évolution de la microstructure et de l'état de contraintes résiduelles qui ont montré une influence déterminante sur le comportement mécanique des joints soudés. En ce qui concerne le soudage laser, l'influence prépondérante se situe dans l'évolution des textures et de l'état de précipitation. Des localisations de déformation assimilables à des bandes de cisaillement ont été identifiées dans chacun des procédés. Une comparaison a été menée en vue d'établir le procédé le mieux adapté à l'assemblage de tôles de magnésium laminées. Le FSW provoque une diminution très importante des propriétés mécaniques et l'utilisation de traitements thermique n'a pas permis de recouvrer les propriétés du matériau de base; tandis que les propriétés mécaniques des joints soudés laser après traitement thermique sont proches de celles du matériau de base. Une comparaison a été effectuée avec les propriétés mécaniques des joints soudés d'alliages de magnésium à durcissement structural (AZ61 et surtout WE43). Enfin, leur potentialité pour remplacer les alliages d'aluminium a été étudiée.*

Mots-clés: *alliages de magnésium, soudage FSW, soudage laser, microstructure, contraintes résiduelles, diffraction des rayons X et des neutrons, textures, EBSD, interférométrie speckle*

JOINING HOT-ROLLED MAGNESIUM ALLOYS USING FSW AND LBW - AN EXPERIMENTAL APPROACH THROUGH MECHANICAL PROPERTIES UNDERSTANDING -

ABSTRACT*: The challenges of weight reduction in aerospace industry have drawn considerable interest in magnesium alloys technologies. Assessing the efficiency of new joining techniques, such as Laser Beam Welding and Friction Stir Welding is then required. The aim of this study is to investigate the relationship between welding parameters and the resulting microstructure and mechanical properties. It was part of the AEROMAG European Project whose objective was the use of wrought Magnesium alloys in aeronautics. Friction Stir Welds and Laser Beam (Nd:YAG and CO_2) Welds were processed using 2 mm thick hot rolled plates of AZ31, AZ61 and WE43 Magnesium alloys. The process window for LBW and FSW was determined. The weld characterisation was focused on AZ31 alloy. A relationship between welding parameters, the temperatures undergone and the weld microstructure was established for each process. FSW induced microstructural changes and complex residual stress distribution, which have a primary influence in FSW mechanical properties. The influence of texture evolution and precipitation evolution on LBW mechanical properties was also determined. Localisation features similar to shear bands were observed in both LBW and FSW. FSW resulted in a dramatic loss in mechanical properties, which could not be recovered after heat treatments, whereas LBW presented after heat treatment mechanical properties similar to those of the base metal. A comparison was made with precipitation hardenened alloys (AZ61 and WE43) mechanical properties. Finally, the potentiality of replacing aluminium alloys with these magnesium alloys was studied.*

Keywords*: magnesium alloys, FSW, LBW, microstructure, residual stress, XRD, neutron diffraction, textures, EBSD, speckle interferometry*

ARTS ET MÉTIERS ParisTech